High Speed Green-Taxiing Motor-Generator Drive System for Mild Hybridization of Turboprop Aircraft

Yuzheng Chen (BEng, MSc)

Thesis submitted to the University of Nottingham

for the degree of Doctor of Philosophy

February 2023

Acknowledgement

Firstly, I am extremely grateful to my supervisors, Dr. Tao Yang and Prof. Serhiy Bozhko for their invaluable advice and expert guidance throughout my PhD study. It would be impossible for me to undertake this PhD without their constant guidance.

I would like to thank Dr. Gaurang Vakil for reviewing my annual reports and acting as my internal examiner.

Then, I would like to thank all my colleagues and friends in ATC and PEMC group at the University of Nottingham, for their support and valuable discussions. I have broadened my visions and learnt many experiences from them. Special thanks to Dr. Zhenyu Wang, Dr. Seang Shen Yeoh, Dr. Mi Tang, Dr. Zhen Huang, Dr. Chen Li, Dr. Linglin Chen, Dr. Cheng Wang, Dr. Yuan Gao, Dr. Feng Guo, Dr. Xiaoyu Lang, Dr. Xiang Zhang, Dr. Ye Liu, Dr. Quanxue Guan, Dr. Linhui Fan, Dr. Mohammad Ilkhani, Dr. Antonino La Rocca, Dr. Usman Nasir, Dr. Muhammad Raza Khowja. I also want to express my thanks to Bo Wang, Habibu Hussaini, Yiren Zhu, Ge Bai, Shengyu Cao and wish you to get your PhD degree soon.

In addition, I also want to thank Dean Evans, Dafydd Kember, Phil Whittles from NEMA Ltd, and Sebastien Detry, Antoine Ferrand from Safran Helicopter Engines for the close collaboration on the ACHIEVE project during my PhD study.

At last but not least, I would like to express my heartfelt appreciation to my parents, Yujie Wang and Wenlai Chen, for the lifetime of support, encouragement and education. Also, I am very appreciated and lucky to meet my partner Miss Weiyao Meng in the University of Nottingham. She brought me tremendous happiness and great supports throughout my PhD study. Her endless love accompanied me over the last four years and gave me the encouragement to finish this work.

Abstract

The More-Electric Aircraft (MEA) has been identified as a major future aircraft due to the urgent requirement to reduce CO2 in the aviation area. Meanwhile, as a commonly used thrust power source in commuter aircraft, turboprop engines can be made more fuel-efficient by the addition of a mechatronic device into their gearbox. In the University of Nottingham, an integrated Motor-Generator (M-G) drive system functioning as this mechatronic device has been developed for the next-generation turboprop. This M-G system provides auxiliary thrust to accelerate the turbo engine start-up on the ground, using electrical power from batteries. The same system is used as a generation system when the aircraft is in the air and supplies electrical power to on-board electrical loads.

This PhD project is focused on the development of this M-G system and is thoroughly described in the thesis, including the machine design, power electronic converters and their control development. Due to redundancy considerations, a dual three-phase machine was developed to ensure uninterrupted power delivery, even if a fault should occur. The corresponding power converter was designed using SiC power modules to achieve high power density. The entire system, including the machine, six-phase converter, and controller, has a customized cooling system, designed to be integrated into the engine gearbox.

The control algorithm was one of the most challenging parts of the M-G system due to the absence of a position sensor and is the main contribution of this PhD research. An I-F open-loop and Model Reference Adaptive System (MRAS) sensorless combined solution was proposed to cover the entire speed range. The stability issue of MRAS for high-speed drives needs to be considered carefully due to a low modulation frequency

(of the power electronic converter) to the electrical machine fundamental frequency ratio (M-F ratio). The entire M-G drive system has been modelled in the z-domain with particular efforts on modelling this non-linear system; in particular, the estimated rotor angle was used in the frame transformations (e.g., ABC to DQ frame). With the discrete z-domain model, eigenvalues of the system model have thus been used to analyse the system stabilities. The PI controller for this high-speed M-G system can thus be designed with confidence that the system will be stable with selected parameters. The developed sensorless control scheme has been validated on the M-G system at full speed, and full power range using testing facilities within the University of Nottingham

Contents

Acknowledgement I
Abstract II
Contents IV
List of Figures VII
List of Tables XII
List of Acronyms XIII
List of Symbols XIV
Chapter 1. Introduction 1
1.1 Climate Change and Net Zero Aviation 1
1.2 More Electric Aircraft 2
1.3 Mild-Hybridized Turboprop (Tech TP) for Commuter Aircraft 6
1.4 Introduction to the ACHIEVE System 10
1.5 Aims and Objectives of Thesis 12
1.6 Thesis Outline 13
1.7 Conclusion 15
Chapter 2. Dual Three-Phase Machine Modelling 16
2.1 Dual Three-Phase Machine Design 17
2.2 Dual Three-Phase Machine Modelling 18
2.2.1 Six-Phase Math Model 18
2.2.2 Dual D-Q Math Model 23
2.3 Comparison of Machine Math Models and Finite Element Model 26
2.4 Conclusion 31
Chapter 3. Current Closed-Loop Control and Position Sensorless Algorithm 32
3.1 Current Controller Design 32
3.2 Current Closed-Loop Control Simulation 36
3.2.1 Step Current Command Scenario 37
3.2.2 Step Speed Command Scenario 38
3.3 Permanent Magnet Machine Position Sensorless Control 41
3.3.1 Position Sensorless Control Methods Review 41
3.3.2 I-F Open-Loop Sensorless Start-Up Control 43
3.3.3 MRAS Sensorless Control 49
3.3.4 I-F Open-Loop Sensorless Start-Up Simulation 51
3.3.5 MRAS Sensorless Control Simulation 55

3.4 Conclusion 59
Chapter 4. Stability Analysis Model of MRAS Sensorless Control 60
4.1 Literature Review of MRAS Sensorless Stability Analysis 61
4.2 MRAS Stability Analysis Challenges for The Dual three-phase Machine 62
4.3 Small Signal Model of MRAS Sensorless System 64
4.3.1 MRAS Sensorless Algorithm in s-domain 64
4.3.2 MRAS Sensorless Algorithm in z-domain and Related Small Signal Models 66
4.4 Current Closed-Loop Small Signal Modelling 74
4.4.1 Current PI Controller 75
4.4.2 Voltage Generation 76
4.4.3 Machine dq Model and Position Integration 80
4.4.4 Current Transformation 81
4.4.5 Current Closed-Loop State Evolution Expression 84
4.5 Conclusion 87
Chapter 5. Stability Analysis Procedure and Simulation Validation 88
5.1 Stability Analysis Procedure 88
5.2 Simulation Validation 94
5.2.1 Simulation Model to Validate The Stability Analysis Method 94
5.2.2 Stability Analysis of MRAS System with 1st-Order Adaptive Model 96
5.2.3 Stability Analysis of MRAS System with 2nd-Order Adaptive Model 101
5.2.4 Stability Comparison of 1st- and 2nd-Order MRAS Adaptive Model 105
5.2.5 Stability Comparison with Different Q-Axis Current 108
5.2.6 Machine Parameters Impacts on MRAS Sensorless Control Stabilities 110
5.2.7 Simulation Result Summary 130
5.3 Conclusion 131
Chapter 6. Experimental Prototype 132
6.1 Power Electronic Converter Hardware 132
6.1.1 Control Board 133
6.1.2 Driver Board 135
6.1.3 Power Board 137
6.1.4 Converter Assembly 139
6.1.5 Converter Efficiency Test 141
6.2 Power Converter Control Software 143
6.2.1 MCU Operation Principle 143
6.2.2 CAN Communication 145
6.2.3 GUI Design on Host PC 146

6.3 Machine and Power Converter Integration 147
6.4 Experimental Test Rig 148
6.5 Conclusion 151
Chapter 7. Experimental Validation of Sensorless Motor-Generator Drive System 152
7.1 Green-Taxiing Motoring Mode Validation 152
7.1.1 Control algorithm switching techniques 153
7.1.2 Control Diagram of Green-Taxiing Motoring Mode 154
7.1.3 Experimental Results 155
7.2 Generation Mode Validation 157
7.2.1 Control Diagram of Generation Mode 158
7.2.2 Experimental Results 158
7.3 Experimental Validation of The Stability Analysis Method 165
7.3.1 1st-Order MRAS Adaptive Model Validation 166
7.3.2 2nd-Order MRAS Adaptive Model Validation 169
7.3.3 Comparison of 1st and 2nd-Order MRAS Adaptive Model 171
7.4 Conclusion 174
Chapter 8. Conclusion and Future Work 175
8.1 Conclusion 175
8.2 Future Work 176
8.3 List of Publications 179
Appendix A 181
Appendix B 186
I. Voltage Generation (Section 4.4.2) Equation Derivation 186
a. The Derivation Process of (4.42) And (4.43) 186
b. The Derivation Process of (4.44) 187
II. Current Transformation (Section 4.4.4) Equation Derivation 188
a. The Derivation Process of (4.59) And (4.60) 188
b. The Derivation Process of (4.61) 189
III. Derivation of $\boldsymbol{\theta\Delta equ}$ in Section 5.1 190
Appendix C 192
Appendix D 197
References 198

List of Figures

Fig 1.1. Power sources distribution in conventional aircraft [8] 3
Fig 1.2. Power sources distribution of MEA [8] 4
Fig 1.3. Electrical power levels for various civil aircraft 5
Fig 1.4. A Beechcraft 1900 with two PT6A turboprops by Pratt & Whitney Canada [12] 6
Fig 1.5. Schematic diagram showing the operation of a turboprop engine [13] 7
Fig 1.6. Tech TP system schematic 8
Fig 1.7. Tech TP main components and energy flow diagram 9
Fig 1.8. ACHIEVE system position inside PAGB (left) and the system diagram (right) 11
Fig 2.1. Section view of the optimized dual three-phase machine 17
Fig 2.2. Winding distribution of the dual three-phase machine 19
Fig 2.3. Equivalent star winding configuration phaser diagram 20
Fig 2.4. d/q-axis and rotor position (θ) definition 23
Fig 2.5. The current waveform used for the FE model, six-phase model, and dual d-q model 26
Fig 2.6. Six-phase math model validation diagram 27
Fig 2.7. Dual d-q math model validation diagram 28
Fig 2.8. Six-phase voltage comparison of FE model, six-phase model, and dual d-q model 29
Fig 2.9. The spectrum of A-phase voltage for the FE model, six-phase model, and dual d-q model 29
Fig 2.10. Torque comparison of FE model, six-phase model, and dual d-q model 30
Fig 3.1. PI current control diagram based on dual d-q math model 33
Fig 3.2. The entire $id1$ current control loop (a) and synthesized (b) transfer function diagram 35
Fig 3.3. Whole (a) and synthesized (b) transfer function diagram for $iq1$ closed-loop 36
Fig 3.4. d/q-axis currents response with iq reference step command 37
Fig 3.5. Electromagnetic torque response with iq reference step command 38
Fig 3.6. Six-phase currents with iq reference step command 38
Fig 3.7. Speed command step change waveform 39
Fig 3.8. d/q-axis currents response with step speed command 39
Fig 3.9. Electromagnetic torque response with step speed command 40
Fig 3.10. Six-phase currents response with step speed command 40

Fig 3.11. Categories of position sensorless control 41
Fig 3.12. Block diagram of I-F open-loop sensorless start-up control system 44
Fig 3.13. I-F open-loop control frame diagram 44
Fig 3.14. Torque-position error relationship and their time-domain waveform with the I-F start-up process 47
Fig 3.15. Scheme diagram of MRAS sensorless estimation 49
Fig 3.16. The control diagram of MRAS sensorless estimation 51
Fig 3.17. Simulation diagram of I-F open-loop sensorless start-up control system 51
Fig 3.18. Simulation results of initial rotor clamping with two different types of iq* 53
Fig 3.19. The simulation comparison of I-F start-up with step and ramping speed commands 54
Fig 3.20. Six-phase currents comparison of I-F start-up with step and ramping speed command 55
Fig 3.21. Block diagram of MRAS sensorless integrated with current closed-loop control 56
Fig 3.22. d/q-current waveforms with iq*=10A and id*=0A of MRAS sensorless simulation 57
Fig 3.23. Estimated speed (a) and estimated position error (b) of MRAS sensorless simulation 58
Fig 3.24. Six-phase current waveforms of MRAS sensorless simulation 58
Fig 4.1. Diagram of MRAS sensorless rotor position estimation algorithm in s-domain 64
Fig 4.2. Diagram of MRAS sensorless rotor position and speed estimation algorithm in z-domain 67
Fig 4.3. MRAS sensorless current closed-loop system diagram 75
Fig 4.4. Voltage generation block diagram 76
Fig 4.5. Voltage generation simplified block diagram 77
Fig 4.6. The rotor position compensation for $\alpha\beta$-to-dq transformation 77
Fig 4.7. Current transformation diagram full (a) and simplified (b) diagram 82
Fig 5.1. The flow chart of stability analysis steps 89
Fig 5.2. Flowchart of equilibrium operating point calculation in MATLAB 93
Fig 5.3. Simulation model structure diagram 95
Fig 5.4. The stable area of k_{pm} and k_{im} selection at different speeds for the 1st-order adaptive model 97
Fig 5.5. The maximum eigenvalues map for the 1st-order adaptive model at all speeds 97
Fig 5.6. The maximum eigenvalue map with k_{im}=5000 for the 1st-order adaptive model 98
Fig 5.7. Stability simulation results at the 8 operating points in Fig 5.6 100
Fig 5.8. The stable area at different speeds for the 2nd-order adaptive model 102

Fig 5.9. The maximum eigenvalues map for the 2st-order adaptive model at all speeds 102

Fig 5.10. The maximum eigenvalue map at 14krpm for the 2nd-order adaptive model 103

Fig 5.11. Stability simulation results at the 8 operating points in Fig 5.10 104

Fig 5.12. Stable area comparison of 1st and 2nd-order adaptive model with speed between 7-14krpm 105

Fig 5.13. Stable area comparison of 1st and 2nd-order adaptive model with k_{im}=5000..... 106

Fig 5.14. Stability simulation results at 4 different operating points (a,b,c,d) in Fig 5.13. 107

Fig 5.15. Stable boundaries with different iq when speed is 14krpm 109

Fig 5.16. Stability simulation results at operating point a and b in Fig 5.15 110

Fig 5.17. Relation between estimated position error and different ratio of estimated to actual permanent magnet flux linkage under n=14krpm, id=0A 112

Fig 5.18. Relation between estimated position error and different ratio of estimated to actual d-/q-axis inductance under n=14krpm, id=0A 112

Fig 5.19. Relation between estimated position error and different ratio of estimated to actual phase resistance under n=14krpm, id=0A 113

Fig 5.20. Stability area with different $\varphi f : \varphi f$ ratio at n=14krpm and i_q^*=0A 114

Fig 5.21. Simulation result at operating point ‘a’ in Fig 5.20 with k_{pm}=2.6, k_{im}=14000 115

Fig 5.22. Simulation result at operating point ‘b’ in Fig 5.20 with k_{pm}=2.4, k_{im}=14000 116

Fig 5.23. Simulation result at operating point ‘c’ in Fig 5.20 with k_{pm}=2.2, k_{im}=14000 116

Fig 5.24. Simulation result at operating point ‘d’ in Fig 5.20 with k_{pm}=2, k_{im}=14000..... 117

Fig 5.25. Stability area with different $L : L$ ratio at n=14krpm and i_q^*=-20A 118

Fig 5.26. Simulation result at operating point ‘a’ in Fig 5.25 with k_{pm}=3.4, k_{im}=14000 118

Fig 5.27. Simulation result at operating point ‘b’ in Fig 5.25 with k_{pm}=3, k_{im}=14000..... 119

Fig 5.28. Simulation result at operating point ‘c’ in Fig 5.25 with k_{pm}=2.4, k_{im}=14000 120

Fig 5.29. Simulation result at operating point ‘d’ in Fig 5.25 with k_{pm}=2, k_{im}=14000..... 120

Fig 5.30. Stability area with different $R : R$ ratio at n=14krpm and i_q^*=20A..... 121

Fig 5.31. Simulation result at operating point ‘a’ in Fig 5.30 with k_{pm}=2.8, k_{im}=10000 122

Fig 5.32. Simulation result at operating point ‘b’ in Fig 5.30 with k_{pm}=2.6, k_{im}=10000..... 123

Fig 5.33. Simulation result at operating point ‘c’ in Fig 5.30 with k_{pm}=2.3, k_{im}=10000 123

Fig 5.34. Simulation result at operating point ‘d’ in Fig 5.30 with k_{pm}=2.1, k_{im}=10000..... 124

Fig 5.35. The flowchart plotting the overall stable area considering n, i_q^*, and $\varphi f : \varphi f$ selections..... 125

Fig 5.36. Stable area with iq=-30A to 30A, n=0.6-14krpm, and φf: φf=0.6-1.4 126

Fig 5.37. The flowchart plotting the overall stable area considering all n, i_q^*, and L: L selections 127

Fig 5.38. Stable area with iq=-30A to 30A, n=0.6-14krpm, and L: L=0.6-1.4 128

Fig 5.39. The flowchart plotting the overall stable area considering all n, i_q^*, and R: R selections..... 129

Fig 5.40. Stable area with iq=-30A to 30A, n=0.6-14krpm, and R: R=0.6-1.4 130

Fig 6.1. Six-phase power converter simple diagram 133

Fig 6.2. Signal diagram of the control board. 134

Fig 6.3. Control board layout views 135

Fig 6.4. Driver board functional diagram 136

Fig 6.5. Driver board layout views 137

Fig 6.6. Power board functional diagram 138

Fig 6.7. Layout views of the power board PCB 139

Fig 6.8. Power converter assembly exploded view 140

Fig 6.9. Power converter boards assembly 140

Fig 6.10. Experimental setup of a SiC-based dual 3-phase converter. 141

Fig 6.11. Test waveform of phase currents and line-line voltages at maximum power 142

Fig 6.12. Experimental result of efficiency and power loss of the converter 142

Fig 6.13. MCU operating procedure flow chart 144

Fig 6.14. CPU and CLA time sequence arrangements 144

Fig 6.15. ePWM peripheral module operating principle 145

Fig 6.16. CAN bus wiring diagram 146

Fig 6.17. MCU firmware upgrade through CAN bus diagram 146

Fig 6.18. GUI layout for CAN communication with control board MCU 147

Fig 6.19. Explosion view of the first ACHIEVE prototype..... 148

Fig 6.20. Final assembly photo of the first ACHIEVE prototype 148

Fig 6.21. Functional test diagram of dual three-phase drive system test rig 149

Fig 6.22. Dual three-phase drive system test rig setup 150

Fig 7.1. Machine acceleration procedure at green-taxiing motoring mode 153

Fig 7.2. Speed and q-axis current reference under I-F open-loop control 153

Fig 7.3. Control diagram for green-taxiing motoring mode 155

Fig 7.4. Speed and current waveform for I-F open loop start-up from 0 to 300rpm. 156

Fig 7.5. Speed and current waveform for MRAS sensorless control acceleration 157

Fig 7.6. Generation mode machine operation diagram..... 158

Fig 7.7. Control diagram for generating mode. 158

Fig 7.8. Experimental stable state results at n=12.4krpm, iq^*=-30A 161

Fig 7.9. Experimental stable state results at speed=14.2rpm, iq^*=-30A 162

(a) Fig 7.10. Experimental dynamic result in scenario 1 with n=13kra) Currents with $iq*$ from 0A to -10A; (b) Speed with $iq*$ from 0A to -10A; (c) Currents with $iq*$ from -10A to -20A; (d) Speed with $iq*$ from -10A to -20I(e) Currents with $iq*$ from -20A to -30A; (f) Speed with $iq*$ from -20A to -30A 164

Fig 7.11. Experimental dynamic result in scenario 2 with i_d^*=0A, i_q^*A 165

Fig 7.12. The maximum eigenvalue map with k_{im}=5000 for the 1st-order adaptive model 166

Fig 7.13. Experimental estimated speed comparison with n=7krpm and 9krpm..... 167

Fig 7.14. Experimental d/q-axis current comparison with n=7krpm (a) and 9krpm (b)..... 168

Fig 7.15. The unstable eigenvalues of operating point f in Fig 7.12 169

Fig 7.16. The maximum eigenvalue map with k_{im}=5000 for the 2nd-order adaptive model..... 170

Fig 7.17. Experimental estimated speed comparison at operating points m and n in Fig 7.16 170

Fig 7.18. Experimental d/q-axis current comparison at operating points m and n in Fig 7.16 171

Fig 7.19. Stability boundaries of 1st and 2nd-order adaptive models with k_{im}=5000 172

Fig 7.20. Experimental estimated speed comparison for 1st and 2nd-order models at operating point ‘a’ in Fig 7.19 172

Fig 7.21. Experimental d/q-axis current comparison for 1st and 2nd-order adaptive models at operating point ‘a’ in Fig 7.19..... 173

List of Tables

Table 2.1. ACHIEVE machine design parameters 18

Table 2.2. Machine parameters from Motor-CAD 22

Table 2.3. Machine parameters for dual d-q math model 24

Table 3.1. Current PI controller parameters 36

Table 3.2. Simulation parameters for I-F open loop start-up 53

Table 3.3. Simulation condition for MRAS sensorless with current closed-loop control 56

Table 4.1. State vectors/variables summary for the system state evolution equation 85

Table 4.2. Intermediate vectors/variables summary for the system state evolution equation 85

Table 5.1. Machine parameters and constant control parameters for stability analysis 88

Table 5.2. MRAS sensorless control parameters range for stability analysis 90

Table 5.3. Machine operating point range 90

Table 5.4. Selected operating points parameters for 1st-order adaptive model 99

Table 5.5. Selected operating points parameters for 2nd-order adaptive model 103

Table 5.6. Operating points selections for 1st and 2nd-order adaptive models comparison 106

Table 5.7. Operating situations and control parameters in the different time slots of Fig 5.16 110

Table 6.1. Power converter requirement and selected power module maximum ratings 138

Table 6.2. Converter test results at maximum power 141

Table 7.1. Cooling system performance during green taxiing acceleration 157

Table 7.2. Test result under generation mode with different q-axis currents 160

Table 7.3. The stabilized temperature under different operating points 162

Table 7.4. Selected operating points parameters for 1st-order adaptive model 166

List of Acronyms

ADC	Analog to Digital Converter
CAD	Computer Aided Design
CAN	Controller Area Network
CLA	Control Law Accelerator
DoE	Design of Experiment
ECS	Environmental Control System
FE	Finite Element
FEA	Finite Element Analysis
GA	Genetic Algorithm
GPIO	General Purpose Input/Output
GUI	Graphical User Interface
I-F	Current-Frequency
LDO	Low Dropout Regulator
MCU	Microcontroller
MEA	More Electric Aircraft
M-F	Modulation Frequency to Fundamental Frequency
M-G	Motor-Generator
MIMO	Multi-Inputs Multi-Outputs
MOSFET	Metal-Oxide-Semiconductor Field-Effect Transistor
MRAS	Model Reference Adaptive System
PAGB	Propeller and Accessory Gearbox
PCB	Printed Circuit Board
PI	Proportional and Integral
PM	Permanent Magnet
PMSM	Permanent Magnet Synchronous Machine
PWM	Pulse-Width Modulation
RTD	Resistance Temperature Detector
SC	Short Circuit
SiC	Silicon Carbide
SVPWM	Space Vector Pulse-Width Modulation
TP	Turboprop
TTL	Transistor–Transistor Logic
V-F	Voltage-Frequency
WIPS	Wing Ice Protection System

List of Symbols

$\hat{}$	Variables with this accent represent the estimated parameters in MRAS (e.g., $\hat{\boldsymbol{I}}_{\boldsymbol{dq}}$).
$(k), (k-1)$ ...	Variables with bracket behind represent the discrete variables at corresponding time instant (e.g., $\hat{\boldsymbol{I}}_{\boldsymbol{dq}}(k)$).
Δ	Variables with this symbol in front represent the small-signal variables (e.g., $\Delta\hat{\boldsymbol{I}}_{\boldsymbol{dq}}(k)$).
$\boldsymbol{L}$	Self and mutual inductance matrix within each three-phase windings
$\boldsymbol{M}$	Mutual inductance matrix between two three-phases
$\boldsymbol{L_s}$	Inductance matrix of the dual three-phase machine
$\boldsymbol{L_{XYZ}}$	Inductance matrix of equivalent 3 phase symmetrical machine
L_d, L_q	d and q-axis inductances
$\boldsymbol{u_s}$	Machine 6 phase voltage vector
$\boldsymbol{i_s}$	Machine 6 phase current vector
$\boldsymbol{\varphi_s}$	Machine 6 phase stator flux linkage vector
T_e	Electromagnetic torque
T_f	Friction torque
J	Inertia
B	Friction factor
p	Machine pole pairs
K_T	Torque constant
θ_m	Mechanical rotor angle
f_e, f_e^*	Electrical rotating frequency and its reference
n, n^*	Speed and its reference in rpm
i_x	Phase currents (x=a,b,c,u,v,w)
u_x	Phase voltages (x=a,b,c,u,v,w)
S_x	Switching state of each phase (x=a,b,c,u,v,w)
f_s	PWM switching/modulation frequency
f_{cc}	Current controller bandwidth
θ^*	Reference rotor position generated by I-F open loop control
ω_e^*	Reference electrical rotating speed

i_d^*, i_q^*	d and q-axis current references
i_d, i_q	d and q-axis currents in real dq frame
$\boldsymbol{I_{dq}}$	2*1 vector containing i_d and i_q
$\tilde{\imath}_d, \tilde{\imath}_q$	Sampled d and q-axis currents in estimated dq frame
$\tilde{\boldsymbol{I}}_{\boldsymbol{dq}}$	2*1 vector containing $\tilde{\imath}_d$ and $\tilde{\imath}_q$
$\hat{\imath}_d, \hat{\imath}_q$	Estimated d and q-axis currents
$\hat{\boldsymbol{I}}_{\boldsymbol{dq}}$	2*1 vector containing $\hat{\imath}_d$ and $\hat{\imath}_q$
$\boldsymbol{I_{equ}}$	2*1 vector containing equilibrium operating point of dq-currents
e_d, e_q	d and q-axis current errors between reference and sampling
$\boldsymbol{e_{dq}}$	2*1 vector containing e_d and e_q
$R, \hat{R}$	Real and estimated phase resistances
$L, \hat{L}$	Real and estimated d/q-axis inductances if $L_d = L_q$
$\varphi_f, \hat{\varphi}_f$	Real and estimated rotor flux linkage
$\omega_e, \hat{\omega}_e$	Real and estimated electrical rotate speed in rad/s
$\theta, \hat{\theta}$	Real and estimated electrical rotor position in rad
u_d^*, u_q^*	d and q-axis voltage references in estimated dq frame
$\boldsymbol{U_{dq}^*}$	2*1 vector containing u_d^* and u_q^*
u_d, u_q	d and q-axis voltage in machine dq frame
$\boldsymbol{U_{dq}}$	2*1 vector containing u_d and u_q
$\boldsymbol{V_{equ}}$	2*1 vector containing equilibrium operating point of dq-voltages
e	Control rule error in MRAS algorithm
k_{pm}, k_{im}	Proportional and integral factors for MRAS PI controller
X_ω	Intermediate state variable to describe discrete MRAS PI controller
k_p, k_i	proportional and integral factors for Current PI controller
$\boldsymbol{X_{dq}}$	Intermediate 2*1 state vector to describe discrete Current PI controller
T_s	Period of PWM and control period
$\boldsymbol{J_1}$	Constant matrix $[0 \quad 1]$
$\boldsymbol{J_2}$	Constant matrix $\begin{bmatrix} 0 & 1 \\ -1 & 0 \end{bmatrix}$
$\boldsymbol{E_2}$	Constant matrix $\begin{bmatrix} 1 & 0 \\ 0 & 1 \end{bmatrix}$

Chapter 1.

Introduction

1.1 Climate Change and Net Zero Aviation

Climate change has become a great challenge for all human beings. Every year billions of tons of CO_2 are released into the atmosphere as a result of coal, oil, and gas production. Human activity is producing greenhouse gas emissions at a record high, with no signs of slowing down [1]. It is recorded that the Earth is now about 1.1°C warmer than it was in the late 1800s, and the last decade (2011-2020) was the warmest. However, the temperature rise is only the beginning of the story. The consequences of it include intense droughts, water scarcity, severe fires, rising sea levels, flooding, melting polar ice, catastrophic storms and declining biodiversity [2].

United Nations (UN) sustainable development goals outline 17 major goals to fulfil by 2030 that address global challenges, and goal No. 13 is directed towards taking urgent actions to combat climate change [3]. In the 2021 United Nations climate change conference (COP26), all countries agree to set a clear goal of securing global net zero by mid-century and keep 1.5°C within reach. The COP26 also released a declaration promoting the development and deployment of innovative new low- and zero-carbon aircraft technologies that can reduce aviation CO2 emissions [4]. As the host of COP26, the UK is the first major aviation sector in the world to commit to net zero CO_2 by 2050 and underlined this pledge with interim decarbonisation targets of at least 15% by 2030 and 40% by 2040. However, commercial aircraft in the sky are predicted to double in

the next 20 years, with emissions soaring in their wake, and by 2050 10 billion passengers will fly every year [5].

To achieve such ambitious targets and deliver net zero aviation, the aerospace industry will take concerted and coordinated actions, taking in clean aircraft technologies and propulsion systems, sustainable aviation fuels, advances in materials, manufacturing and aircraft maintenance and more efficient airspace and airport operations [5]. Aircraft electrification is one way to deliver net zero aviation and can increase the fuel and energy efficiencies of the engine and reduce environmental impact. This ambition should be achieved regardless of whether the engine is powering a large airliner or a small utility aircraft, meaning more thrust while burning less fuel and emitting less CO2, NOx and noise [5].

1.2 More Electric Aircraft

In the early 1990s, the need for more energy-efficient aircraft promoted the More-Electric Aircraft (MEA) concept [6]. For an MEA, subsystems such as mechanical (e.g., pumps), hydraulic (e.g., actuation systems), pneumatic (e.g., Environmental Control System (ECS), and Wing Ice Protection System (WIPS)) subsystems are replaced with electrical alternatives. In the following part of this section, the energy utilization of conventional aircraft and MEA will be discussed and compared.

The distributions of gas turbine power in conventional aircraft are shown in Fig 1.1. As can be seen, most of the energy from jet fuel is used to provide propulsion thrust (40MW), whilst only a small percentage (up to 4%) is converted to other forms of energy supplying different loads on board (i.e., mechanical, pneumatic, hydraulic, and electrical power) [7].

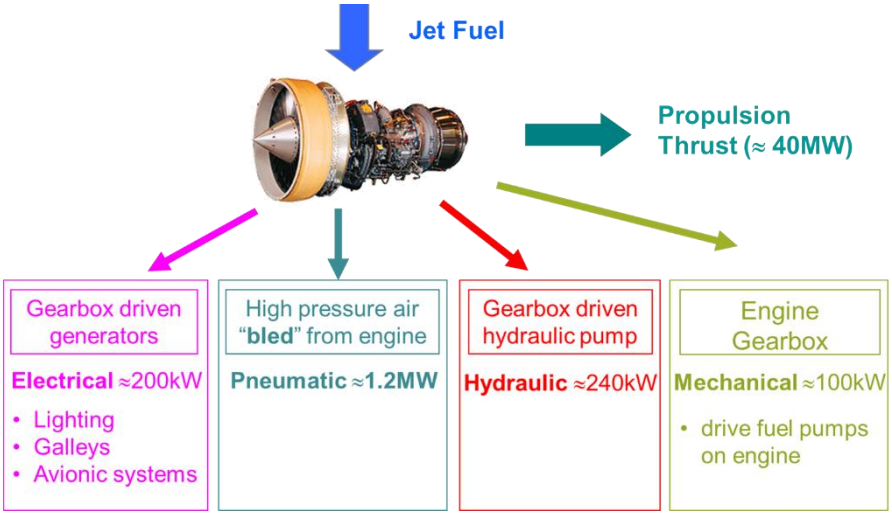


Fig 1.1. Power sources distribution in conventional aircraft [8]

Pneumatic power provides hot air to WIPS and ECS. WIPS has two working modes: Anti-Icing mode and De-Icing mode. The Anti-Icing mode is turned on before the aircraft enters icing conditions, whilst the De-Icing mode is reactive until the ice has already accumulated. The disadvantages of the pneumatic system are low efficiency and difficulties in maintenance and repair [9].

Hydraulic power on conventional aircraft is derived from an engine-driven hydraulic pump and supply power to flight control actuators.

Mechanical power is transferred through gearboxes from the engine to several devices. These devices include central hydraulic pumps, fuel pumps, local pumps for engine equipment, the main electrical generator, and other mechanically driven subsystems. The mechanical system includes large and heavy gearboxes and is with high maintenance costs [8].

Electrical power is from gearbox-driven generators and distributed throughout the aircraft for avionics, utility actuators, cabin electronics, lighting and galleys [7]. As can be seen from Fig 1.1, electrical power is only a small percentage of all secondary power sources (non-thrust power) within a conventional aircraft. In contrast with the pneumatic, hydraulic, and mechanical power systems, the electrical power system owns

many outstanding advantages such as high efficiency, low maintenance fees, good controllability and so on. Due to these advantages, applying more electrical power on aircraft has become a major trend on aircraft.

The concept of MEA is proposed to follow the above trend to increase the penetration of electrical power in aircraft systems [7]. As illustrated in Fig 1.2, many on board devices used to be powered by non-electrical power (such as hydraulic actuation systems, pneumatic, environmental control and wing ice protection system) are replaced by electrical devices. Replacing hydraulic and pneumatic systems with their electrical alternatives will result in improved efficiency and reduced weight and thus help reduce the weight, cost, and complexity of the system.

Furthermore, the use of electrical power with an appropriate distribution system provides options for reconfigurability, prognostics and diagnostics. It enables monitoring the health condition of the power system and thereby predicts its maintenance period. These features offer increased flexibility and availability of the entire system as well as reduced unscheduled downtime [8].

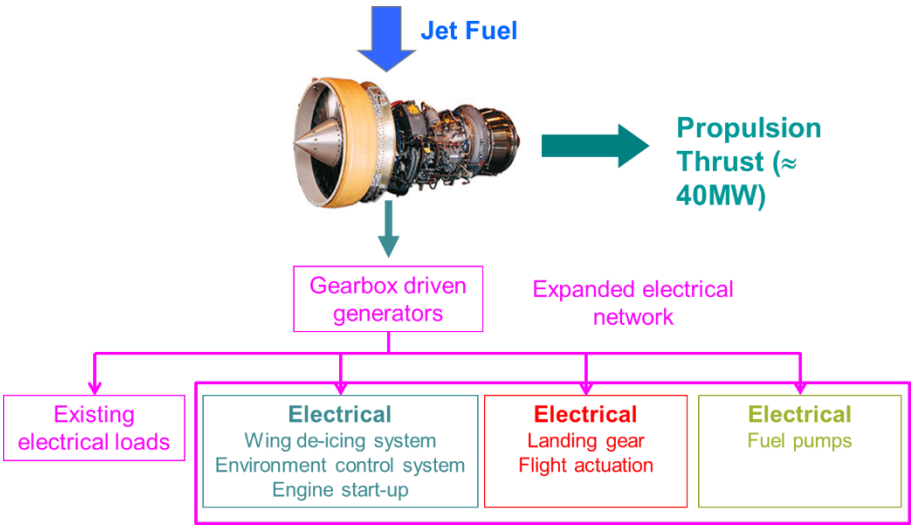


Fig 1.2. Power sources distribution of MEA [8]

Fig 1.3 shows the electrical power levels of several civil aircraft in the past decades. It shows that the onboard generation power capability of aircraft has increased over the

past years. Especially, the Boeing 787 reaches up to 1,450 KVA [7]. The Boeing 787 is a prime example of an aircraft that has implemented several MEA solutions, leading to 20%-25% more fuel efficient than the aircraft it replaces (Boeing 767) [10]. This trend will continue as electrical power becomes more important on board in future aircraft.

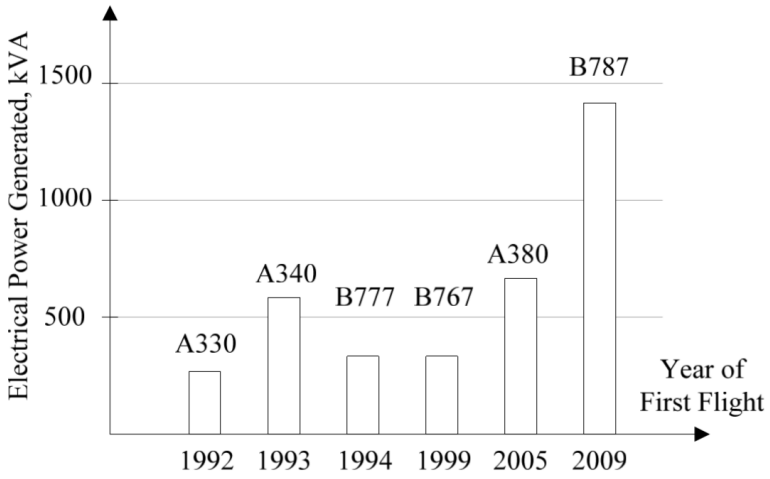


Fig 1.3. Electrical power levels for various civil aircraft

Within the aviation industry, one-third of the emissions come from flights of less than 1,500 km range, and two-thirds from flights less than 4,000km range, making more-electric regional and commuter aircraft has become inevitable to reduce overall CO2 emissions in the aviation industry [11].

With the agility to take off and land in regional or remote utility airports, commuter aircraft are frugal when it comes to fuel consumption. Commuter aircraft have fast turnaround times, and can be deployed on routes that would not be geographically or economically viable by rail or road, nor by larger aircraft such as regional turboprops or jets. To meet the Flightpath 2050 target whereby “90% of travellers within Europe can complete their journey, door-to-door within 4 hours”, commuter aircraft plugs a gap that many other travel paradigms struggle to fill [11]. Therefore, lower environmental impact (noise, fuel) is a key improving area for commuter aircraft.

1.3 Mild-Hybridized Turboprop (Tech TP) for Commuter Aircraft

Turboprop engines are commonly used as the thrust power source of commuter aircraft. A good example of this type of aircraft is the Beechcraft 1900 (Fig 1.4). This is a 19-passenger, twin-engine turboprop fixed-wing aircraft manufactured by Beechcraft. It was designed as a regional airliner with the capability of flying over 600 miles (970 km), and is one of the most popular 19-passenger airliners in history. The thrust power is from two Pratt & Whitney Canada PT6A turboprop engines with each flat rated at 1,100 shaft horsepower (820 kW) [12].



Fig 1.4. A Beechcraft 1900 with two PT6A turboprops by Pratt & Whitney Canada [12]

Commuter aircraft commonly use their turbine engine to drive a propeller to provide thrust, as shown in Fig 1.5. The in-take air is firstly compressed by a compressor before entering the combustion chamber, where the fuel is injected and mixed with the compressed air. After ignition, the fuel-air mixture will combust and the hot combustion gases expand through the turbine stages, generating power at the point of exhaust. The thrust is thus provided by the propeller, which is coupled and driven by the turbine through a reduction gearbox [13].

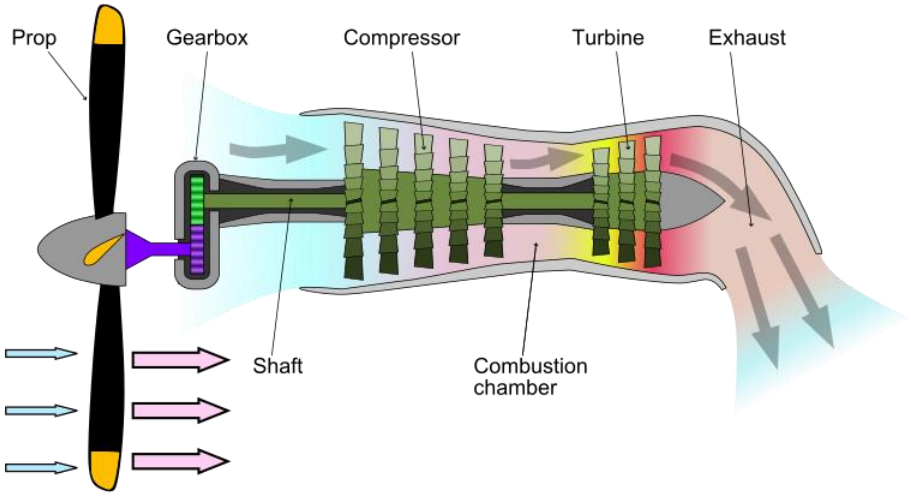


Fig 1.5. Schematic diagram showing the operation of a turboprop engine [13]

To make a more fuel-efficient turboprop, Safran and its partners within CleanSky 2 programme have developed a technological demonstrator (Tech TP), aiming to validate the technologies necessary to develop a new-generation turboprop. This paves the way for low-fuel and low-noise engines for use in general aviation and small commuter-sized aircraft (up to 19 passengers). The final aim of Tech TP is to reduce CO_2 emissions by 15% and decrease noise levels by up to 5 decibels compared to current engines in service [14]. One important measure to achieve that target would be to add a mechatronic system (developed by the ACHIEVE project - Advanced mechatronics devices for a novel turboprop electric starter-generator and health monitoring system, project No. 737814 within the EU CleanSky 2 programme) into Tech TP to achieve a mild-hybridized engine. The Tech TP system is shown in Fig 1.6. As can be seen, the system is mainly composed of PAGB (propeller and accessory gearbox), turbo engine, and propeller (marked as ‘a’,’b’,’d’ in Fig 1.6 respectively). The air inlet and exhaust of the turbo engine are marked as ‘e’ and ‘f’ in Fig 1.6. The ACHIEVE system is integrated into the PAGB, and its location is marked in Fig 1.6 at ‘c’. A starter will drive the turbo engine to idle speed to ignite the engine, and then the engine will provide up to 1MW thrust power to the propeller through PAGB.

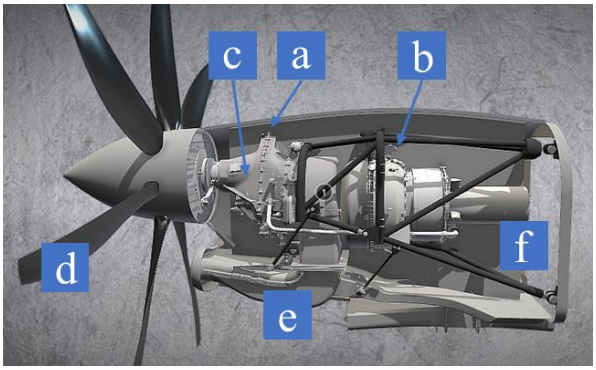


Fig 1.6. Tech TP system schematic

(a) Propeller and accessory gearbox (PAGB); (b) Turbo engine; (c) ACHIEVE system in PAGB; (d) 7-blade propeller; (e) Air inlet; (f) Exhaust [15]

The mechatronic system was developed within the ACHIEVE project. This mechatronic device is essentially a motor-generator drive system developed by the University of Nottingham, NEMA Ltd and PST company. This PhD research is working on this project and provides an advanced sensorless control scheme for the new motor-generator system.

The energy flow diagram among the main components of Tech TP is shown in Fig 1.7. The turbo engine is based on Safran's Ardiden 3 core engine, which was developed for helicopter application and is already certified by EASA. It can provide up to 1MW power to the propeller through the gearbox. Meanwhile, the ACHIEVE's rotor shaft is coupled with gearbox as well. This can either generate up to 20kW electrical power to charge the battery (as a generator), or provide up to 20kW mechanical power to the propeller through the gearbox (as a motor). The 20kW generation capacity thus makes more electrical and electronic devices onboard available to next-generation turboprop engines. When it works as a motor, ACHIEVE can be used as a booster of the turbo engine to assist its start-up. Although the maximum power of the ACHIEVE system (20kW) is much smaller than the turbo engine (1MW), it can still be used as an auxiliary thrust source for the propeller, which helps the turbo engine to reduce fuel consumption.

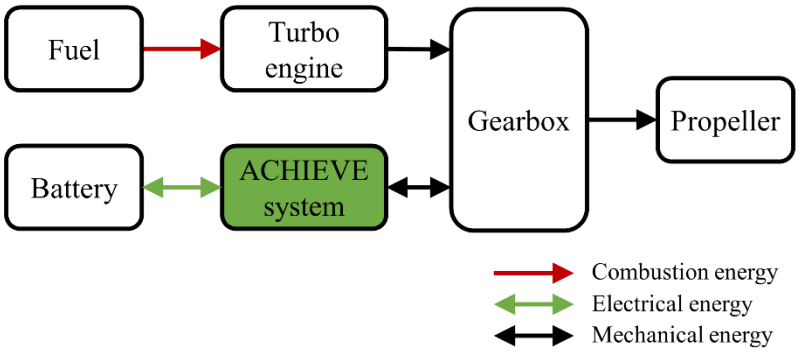


Fig 1.7. Tech TP main components and energy flow diagram

To achieve such functionalities, there are a few challenges which need to be addressed:

- Limited space available

Since the ACHIEVE system needs to be integrated into the propeller gearbox, very limited space is available inside the gearbox and this space is irregular. Therefore, the machine and converter must be bespoke to fit into the limited space.

- High-temperature environment

The ambient temperature inside the gearbox can reach 130°C in extreme cases as it is close to the turboprop engine and the space is exposed to high-temperature engine oil mist for gear and bearing lubrication (open bearing technology is used for this engine).

- High power density requirement (>20kW))

Since at least 20kW power capacity is required for the ACHIEVE system in such a limited space, the high power density of both the machine and drive system is necessary.

- Highly integrated design

The project requires all drive system components (machine, converter, controller, heatsink) to be integrated into the gearbox, so the ACHIEVE system must involve a highly integrated design.

- Fault tolerance design

In order to enhance the reliability of the ACHIEVE system to meet the aerospace standard, a dual 3-phase machine with two independent AC/DC channels is developed to make the system more redundant.

- Sensorless control for high-speed machines

Due to the high ambient temperature within the gearbox and limited space available for ACHIEVE system, It is required by our project partner to apply sensorless control in ACHIEVE system as it can get rid of the position sensor as well as save the space for the machine and converter. This is the most challenging part of this project since sensorless control should cover all speed ranges, from zero to the maximum speed (14.2krpm). Development of a sensorless algorithm which is suitable for such a high-speed electric drive, for both motoring and generation, and covering the entire speed range is thus the main focus of this PhD research.

1.4 Introduction to the ACHIEVE System

The location of the ACHIEVE system in the turboprop is demonstrated in Fig 1.8. As it is integrated within the gear box, it occupies the limited circular space between the propeller shaft and PAGB housing. The environment is hostile due to the high-temperature lubrication oil mist (up to 130°C), and thus requires a dedicated and highly-efficient cooling system, as well as good sealing performance. The ACHIEVE shaft has teeth on its right end to mechanically couple with the gears in the PAGB. Through these gears, the shaft can drive the propeller and also be driven by the turbo engine shaft.

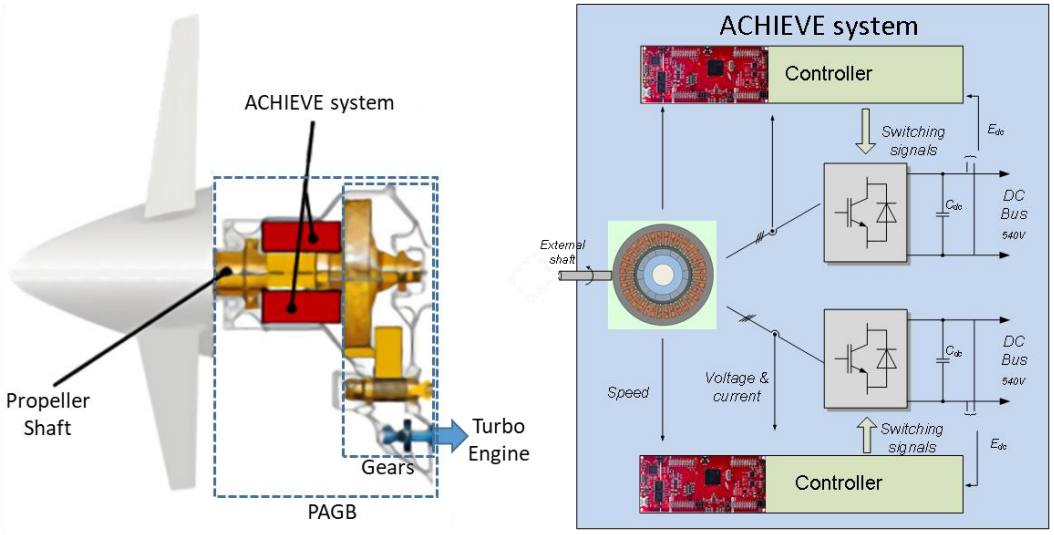


Fig 1.8. ACHIEVE system position inside PAGB (left) and the system diagram (right)

As an auxiliary mechatronic device, the ACHIEVE system can work as a motor to drive the turbo engine shaft from stop status to the ignition speed together with the existing starter/generator of the turbo engine, which can accelerate the engine start-up process. In addition, ACHIEVE can also be driven by the turbo engine as a generator to charge the battery during aircraft cruising.

A structure diagram of the ACHIEVE system is shown in the right figure of Fig 1.8. ACHIEVE machine is a dual three-phase machine, with two power channels. Each channel has three-phase windings from the machine feeding into one AC/DC converter with its dedicated controller. Compared with the traditional 270V onboard DC-bus, the 540V DC-bus allows the machine to have higher back-EMF and higher maximum speed.

Due to the project requirement, sensorless control has been implemented for the ACHIEVE machine. Because there is not a single sensorless method which can behave well at both low and high speeds, a hybrid sensorless algorithm was developed to ensure stable operation from zero to maximum speed. The stability of the sensorless control at extremely high speed with a low PWM to fundamental frequency ratio will also be investigated in this thesis.

1.5 Aims and Objectives of Thesis

The thesis aims to discuss the development of ACHIEVE motor-generator system for mild-hybridized turboprop application. The specific objectives are as follows:

- Develop the math model of the dual three-phase machine and corresponding control algorithm for the ACHIEVE project. The control algorithm will include the current closed-loop control, speed closed-loop control, and position sensorless estimation. Although the dual three-phase machine can even work with only one three-phase, fault-tolerant control is not in the scope of this thesis.
- Develop the sensorless control algorithm covering the full speed range. As no sensorless algorithm can have good performance at both low speed and high speed, a hybrid sensorless control algorithm will be developed.
- As the machine will run at a very high speed with low power electronic modulation frequency to the electrical fundamental frequency ratio, it will cause serious stability issues if the control parameters are not selected carefully. Therefore, the stability analysis of the MRAS (Model Reference Adaptive System) sensorless algorithm is necessary to provide useful conclusions on control parameter selection and MRAS algorithm development.
- The power converter and hardware controller will be developed for this dual three-phase machine. Due to the high-integration requirement, the power converter is customized to achieve high power density. The control algorithm based on microcontrollers also needs to be developed.

- The experiment of the prototype is necessary to validate the dual three-phase drive system. The test results are aimed to demonstrate the full power delivery ability of this system. This dual three-phase drive system needs to be worked in full speed and full power stably with sensorless control algorithm and efficient cooling performance.

1.6 Thesis Outline

The rest of this thesis is structured as follows:

Chapter 2 starts with introducing the structure of the dual three-phase machine. Then, the math models of the machine are derived based on the machine parameters from the FE model. The most accurate model is the six-phase math model, which has been proven its consistency with the FE model by simulation. The dual d-q math model is more convenient for control algorithm design.

Chapter 3 introduces the current closed-loop control and position sensorless algorithm for the dual three-phase machine. The current closed-loop control topology based on the proposed dual d-q machine math model is developed and validated in simulation. Position sensorless algorithms are investigated for this machine, and I-F open-loop sensorless and MRAS (Model Reference Adaptive System) sensorless are selected as low and high-speed sensorless algorithms respectively. Their principles are introduced, and corresponding simulations are achieved.

Chapter 4 develops the stability analysis model for MRAS sensorless control system. Firstly, a literature review of sensorless stability analysis is given, coming with challenges of applying MRAS sensorless to high-speed drive applications. Then, the

small-signal models of entire current closed loops, including the MRAS sensorless control algorithm, current PI controller, machine model and frame transformations, are derived and developed in the discrete-time domain.

Chapter 5 proposes a stability analysis procedure to analyse the overall stability performance of the MRAS sensorless system and provides simulation results. The stability boundary of the MRAS sensorless control system is calculated under different operating conditions with different parameters. The stable areas are validated by simulations and some useful conclusions are derived to guide stable control parameter selections.

Chapter 6 introduces the experimental prototype of the dual three-phase machine and its drive system. The hardware and software of the customized six-phase power converter will be introduced first. Then, the integrated assembly of the dual three-phase machine and the power converter is introduced. Finally, the experimental test setup is introduced. All the content in this chapter tries to give an overall picture of the experimental prototype to readers.

Chapter 7 demonstrates the test results of sensorless control. Both green-taxiing and generation operation modes are validated using testing facilities in Nottingham. The experimental tests prove that the prototype can accelerate to the designed maximum speed (14.2krpm) and generate rated power (20kW) as required. In addition, this chapter also shows the experimental results to validate the stability analysis method proposed in the previous chapters.

Finally, Chapter 8 concludes the Thesis with the overall work and main outcomes. Possible future research work is also discussed in this Chapter. A list of publications which resulted from the research is also given.

1.7 Conclusion

In this chapter, the consequences of climate change and the urgent need for reducing CO2 emissions, especially in the aviation area, were first presented. Aircraft electrification (also known as MEA (More Electric Aircraft)) can help increase fuel efficiency by replacing the mechanical, hydraulic, and pneumatic subsystems with electrical alternatives. The structures of conventional aircraft and MEA have been compared to illustrate the superiority of MEA and reveal the future trend of MEA.

As a commonly used thrust power source of commuter aircraft, a turboprop engine can become more fuel-efficient with the addition of a mechatronic device into its gearbox. The project ACHIEVE at the University of Nottingham has developed a motor-generator drive system for the next-generation turboprop demonstrator (Tech TP) at Safran. It can work as a motor to drive the turbo engine shaft from stop status to the ignition speed together with the existing starter/generator of the turbo engine, which can accelerate the engine start-up process. The same system can be used as a generator when the aircraft is in the air and supply electrical power to on board load.

The ACHIEVE system includes a 20kW dual 3-phase PMSM, together with its power converter and cooling system. The dual 3-phase channel design guarantees unceasing electric power generation, even if one channel fails. Due to the space limitation and the high-temperature environment, the position sensor (encoder or resolver) would be impossible to integrate, so sensorless control was implemented for the ACHIEVE machine. The aims and objectives of this thesis have been formulated in this chapter along with an outline of the thesis.

Chapter 2.

Dual Three-Phase Machine Modelling

The multi three-phase machine has many advantages to be applied in aerospace applications. Compared with the single 3-phase machine, multi three-phase machines can reduce the current per phase without increasing the voltage per phase [16], which makes it possible to use multiple small power modules to achieve an overall high power rate. The multiphase machine also has higher reliability with a higher degree of redundancy, which is preferable in some safety-critical areas such as aerospace applications.

A dual three-phase permanent magnet synchronous machine has been designed for this project. The optimized machine structure will be discussed in this chapter first. Then, the mathematical modelling of this machine is discussed in the following part of this chapter. Two models (the six-phase math model and the dual d-q math model) are derived based on the machine parameters from finite element analysis. Both of them match well with the finite element model but have their advantages and disadvantages.

2.1 Dual Three-Phase Machine Design

The ACHIEVE machine is required to deliver at least 20kW power to the DC-bus between rated speed (12.4krpm) and maximum speed (14.2krpm) within a limited space envelope. The researchers at the University of Nottingham have conducted a trade-off study to design a high power density machine meeting the mild-hybridized turboprop application requirement [17]. They compared several slot-pole combinations and winding configurations, and finalized the machine with 18 slots/12 poles permanent magnet synchronous machine with concentrated windings.

The optimized machine has the section view in Fig 2.1. As can be seen, the rotor includes a hollow shaft, rotor lamination, permanent magnets (PMs) and the sleeve. The permanent magnet on the rotor is with a Holbach structure, which can reduce the rotor size and increase the power density. The magnet magnetization direction is shown in the figure with red arrows. The stator includes coils and stator lamination.

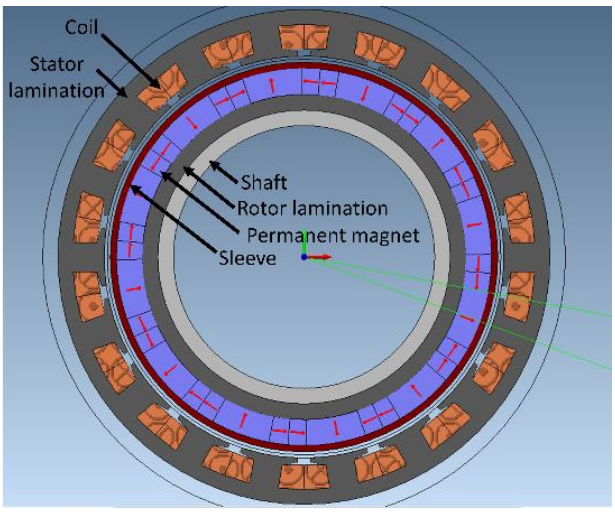


Fig 2.1. Section view of the optimized dual three-phase machine

Based on the finite element analysis result, this machine has the designed parameters shown in Table 2.1. The maximum winding temperature is 132^{o}C which has a good margin with the allowed maximum winding temperature (180 ^{o}C). The output power at

both rated speed and maximum speed are above 20kW (24.6kW and 26.7kW), and the efficiency and torque ripple results satisfy the project requirements.

Table 2.1. ACHIEVE machine design parameters

PARAMETERS	Value
Maximum Winding Temperature (°C)	132
Current Density (A/mm^2)	24.86
Phase Resistance (ohm)	0.035
Phase Inductance per channel (μH)	450
Leakage Inductance per channel (μH)	71.5
Peak no-load flux linkage per channel (Vs)	0.033
Output Power at 12.4krpm per channel (kW)	24.6
Output Power at 14.2krpm per channel (kW)	26.7
Load Torque Ripple at 12.4krpm (%)	3.0
Load Torque Ripple at 14.2krpm (%)	0.83
Efficiency at 12.4krpm (%)	93.6
Efficiency at 14.2krpm (%)	94.1

2.2 Dual Three-Phase Machine Modelling

2.2.1 Six-Phase Math Model

The windings distribution of the developed machine is shown in Fig 2.2. As can be seen, each three-phase winding is placed in a semicircle of the stator. This kind of winding distribution is specifically designed for fault-tolerant purposes. The design allows the properties of electrical separation, magnetic separation and physical separation[18]. Splitting the stator into 2 sectors can achieve minimum mutual inductance between the two three-phase windings.

Due to the layout of the unique winding, the mutual inductances between two sectors are relatively small than self-inductances within one sector. The purpose of this design is to decouple the two sectors magnetically as much as possible. This allows single-sector operation if the other sector has problems (e.g., winding short-circuit, drive failure). However, this winding topology will also cause the disagreement of mutual inductances, but the impact can be minimized if loads of the two sectors are equal.

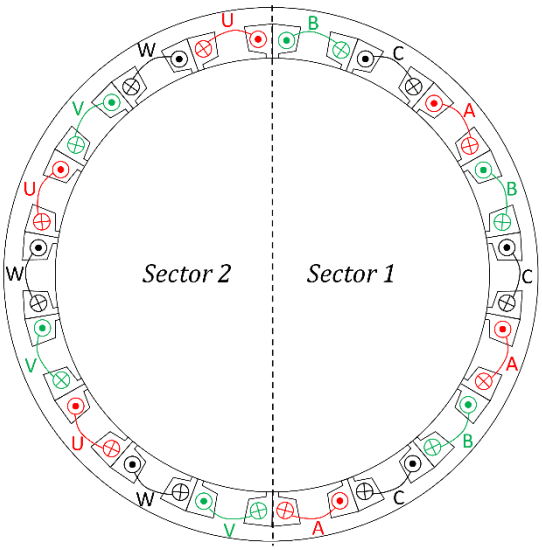


Fig 2.2. Winding distribution of the dual three-phase machine

As there are 18 slots and 12 poles, the electrical angle between two adjacent windings (θ_{shift}) is 120° as:

$$\theta_{shift} = \frac{360° * p}{2N} \tag{2.1}$$

where p = 12 represents pole number and $N = 18$ represents slot number.

With the 120° of adjacent windings angle shift, the phasor diagram of winding distribution can be derived as shown in Fig 2.3. The two sectors (denoted as A/B/C phase sector, and U/V/W phase sector) are separated by a dashed line to reflect that they are physically separated in a stator. Within one sector, the electrical phase shift between any two phases (e.g., A-B, A-C) is 120°. Between two sectors, the phase shift of the corresponding two phases (e.g., A to U, B to V, C to W) is 180°. It is because the flux direction generated by the currents in phase A and phase U are opposite as shown in Fig.2.9.

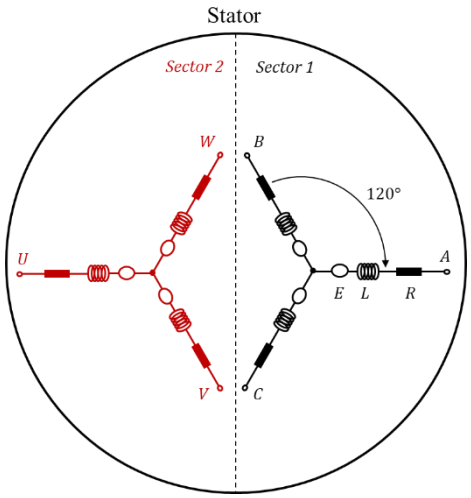


Fig 2.3. Equivalent star winding configuration phaser diagram

Within a traditional dual three-phase machine, the symmetrical three-phase windings should be alternated along the entire stator with the same spatial intervals. This winding pattern will result in the same self-inductance and mutual inductance for each phase. In this machine, however, each three-phase windings are only placed on half of the stator and thus mutual inductances between phases would not be equal but depending on the location of the windings (e.g., $L_{AB} \neq L_{AC}$). The inductance matrix for the 6 phases of this machine is calculated from FEA software (MAGNET [19]) and shown in equation (2.2). $\boldsymbol{L}$ (3x3) represents the self and mutual inductance within each three-phase windings, and $\boldsymbol{M}$ (3x3) represents the mutual inductance between two three-phases.

$$\boldsymbol{L_s} = \begin{bmatrix} \boldsymbol{L} & \boldsymbol{M} \\ \boldsymbol{M} & \boldsymbol{L} \end{bmatrix}_{6\times6} \tag{2.2}$$

where $\boldsymbol{L} = \begin{bmatrix} 326 & -81 & -111 \\ -81 & 326 & -111 \\ -111 & -111 & 326 \end{bmatrix} \mu H$, $\boldsymbol{M} = \begin{bmatrix} 20 & 50 & 20 \\ 50 & 20 & 20 \\ 20 & 20 & 20 \end{bmatrix} \mu H$

For a symmetrical dual three-phase machine, the self-inductance is the same for different phases. This is also true for mutual inductances. Thus the self-inductance matrix $\boldsymbol{L}$ should be with one value for the diagonal line items (self-inductance) and the mutual inductance matrix $\boldsymbol{M}$ should be with another value for non-diagonal items (mutual inductance). However, for this studied machine, the mutual inductance matrix

$\boldsymbol{M}$ embedded different values, for example, $M_{AB} \neq M_{AC}, M_{AV} \neq M_{AW}$. Here, M_{AB} is smaller than M_{AC} and it is because the windings A and C are always next to each other but A and B are discontinuous near the boundary of the one sector. Due to this phenomenon, the inductance matrix $\boldsymbol{L_s}$ cannot be transferred to a diagonal matrix by Clarke-Park transformation. This means the decoupled d-q current control is not achievable using conventional Clarke-Park transformation. Thus, some further modelling techniques for control design are required.

For this dual three-phase machine, its voltage equation is given as follows:

$$\boldsymbol{u_s} = R\boldsymbol{i_s} + \frac{d\boldsymbol{\varphi_s}}{dt} \tag{2.3}$$

where R represents the phase resistance, and $\boldsymbol{u_s}, \boldsymbol{i_s}, \boldsymbol{\varphi_s}$ represent phase voltages, currents, and stator flux linkage respectively. They have expressions as follows:

$$\boldsymbol{u_s} = \begin{bmatrix} \boldsymbol{u_1} \\ \boldsymbol{u_2} \end{bmatrix} = [u_a \quad u_b \quad u_c | u_u \quad u_v \quad u_w]^T \tag{2.4}$$

$$\boldsymbol{i_s} = \begin{bmatrix} \boldsymbol{i_1} \\ \boldsymbol{i_2} \end{bmatrix} = [i_a \quad i_b \quad i_c | i_u \quad i_v \quad i_w]^T \tag{2.5}$$

$$\boldsymbol{\varphi_s} = \begin{bmatrix} \boldsymbol{\varphi_1} \\ \boldsymbol{\varphi_2} \end{bmatrix} = [\varphi_a \quad \varphi_b \quad \varphi_c | \varphi_u \quad \varphi_v \quad \varphi_w]^T \tag{2.6}$$

The vector with subscript "1" represents variables associated with ABC windings. The vector with subscript "2" represents variables with UVW windings. The stator flux linkage comes from two sources, i.e., stator currents and permanent magnet, and can be expressed as

$$\boldsymbol{\varphi_s} = \boldsymbol{L_s}\boldsymbol{i_s} + \varphi_f \boldsymbol{\lambda} \tag{2.7}$$

where φ_f represents the rotor flux linkage magnitude per phase associated with permanent magnet; $\boldsymbol{\lambda}$ represents the angle shift between the rotor and each stator windings and can be given as

$$\boldsymbol{\lambda} = \begin{bmatrix} \boldsymbol{\lambda_1} \\ \boldsymbol{\lambda_2} \end{bmatrix} \tag{2.8}$$

$$\boldsymbol{\lambda_1} = \left[\cos(\theta) \quad \cos\left(\theta - \frac{2\pi}{3}\right) \quad \cos\left(\theta + \frac{2\pi}{3}\right)\right]^T \tag{2.9}$$

$$\boldsymbol{\lambda_2} = \left[\cos\left(\theta - \pi\right) \quad \cos\left(\theta + \frac{\pi}{3}\right) \quad \cos\left(\theta - \frac{\pi}{3}\right)\right]^T \tag{2.10}$$

where θ represents the electrical angle shift between rotor N-pole and phase-A.

The voltage equation of the machine in the six-phase frame can thus be derived by substituting flux linkage expression (2.7) – (2.10) into voltage expression (2.3). Thus we have

$$\boldsymbol{u_s} = R\boldsymbol{i_s} + \boldsymbol{L_s}\frac{d\boldsymbol{i_s}}{dt} - \omega_e \varphi_f \boldsymbol{\lambda_d} \tag{2.11}$$

where

$$\boldsymbol{\lambda_d} = \begin{bmatrix}\boldsymbol{\lambda_{d1}} \\ \boldsymbol{\lambda_{d2}}\end{bmatrix} \tag{2.12}$$

$$\boldsymbol{\lambda_{d1}} = \left[\sin(\theta) \quad \sin\left(\theta - \frac{2\pi}{3}\right) \quad \sin\left(\theta + \frac{2\pi}{3}\right)\right]^T \tag{2.13}$$

$$\boldsymbol{\lambda_{d2}} = \left[\sin\left(\theta - \pi\right) \quad \sin\left(\theta + \frac{\pi}{3}\right) \quad \sin\left(\theta - \frac{\pi}{3}\right)\right]^T \tag{2.14}$$

In (2.11), the inductance matrix $\boldsymbol{L_s}$ is given in (2.2), and R, φ_f are given in Table 2.2 below. All of them are derived from the finite element model of the optimized machine.

Table 2.2. Machine parameters from Motor-CAD

Machine parameter	Symbol	Value
Pole pairs	p	6
Phase resistance	R	0.035Ω
Flux induced by magnet	φ_f	0.033Vs

The electromagnetic torque can be determined as the first derivative of the field energy W_m [20] and given as

$$T_e = \frac{\mathrm{d}W_m}{\mathrm{d}\theta_m} = p\frac{d}{d\theta}\left(\frac{1}{2}\boldsymbol{i_s}^T\boldsymbol{L_s}\boldsymbol{i_s} + \boldsymbol{i_s}^T \cdot \varphi_f \boldsymbol{\lambda}\right) \tag{2.15}$$

where θ_m is the mechanical rotor angle of the machine which has a relationship with the electrical rotor angle as follows:

$$\theta = p\theta_m \tag{2.16}$$

It can be seen from (2.15) that the torque is only proportional to the product of stator

currents and magnet flux. Because $\boldsymbol{i_s}$ is the function of time and $\boldsymbol{L_s}$ is constant, the first item of (2.15) is not associated with the rotor position θ_m and will become zero after derivation. This item will not contribute to any torque. Thus (2.16) can be simplified as:

$$T_e = -p\varphi_f \boldsymbol{i_s^T \lambda_d} \tag{2.17}$$

2.2.2 Dual D-Q Math Model

The six-phase math model developed just above is the most intrinsic math description of the dual three-phase machine. However, it is not friendly for machine control engineers because all variables on the six-phase frame are sinusoidal. To make a convenience of control algorithm development, a decoupled machine math model based on the rotor frame (d-q frame) will be developed in this section.

This decoupled machine model is called the dual d-q math model because there are two sets of d-q frames defined for the two three-phase, which are $d1/q1$ and $d2/q2$ shown in Fig 2.4 for ABC and UVW phases respectively. As can be seen from it, the $d1$-axis is aligned with rotor N-pole. The $d2$-axis has 180-degree shift with $d1$-axis due to the 180-degree phase shift between the A phase and U phase. The $q1$ and $q2$ axes are 90° shift anti-clockwise from $d1$ and $d2$ axes.

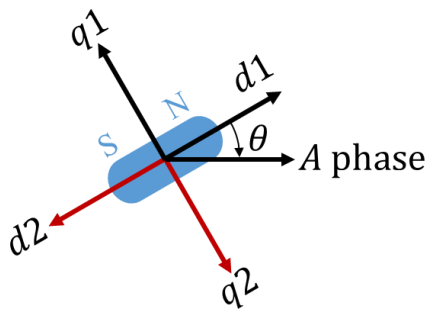


Fig 2.4. d/q-axis and rotor position (θ) definition

After the definition of the d-q frame, the Clarke-Park transformation equation (2.18) is multiplied on both sides of the six-phase model (2.11), which can derive the final

decoupled dual d-q frame equation like (2.19-a) and (2.19-b), which represent A/B/C-phase and U/V/W-phase respectively.

$$\boldsymbol{C_2} = \begin{bmatrix} \boldsymbol{C_1} & \\ & -\boldsymbol{C_1} \end{bmatrix} \tag{2.18}$$

where $\boldsymbol{C_1} = \frac{2}{3}\begin{bmatrix} \cos\theta & \cos\left(\theta - \frac{2\pi}{3}\right) & \cos\left(\theta + \frac{2\pi}{3}\right) \\ -\sin\theta & -\sin\left(\theta - \frac{2\pi}{3}\right) & -\sin\left(\theta + \frac{2\pi}{3}\right) \end{bmatrix}$.

$$\begin{bmatrix} u_{d1} \\ u_{q1} \end{bmatrix} = R\begin{bmatrix} i_{d1} \\ i_{q1} \end{bmatrix} + \begin{bmatrix} L_d & 0 \\ 0 & L_q \end{bmatrix}\frac{d}{dt}\begin{bmatrix} i_{d1} \\ i_{q1} \end{bmatrix} + \omega_e \begin{bmatrix} -L_q i_{q1} \\ L_d i_{d1} + \varphi_f \end{bmatrix} + \boldsymbol{d} \tag{2.19-a}$$

$$\begin{bmatrix} u_{d2} \\ u_{q2} \end{bmatrix} = R\begin{bmatrix} i_{d2} \\ i_{q2} \end{bmatrix} + \begin{bmatrix} L_d & 0 \\ 0 & L_q \end{bmatrix}\frac{d}{dt}\begin{bmatrix} i_{d2} \\ i_{q2} \end{bmatrix} + \omega_e \begin{bmatrix} -L_q i_{q2} \\ L_d i_{d2} + \varphi_f \end{bmatrix} - \boldsymbol{d} \tag{2.19-b}$$

where R, φ_f, L_d, L_q have their values shown in Table 2.3, and $\boldsymbol{d}$ has the expression in (2.20). The R and φ_f don't change after Clarke-Park transformation so they are the same as the parameters of the six-phase model in Table 2.2. The L_d and L_q are unique for dual d-q model and calculated based on the inductance matrix $\boldsymbol{L_s}$ in (2.2).

Table 2.3. Machine parameters for dual d-q math model

Machine parameter	Symbol	Value
Phase resistance	R	0.035Ω
Flux induced by magnet	φ_f	0.033Vs
d- and q-axis inductance	L_d, L_q	437μH

Comparing (2.19-a) and (2.19-b) with the traditional three-phase PMSM model, the dual d-q model has an extra item $\boldsymbol{d}$, which has the expression as follows:

$$\boldsymbol{d} = \boldsymbol{M_d}\left\{\begin{bmatrix} i_{d1} - i_{d2} \\ i_{q1} - i_{q2} \end{bmatrix}' - \omega_e \begin{bmatrix} i_{q1} - i_{q2} \\ i_{d2} - i_{d1} \end{bmatrix}\right\} \tag{2.20}$$

where $\boldsymbol{M_d} = \begin{bmatrix} -8 & 20 \\ 20 & -12 \end{bmatrix}\mu H$ is calculated based on the inductance matrix $\boldsymbol{L_s}$ in (2.2).

It can be seen the L_d and L_q are much larger than $\boldsymbol{M_d}$. In addition, during normal operations, i_{d1} and i_{d2} will follow the same reference value and so do the i_{q1} and i_{q2},

thus making $\boldsymbol{d}$ to be even smaller. Therefore, $\boldsymbol{d}$ can be neglected and this machine can be regarded as two separate three-phase PMSM as follows:

$$\begin{bmatrix} u_{d1} \\ u_{q1} \end{bmatrix} = R \begin{bmatrix} i_{d1} \\ i_{q1} \end{bmatrix} + \begin{bmatrix} L_d & 0 \\ 0 & L_q \end{bmatrix} \frac{d}{dt} \begin{bmatrix} i_{d1} \\ i_{q1} \end{bmatrix} + \omega_e \begin{bmatrix} -L_q i_{q1} \\ L_d i_{d1} + \varphi_f \end{bmatrix} \quad (2.21\text{-a})$$

$$\begin{bmatrix} u_{d2} \\ u_{q2} \end{bmatrix} = R \begin{bmatrix} i_{d2} \\ i_{q2} \end{bmatrix} + \begin{bmatrix} L_d & 0 \\ 0 & L_q \end{bmatrix} \frac{d}{dt} \begin{bmatrix} i_{d2} \\ i_{q2} \end{bmatrix} + \omega_e \begin{bmatrix} -L_q i_{q2} \\ L_d i_{d2} + \varphi_f \end{bmatrix} \quad (2.21\text{-b})$$

Therefore, the total electromagnetic torque can be regarded as the sum of two 3-phase machines and has its expression as follows:

$$T_e = 1.5 p \varphi_f \left(i_{q1} + i_{q2} \right) \quad (2.22)$$

2.3 Comparison of Machine Math Models and Finite Element Model

In this section, the two machine math models (i.e., six-phase model, dual d-q model) derived above will be compared with the machine finite element (FE) model. With the same current inputs, the two math models are expected to have the same voltage and torque output as the FE model, so that to prove the correctness of the two math models.

It is assumed that the rotor is rotating constantly at 10,000rpm ($\omega_e = 6283\text{rad}/s$), and the six phase windings are injected with sinusoidal currents given by (2.23) with one period waveform shown in Fig 2.5. The magnitude of currents (i.e., I) is set to 10A.

$$\begin{cases} i_a = I \cdot \sin(\omega_e t) \\ i_b = I \cdot \sin\left(\omega_e t - \frac{2\pi}{3}\right) \\ i_c = I \cdot \sin\left(\omega_e t + \frac{2\pi}{3}\right) \\ i_u = I \cdot \sin(\omega_e t - \pi) \\ i_v = I \cdot \sin\left(\omega_e t + \frac{\pi}{3}\right) \\ i_w = I \cdot \sin\left(\omega_e t - \frac{\pi}{3}\right) \end{cases} \tag{2.23}$$

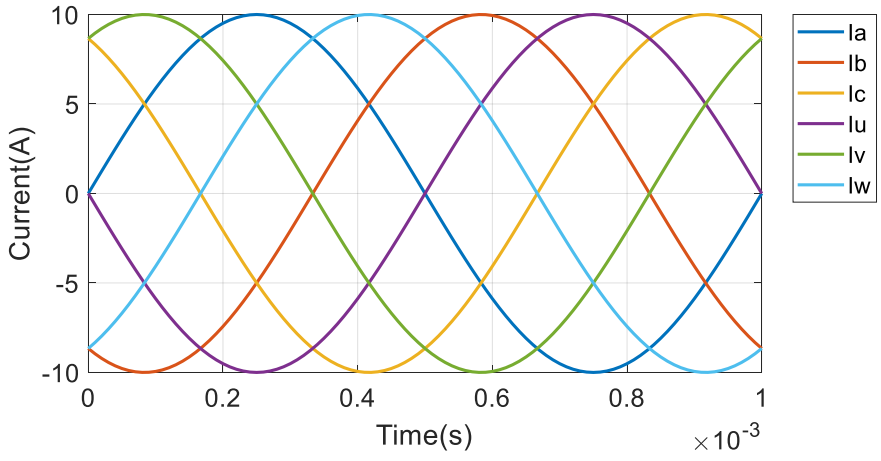


Fig 2.5. The current waveform used for the FE model, six-phase model, and dual d-q model

For the FE model, the current injections can be achieved by simply connecting six current sources (with the waveforms in Fig 2.5) to the six windings. Then, running the finite element simulation can obtain the six-phase voltages and torque waveforms.

For the six-phase math model, the six-phase voltages and torque are calculated with the model shown in Fig 2.6 below. Firstly, the $\boldsymbol{\lambda_d}$ is calculated using (2.12)-(2.14) with the input of rotor position (θ). Then, the six-phase voltages ($\boldsymbol{u_s}$) can be calculated by (2.11) with ω_e, $\boldsymbol{\lambda_d}$, and injected currents ($\boldsymbol{i_s}$). The torque (T_e) can be calculated through (2.17).

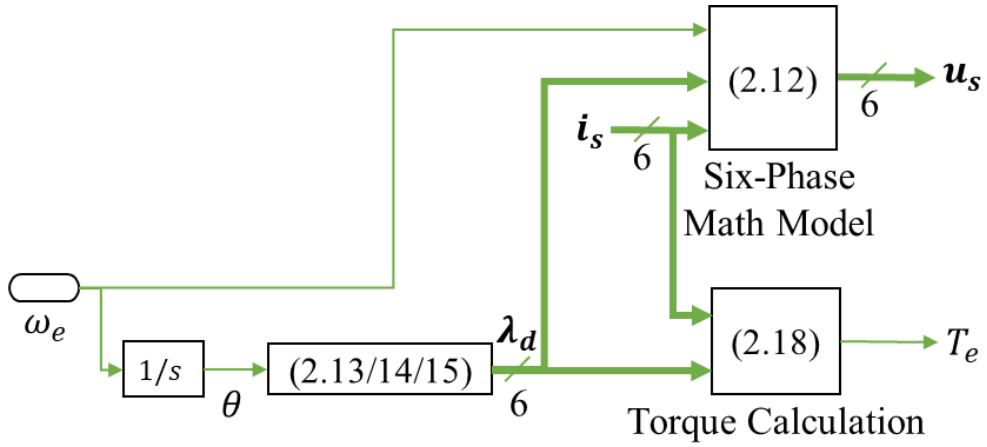


Fig 2.6. Six-phase math model validation diagram

For the dual d-q math model, the six-phase voltages and torque calculation diagram is shown in Fig 2.7. Because this math model is built on the d-q frame, the six-phase currents should be transformed to the d-q frame by Clarke-Park transformation using (2.18), and the six-phase voltages also need to be transformed from the d-q voltages by inverse Clarke-Park transformation using the equation (2.24) below. The voltages in the d-q frame are calculated from d-q frame currents by (2.21-a/b), and the torque is calculated by (2.22) with i_{q1} and i_{q2}.

$$\boldsymbol{C_{2inv}} = \begin{bmatrix} \boldsymbol{C_{1inv}} & \\ & -\boldsymbol{C_{1inv}} \end{bmatrix} \tag{2.24}$$

where $\boldsymbol{C_{1inv}} = \frac{2}{3}\begin{bmatrix} \cos\theta & -\sin\theta \\ \cos\left(\theta - \frac{2\pi}{3}\right) & -\sin\left(\theta - \frac{2\pi}{3}\right) \\ \cos\left(\theta + \frac{2\pi}{3}\right) & -\sin\left(\theta + \frac{2\pi}{3}\right) \end{bmatrix}$.

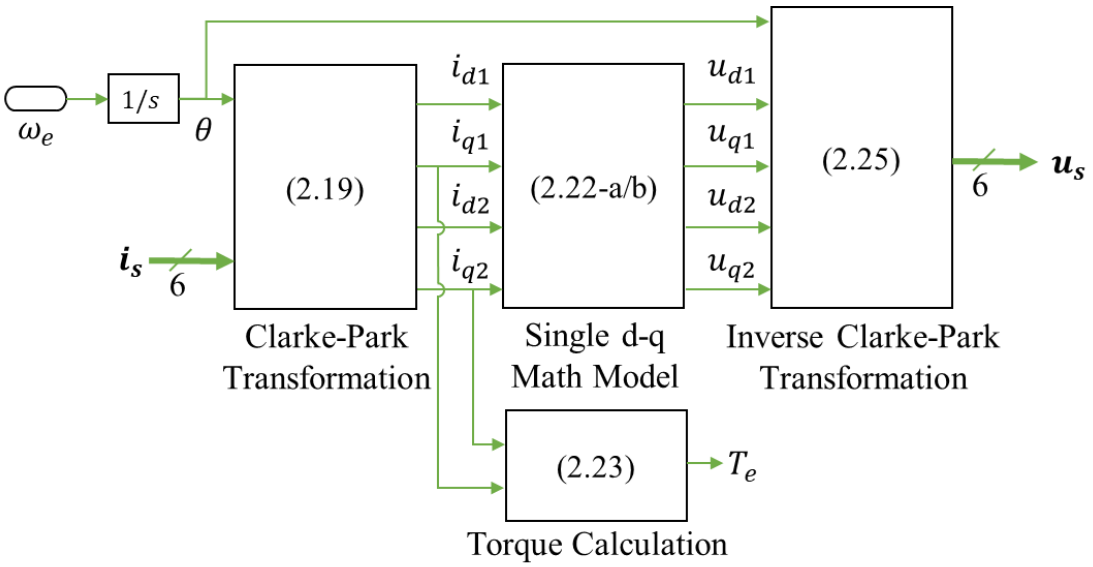


Fig 2.7. Dual d-q math model validation diagram

After injecting the same six-phase currents into the 3 models (i.e., FE model, six-phase model, dual d-q model), the output phase voltages and torque have the results in Fig 2.8-Fig 2.10.

Fig 2.8 demonstrates one period of the six-phase voltages in the time domain, and Fig 2.9 compares the spectrum of A-phase voltage for the 3 models. From Fig 2.8, it can be seen the six-phase model and dual d-q model have exactly the same voltage waveforms, and the FE model has almost the same waveforms but with a small distortion.

Their minor difference can be explained from their spectrum in Fig 2.9. There, we can see that the fundamental voltage components (1,000Hz) are the same for the six-phase model and dual d-q model (208V), but is a little different for the FE model (206.7V). However, the voltage waveforms from the six-phase model and dual d-q model are ideal sinusoidal and only contain fundamental components, while voltage waveforms from the FE model contain harmonics due to impacts such as lamination saturation, slots and magnets shapes, uneven flux distribution, etc.

For the control design, only the fundamental components are relevant, therefore, it is adequate to use the six-phase model or the dual d-q model to represent the relationship

between machine phase voltages and phase currents.

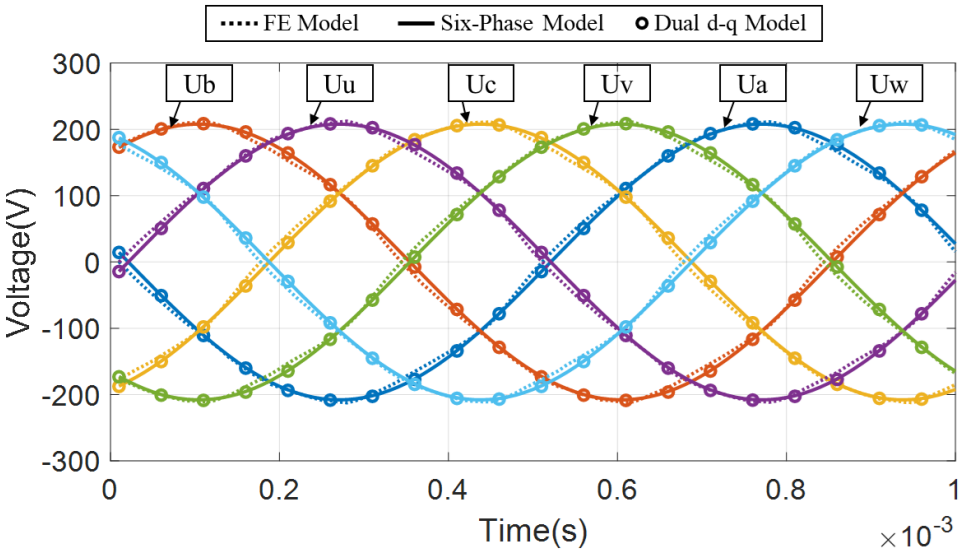


Fig 2.8. Six-phase voltage comparison of FE model, six-phase model, and dual d-q model

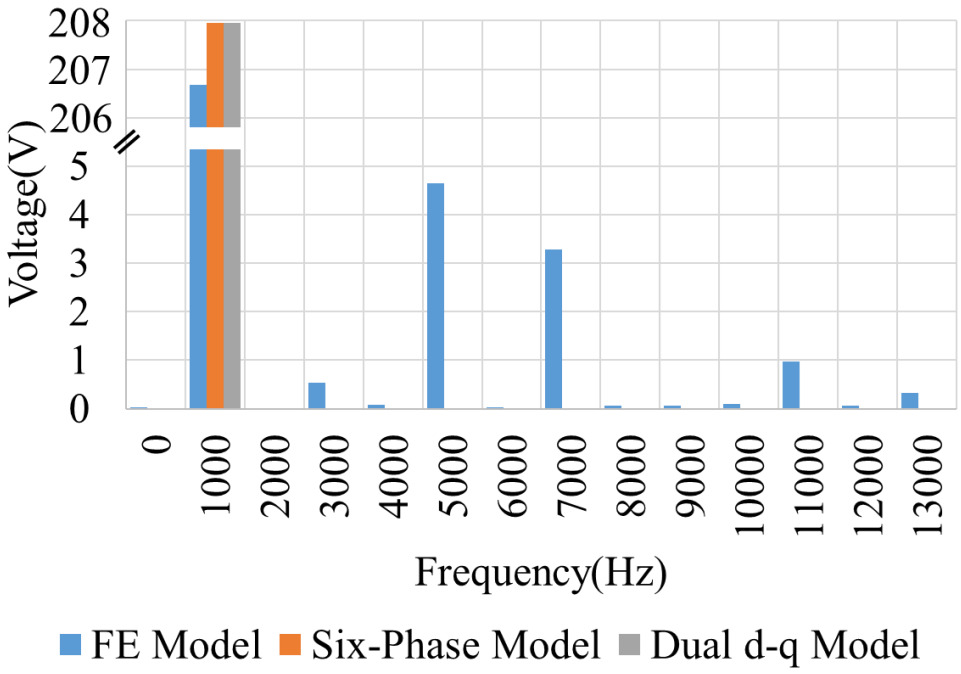


Fig 2.9. The spectrum of A-phase voltage for the FE model, six-phase model, and dual d-q model

The comparison of electromagnetic torque waveform, given by Fig 2.10, shows that the torques from the six-phase model and dual d-q model are constant, whilst the torque from the FE model contains ripple caused by cogging torque and harmonics of magnet flux. However, they have similar average values as expected.

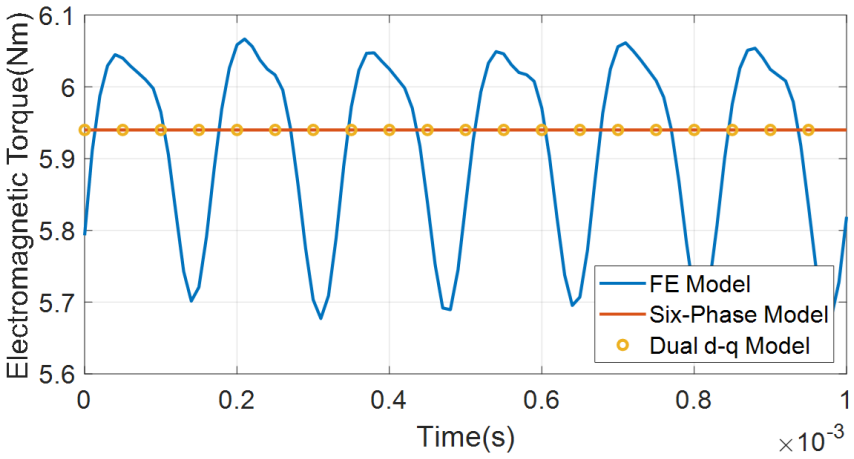


Fig 2.10. Torque comparison of FE model, six-phase model, and dual d-q model

Above all, this section proves the two machine math models (six-phase model and dual d-q model) have a good match with the FE model. Therefore, control algorithms can be proposed and simulated based on the six-phase model or dual d-q model instead of the time-consuming FE model with much confidence. However, from the FE model, the cogging torque and voltage harmonics can be observed, which is impossible for the two math models. Therefore, the FE model is prone to be used for torque ripple analysis.

2.4 Conclusion

In this chapter, the dual three-phase permanent magnet synchronous machine designed for mild-hybridized turboprop is first introduced. Its section view is provided to give a better understanding of the machine structure. The machine parameters are derived from finite element analysis, and the machine performance from simulation satisfies the requirement of the machine from the project.

Then, two math models of this dual three-phase machine are developed (i.e., six-phase math model, dual d-q math model). The six-phase math model is the most intrinsic, but not friendly for control algorithm design because all variables in the six-phase frame are sinusoidal in steady state. Another machine model, the dual d-q math model, is derived from the six-phase math model but based on the rotor d-q frame. It can fulfil the decoupling of machine variables and is easier for control design.

At the end of this chapter, the 3 models (finite element model, six-phase model, and dual d-q model) are compared by using the same six-phase currents as input. The output voltages and torque of them are compared to validate their consistency.

Chapter 3.

Current Closed-Loop Control and Position Sensorless Algorithm

The dual three-phase machine math models (six-phase model and dual d-q model) have been developed in the last chapter. In this chapter, the current closed-loop control algorithm will be designed based on the dual d-q machine model. Then, the rotor position estimation methods will be reviewed based on previous literature. The I-F (current-frequency) open-loop sensorless control is selected for zero to low speed, and the Model Reference Adaptive System (MRAS)-based estimation method is adopted for high speed. The principles of these two sensorless controls will be introduced in detail and corresponding simulation results will validate their ability to control this machine without position sensor. The speed control loop is not considered in this chapter, whilst it will be implemented in the ACHIEVE experiment and introduced in Chapter 7.

3.1 Current Controller Design

In this section, the PI (proportional-Integral) current controller is designed based on the dual d-q math model proposed in section 2.2.2. The machine dual d-q model can be summarized as:

$$\begin{bmatrix} u_{d1} \\ u_{q1} \end{bmatrix} = R \begin{bmatrix} i_{d1} \\ i_{q1} \end{bmatrix} + \begin{bmatrix} L_d & 0 \\ 0 & L_q \end{bmatrix} \frac{d}{dt} \begin{bmatrix} i_{d1} \\ i_{q1} \end{bmatrix} + \omega_e \begin{bmatrix} -L_q i_{q1} \\ L_d i_{d1} + \varphi_f \end{bmatrix} \qquad (3.1\text{-a})$$

$$\begin{bmatrix} u_{d2} \\ u_{q2} \end{bmatrix} = R \begin{bmatrix} i_{d2} \\ i_{q2} \end{bmatrix} + \begin{bmatrix} L_d & 0 \\ 0 & L_q \end{bmatrix} \frac{d}{dt} \begin{bmatrix} i_{d2} \\ i_{q2} \end{bmatrix} + \omega_e \begin{bmatrix} -L_q i_{q2} \\ L_d i_{d2} + \varphi_f \end{bmatrix} \quad (3.1\text{-b})$$

Each 3-phase channel can be regarded as an independent 3-phase machine. Therefore, the two channels can be controlled separately with the current closed-loop control diagram shown in Fig 3.1 below. Each 3-phase channel has its own current PI controllers, current decouple module and SVPWM module. Because the two channels have the same expression and parameters, only the ABC 3-phase channel will be analysed in the following part of this section, and the derived control parameters can be used for the UVW channel directly.

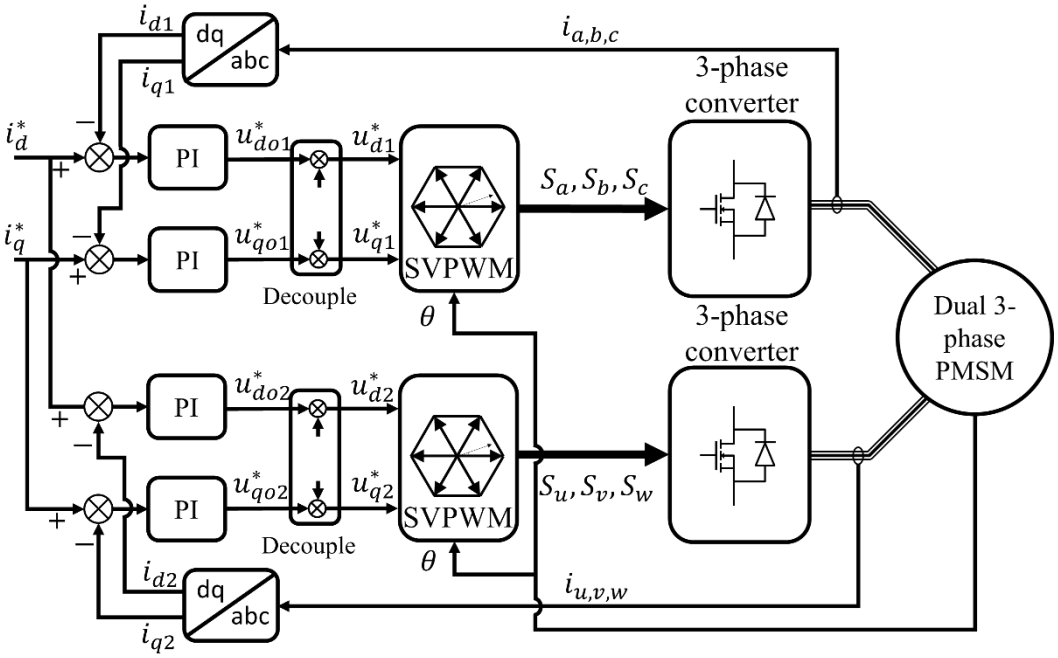


Fig 3.1. PI current control diagram based on dual d-q math model

Transforming the time-domain expression (3.1-a) to the s-domain, the machine transfer function of the ABC channel is shown as follows:

$$u_{d1} = (sL_d + R)i_{d1} - \omega_e L_q i_{q1} \quad (3.2\text{-a})$$

$$u_{q1} = (sL_q + R)i_{q1} + \omega_e(L_d i_{d1} + \varphi_f) \quad (3.2\text{-b})$$

The PI controllers in Fig 3.1 have the transfer function as follows:

$$u_{do1}^* = \left(k_p + \frac{k_i}{s}\right)(i_d^* - i_{d1}) \quad (3.3\text{-a})$$

$$u_{qo1}^{*} = \left(k_p + \frac{k_i}{s}\right)\left(i_q^{*} - i_{q1}\right) \tag{3.3-b}$$

where k_p, k_i are proportional and integral factors respectively.

The purpose of the 'Decouple' module in Fig 3.1 is to compensate the cross-coupling voltage drop on back-EMF and d/q-axis inductances. It has the expressions as follows:

$$u_{d1}^{*} = u_{do1}^{*} - \omega_e L_q i_{q1} \tag{3.4-a}$$

$$u_{q1}^{*} = u_{qo1}^{*} + \omega_e\left(L_d i_{d1} + \varphi_f\right) \tag{3.4-b}$$

The u_{d1}^{*} and u_{q1}^{*} in Fig 3.1 are the voltage references which go to the SVPWM module to generate switching signals of the A/B/C-phase. The SVPWM usually causes a delay between voltage reference and real voltage, which is one switching period. Therefore, this delay can be described as a first-order process as follows:

$$u_{d1} = \frac{1}{sT_s+1} u_{d1}^{*} \tag{3.5-a}$$

$$u_{q1} = \frac{1}{sT_s+1} u_{q1}^{*} \tag{3.5-b}$$

where T_s represents the switching period which is the same as the carrier period.

Based on the transfer function derived above, the entire transfer function diagram of the d-axis current control loop can be derived and displayed in Fig 3.2-(a), where the three blocks represent models of PI controller, SVPWM delay, and electrical machine respectively. One compensation term $\omega_e L_q i_{q1}$ after the SVPWM delay represents the coupling item from q-axis to d-axis inside the machine. The other compensation term $\omega_e L_q i_{q1}$ before SVPWM delay is the decoupling item in the controller. As can be seen in Fig 3.2-(a), the two compensations are the same but have opposite symbols, which can be counteracted in further analysis. Therefore, Fig 3.2-(a) can be synthesized into Fig 3.2-(b) with an open-loop transfer function shown in (3.6).

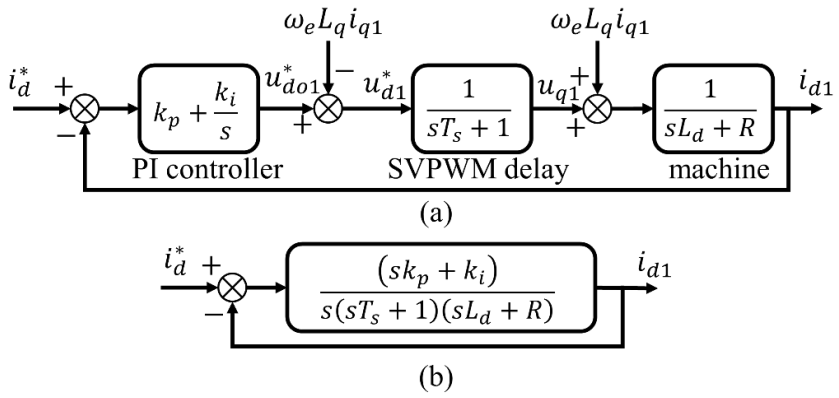


Fig 3.2. The entire i_{d1} current control loop (a) and synthesized (b) transfer function diagram

$$G(s) = \frac{(sk_p+k_i)}{s(sT_s+1)(sL_d+R)} \tag{3.6}$$

It can be seen from Fig 3.2-(b), the open-loop transfer function has two poles ($s = -1/T_s, -R/L_d$) and one zero ($s = -k_i/k_p$). The design principle of k_p and k_i is to make the zero cancel the pole which is close to the origin and has a greater impact on system performance. Therefore, the PI factors are selected as follows:

$$k_p = L_d\omega_{cc} \tag{3.7-a}$$

$$k_i = R\omega_{cc} \tag{3.7-b}$$

where ω_{cc} is associated with the system's closed-loop bandwidth with a unit of rad/s. Substituting (3.7-a) and (3.7-b) to (3.6), the open-loop transfer function has an expression as follows:

$$G(s) = \frac{(sL_d\omega_{cc}+R\omega_{cc})}{s(sT_s+1)(sL_d+R)} = \frac{\omega_{cc}}{s(sT_s+1)} \tag{3.8}$$

Therefore, the closed-loop transfer function is shown as follows:

$$\begin{aligned} G_c(s) &= \frac{G(s)}{1+G(s)} = \frac{\omega_{cc}}{s^2T_s+s+\omega_{cc}} \\ &\approx \frac{\omega_{cc}}{s+\omega_{cc}} = \frac{1}{T_{cc}s+1} \end{aligned} \tag{3.9}$$

where the second order item (s^2T_s) can be neglected as its factor T_s is much smaller than the first-order factor 1. T_{cc} is defined $T_{cc} = 1/\omega_{cc}$.

As can be seen from the close-loop transfer function (3.9), the current closed-loop is a first-order system. Its time constant T_{cc} is a measure of how quickly the first order

system responds to a unit step input. The bandwidth of this system is defined as $f_{cc} = 1/(2\pi T_{cc})$, which represents the frequency of the system with a -3dB drop.

The transfer function diagram of i_{q1}-loop is similar to that of i_{d1} control loop and is shown in Fig 3.3. As L_d is assumed to be equal to L_q for this surface-mounted machine, the close-loop transfer function of i_{q1} close-loop is thus the same with i_{d1} close-loop and the selection of k_p, k_i in the i_{q1} close-loop can follow (3.7-a) and (3.7-b).

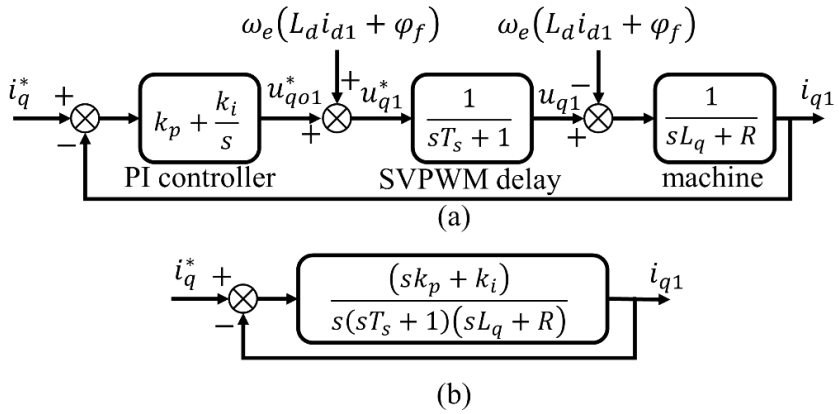


Fig 3.3. Whole (a) and synthesized (b) transfer function diagram for i_{q1} closed-loop

With (3.7)-(3.9), the PI controllers for the current loop can be defined for a selected bandwidth f_{cc}. For the specific ACHIEVE machine, we select the bandwidth to be f_{cc}=1000Hz, the control parameters can be derived and shown in the following table.

Table 3.1. Current PI controller parameters

Simulation condition	Symbol
Controller bandwidth ($\boldsymbol{f_{cc}}$)	1000Hz
Proportional factor ($\boldsymbol{k_p}$)	2.74
Integral factor ($\boldsymbol{k_i}$)	220

3.2 Current Closed-Loop Control Simulation

A simulation model shown in Fig.A.3 in Appendix A is built in PLECS. It will be used in this section to validate the current closed-loop control algorithm proposed in Section 3.1. The motor drive system with designed current loops is tested under two scenarios, i.e., step current command scenario and step speed command scenario.

3.2.1 Step Current Command Scenario

During the simulation, we kept the machine speed constant at 1krpm and the d-axis current reference i_d^* is zero. At t=0s, the q-axis current reference (i_q^*) changes from 0A to 10A. At t=0.01s, the i_q^* changes from 10A to 20A. The PI controller bandwidth is selected to 1000Hz with k_p, k_i shown in Table 3.1.

The simulation results of q- and d-axis currents are shown in Fig 3.4. It can be seen in Fig 3.4 that the i_q follows the reference i_q^* very well without any overshoot. The d-axis currents are not affected at all by the q-axis current change.

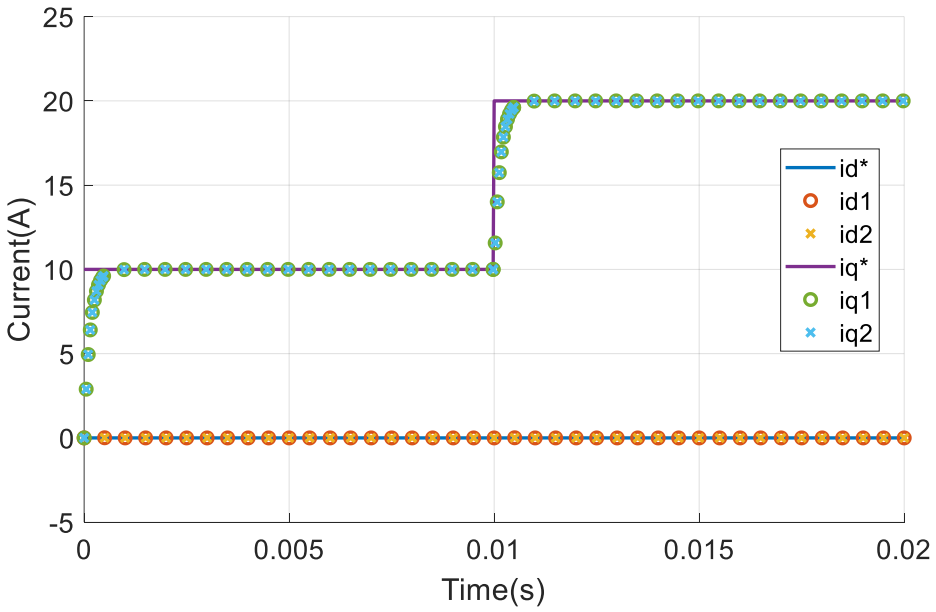


Fig 3.4. d/q-axis currents response with iq reference step command

Fig 3.5 shows the electromagnetic torque under this scenario. This torque changes smoothly during the dynamic state and keeps very stable during the steady state. As this machine is assumed to have equal d- and q-axis inductances, the electromagnetic torque does not have the reluctance torque component. Therefore, the torque is proportional to iq exactly.

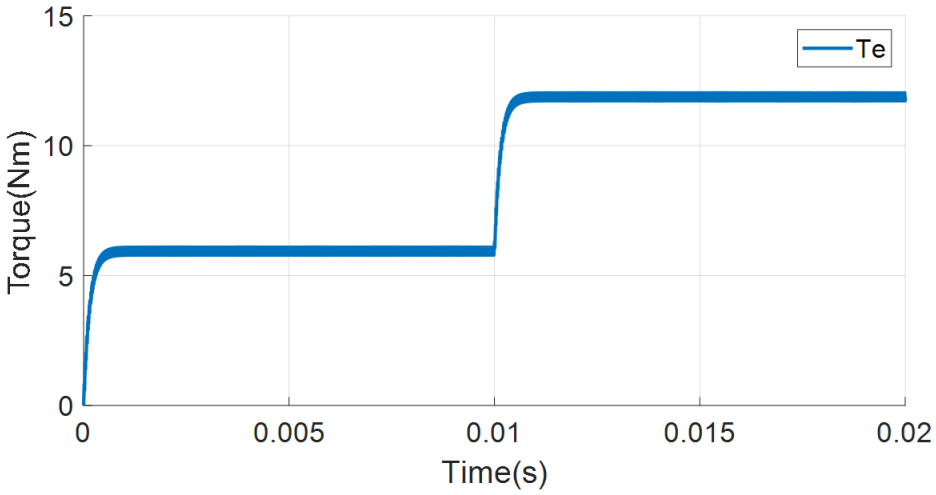


Fig 3.5. Electromagnetic torque response with iq reference step command

The six-phase currents, given in Fig 3.6, have their magnitude the same as the q-axis current since the d-axis current is zero. The current waveforms also include high-frequent harmonics caused by the PWM voltages.

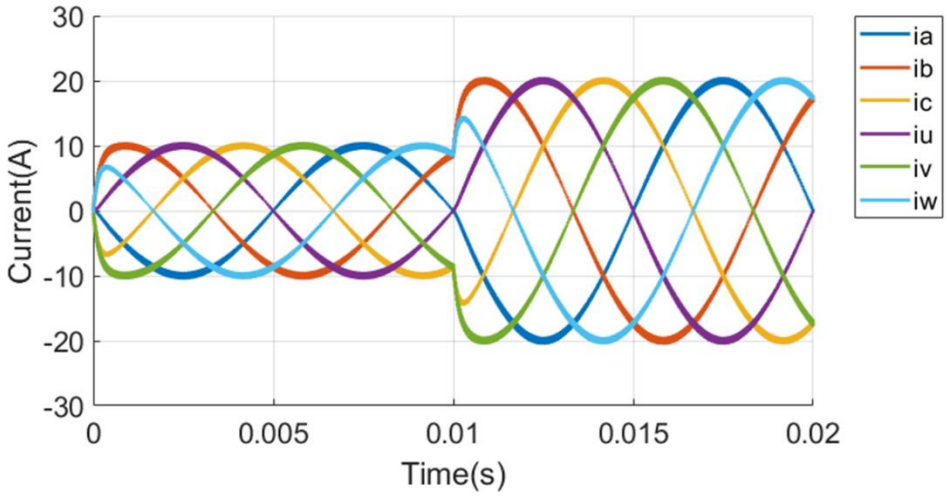


Fig 3.6. Six-phase currents with iq reference step command

3.2.2 Step Speed Command Scenario

In this scenario, we applied a step change of machine speed at t=0s from 0rpm to 1krpm and t=0.01s from 1krpm to 5krpm. Although the step speed change is impossible in reality, it is a good assumption when only analysing the anti-disturbance performance of the current loop.

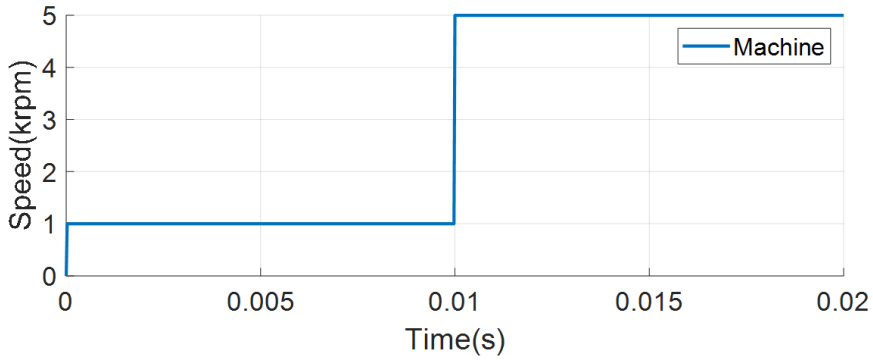


Fig 3.7. Speed command step change waveform

The d- and q-axis current waveforms, given in Fig 3.8, show the currents are not influenced by the speed step changes and display good anti-disturbance ability. The torque waveform, given in Fig 3.9, is always constant even with these speed step changes. The torque ripple at a higher speed (5krpm) is also larger than the torque ripple at 1krpm, which is caused by the lower modulation to fundamental frequency ratio at 5krpm.

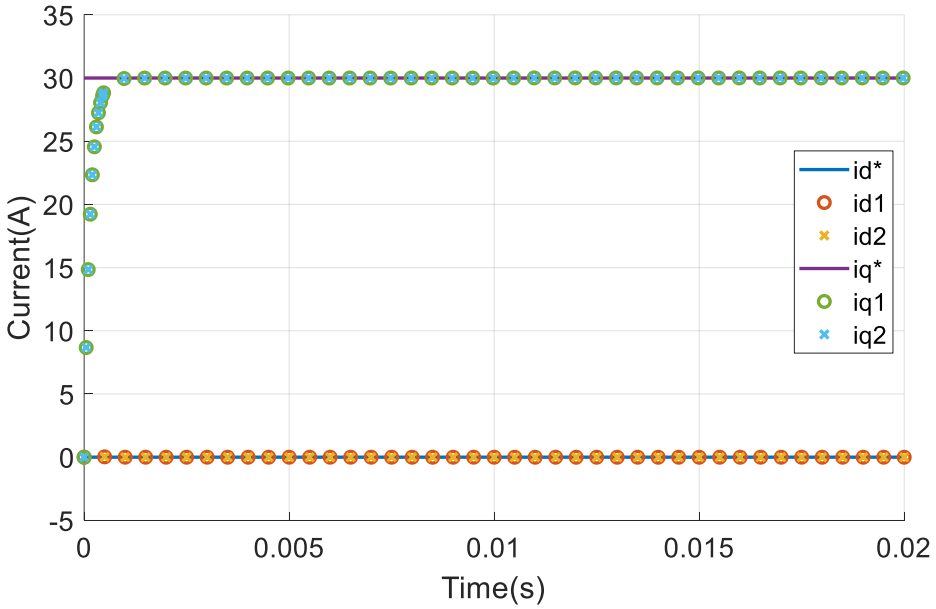


Fig 3.8. d/q-axis currents response with step speed command

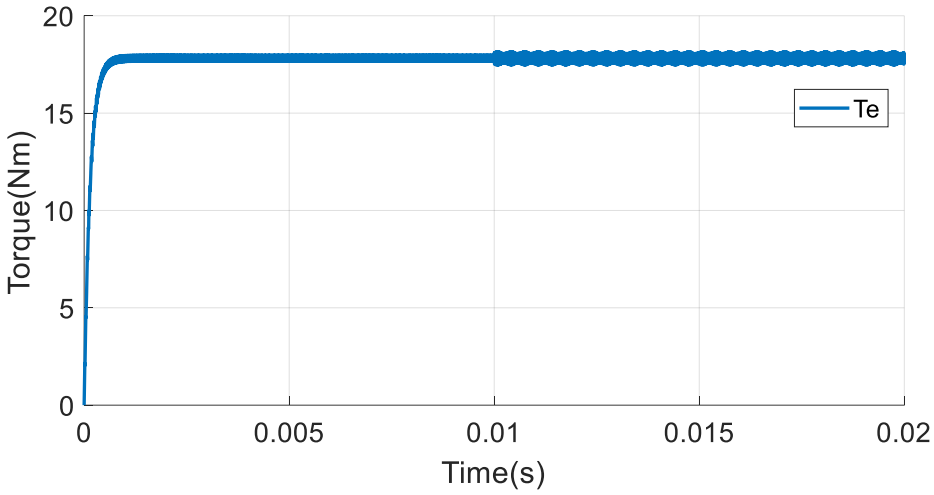


Fig 3.9. Electromagnetic torque response with step speed command

The six-phase current waveforms, given in Fig 3.10, show the current frequency increases with higher speed, but the magnitude is not affected by the speed change.

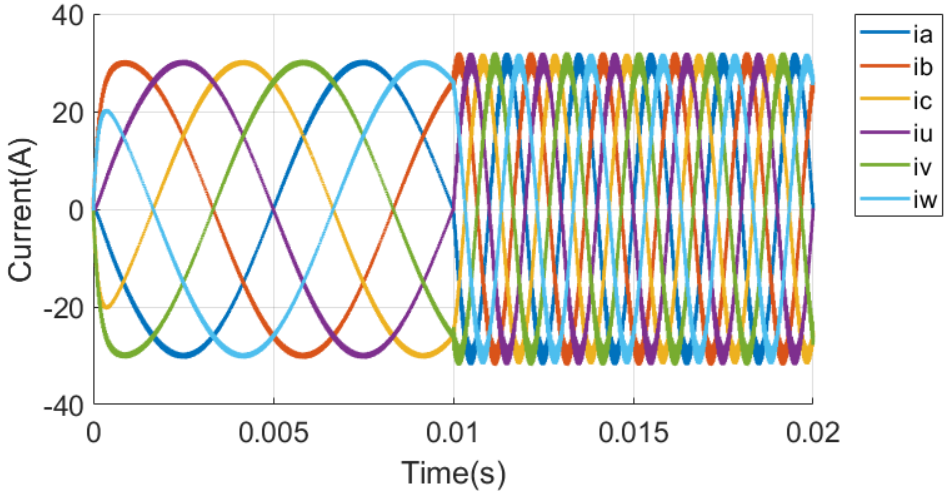


Fig 3.10. Six-phase currents response with step speed command

3.3 Permanent Magnet Machine Position Sensorless Control

In this section, the position sensorless control algorithm for the dual three-phase machine will be discussed. Firstly, a short literature review will be introduced regarding commonly used sensorless control methods for permanent magnet machines. The selection of I-F open-loop sensorless and MRAS sensorless methods is discussed for this high-speed motor/generator system application in detail. Finally, the sensorless control simulation models are built in PLECS and their performance is demonstrated.

3.3.1 Position Sensorless Control Methods Review

For field-oriented control, the rotor position, which is usually measured by an encoder or a resolver, is used in frame transformations for a permanent magnet machine. However, due to the project requirement, position sensorless control is the only option.

Sensorless control of AC machines has been well-studied over the past few decades. Many approaches have been proposed for machine sensorless control and are categorized in Fig 3.11.

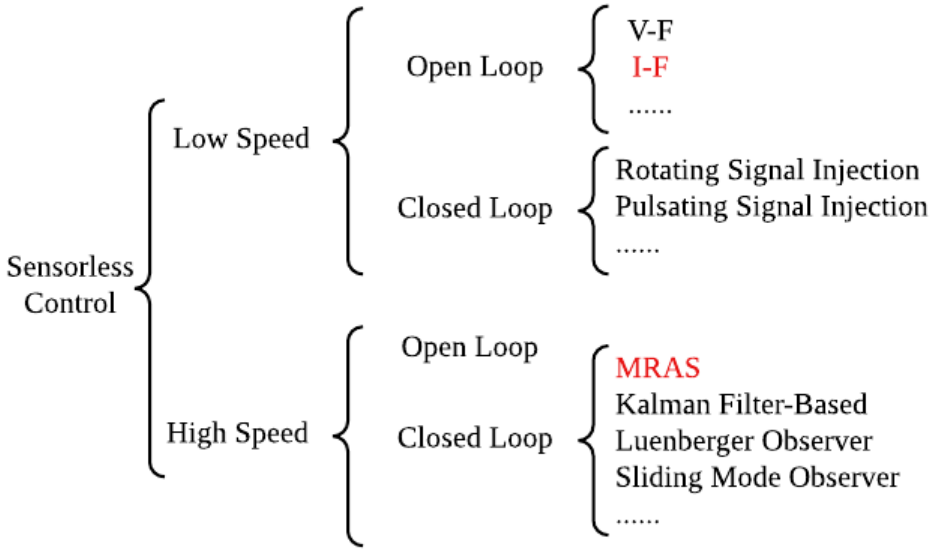


Fig 3.11. Categories of position sensorless control

Based on their operation speed range, sensorless control techniques are categorised into two groups, low-speed sensorless control techniques and high-speed sensorless control techniques. Each group can be further divided into open-loop methods and closed-loop methods depending on whether the measured variables (e.g., phase current) are fed into the sensorless algorithm as a correction term [21]. The open loop sensorless methods, either in the low-speed or high-speed group, have the advantage of convenience for implementation. However, these open loops based sensorless controls may not satisfy performance requirements during transients and have the risk of position tracking failure.

On the contrary, closed-loop sensorless methods are more reliable and robust. The closed loop methods for low speed can be categorized as rotating signal injection [22], [23], pulsating signal injection [24], [25] and others. The rotating signal injection methods inject phase-modulated signals into $\alpha\beta$ frame, whilst the pulsating signal injection methods inject magnitude modulated signals into dq frame. Both of them essentially relies on rotor saliency, which limits their applications on the machines with little difference between d and q-axis inductances.

The high-speed closed-loop sensorless methods include MRAS-based [26], Kalman filter-based [27], Luenberger observer [28], sliding mode observer [29], and so on. For these methods, the control inputs of the plant (actual machine) and the tracking error of the observer (i.e., the error between plant and observer outputs), are often used as the input signals to the observer. The observer gains are designed such that the observer outputs converge to the plant output. Thus, the estimated values for the states of interest can be forced to converge to their actual values [30]. When the speed is high, the back-EMF and flux are easier to be extracted from the phase voltages and the impact of noise and converter nonlinearity can be neglected. Therefore, these two variables can be used

for observer and can have higher accuracy in high speed within sensorless control.

In this thesis, the widely-used MRAS sensorless method is the major research objective not only because it is well developed during the past several decades, but also because it has a simple structure and is robust to parameter variation [26], [27], [39]–[42], [31]–[38]. In this application, the machine will run at a high speed (>6000rpm) range most of the time, and only runs at the low speed with limited time duration during start-up acceleration. Therefore, the I-F (Current-Frequency) open-loop control is adopted during the short start-up period. Compared with V-F (Voltage-Frequency) open loop control, the current in I-F open loop control is under closed-loop control so that it will not become overcurrent [43]–[45]. Although the low-speed closed-loop sensorless methods (e.g., signal injection) are more reliable than I-F open-loop control, they have more complicated control rules, thus more computation time will be required.

In the following section, the theory of I-F open-loop control and MRAS sensorless control will be introduced separately. Their simulation models will also be built in PLECS to validate their effectiveness.

3.3.2 I-F Open-Loop Sensorless Start-Up Control

The I-F open-loop sensorless control diagram is shown in Fig 3.12. As can be seen, the reference rotor position (θ^*) is generated from integration of reference speed (ω_e^*) instead of the rotor position from machine. The references i_q^* and ω_e^* are the outputs of I-F open-loop sensorless algorithm. They can be step signals or ramping signals depending on the requirement, and they should also follow a proper sequence to ensure a successful start-up. The I-F control principle will be discussed below in detail.

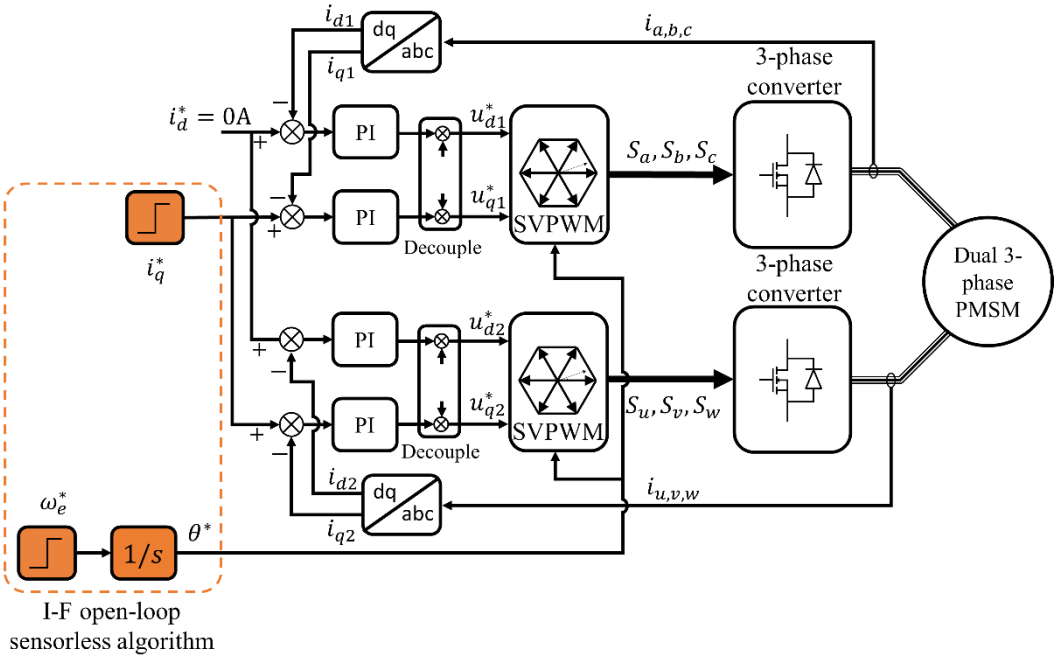


Fig 3.12. Block diagram of I-F open-loop sensorless start-up control system

3.3.2.1 I-F Open-Loop Control Process

The whole I-F open-loop sensorless start-up period can be classified into two stages. They are the initial clamping stage and rotating stage shown in Fig 3.13(a) and (b) respectively.

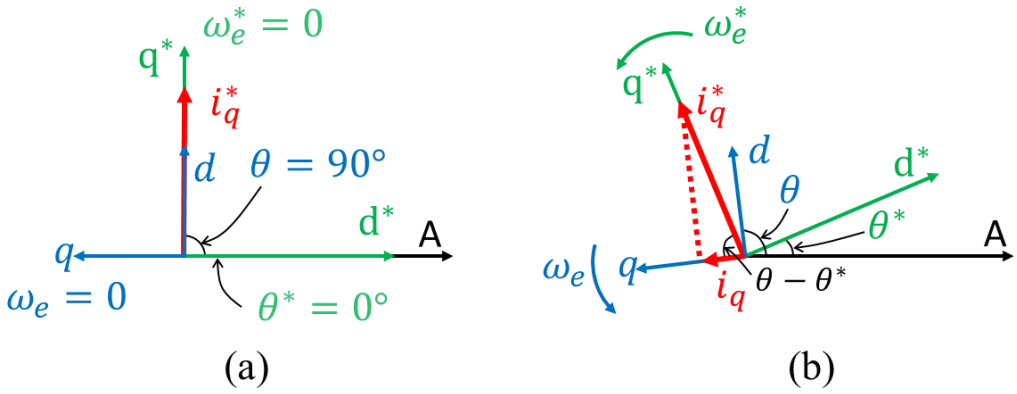


Fig 3.13. I-F open-loop control frame diagram

(a) initial clamping stage; (b) rotating stage.

(1). Initial clamping stage

As the actual d-axis position is completely random initially, the starting position of the reference rotating frame (green d*and q*-axis in Fig 3.13(a)) is defined to be aligned on A-phase. At the same time, a non-zero reference current (red i_q^* in Fig 3.13(a)) is

given to the current controller. Due to the electromagnetic torque generated by the current, the d-axis which is aligned to the rotor (marked as blue in Fig 3.13(a)) will be forced to align with q*-axis.

The final stable state of this initial clamping stage is shown in Fig 3.13(a). As the current i_q^* does not have any component projected on the actual q-axis, there will be no electromagnetic torque anymore, so the rotor will remain in the position shown in Fig 3.13(a).

In Fig 3.13(a), the angle between d*-axis and A-phase (θ^*) is defined as the position of reference rotating frame (d*-q* frame), and it is always zero during this initial clamping stage. The angle between the actual rotor d-axis and A-phase (θ) is defined as the position of rotor, and it becomes 90° at the end of the initial clamping stage.

(2). Rotating stage

In this stage, a step change will be given to ω_e^* and thus the reference rotating frame (d*-q* frame) starts to rotate, as shown in Fig 3.13(b). Due to the rotor inertia and load torque, the actual d-axis will lag behind the reference q*-axis. In this case, the projection of the current reference i_q^* to the machine actual q-axis (i_q) will not be zero anymore and electromagnetic torque will be generated and drives the rotor to rotate. As the i_q^* keeps constant during this stage, the electromagnetic torque totally depends on the angle between d-axis and d*-axis ($\theta - \theta^*$) which is the same with angle between q-axis and q*-axis.

3.3.2.2 Speed Transfer Function of I-F Open-Loop Control

The mathematical relationship between real rotor speed (ω_e) and its reference (ω_e^*) will be discussed below:

First of all, equation (3.10) demonstrates the relationship between electromagnetic torque and current on the real q-axis i_q. The K_T represents the torque constant of an

electrical machine. Equation (3.11) shows the relationship between i_q and i_q^*. It is convenient to derive from the Fig 3.13(b), where i_q is the projection of i_q^* on the actual q-axis.

$$T_e = K_T i_q \tag{3.10}$$

$$i_q = i_q^* \cos(\theta - \theta^*) \tag{3.11}$$

Combining (3.10) and (3.11) gives

$$T_e = K_T i_q^* \cos(\theta - \theta^*) \tag{3.12}$$

In I-F open-loop control, the i_q^* is always set to be constant, thus the torque T_e is a linear relation with $\cos(\theta - \theta^*)$. The relation between T_e and $\theta - \theta^*$ is shown in Fig 3.14 (the black curve). The red initial point represents the initial starting state demonstrated in Fig 3.13(a). The position error $\theta - \theta^*$ is 90° at this state. When the reference frame (d*-q*) starts to rotate, a torque will be produced and the machine starts to rotate. Thus, the angle difference $\theta - \theta^*$ will become less than 90°. Thus, the operating point will move along the red arrow shown in the Fig 3.14. After the transient, the final stable-state point on the curve shown in Fig 3.14 will be with $\omega_e = \omega_e^*$ and the machine torque T_e is equal to the load torque. The position error $\theta - \theta^*$ will remain constant during the steady state. The two blue lines in Fig 3.14 demonstrate how T_e and $\theta - \theta^*$ change during the I-F start-up period.

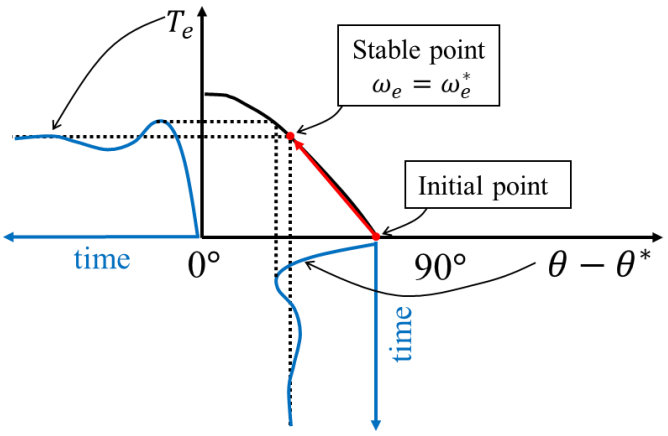


Fig 3.14. Torque-position error relationship and their time-domain waveform with the I-F start-up process

The cosine function in (3.12) is not convenient to analyse, thus it is linearized around the initial point ($\theta - \theta^* = 90°$) to the equation as follows:

$$T_e \approx -K_T i_q^* (\theta - \theta^*) \tag{3.13}$$

The relationship between position error and speed error is as follows:

$$\frac{d(\theta-\theta^*)}{dt} = \omega_e - \omega_e^* \tag{3.14}$$

Combining (3.13) and (3.14) together, a new equation of T_e is derived as follows:

$$\frac{dT_e}{dt} = -K_T i_q^* (\omega_e - \omega_e^*) \tag{3.15}$$

The mechanical equation of an electrical machine is given as

$$T_e - T_f = J\frac{d\omega_m}{dt} \tag{3.16}$$

where ω_m is the mechanical rotating speed of an electric machine. The T_f is friction torque and J is inertia. The friction torque usually has three components: Coulomb friction, stiction friction and viscous friction[46]. In this study, only viscous friction is considered, thus we have

$$T_f = B\omega_m \tag{3.17}$$

where B represents the friction factor. Combining (3.16) and (3.17) together gives

$$T_e = J\frac{d\omega_m}{dt} + B\omega_m \tag{3.18}$$

The ratio of electrical rotating speed to mechanical rotating speed (ω_e/ω_m) is pole pairs (p). Therefore, ω_m in (3.18) can be replaced by ω_e to derive a new equation as follows:

$$T_e = \frac{J}{p}\frac{d\omega_e}{dt} + \frac{B}{p}\omega_e \tag{3.19}$$

Till now, two expressions of T_e have been derived as (3.15) and (3.19). As both of them have derivatives, their expressions after Laplace transform are more convenient

for further analysis. Therefore, the expressions in the s-domain of (3.15) and (3.19) are derived as follows:

$$sT_e(s) = -K_T i_q^*[\omega_e(s) - \omega_e^*(s)] \tag{3.20}$$

$$T_e(s) = \frac{B+Js}{p}\omega_e(s) \tag{3.21}$$

Combining (3.20) and (3.21), $T_e(s)$ can be eliminated and the transfer function from $\omega_e^*(s)$ to $\omega_e(s)$ is derived as follows:

$$\frac{\omega_e(s)}{\omega_e^*(s)} = \frac{pK_T i_q^*}{pK_T i_q^* + sB + s^2 J} \tag{3.22}$$

Thus, the relationship between speed reference and actual speed is finally derived. It is a second-order system, which has the typical expression as (3.23)

$$H(s) = \frac{\omega_n^2}{\omega_n^2 + 2\zeta\omega_n s + s^2} \tag{3.23}$$

with natural frequency ω_n and damping factor ζ. We prefer to have $\zeta > 1$ because it can avoid the fluctuation of the rotor.

Comparing (3.22) with (3.23), the expression of the damping factor is derived like (3.24).

$$\zeta = \frac{B}{2\sqrt{JpK_T i_q^*}} \tag{3.24}$$

As can be seen from (3.24), the damping factor has a positive correlation with the friction factor B, and has negative correlation with inertia J, pole pairs p, torque constant K_T, and i_q^*.

The above derivation gives a mathematical understanding of the relationship between speed reference and actual speed for I-F open-loop control. It is a second-order system and the damping factor is related to friction factor B, inertia J, pole pairs p, torque constant K_T, and i_q^*. Since B and J are difficult to measure in practical tests, the actual damping factor is difficult to derive too, but it still gives us a rule that the i_q^* cannot be

selected too large. Otherwise, it will cause the oscillation of actual speed.

3.3.3 MRAS Sensorless Control

The model reference adaptive system (MRAS) is an effective scheme for rotor position estimation [36], [47], [48]. In a common scheme diagram of MRAS, as shown in Fig 3.15, an adaptive model and a reference model are connected in parallel. They are fed with the same inputs. The output of the adaptive model is expected to converge to the output of the reference model using a proper control rule and adaptive mechanism. The output of the adaptive mechanism will be fed back into the adaptive model. If the output of the adaptive model tracks that of the reference model accurately, the internal states of these two models should be identical.

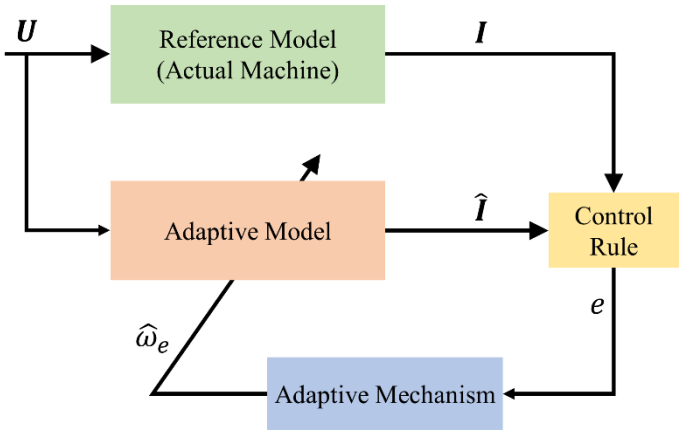


Fig 3.15. Scheme diagram of MRAS sensorless estimation

When it comes to the MRAS sensorless algorithm of the permanent magnet machine, the reference model represents the SVPWM calculation, power converter, and the actual machine. The input $\boldsymbol{U}$ is the voltage given to the machine and the output $\boldsymbol{I}$ represents the machine current.

The adaptive model is the machine d-q math model developed in section 2.2.2 with its expression rewritten as

$$\hat{L}\frac{d}{dt}\begin{bmatrix}\hat{\imath}_d\\ \hat{\imath}_q\end{bmatrix} = \begin{bmatrix}u_d\\ u_q\end{bmatrix} - \hat{R}\begin{bmatrix}\hat{\imath}_d\\ \hat{\imath}_q\end{bmatrix} - \hat{\omega}_e\begin{bmatrix}-\hat{L}\hat{\imath}_q\\ \hat{L}\hat{\imath}_d + \hat{\varphi}_f\end{bmatrix} \tag{3.25}$$

where u_d and u_q are the inputs $\boldsymbol{U}$ of the adaptive model in Fig 3.15, and the estimated currents $\hat{\imath}_d$ and $\hat{\imath}_q$ are the outputs $\hat{\boldsymbol{I}}$ of the adaptive model. $\hat{L}$ denotes the estimated d and q-axis inductances, $\hat{R}, \hat{\varphi}_f$ denote estimated phase resistance and permanent magnet flux respectively.

As both $\boldsymbol{U}$ and $\hat{\boldsymbol{I}}$ are 2*1 vectors, the scalar error (e) cannot simply be the difference between the two vectors ($\boldsymbol{I} - \hat{\boldsymbol{I}}$). In addition, the control rule and adaptive mechanism should also guarantee the stability of the MRAS system. Therefore, based on the Popov super stability theory [49] [26], [34], [41], the control rule is designed to be like (3.26), and the adaptive mechanism is like (3.27). They can guarantee the global convergence of the MRAS estimated position to the actual position. Whilst, the control rule and adaptive mechanism are derived in the s-domain and ignore the control delays in the actual system. Therefore, the stability needs to be investigated furthermore for our high-speed application.

$$e = i_d\hat{\imath}_q - i_q\hat{\imath}_d - \left(i_q - \hat{\imath}_q\right)\hat{\varphi}_f/\hat{L} \tag{3.26}$$

$$\hat{\omega}_{\boldsymbol{e}} = k_{pm}e + \int k_{im}edt \tag{3.27}$$

Finally, the MRAS sensorless control algorithm for the surface-mounted permanent magnet machine is derived with its full diagram shown in Fig 3.16. The voltage u_d and u_q are the inputs of machine as well as the adaptive model. The actual currents from the machine (i_d, i_q) and the estimated currents from adaptive model ($\hat{\imath}_d, \hat{\imath}_q$) will be used as the inputs of control rule to calculate the error (e), and the estimated speed and position are calculated from the adaptive mechanism and integrator respectively.

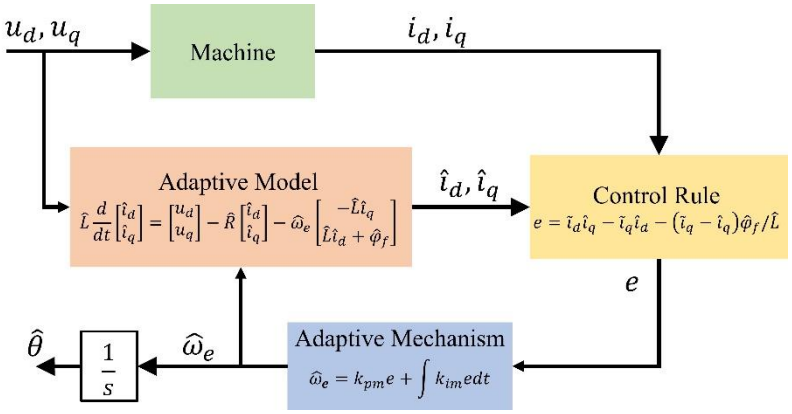


Fig 3.16. The control diagram of MRAS sensorless estimation

Above all, the MRAS rotor position and speed estimation algorithm is introduced briefly. It is a nonlinear, strong-coupled algorithm and depends on the machine parameters.

3.3.4 I-F Open-Loop Sensorless Start-Up Simulation

In this section, several simulations of I-F open-loop control based on the diagram in Fig 3.17 will be presented to analyse the start-up performance. The simulation model built in PLECS is shown in Fig.A.6.

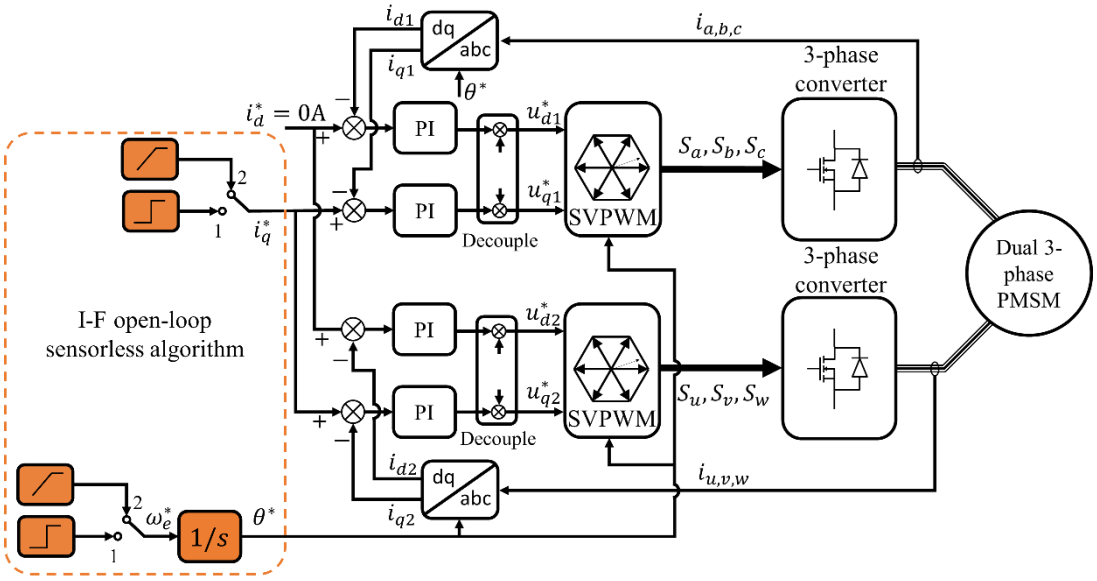


Fig 3.17. Simulation diagram of I-F open-loop sensorless start-up control system

3.3.4.1 Initial Rotor Clamping

As mentioned in section 3.3.2, the rotor will be clamped to an initial position before the reference current starts to rotate. The rotor is in a random position before the reference current i_q^* applied. Once a non-zero i_q^* is applied to the windings, the rotor will be clamped to a position. This process happens quickly but may cause damage to the bearing if not dealt with carefully.

To smooth the clutching process, a ramping i_q^* instead of a step command can be applied at the beginning. Fig 3.18 compares the currents, speed and $\theta - \theta^*$ of the ramping i_q^* and step i_q^* scenarios. Fig 3.18(a) and (b) are the d- and q-axis currents response with a step i_q^* and a ramping i_q^* respectively. It can be seen that with a step i_q^* , the machine current i_{q1} and i_{q2} are with noticeable overshoot, which is not ideal for real applications. Fig 3.18(c) compares the rotor speed variation when applying different types of $i_q{}^*$. As can be seen, the maximum transient speed with a ramping i_q^* is with much lower peak speed compared with that from a step $i_q{}^*$ demand. The waveform of position error ($\theta - \theta^*$), is given in Fig 3.18(d). There, we can see the angle error $\theta - \theta^*$is more linear with a ramping i_q^*. Therefore, in the real application, ramping i_q^* is adopted in the I-F open-loop sensorless control.

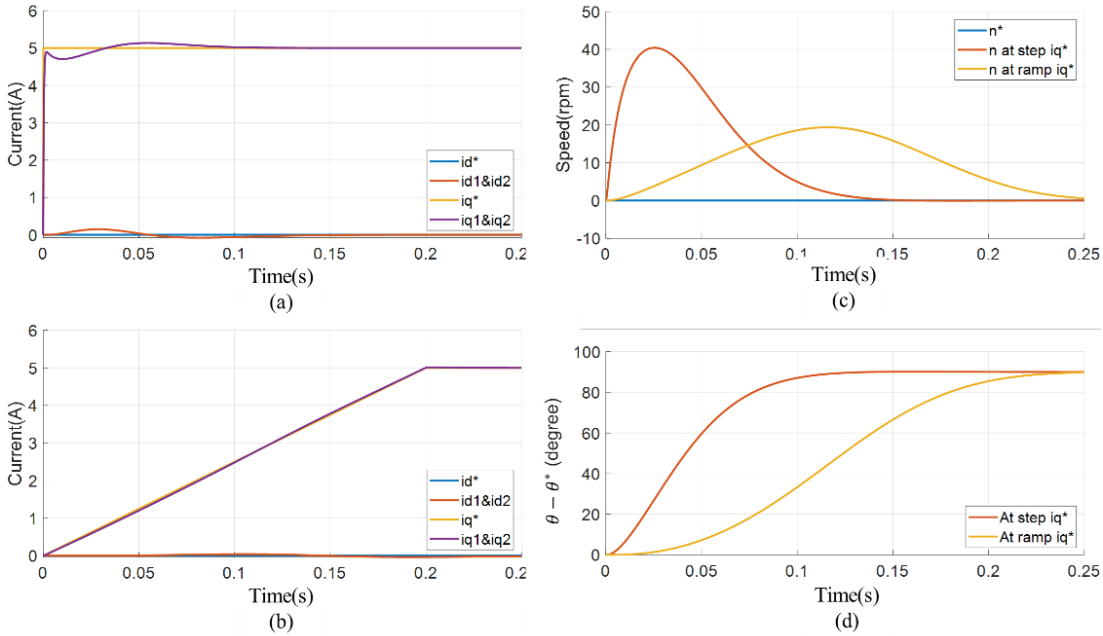


Fig 3.18. Simulation results of initial rotor clamping with two different types of iq*
(a) Current with step iq*, (b) Current with ramp iq*, (c) Rotor speed, (d) Position error

3.3.4.2 I-F Speed Control Start-Up Simulation

In this section, two I-F speed control start-up scenarios will be compared in simulations. The first scenario has a ramping speed command, and the second scenario has a step speed command. The parameters of machine Inertia J, friction factor B and i_q^* are shown in Table 3.2.

Table 3.2. Simulation parameters for I-F open loop start-up

Item	Value
Inertia J	2e-5 kg · m^2
Friction factor B	0.05 Nm · s
i_q^*	6A

The simulation results are shown in Fig 3.19 and Fig 3.20. The rotor position has already been clamped by applying i_q^*=6A before 0s. At 0s, the speed command steps to 300rpm in scenario 1 and ramps up to 300rpm in scenario 2. In Fig 3.19(a), the actual speed in scenario 1 has an obvious overshoot to follow the step command, whilst the actual speed in scenario 2 follows the ramping speed command closely without an

obvious overshoot. Similarly, current overshoots are observed in d/q-axis currents as well with step speed command in Fig 3.19(b).

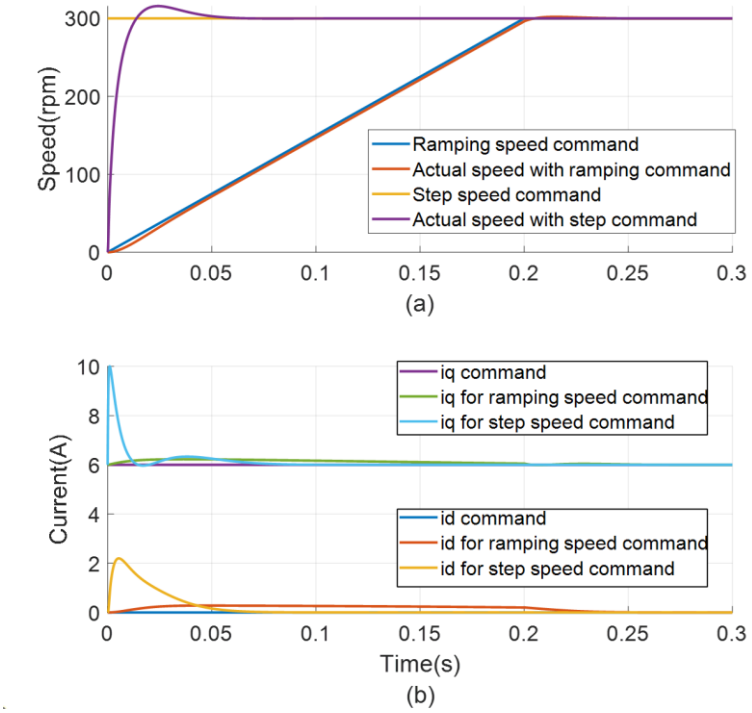


Fig 3.19. The simulation comparison of I-F start-up with step and ramping speed commands (a) Speed comparison; (b) d/q-axis currents comparison

The current overshoot can also be observed from the six-phase current waveforms in Fig 3.20(b) with step speed command. The current magnitude increases nearly to 10A when the current command is only 6A, which has a 66.7% current overshoot. This should be avoided as it may cause overcurrent and damage power electronics if a larger current command is applied. On the contrary, the six-phase currents with ramping speed command do not have current overshoot during the whole process in Fig 3.20(a).

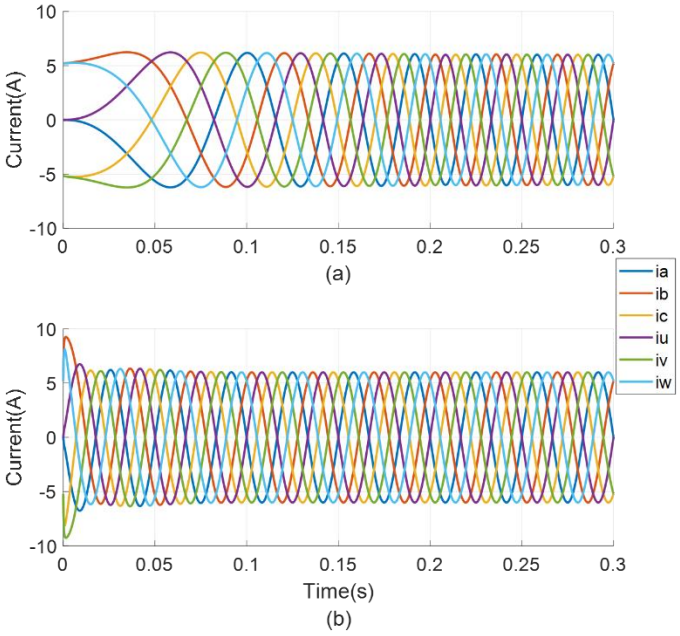


Fig 3.20. Six-phase currents comparison of I-F start-up with step and ramping speed command
(a) Ramping speed command; (b) Step speed command

Above all, the simulation results above about the I-F open-loop sensorless validate the I-F initial rotor clamping stage and the start-up accelerating stage up to 300rpm. Both stages compare the ramping and step commands (both i_q^* and n*). It is concluded that ramping clamping current command (i_q^*) and ramping speed command (n*) can have a smoother acceleration process and reduce the current and speed overshoots than step commands, which is a good method to apply I-F sensorless control in real applications.

3.3.5 MRAS Sensorless Control Simulation

In this section, the MRAS sensorless algorithm will be validated through simulations using the PLECS simulation platform. The validation is to demonstrate that the MRAS algorithm can estimate the rotor angle position and speed correctly. Thus, only the current loop is implemented in the simulation scheme as shown in Fig 3.21. The machine is assumed to be driven by a dynamometer at a constant speed of 1,000 rpm. The MRAS will estimate the rotor speed and position and feed these estimated variables

to the control scheme. Although the two channels are controlled separately, both channels use the estimated speed and position only from the ABC channel. There is no need to estimate the position again from the UVW channel as both channels share the same rotor. (The corresponding simulation model in PLECS is shown in the appendix Fig.A.7, and the detail of the 'MRAS sensorless' block is displayed in Fig.A.8.

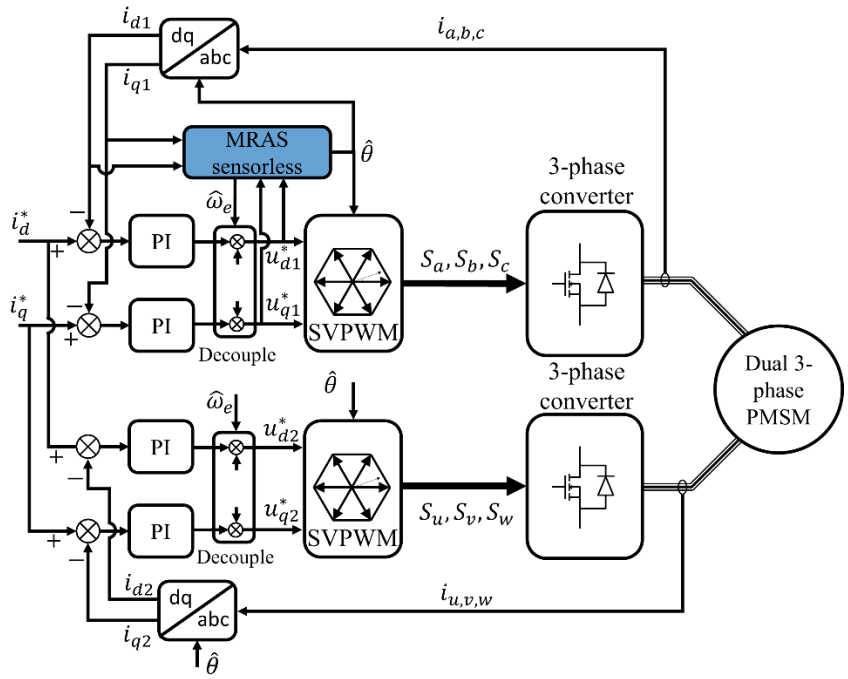


Fig 3.21. Block diagram of MRAS sensorless integrated with current closed-loop control

Other control parameters and settings during the simulation are shown in the table below. The current PI controller factors are calculated based on the model of the current loop developed in Chapter 3.1, and the MRAS PI controller factors are selected based on the stability analysis in Chapter 5.

Table 3.3. Simulation condition for MRAS sensorless with current closed-loop control

Simulation parameters	**Value**
Speed	1krpm
$\boldsymbol{i_d^*}$	0A
$\boldsymbol{i_q^*}$	10A
Current controller bandwidth ($\boldsymbol{f_{cc}}$)	1000Hz
Current controller proportional factor ($\boldsymbol{k_p}$)	2.74
Current controller integral factor ($\boldsymbol{k_i}$)	220
MRAS proportional factor ($\boldsymbol{k_{pm}}$)	10
MRAS integral factor ($\boldsymbol{k_{im}}$)	5000

The simulation results are displayed in Fig 3.22-Fig 3.24. In Fig 3.22, the q-axis currents increase quickly from 0A to the reference value (10A) without any overshoot. This is because the k_p and k_i are properly selected in section 3.1 to make the current closed-loop equivalent to a first-order system. In Fig 3.23(a), it can be seen that the estimated speed converges to the actual speed (1000rpm) quickly. The position estimation error, shown in Fig 3.23(b), converges to 0 within 0.01s, and the stable error is smaller than ±0.1 degrees. The six phase currents, shown in Fig 3.24, are well-balanced sinusoidal waveforms with PWM harmonics on them. Therefore, all these results indicate the MRAS sensorless estimation can work well when integrated into the current closed-loop control algorithm.

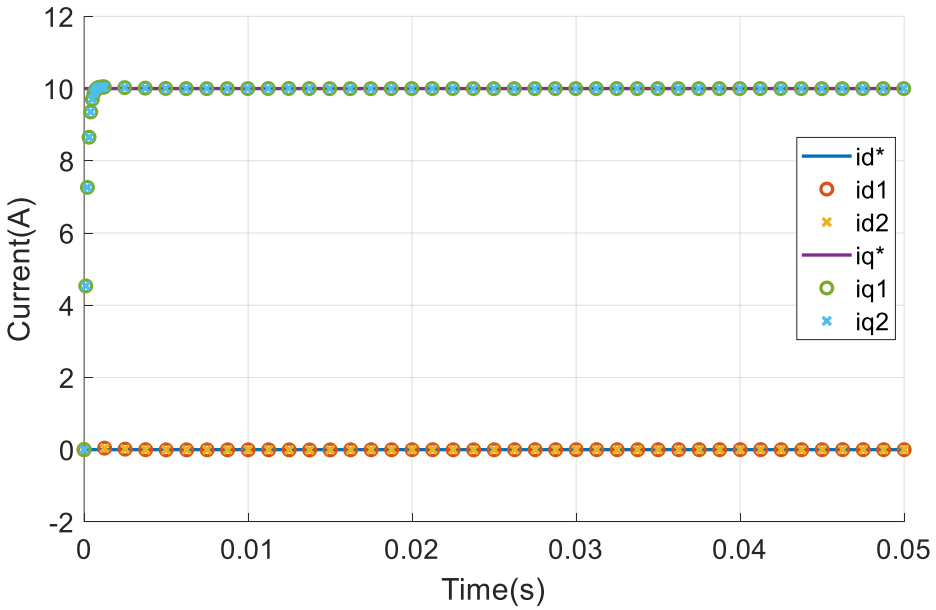


Fig 3.22. d/q-current waveforms with iq*=10A and id*=0A of MRAS sensorless simulation

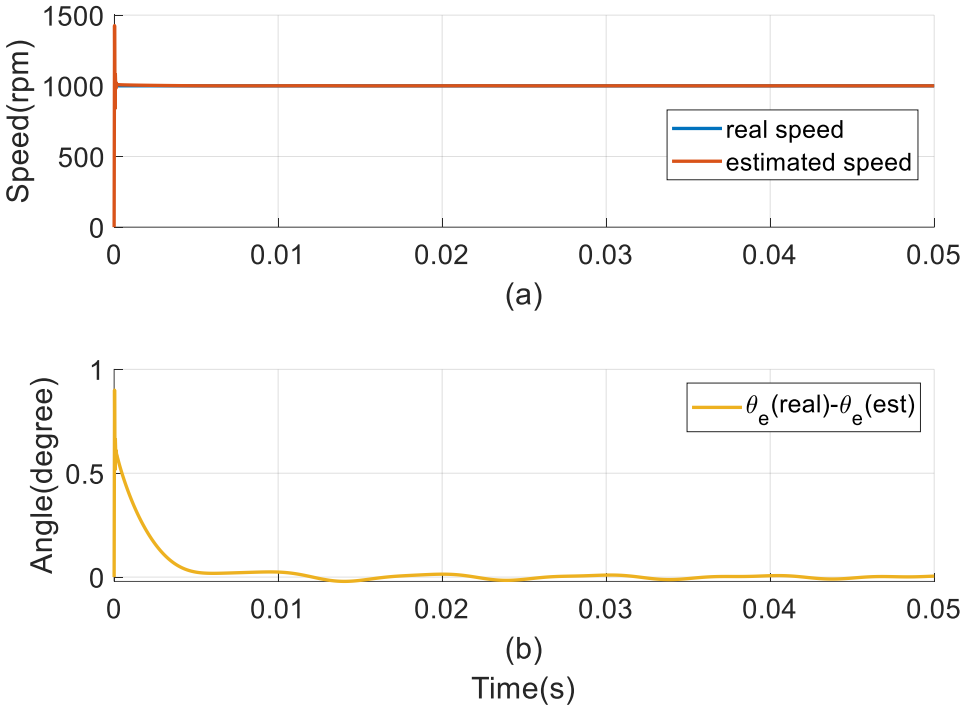


Fig 3.23. Estimated speed (a) and estimated position error (b) of MRAS sensorless simulation

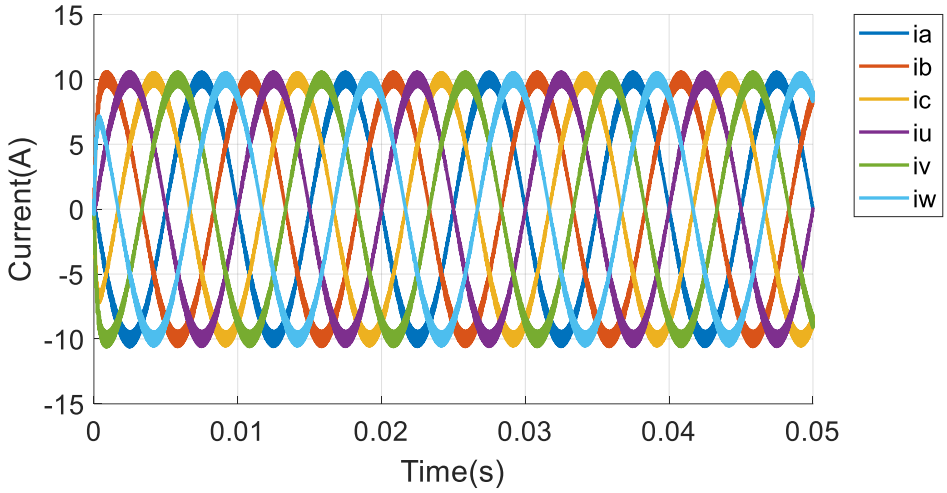


Fig 3.24. Six-phase current waveforms of MRAS sensorless simulation

3.4 Conclusion

In this chapter, the current closed-loop control topology based on the dual d-q model is designed for the dual three-phase machine application. The control scheme can control the two 3-phase channels independently. The closed-loop transfer function of the current loop is derived, and PI factors are designed based on the bandwidth requirement. Simulation results in Section 3.2 indicate the current control algorithm has good dynamic and stable performances. In Section 3.3, the position sensorless algorithm of the dual three-phase machine has been discussed. The simple I-F open-loop sensorless is adopted during the machine start-up period (low-speed range), and the MRAS sensorless control method is adopted as our major sensorless approach at high speed due to its simple structure and reliability. Finally, the simulation models of I-F open-loop sensorless control and MRAS sensorless estimation are validated using simulation results from PLECS.

Chapter 4.

Stability Analysis Model of MRAS Sensorless Control

The MRAS sensorless control algorithm developed in Chapter 3 has been approved to be effective to control a dual three-phase machine. However, the control scheme proposed is in the continuous time domain (s-domain). For electric motor drives, control design in the s-domain is very common and makes sense when the ratio of power electronic modulation frequency to the electrical fundamental frequency (M-F ratio) is high. However, for our studied high-speed dual three-phase machine drive, the M-F ratio can be as low as 28, thus, the conventional s-domain MRAS design may not be sufficient, and a z-domain MRAS design is required. Therefore, this chapter will focus on building the z-domain MRAS sensorless control model and its stability analysis.

In this chapter, a review of previous MRAS sensorless stability analysis approaches will be introduced first. Based on the literature review, a state-evolution and small-signal-based MRAS model will be developed in the z-domain. The eigenvalues of the proposed model can evaluate the stability of the MRAS sensorless control system.

4.1 Literature Review of MRAS Sensorless Stability Analysis

The MRAS method has been widely studied and applied to AC machine drives in the past two decades [26], [27], [39]–[42], [31]–[38]. Although there are different MRAS sensorless algorithms proposed for PMSM applications, all these control designs are based on the s-domain and the modulation to the electrical fundamental frequency (M-F) ratio is relatively high. For high-speed PMSM drives with low M-F ratios, the stability issues need to be properly addressed. It is a very important issue as instability issue in aircraft can cause serious safety problems.

Although there are many publications on sensorless control design, analysis of the stability of sensorless control drive systems has gained much less attention. Nevertheless, we have identified several literatures where authors have proposed their methods to analyse the stability of MRAS sensorless control system [31], [32], [36]. In [31], the eigenvalues of the adaptive model are placed to be close to the reference model eigenvalues. With this method, the proportional and integral factors of MRAS PI controller can be determined but this does not prove the stability of the entire system. In [36], authors found that PMSM drive systems with MRAS control algorithm have different stability regions under different reference frames, i.e. d-q rotating reference frame and αβ stationary frame. They concluded that frame transformation should be considered in stability analysis. In [32], the authors concluded that the gains of the MRAS PI controller can be selected as high as possible to provide quick tracking of the estimation. However, this conclusion obtained from the continuous time domain (s-domain) might not be true when the M-F ratio is low and the control algorithm is designed in the discrete-time domain (z-domain). In addition, the literature [32] ignores

the difference between the real applied voltage and reference voltage caused by the frame transformation.

Indeed, all the stability analyses of MRAS sensorless control in the literature mentioned above are designed in the s-domain. This is sufficient as these literatures are focusing on low-speed applications. However, when it comes to high-speed machine drive applications, especially when the M-F ratio is low, the conclusion has been drawn that MRAS control design in the s-domain will not be sufficient anymore and the stability design and analysis in the z-domain are necessary.

4.2 MRAS Stability Analysis Challenges for The Dual three-phase Machine

The motivation to pursue high-speed machine drive systems is due to its high power-density and thus reduced volume and weight, but it also brings challenges to sensorless control as discussed below.

1) Low modulation to fundamental frequency (M-F) ratio

The permanent magnet machine studied in this project is with 6 pole pairs and a maximum operating speed of up to 14,200 rpm, i.e. 1,420 Hz electrical frequency (f_e). The modulation frequency (f_s) is 40 kHz, which is from trade-off studies between control accuracy and switching losses. Therefore, the smallest M-F ratio is only 28.2. The time delays in current sampling and PWM voltage application cannot be neglected in low ratio conditions. In addition, these time delays will also influence the accuracy and stability of the sensorless estimation algorithm as measured currents and PWM voltage references are inputs of the sensorless algorithm. Therefore, it is necessary to design and analyse the controller in the z-domain as time delays can be considered more conveniently.

2) The nonlinearity of MRAS sensorless control system

A traditional machine control algorithm with position feedback normally includes a speed PI controller, current PI controllers, Clarke-Park transformation, inverse Clarke-Park transformation, PWM duty cycle calculation, etc. Many matured methods have been developed to analyse control system stability in the synchronous rotating frame (d/q-axis). However, with the application of MRAS sensorless control, the currents in the d- and q-axis are seriously coupled together. The MRAS control rule has the items of i_d and i_q, which is undesirable for a linear control system. In addition, the estimated rotor position will be used in frame transformations. This makes the coupling between the d- and q-axis even stronger. Therefore, a small signal analysis method needs to be used to linearize the control system near equilibrium operating points.

3) Multi-state variables

The traditional stability analysis of PMSM is usually conducted in a synchronous rotating dq frame, where two scalars or one complex vector is enough to represent three-phase currents or voltages [50]–[52]. However, the estimated position error causes the misalignment of the estimated d-axis and actual d-axis. Therefore, more state variables are required to describe voltage and current when analysing the MRAS sensorless system. In addition, more state variables are required if control delay is considered. Therefore, the stability analysis method for the multi-inputs multi-outputs (MIMO) state evolution model is a better option other than the transfer-function-based analysis method.

Above all, the stability analysis method based on the z-domain, small-signal and state-evolution model will be proposed in the following sections of this chapter.

4.3 Small Signal Model of MRAS Sensorless System

As mentioned before, MRAS sensorless controls for electric drives in the literature are proposed in the s-domain due to low machine speed. However, for high-speed electrical machines with low M-F ratios, the MRAS sensorless control needs to be designed in z-domain. Therefore, this section has the outline as follows:

1) Introduce the MRAS sensorless algorithm in the s-domain.
2) Convert the s-domain model to the z-domain and derive its small signal model.

4.3.1 MRAS Sensorless Algorithm in s-domain

Traditional MRAS sensorless algorithm in the s-domain has been well developed for various machines in different kinds of literature recently. The MRAS sensorless algorithm diagram has been demonstrated in section 3.3.3 with Fig 3.16. However, in this chapter, the measured d/q-axis currents feedback into the control rule block has considered the position estimation error during abc/dq transformation and represented as $\tilde{\imath}_d$ and $\tilde{\imath}_q$.

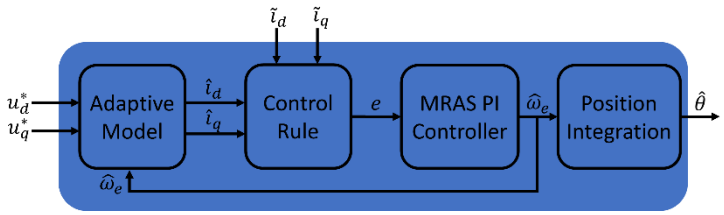


Fig 4.1. Diagram of MRAS sensorless rotor position estimation algorithm in s-domain

4.3.1.1 Adaptive Model

The adaptive model has its expression (3.25) in section 3.3.3, and it is rewritten as (4.1) in the format of matrices because it looks simpler and easier for equation derivation.

$$\frac{d}{dt}\hat{\boldsymbol{I}}_{\boldsymbol{dq}} = \hat{\boldsymbol{A}}\hat{\boldsymbol{I}}_{\boldsymbol{dq}} + \hat{\boldsymbol{B}}_{\boldsymbol{v}}\boldsymbol{U}^{*}_{\boldsymbol{dq}} + \hat{\boldsymbol{B}}_{\boldsymbol{\varphi}}\hat{\varphi}_f \tag{4.1}$$

In (4.1), the $\hat{\varphi}_f$ represents estimated rotor flux linkage, $\hat{\boldsymbol{I}}_{\boldsymbol{dq}} = [\hat{\imath}_d \quad \hat{\imath}_q]^T$ represents the estimated d/q-axis currents, and $\boldsymbol{U}^{*}_{\boldsymbol{dq}} = [u^{*}_d \quad u^{*}_q]^T$ represents the d/q-axis voltage reference. The three parameter matrices in (4.1) have their expression as follows:

$$\hat{\boldsymbol{A}} = \begin{bmatrix} -\hat{R}/\hat{L} & \hat{\omega}_e \\ -\hat{\omega}_e & -\hat{R}/\hat{L} \end{bmatrix} \tag{4.2-a}$$

$$\hat{\boldsymbol{B}}_{\boldsymbol{v}} = \begin{bmatrix} 1/\hat{L} & 0 \\ 0 & 1/\hat{L} \end{bmatrix} \tag{4.2-b}$$

$$\hat{\boldsymbol{B}}_{\boldsymbol{\varphi}} = [0 \quad -\hat{\omega}_e/\hat{L}]^T \tag{4.2-c}$$

where $\hat{R}, \hat{L}, \hat{\omega}_e$ represent the estimated phase resistance, d/q-axis inductance, and estimated electrical rotate speed respectively.

4.3.1.2 Control Rule

The control rule is expressed as (3.26) in section 3.3.3 and it is rewritten in matrices format as

$$\begin{aligned} e &= \tilde{\imath}_d\hat{\imath}_q - \tilde{\imath}_q\hat{\imath}_d - \left(\tilde{\imath}_q - \hat{\imath}_q\right)\hat{\varphi}_f/\hat{L} \\ &= \tilde{\boldsymbol{I}}^T_{\boldsymbol{dq}}\boldsymbol{J}_{\boldsymbol{2}}\hat{\boldsymbol{I}}_{\boldsymbol{dq}} - \boldsymbol{J}_{\boldsymbol{1}}\left[\tilde{\boldsymbol{I}}_{\boldsymbol{dq}} - \hat{\boldsymbol{I}}_{\boldsymbol{dq}}\right]\frac{\hat{\varphi}_f}{\hat{L}} \end{aligned} \tag{4.3}$$

where $\hat{\boldsymbol{I}}_{\boldsymbol{dq}} = [\hat{\imath}_d \quad \hat{\imath}_q]^T$, $\tilde{\boldsymbol{I}}_{\boldsymbol{dq}} = [\tilde{\imath}_d \quad \tilde{\imath}_q]^T$, $\boldsymbol{J}_{\boldsymbol{1}} = [0 \quad 1]$ and $\boldsymbol{J}_{\boldsymbol{2}} = \begin{bmatrix} 0 & 1 \\ -1 & 0 \end{bmatrix}$.

It is important to note the sampled currents in the estimated dq frame ($\tilde{\imath}_d, \tilde{\imath}_q$) may not equate to the actual d/q-axis currents (i_d, i_q). This is because the estimated dq frame is based on the estimated rotor position ($\hat{\theta}$) instead of the real rotor position. This control rule expression (4.3) is specifically designed to ensure the algorithm stability is guaranteed by Popov Super Stability Theorem [26]. When $\hat{\boldsymbol{I}}_{\boldsymbol{dq}} = \tilde{\boldsymbol{I}}_{\boldsymbol{dq}}$, the adaptive model running in the microcontroller can be regarded as identical to the running machine, and in that case the estimated speed and position from adaptive model can represent the actual machine speed and position, which in simulations are available for

stability studies.

4.3.1.3 MRAS PI Controller

The expression of the MRAS PI controller is rewritten as:

$$\widehat{\omega}_e = k_{pm}e + \int k_{im}edt \tag{4.4}$$

where k_{pm}, k_{im} represent the proportional and integral factors, and $\widehat{\omega}_e$ represents the estimated electrical rotational speed.

When $\hat{\boldsymbol{I}}_{\boldsymbol{dq}} \neq \tilde{\boldsymbol{I}}_{\boldsymbol{dq}}$, the result of e from (4.3) cannot be zero, which will force the MRAS PI controller to adjust the estimated speed to make the speed from the adaptive model match that from the real machine.

4.3.1.4 Estimated Position Integration

The estimated rotor position ($\hat{\theta}$) is the integration of $\widehat{\omega}_e$ coming with its expression as:

$$\hat{\theta} = \int \widehat{\omega}_e dt \tag{4.5}$$

4.3.2 MRAS Sensorless Algorithm in z-domain and Related Small Signal Models

As mentioned before, the dual three-phase machine studied has 6 pole pairs and a maximum operating speed of 14,200 rpm, i.e. 1,420 Hz electrical frequency (f_e). The modulation frequency (f_s) is selected as 40 kHz to ensure the power loss of the converter is below the heatsink capacity. Thus, the M-F (modulation to fundamental frequency) ratio can be as low as 28 for our studied drive system. In this case, the control delays in current sampling and PWM voltage application cannot be neglected anymore. Due to the convenient description of delays in the z-domain and the discrete nature of the microcontroller, it is necessary to design and analyse the MRAS algorithm in z-domain.

Similar to s-domain models, four basic function blocks (i.e., adaptive model, control rule, MRAS PI controller, position integration), given by Fig 4.2, can describe the discrete MRAS sensorless control algorithm in z-domain, and the details of each block will be derived in the following sections.

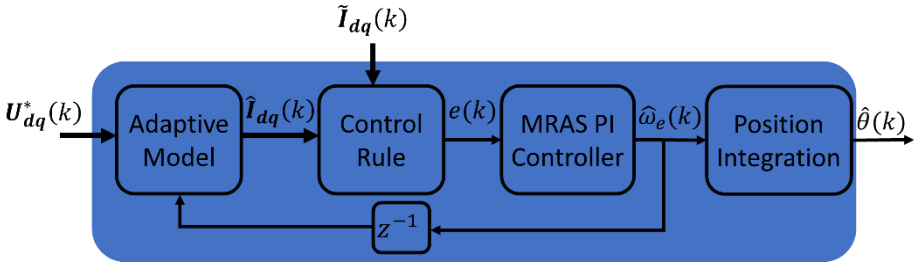


Fig 4.2. Diagram of MRAS sensorless rotor position and speed estimation algorithm in z-domain

4.3.2.1 Adaptive Model

The z-domain adaptive model can be derived from its s-domain model (4.1). The reference [53] proposed the discrete state-evolution model of 3-phase PMSM like (4.6) and (4.7-a/b/c).

$$\hat{\boldsymbol{I}}_{\boldsymbol{dq}}(k+1) = \hat{\boldsymbol{F}}(k)\hat{\boldsymbol{I}}_{\boldsymbol{dq}}(k) + \hat{\boldsymbol{G}}_{\boldsymbol{v}}(k)\boldsymbol{U}^*_{\boldsymbol{dq}}(k) + \hat{\boldsymbol{G}}_{\boldsymbol{\varphi}}(k)\hat{\varphi}_f \tag{4.6}$$

where $\hat{\boldsymbol{I}}_{\boldsymbol{dq}}(k) = [\hat{\imath}_d(k) \quad \hat{\imath}_q(k)]^T$ represents the estimated currents at time step k, and $\hat{\boldsymbol{I}}_{\boldsymbol{dq}}(k+1)$ is the value at time instant k+1. The parameter matrices (i.e., $\hat{\boldsymbol{F}}(k), \hat{\boldsymbol{G}}_{\boldsymbol{v}}(k), \hat{\boldsymbol{G}}_{\boldsymbol{\varphi}}(k)$) can be derived from s-domain parameter matrices (i.e., $\hat{\boldsymbol{A}}, \hat{\boldsymbol{B}}_{\boldsymbol{v}}, \hat{\boldsymbol{B}}_{\boldsymbol{\varphi}}$) and are given below

$$\hat{\boldsymbol{F}}(k) = \boldsymbol{e}^{\hat{\boldsymbol{A}}(k)T_S} \tag{4.7-a}$$

$$\hat{\boldsymbol{G}}_{\boldsymbol{v}}(k) = \left(\hat{\boldsymbol{F}}(k) - \boldsymbol{E_2}\right)\hat{\boldsymbol{A}}(k)^{-1}\hat{\boldsymbol{B}}_{\boldsymbol{v}}(k) \tag{4.7-b}$$

$$\hat{\boldsymbol{G}}_{\boldsymbol{\varphi}}(k) = \left(\hat{\boldsymbol{F}}(k) - \boldsymbol{E_2}\right)\hat{\boldsymbol{A}}(k)^{-1}\hat{\boldsymbol{B}}_{\boldsymbol{\varphi}}(k) \tag{4.7-c}$$

where $\boldsymbol{E_2} = \begin{bmatrix} 1 & 0 \\ 0 & 1 \end{bmatrix}$.

Based on the equation (4.6) and (4.7-a/b/c) from [53], the MRAS discrete adaptive model will be derived in this section using Taylor expansion. As can be seen from (4.7-

a), the expression of $\widehat{\boldsymbol{F}}(k)$ includes an exponential term $\boldsymbol{e}^{\widehat{\boldsymbol{A}}(k)T_S}$. This term must be linearized for hardware implementation. Here we have two options to linearize it (i.e., first-order Taylor expansion, and second-order Taylor expansion), and both of them will be discussed below in detail. The stability analysis as well as test results in the following chapters will demonstrate the superiority of using second-order Taylor expansion to improve the system stability.

a) First-order Taylor expansion

Using first-order Taylor expansion, the $\widehat{\boldsymbol{F}}(k)$ can be linearized as

$$\widehat{\boldsymbol{F}}(k) = \boldsymbol{e}^{\widehat{\boldsymbol{A}}(k)T_S} \approx \boldsymbol{E_2} + \widehat{\boldsymbol{A}}(k)T_S = \widehat{\omega}_e(k)T_S\boldsymbol{J_2} + \left(1 - \frac{\hat{R}T_S}{\hat{L}}\right)\boldsymbol{E_2} \tag{4.8-a}$$

Substituting (4.8-a) to (4.7-b), the final expressions of $\widehat{\boldsymbol{G}}_{\boldsymbol{v}}(k)$ can be derived as:

$$\begin{aligned}\widehat{\boldsymbol{G}}_{\boldsymbol{v}}(k) &= \left(\widehat{\boldsymbol{F}}(k) - \boldsymbol{E_2}\right)\widehat{\boldsymbol{A}}(k)^{-1}\widehat{\boldsymbol{B}}_{\boldsymbol{v}}(k) \\ &\approx \left(\boldsymbol{E_2} + \widehat{\boldsymbol{A}}(k)T_S - \boldsymbol{E_2}\right)\widehat{\boldsymbol{A}}(k)^{-1}\widehat{\boldsymbol{B}}_{\boldsymbol{v}}(k) \\ &= T_S\widehat{\boldsymbol{B}}_{\boldsymbol{v}}(k) = \frac{T_S}{\hat{L}}\boldsymbol{E_2}\end{aligned} \tag{4.8-b}$$

Substituting (4.8-a) to (4.7-c), the final expressions of $\widehat{\boldsymbol{G}}_{\boldsymbol{\varphi}}(k)$ can be derived as

$$\begin{aligned}\widehat{\boldsymbol{G}}_{\boldsymbol{\varphi}}(k) &= \left(\widehat{\boldsymbol{F}}(k) - \boldsymbol{E_2}\right)\widehat{\boldsymbol{A}}(k)^{-1}\widehat{\boldsymbol{B}}_{\boldsymbol{\varphi}}(k) \\ &\approx \left(\boldsymbol{E_2} + \widehat{\boldsymbol{A}}(k)T_S - \boldsymbol{E_2}\right)\widehat{\boldsymbol{A}}(k)^{-1}\widehat{\boldsymbol{B}}_{\boldsymbol{\varphi}}(k) \\ &= T_S\widehat{\boldsymbol{B}}_{\boldsymbol{\varphi}}(k) \\ &= -\frac{T_S}{\hat{L}}\widehat{\omega}_e(k)\boldsymbol{J_1^T}\end{aligned} \tag{4.8-c}$$

Substituting (4.8-a)-(4.8-c) into (4.6), the final expression of the discrete adaptive model can be derived as follows:

$$\begin{aligned}\widehat{\boldsymbol{I}}_{\boldsymbol{dq}}(k+1) = &\left[\widehat{\omega}_e(k)T_S\boldsymbol{J_2} + \left(1 - \frac{\hat{R}T_S}{\hat{L}}\right)\boldsymbol{E_2}\right]\widehat{\boldsymbol{I}}_{\boldsymbol{dq}}(k) \\ &+ \frac{T_S}{\hat{L}}\boldsymbol{U}^*_{\boldsymbol{dq}}(k) - \frac{T_S}{\hat{L}}\widehat{\omega}_e(k)\boldsymbol{J_1^T}\hat{\varphi}_f\end{aligned} \tag{4.9}$$

As can be seen from (4.9), it contains the state multiplication items such $\widehat{\omega}_e(k)\widehat{\boldsymbol{I}}_{\boldsymbol{dq}}(k)$. In order to decouple all state variables to conduct stability analysis, the small signal equation of (4.9) is derived as

$$\begin{aligned}\Delta\hat{\boldsymbol{I}}_{\boldsymbol{dq}}(k+1)=& \, equ\left[\hat{\omega}_e(k)T_s\boldsymbol{J_2}+\left(1-\frac{\hat{R}T_s}{\hat{L}}\right)\boldsymbol{E_2}\right]\Delta\hat{\boldsymbol{I}}_{\boldsymbol{dq}}(k)\\&+\Delta\hat{\omega}_e(k)T_s\boldsymbol{J_2}\hat{\boldsymbol{I}}_{\boldsymbol{equ}}+\frac{T_s}{\hat{L}}\Delta\boldsymbol{U}^*_{\boldsymbol{dq}}(k)-\frac{T_s}{\hat{L}}\Delta\hat{\omega}_e(k)\boldsymbol{J_1}^T\hat{\varphi}_f\\=&\left[\omega_eT_s\boldsymbol{J_2}+\left(1-\frac{\hat{R}T_s}{\hat{L}}\right)\boldsymbol{E_2}\right]\Delta\hat{\boldsymbol{I}}_{\boldsymbol{dq}}(k)\\&+T_s\boldsymbol{J_2}\hat{\boldsymbol{I}}_{\boldsymbol{equ}}\Delta\hat{\omega}_e(k)+\frac{T_s}{\hat{L}}\Delta\boldsymbol{U}^*_{\boldsymbol{dq}}(k)-\frac{T_s}{\hat{L}}\boldsymbol{J_1}^T\hat{\varphi}_f\Delta\hat{\omega}_e(k)\\=&\left[\omega_eT_s\boldsymbol{J_2}+\left(1-\frac{\hat{R}T_s}{\hat{L}}\right)\boldsymbol{E_2}\right]\Delta\hat{\boldsymbol{I}}_{\boldsymbol{dq}}(k)\\&+T_s\left(\boldsymbol{J_2}\hat{\boldsymbol{I}}_{\boldsymbol{equ}}-\frac{\boldsymbol{J_1}^T\hat{\varphi}_f}{\hat{L}}\right)\Delta\hat{\omega}_e(k)+\frac{T_s}{\hat{L}}\Delta\boldsymbol{U}^*_{\boldsymbol{dq}}(k)\end{aligned}\tag{4.10}$$

where $equ[*]$ represent the equilibrium operating point value of * when the system is in steady state, $\hat{\boldsymbol{I}}_{\boldsymbol{equ}}$ represents the equilibrium operating point value of the estimated current, and $\Delta\hat{\boldsymbol{I}}_{\boldsymbol{dq}}(k)$, $\Delta\hat{\omega}_e(k)$, $\Delta\boldsymbol{U}^*_{\boldsymbol{dq}}(k)$ represent the corresponding small signal variables. Replacing the constant parameters in (4.10) gives

$$\Delta\hat{\boldsymbol{I}}_{\boldsymbol{dq}}(k+1)=\hat{\boldsymbol{A}}\Delta\hat{\boldsymbol{I}}_{\boldsymbol{dq}}(k)+\hat{\boldsymbol{B}}\Delta\hat{\omega}_e(k)+\hat{\boldsymbol{D}}\Delta\boldsymbol{U}^*_{\boldsymbol{dq}}(k)\tag{4.11}$$

where

$$\hat{\boldsymbol{A}}=\omega_eT_s\boldsymbol{J_2}+\left(1-\frac{T_s\hat{R}}{\hat{L}}\right)\boldsymbol{E_2}\tag{4.12-a}$$

$$\hat{\boldsymbol{B}}=T_s\left(\boldsymbol{J_2}\hat{\boldsymbol{I}}_{\boldsymbol{equ}}-\frac{\boldsymbol{J_1}^T\hat{\varphi}_f}{\hat{L}}\right)\tag{4.12-b}$$

$$\hat{\boldsymbol{D}}=\frac{T_s}{\hat{L}}\tag{4.12-c}$$

b) Second-order Taylor expansion

Using second-order Taylor expansion, the equation of $\hat{\boldsymbol{F}}(k)$ is expressed as follows:

$$\begin{aligned}\hat{\boldsymbol{F}}(k)=&\,\boldsymbol{e}^{\hat{\boldsymbol{A}}(k)T_s}\approx\boldsymbol{E_2}+\hat{\boldsymbol{A}}(k)T_s+\frac{1}{2}\hat{\boldsymbol{A}}(k)^2{T_s}^2\\=&\,\boldsymbol{\beta_1}\hat{\omega}_e(k)^2+\boldsymbol{\beta_2}\hat{\omega}_e(k)+\boldsymbol{\beta_0}\boldsymbol{E_2}\end{aligned}\tag{4.13}$$

where

$$\boldsymbol{\beta_0}=1-\frac{\hat{R}T_s}{\hat{L}}+\frac{\hat{R}^2T_s^2}{2\hat{L}^2}\tag{4.14-a}$$

$$\boldsymbol{\beta_1}=-\frac{T_s^2}{2}\boldsymbol{E_2}\tag{4.14-b}$$

$$\boldsymbol{\beta_2}=\left(T_s-\frac{\hat{R}T_s^2}{\hat{L}}\right)\boldsymbol{J_2}\tag{4.14-c}$$

Substituting the final expression of $\widehat{\boldsymbol{F}}(k)$ in (4.13) to (4.7-b), the final expression of $\widehat{\boldsymbol{G}}_{\boldsymbol{v}}(k)$ can be derived as follows:

$$\begin{aligned}\widehat{\boldsymbol{G}}_{\boldsymbol{v}}(k) &= \left(\widehat{\boldsymbol{F}}(k) - \boldsymbol{E_2}\right)\widehat{\boldsymbol{A}}(k)^{-1}\boldsymbol{B_v} \\ &= \boldsymbol{\beta_3}\hat{\omega}_e(k) + \boldsymbol{\beta_4}\end{aligned} \tag{4.15}$$

where

$$\boldsymbol{\beta_3} = \frac{T_S^2}{2\hat{L}}\boldsymbol{J_2} \tag{4.16-a}$$

$$\boldsymbol{\beta_4} = \left(\frac{T_S}{\hat{L}} - \frac{\hat{R}T_S^2}{2\hat{L}^2}\right)\boldsymbol{E_2} \tag{4.16-b}$$

Substituting the expression of $\widehat{\boldsymbol{F}}(k)$ in (4.13) to (4.7-c), the final expression of $\widehat{\boldsymbol{G}}_{\boldsymbol{\varphi}}(k)$ can be derived as follows:

$$\begin{aligned}\widehat{\boldsymbol{G}}_{\boldsymbol{\varphi}}(k) &= \left(\widehat{\boldsymbol{F}}(k) - \boldsymbol{E_2}\right)\widehat{\boldsymbol{A}}(k)^{-1}\widehat{\boldsymbol{B}}_{\boldsymbol{\varphi}}(k) \\ &= \boldsymbol{\beta_5}\hat{\omega}_e(k)^2 + \boldsymbol{\beta_6}\hat{\omega}_e(k)\end{aligned} \tag{4.17}$$

where

$$\boldsymbol{\beta_5} = -\boldsymbol{\beta_3}\boldsymbol{J_1^T} \tag{4.18-a}$$

$$\boldsymbol{\beta_6} = -\boldsymbol{\beta_4}\boldsymbol{J_1^T} \tag{4.18-b}$$

Therefore, by substituting the expression of $\widehat{\boldsymbol{F}}(k)$ in (4.13), $\widehat{\boldsymbol{G}}_{\boldsymbol{v}}(k)$ in (4.15), and $\widehat{\boldsymbol{G}}_{\boldsymbol{\varphi}}(k)$ in (4.17) to the adaptive discrete model (4.6), an explicit second-order adaptive model is derived as follows:

$$\begin{aligned}\hat{\boldsymbol{I}}_{\boldsymbol{dq}}(k+1) &= \widehat{\boldsymbol{F}}(k)\hat{\boldsymbol{I}}_{\boldsymbol{dq}}(k) + \widehat{\boldsymbol{G}}_{\boldsymbol{v}}(k)\boldsymbol{U}_{\boldsymbol{dq}}^{*}(k) + \widehat{\boldsymbol{G}}_{\boldsymbol{\varphi}}(k)\hat{\varphi}_f \\ &= (\boldsymbol{\beta_1}\hat{\omega}_e(k)^2 + \boldsymbol{\beta_2}\hat{\omega}_e(k) + \boldsymbol{\beta_0}\boldsymbol{E_2})\hat{\boldsymbol{I}}_{\boldsymbol{dq}}(k) \\ &\quad + (\boldsymbol{\beta_3}\hat{\omega}_e(k) + \boldsymbol{\beta_4})\boldsymbol{U}_{\boldsymbol{dq}}^{*}(k) \\ &\quad + \left(\boldsymbol{\beta_5}\hat{\omega}_e(k)^2 + \boldsymbol{\beta_6}\hat{\omega}_e(k)\right)\hat{\varphi}_f\end{aligned} \tag{4.19}$$

Applying the same small signal derivation method in the first-order Taylor expansion, the small signal equation of (4.23) can be derived as follows:

$$
\begin{aligned}
&\Delta\hat{\boldsymbol{I}}_{\boldsymbol{dq}}(k+1)\\
&= equ[\boldsymbol{\beta_1}\hat{\omega}_e(k)^2 + \boldsymbol{\beta_2}\hat{\omega}_e(k) + \boldsymbol{\beta_0 E_2}]\Delta\hat{\boldsymbol{I}}_{\boldsymbol{dq}}(k)\\
&\quad +\Delta[\boldsymbol{\beta_1}\hat{\omega}_e(k)^2 + \boldsymbol{\beta_2}\hat{\omega}_e(k) + \boldsymbol{\beta_0 E_2}]\hat{\boldsymbol{I}}_{\boldsymbol{equ}}\\
&\quad +equ[\boldsymbol{\beta_3}\hat{\omega}_e(k) + \boldsymbol{\beta_4}]\Delta\boldsymbol{U}^*_{\boldsymbol{dq}}(k)\\
&\quad +\Delta[\boldsymbol{\beta_3}\hat{\omega}_e(k) + \boldsymbol{\beta_4}]\boldsymbol{V}^*_{\boldsymbol{equ}}\\
&\quad +\Delta[\boldsymbol{\beta_5}\hat{\omega}_e(k)^2 + \boldsymbol{\beta_6}\hat{\omega}_e(k)]\hat{\varphi}_f\\
&= (\boldsymbol{\beta_1}\omega_e^2 + \boldsymbol{\beta_2}\omega_e + \boldsymbol{\beta_0 E_2})\Delta\hat{\boldsymbol{I}}_{\boldsymbol{dq}}(k) + (\boldsymbol{\beta_3}\omega_e + \boldsymbol{\beta_4})\Delta\boldsymbol{U}^*_{\boldsymbol{dq}}(k)\\
&\quad +\big(2\boldsymbol{\beta_1}\hat{\boldsymbol{I}}_{\boldsymbol{equ}}\omega_e + \boldsymbol{\beta_2}\hat{\boldsymbol{I}}_{\boldsymbol{equ}} + \boldsymbol{\beta_3}\boldsymbol{V}^*_{\boldsymbol{equ}} + 2\boldsymbol{\beta_5}\omega_e\hat{\varphi}_f + \boldsymbol{\beta_6}\hat{\varphi}_f\big)\Delta\hat{\omega}_e(k)
\end{aligned}
\tag{4.20}
$$

where $equ[*]$ represents the equilibrium operating point value of * when the system is in steady state, $\Delta[*]$ represents the small signal expression of *, $\hat{\boldsymbol{I}}_{\boldsymbol{equ}}$ represents the equilibrium operating point value of the estimated current $\hat{\boldsymbol{I}}_{\boldsymbol{dq}}(k)$, $\boldsymbol{V}^*_{\boldsymbol{equ}}$ represents the equilibrium operating point value of $\boldsymbol{U}^*_{\boldsymbol{dq}}(k)$, and $\Delta\hat{\boldsymbol{I}}_{\boldsymbol{dq}}(k)$, $\Delta\hat{\omega}_e(k)$, $\Delta\boldsymbol{U}^*_{\boldsymbol{dq}}(k)$ represent the corresponding small signal variables.

A brief expression of (4.20) is derived by replacing the complicated parameters with three new symbols (i.e., $\hat{\boldsymbol{A}}$, $\hat{\boldsymbol{B}}$, $\hat{\boldsymbol{D}}$) as follows:

$$\Delta\hat{\boldsymbol{I}}_{\boldsymbol{dq}}(k+1) = \hat{\boldsymbol{A}}\Delta\hat{\boldsymbol{I}}_{\boldsymbol{dq}}(k) + \hat{\boldsymbol{B}}\Delta\hat{\omega}_e(k) + \hat{\boldsymbol{D}}\Delta\boldsymbol{U}^*_{\boldsymbol{dq}}(k) \tag{4.21}$$

where:

$$\hat{\boldsymbol{A}} = \boldsymbol{\beta_1}\omega_e^2 + \boldsymbol{\beta_2}\omega_e + \boldsymbol{\beta_0 E_2} \tag{4.22-a}$$

$$\hat{\boldsymbol{B}} = 2\boldsymbol{\beta_1}\hat{\boldsymbol{I}}_{\boldsymbol{equ}}\omega_e + \boldsymbol{\beta_2}\hat{\boldsymbol{I}}_{\boldsymbol{equ}} + \boldsymbol{\beta_3}\boldsymbol{V}^*_{\boldsymbol{equ}} + 2\boldsymbol{\beta_5}\omega_e\hat{\varphi}_f + \boldsymbol{\beta_6}\hat{\varphi}_f \tag{4.22-b}$$

$$\hat{\boldsymbol{D}} = \boldsymbol{\beta_3}\omega_e + \boldsymbol{\beta_4} \tag{4.22-c}$$

Above all, the small signal equations of 1st and 2nd-order adaptive models are established in (4.11) and (4.21) respectively. They will be used for the stability analysis and their difference in control performance will be compared in the later content.

4.3.2.2 Control Rule

The control rule in the s-domain expressed in (4.3) does not have any derivative or integration terms, thus we can directly derive the control rule in the z-domain as:

$$\begin{aligned} e(k) =& \tilde{\imath}_d(k)\hat{\imath}_q(k) - \tilde{\imath}_q(k)\hat{\imath}_d(k) - \left[\tilde{\imath}_q(k) - \hat{\imath}_q(k)\right]\frac{\hat{\varphi}_f}{\hat{L}} \\ =& \tilde{\boldsymbol{I}}_{\boldsymbol{dq}}^T(k)\boldsymbol{J_2}\hat{\boldsymbol{I}}_{\boldsymbol{dq}}(k) - \boldsymbol{J_1}\left[\tilde{\boldsymbol{I}}_{\boldsymbol{dq}}(k) - \hat{\boldsymbol{I}}_{\boldsymbol{dq}}(k)\right]\frac{\hat{\varphi}_f}{\hat{L}} \end{aligned} \tag{4.23}$$

where $\tilde{\boldsymbol{I}}_{\boldsymbol{dq}}(k) = [\tilde{\imath}_d(k) \quad \tilde{\imath}_q(k)]^T$ and $\hat{\boldsymbol{I}}_{\boldsymbol{dq}}(k) = [\hat{\imath}_d(k) \quad \hat{\imath}_q(k)]^T$ are sampled and estimated d- and q-axis currents at time instant *k* respectively.

The small signal equation of the discrete control rule (4.23) is derived as follows:

$$\begin{aligned} \Delta e(k) =& equ\left[\tilde{\boldsymbol{I}}_{\boldsymbol{dq}}^T(k)\right]\boldsymbol{J_2}\Delta\hat{\boldsymbol{I}}_{\boldsymbol{dq}}(k) + \Delta\tilde{\boldsymbol{I}}_{\boldsymbol{dq}}^T(k)\boldsymbol{J_2}equ\left[\hat{\boldsymbol{I}}_{\boldsymbol{dq}}(k)\right] \\ & - \frac{\hat{\varphi}_f}{\hat{L}}\boldsymbol{J_1}\left[\Delta\tilde{\boldsymbol{I}}_{\boldsymbol{dq}}(k) - \Delta\hat{\boldsymbol{I}}_{\boldsymbol{dq}}(k)\right] \\ =& \boldsymbol{I}_{\boldsymbol{equ}}^{*T}\boldsymbol{J_2}\Delta\hat{\boldsymbol{I}}_{\boldsymbol{dq}}(k) + \Delta\tilde{\boldsymbol{I}}_{\boldsymbol{dq}}^T(k)\boldsymbol{J_2}\hat{\boldsymbol{I}}_{\boldsymbol{equ}} - \frac{\hat{\varphi}_f}{\hat{L}}\boldsymbol{J_1}\left[\Delta\tilde{\boldsymbol{I}}_{\boldsymbol{dq}}(k) - \Delta\hat{\boldsymbol{I}}_{\boldsymbol{dq}}(k)\right] \\ =& \boldsymbol{I}_{\boldsymbol{equ}}^{*T}\boldsymbol{J_2}\Delta\hat{\boldsymbol{I}}_{\boldsymbol{dq}}(k) - \hat{\boldsymbol{I}}_{\boldsymbol{equ}}^T\boldsymbol{J_2}\Delta\tilde{\boldsymbol{I}}_{\boldsymbol{dq}}(k) + \frac{\hat{\varphi}_f}{\hat{L}}\boldsymbol{J_1}\left[\Delta\hat{\boldsymbol{I}}_{\boldsymbol{dq}}(k) - \Delta\tilde{\boldsymbol{I}}_{\boldsymbol{dq}}(k)\right] \\ =& \left(\boldsymbol{I}_{\boldsymbol{equ}}^{*T}\boldsymbol{J_2} + \frac{\hat{\varphi}_f}{\hat{L}}\boldsymbol{J_1}\right)\Delta\hat{\boldsymbol{I}}_{\boldsymbol{dq}}(k) - \left(\hat{\boldsymbol{I}}_{\boldsymbol{equ}}^T\boldsymbol{J_2} + \frac{\hat{\varphi}_f}{\hat{L}}\boldsymbol{J_1}\right)\Delta\tilde{\boldsymbol{I}}_{\boldsymbol{dq}}(k) \end{aligned} \tag{4.24}$$

where $equ[*]$ represent the equilibrium operating point value of * when the system is in steady state. The $\Delta\hat{\boldsymbol{I}}_{\boldsymbol{dq}}(k)$ and $\Delta\tilde{\boldsymbol{I}}_{\boldsymbol{dq}}(k)$ represent the small signal variables of estimated and sampled currents respectively. $\hat{\boldsymbol{I}}_{\boldsymbol{equ}}$ represents the equilibrium operating point value of the estimated current $\hat{\boldsymbol{I}}_{\boldsymbol{dq}}(k)$. $\boldsymbol{I}_{\boldsymbol{equ}}^{*}$ represents the equilibrium operating point of sampled current $\tilde{\boldsymbol{I}}_{\boldsymbol{dq}}(k)$, which is the same as the current reference because the current PI controller will ultimately reduce their error to zero.

A brief expression of (4.24) is given in (4.25) by replacing the constant part with symbols $\hat{\boldsymbol{C}}_{\boldsymbol{1}}$, $\hat{\boldsymbol{C}}_{\boldsymbol{2}}$ as follows:

$$\Delta e(k) = \hat{\boldsymbol{C}}_{\boldsymbol{1}}\Delta\hat{\boldsymbol{I}}_{\boldsymbol{dq}}(k) - \hat{\boldsymbol{C}}_{\boldsymbol{2}}\Delta\tilde{\boldsymbol{I}}_{\boldsymbol{dq}}(k) \tag{4.25}$$

where

$$\hat{\boldsymbol{C}}_{\boldsymbol{1}} = \boldsymbol{I}_{\boldsymbol{equ}}^{*T}\boldsymbol{J_2} + \frac{\hat{\varphi}_f}{\hat{L}}\boldsymbol{J_1} \tag{4.26-a}$$

$$\hat{\boldsymbol{C}}_{\boldsymbol{2}} = \hat{\boldsymbol{I}}_{\boldsymbol{equ}}^{T}\boldsymbol{J_2} + \frac{\hat{\varphi}_f}{\hat{L}}\boldsymbol{J_1} \tag{4.26-b}$$

4.3.2.3 MRAS PI Controller

The MRAS PI controller in the s-domain expressed in (4.4) includes continuous time

integration. To discretize it, a new state variable $X_\omega(k)$ is introduced for the integration part and defined as follows:

$$X_\omega(k+1) = X_\omega(k) + e(k) \tag{4.27-a}$$

The (4.27-a) is an iterative equation which shows the relationship between $X_\omega(k+1)$ and $X_\omega(k)$. Therefore, the expression of $X_\omega(k)$ can be obtained as a summation of $e(k)$ by substituting (4.27-a) repeatedly, and its result is shown as follows:

$$\begin{aligned} X_\omega(k) &= e(k-1) + X_\omega(k-1) \\ &= e(k-1) + e(k-2) + X_\omega(k-2) \\ &= \cdots \\ &= \textstyle\sum_{i=0}^{k-1} e(i) \end{aligned} \tag{4.27-b}$$

Therefore, the discrete format of the s-domain expression (4.4) can be derived as follows:

$$\begin{aligned} \hat{\omega}_e(k) &= k_{pm}e(k) + \textstyle\sum_{i=0}^{k} e(i)k_{im}T_s \\ &= k_{pm}e(k) + k_{im}T_s\big(e(k) + \textstyle\sum_{i=0}^{k-1} e(i)\big) \\ &= \big(k_{pm} + k_{im}T_s\big)e(k) + k_{im}T_s X_\omega(k) \end{aligned} \tag{4.27-c}$$

By defining two new variables (i.e., $P_\omega = k_{im}T_s, I_\omega = k_{pm} + k_{im}T_s$), equation (4.27-c) can be simplified as (4.27-d) below.

$$\hat{\omega}_e(k) = P_\omega X_\omega(k) + I_\omega e(k) \tag{4.27-d}$$

Finally, the discrete MRAS PI controller is modelled by (4.27-a) and (4.27-d). The small-signal equations of them can be easily derived as follow as both of them are linear.

$$\Delta X_\omega(k+1) = \Delta X_\omega(k) + \Delta e(k) \tag{4.28}$$

$$\Delta\hat{\omega}_e(k) = P_\omega \Delta X_\omega(k) + I_\omega \Delta e(k) \tag{4.29}$$

4.3.2.4 Estimated Position Integration

The estimated rotor position is from the integration of the estimated speed shown in the s-domain position integration equation (4.5). To discretize (4.5), the Forward Euler

method is adopted, and the discrete model of estimated position integration is expressed as follows:

$$\hat{\theta}(k+1) = \hat{\theta}(k) + T_s\hat{\omega}_e(k) \tag{4.30}$$

where $\hat{\theta}(k)$ is the estimated result of the rotor position at current time step k.

The small-signal equation of (4.30) can be easily derived and it is listed as follows:

$$\Delta\hat{\theta}(k+1) = \Delta\hat{\theta}(k) + T_s\Delta\hat{\omega}_e(k) \tag{4.31}$$

4.4 Current Closed-Loop Small Signal Modelling

Since the bandwidth of the current control loop is normally much higher than that of the speed control loop (>10 times at least) and the propeller has large inertia, the speed can be regarded as constant and thus we will only focus on the stability analysis of the current closed loop.

The current closed-loop system can be regarded as the composition of 5 different blocks shown in Fig 4.3 with different colours. The grey blocks denote the dual three-phase machine model, which include the rotor position integration and the math model between machine currents and voltages. The 'Current PI controller' block calculates the voltage references based on current errors. The 'Voltage generation' block includes the voltage commands transformation from d/q-frame to a/b/c-frame as well as the actual voltage transformation from a/b/c-frame to d/q-frame. Similarly, the 'Current transformation' block also includes all the transformations from the actual d/q-currents to the d/q-currents used for current PI control. All the 4 blocks mentioned above can also be found in the machine control algorithm with a position sensor, but the 'Rotor position and speed estimation' block is unique for sensorless control and the small

signal model of it has been discussed in the last section. The outputs of this block are the estimated speed $\hat{\omega}_e$ and position $\hat{\theta}$ at time $k-1$ instead of time k in Fig 4.3 because, at every period, this block is executed after all the other blocks. Thus, only the estimated speed and position from the last period are available.

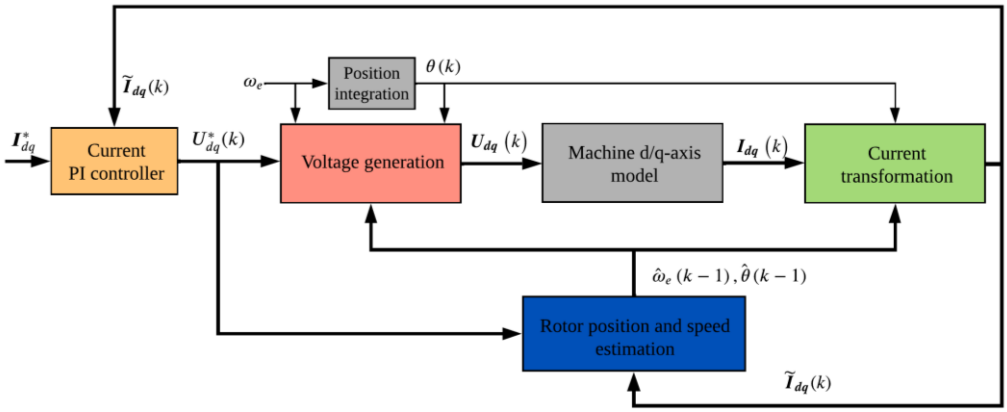


Fig 4.3. MRAS sensorless current closed-loop system diagram

Therefore, in the following sections, the other 4 blocks (i.e. current PI controller, voltage generation, current transformation, and machine dq model with position integration) in Fig 4.3 of the current closed-loop system will be modelled in z-domain with their small signal models. Then, the state evolution equation of the whole system will be derived for stability analysis.

4.4.1 Current PI Controller

The 'Current PI controller' in Fig 4.3 provides d/q-axis voltage references based on current reference and feedback. To simplify the controller structure, the PI controllers of the d-axis and q-axis are designed without considering the decoupling items. This design consideration will influence the dynamic performance but will not affect steady error. The PI controller takes the error of current at each time instant k with the equation as follows:

$$\boldsymbol{e_{dq}}(k) = \boldsymbol{I^*_{dq}} - \tilde{\boldsymbol{I}}_{\boldsymbol{dq}}(k) \tag{4.32}$$

where $\boldsymbol{e_{dq}}(k) = [e_d(k) \quad e_q(k)]^T$ represents the current error, $\boldsymbol{I^*_{dq}} = [i^*_d \quad i^*_q]^T$ is the constant current reference, and $\tilde{\boldsymbol{I}}_{\boldsymbol{dq}}(k) = [\tilde{\imath}_d(k) \quad \tilde{\imath}_q(k)]^T$ is the sampled current in the estimated dq frame. Similar to the discrete MRAS PI controller design process mentioned in Section 4.3.2.3, a state vector $\boldsymbol{X_{dq}}(k) = [x_d(k) \quad x_q(k)]^T$ is defined here to represent the integration. Therefore, the current PI controller can be expressed as follows:

$$\boldsymbol{X_{dq}}(k+1) = \boldsymbol{X_{dq}}(k) + \boldsymbol{e_{dq}}(k) \tag{4.33-a}$$

$$\boldsymbol{U^*_{dq}}(k) = P_i \boldsymbol{X_{dq}}(k) + I_i \boldsymbol{e_{dq}}(k) \tag{4.33-b}$$

where $P_i = k_i T_s$, $I_i = k_p + k_i T_s$. $\boldsymbol{U^*_{dq1}}(k)$ is the output result of the current PI controller.

Thus, the small-signal expressions of (4.32), (4.33-a)and (4.33-b) are as follows:

$$\Delta \boldsymbol{e_{dq}}(k) = -\Delta \tilde{\boldsymbol{I}}_{\boldsymbol{dq}}(k) \tag{4.34}$$

$$\Delta \boldsymbol{X_{dq}}(k+1) = \Delta \boldsymbol{X_{dq}}(k) + \Delta \boldsymbol{e_{dq}}(k) \tag{4.35}$$

$$\Delta \boldsymbol{U^*_{dq}}(k) = P_i \Delta \boldsymbol{X_{dq}}(k) + I_i \Delta \boldsymbol{e_{dq}}(k) \tag{4.36}$$

The current reference $\boldsymbol{I^*_{dq}}$ is regarded as constant as only the steady state is analysed here. Therefore, the term $\Delta \boldsymbol{I^*_{dq}}$ can be neglected in (4.34).

4.4.2 Voltage Generation

The 'Voltage Generation' block in Fig 4.3 has its full diagram in Fig 4.4. This diagram shows the processes from the PI current controller output $\boldsymbol{U^*_{dq}}(k)$ to the actual voltage $\boldsymbol{U_{dq}}(k)$ applied to the machine.

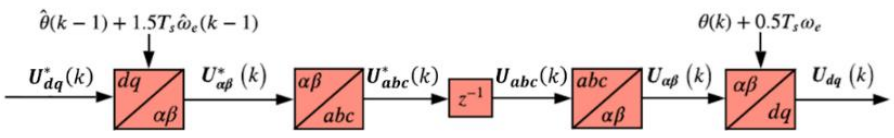


Fig 4.4. Voltage generation block diagram

In the diagram Fig 4.4, the voltage reference $\boldsymbol{U^*_{dq}}(k)$ is fed into a dq-to-$\alpha\beta$ block and

then a $\alpha\beta$-to-dq transformations block to get 3-phase voltages reference $\boldsymbol{U}^*_{\boldsymbol{abc}}(k)$. The $\boldsymbol{U}^*_{\boldsymbol{abc}}(k)$ will only be applied to the machine at the next sample time instant *k*+1. Therefore, a unit delay, i.e. a Z^{-1} block, is placed between the reference $\boldsymbol{U}^*_{\boldsymbol{abc}}(k)$ and the real 3-phase voltages $\boldsymbol{U}_{\boldsymbol{abc}}(k)$. Based on the machine dq model theory, the dq-voltage $\boldsymbol{U}_{\boldsymbol{dq}}(k)$ is derived from 3-phase voltage $\boldsymbol{U}_{\boldsymbol{abc}}(k)$ by using Clarke (abc-to-$\alpha\beta$) and Park ($\alpha\beta$-to-dq) transformation.

Fig 4.4 can be further simplified by neglecting the $\alpha\beta$-to-abc and abc-to-$\alpha\beta$ transformations. This neglection will not influence the final result as these transformations are based on the static frame and do not have any relation with rotor position and speed. The simplified voltage generation block diagram is shown in Fig 4.5.

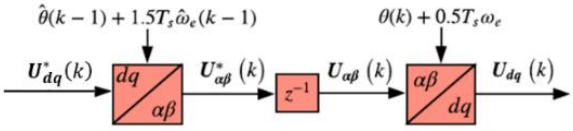


Fig 4.5. Voltage generation simplified block diagram

Readers may have started to wonder why $\theta(k)+0.5T_s\omega_e$ is used instead of $\theta(k)+T_s\omega_e$ during the $\alpha\beta$-to-dq transformation in Fig 4.5. This can be explained by the following figure.

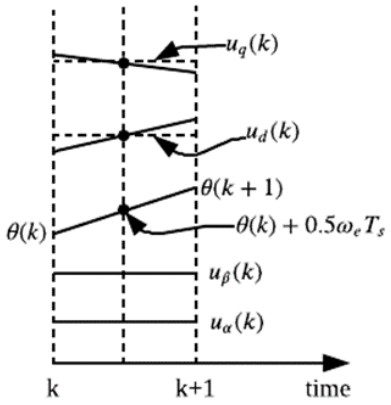


Fig 4.6. The rotor position compensation for $\alpha\beta$-to-dq transformation

As can be seen from Fig 4.6, during the period from time instant k to k+1, $u_\alpha(k)$ and $u_\beta(k)$ hold constant during this one sample time. However, the actual rotor position

actually changes continuously from $\theta(k)$ to $\theta(k+1)$. As a result, d and q-axis voltages after Park ($\alpha\beta$-to-dq) transformation change continuously, as shown in Fig 4.6. To discretize the continuous dq-axes voltages, the $\boldsymbol{U_{dq}}(k) = [u_d(k) \quad u_q(k)]$ chosen are at the middle of one period. Therefore, a half period time rotor angle $0.5T_s\omega_e$ is added to compensate to the $\theta(k)$ for the $\alpha\beta$-to-dq transformation.

For the dq-to-$\alpha\beta$ transformation in Fig 4.5, it is noticed that the rotor angle is used as $\hat{\theta}(k-1) + 1.5T_s\hat{\omega}_e(k-1)$. The $1.5T_s\hat{\omega}_e(k-1)$ compensates the one period unit delay due to the PWM converter as well as the 0.5-period delay of the $\boldsymbol{U_{dq}}(k)$ to $\boldsymbol{U_{\alpha\beta}}(k)$ [54]. The transforming matrices of inverse Park (dq to $\alpha\beta$-frame) and Park ($\alpha\beta$ to dq-frame) transformation used in Fig 4.5 are listed below:

$$\boldsymbol{T}^{-1}(\theta) = \begin{bmatrix} \cos\theta & -\sin\theta \\ \sin\theta & \cos\theta \end{bmatrix} \tag{4.37}$$

$$\boldsymbol{T}(\theta) = \begin{bmatrix} \cos\theta & \sin\theta \\ -\sin\theta & \cos\theta \end{bmatrix} \tag{4.38}$$

where θ represents the angle between d-axis and α-axis.

Therefore, the three blocks from left to right in Fig 4.5 can be expressed with equations as follows:

$$\boldsymbol{U^*_{\alpha\beta}}(k) = \boldsymbol{T}^{-1}\big(\hat{\theta}(k-1) + 1.5T_s\hat{\omega}_e(k-1)\big)\boldsymbol{U^*_{dq}}(k) \tag{4.39}$$

$$\boldsymbol{U_{\alpha\beta}}(k) = \boldsymbol{U^*_{\alpha\beta}}(k-1) \tag{4.40}$$

$$\boldsymbol{U_{dq}}(k) = \boldsymbol{T}(\theta\ (k) + 0.5T_s\omega_e)\boldsymbol{U_{\alpha\beta}}(k) \tag{4.41}$$

where $\boldsymbol{U^*_{\alpha\beta}}(k)$ and $\boldsymbol{U^*_{dq1}}(k)$ are the voltage reference at time instant k in $\alpha\beta$ and dq-frame respectively, $\boldsymbol{U_{\alpha\beta}}(k)$ and $\boldsymbol{U_{dq}}(k)$ are the machine voltage at time instant k in $\alpha\beta$ and dq-frame respectively. It can be seen that the discrete math model of the voltage transformation part in (4.39) and (4.41) are nonlinear and their small-signal equations cannot be derived directly.

Substituting (4.39) and (4.40) to (4.41), the relation between the input and output of

voltage transformation can be obtained as follows, and the detail derivation of (4.42) and (4.43) are in Appendix B.I.a.

$$\boldsymbol{U_{dq}}(k)= \boldsymbol{T_1}(k)\boldsymbol{U^*_{dq}}(k-1) \tag{4.42}$$

where $\boldsymbol{T_1}(k)$ has the expression shown in (4.43).

$$\boldsymbol{T_1}(k)= (1-\theta_u^2/2)\boldsymbol{E_2} + (\theta_u - \theta_u^3/6)\boldsymbol{J_2} \tag{4.43}$$

In (4.43), the θ_u has the expression: $\theta_u = \theta(k) - \hat{\theta}(k-2) + T_s\big(0.5\omega_e - 1.5\hat{\omega}_e(k-2)\big)$.

The small signal equation of (4.42) is shown in (4.44). The detail derivation of this equation can be found in Appendix B.I.b.

$$\begin{aligned}\Delta\boldsymbol{U_{dq}}(k) =&\big[\big(1-\theta^2_{\Delta equ}/2\big)\boldsymbol{E_2} - \big(\theta_{\Delta equ} - \theta^3_{\Delta equ}/6\big)\boldsymbol{J_2}\big]\Delta\boldsymbol{U^*_{dq}}(k-1)\\ &+\big[\boldsymbol{J_2}\big(1-0.5\theta^2_{\Delta equ}\big)+\boldsymbol{E_2}\theta_{\Delta equ}\big]\boldsymbol{V^*_{equ}}\Delta\theta_u\end{aligned} \tag{4.44}$$

The purpose of the small signal equation is to construct the system state evolution equation, which has the format like $\boldsymbol{x}(k+1) = \boldsymbol{A}\cdot\boldsymbol{x}(k)$, where $\boldsymbol{x}(k)$ is the state vector at time instant k, and $\boldsymbol{A}$ is the state matrix. Because (4.44) has variables not only at time instant k (i.e., $\Delta\theta(k)$ in (B.12)) but also at previous time instant (i.e., $\Delta\boldsymbol{U^*_{dq}}(k-1)$ in (4.44), $\Delta\hat{\theta}(k-2)$, $\Delta\hat{\omega}_e(k-2)$ in (B.12)). Therefore, it's necessary to define 5 new state vector/variables as follows to modify (4.44).

$$\Delta\boldsymbol{U^*_{dq1}}(k+1) = \Delta\boldsymbol{U^*_{dq}}(k) \tag{4.45}$$

$$\Delta\hat{\theta}_1(k+1) = \Delta\hat{\theta}(k) \tag{4.46}$$

$$\Delta\hat{\theta}_2(k+1) = \Delta\hat{\theta}_1(k) \tag{4.47}$$

$$\Delta\hat{\omega}_{e1}(k+1) = \Delta\hat{\omega}_e(k) \tag{4.48}$$

$$\Delta\hat{\omega}_{e2}(k+1) = \Delta\hat{\omega}_{e1}(k) \tag{4.49}$$

The numbers in the subscripts of the 5 newly defined vector/variables represent how many delays they have when compared with their original vector/variables. For example, $\Delta\hat{\omega}_{e2}(k)$ has two unit-delays compared with $\Delta\hat{\omega}_e(k)$, which means

$\Delta\hat{\omega}_{e2}(k) = \Delta\hat{\omega}_e(k-2)$. Replacing $\Delta\boldsymbol{U}^*_{\boldsymbol{dq}}(k-1)$, $\Delta\hat{\theta}(k-2)$, $\Delta\hat{\omega}_e(k-2)$ in (4.44) with newly defined state vector/variables (i.e., $\Delta\boldsymbol{U}^*_{\boldsymbol{dq1}}(k)$, $\Delta\hat{\theta}_2(k)$, $\Delta\hat{\omega}_{e2}(k)$), this small signal equation can be rewritten as follows:

$$\begin{aligned}&\Delta\boldsymbol{U}_{\boldsymbol{dq}}(k)\\&= \left[\left(1-\theta^2_{\Delta equ}/2\right)\boldsymbol{E_2} - \left(\theta_{\Delta equ} - \theta^3_{\Delta equ}/6\right)\boldsymbol{J_2}\right]\Delta\boldsymbol{U}^*_{\boldsymbol{dq1}}(k)\\&+\left[\boldsymbol{J_2}\left(1-0.5\theta^2_{\Delta equ}\right)+\boldsymbol{E_2}\theta_{\Delta equ}\right]\boldsymbol{V}^*_{\boldsymbol{equ}}\left[\Delta\theta(k) - \Delta\hat{\theta}_2(k) - 1.5T_s\Delta\hat{\omega}_{e2}(k)\right]\end{aligned} \tag{4.50}$$

Equation (4.50) only has state vectors/variables at time instant k, which cannot be regarded as a state evolution equation. However, it can still be integrated into the system state evolution equation by substituting it into other state evolution equations which have the item $\Delta\boldsymbol{U}_{\boldsymbol{dq}}(k)$.

4.4.3 Machine dq Model and Position Integration

The machine d/q-axis model in the discrete-time domain, shown as the grey block in Fig 4.3, has a similar expression as the discrete MRAS adaptive model given by (4.6). The only difference is the parameter matrices. Equation (4.6) uses estimated machine parameters (i.e., $\hat{R}, \hat{L}, \hat{\varphi}_f$) and estimated speed ($\hat{\omega}_e(k)$) to build the machine MRAS adaptive model, but the machine d/q-axis model in this subsection should be built with the actual machine parameters (i.e., R, L, φ_f) and actual speed (ω_e). Although the estimated machine parameters are assumed the same as actual parameters in this section for simplification, the estimated speed ($\hat{\omega}_e(k)$) cannot be regarded as the same as the actual machine speed (ω_e).

Therefore, based on the discrete MRAS adaptive model (4.6), the machine d/q-axis model in z-domain is expressed as follows:

$$\boldsymbol{I}_{\boldsymbol{dq}}(k+1) = \boldsymbol{F}\boldsymbol{I}_{\boldsymbol{dq}}(k) + \boldsymbol{G}_{\boldsymbol{v}}\boldsymbol{U}_{\boldsymbol{dq}}(k) + \boldsymbol{G}_{\boldsymbol{\varphi}}\varphi_f \tag{4.51}$$

where

$$\boldsymbol{F} = \boldsymbol{e}^{\boldsymbol{A}T_S} \tag{4.52-a}$$

$$\boldsymbol{G_v} = (\boldsymbol{F} - \boldsymbol{E_2})\boldsymbol{A^{-1}}\boldsymbol{B_v} \tag{4.52-b}$$

$$\boldsymbol{G_\varphi} = (\boldsymbol{F} - \boldsymbol{E_2})\boldsymbol{A^{-1}}\boldsymbol{B_\varphi} \tag{4.52-c}$$

The expressions of matrices $\boldsymbol{A}, \boldsymbol{B_v}, \boldsymbol{B_\varphi}$ are shown as follows:

$$\boldsymbol{A} = \begin{bmatrix} -R/L & \omega_e \\ -\omega_e & -R/L \end{bmatrix} \tag{4.52-d}$$

$$\boldsymbol{B_v} = \begin{bmatrix} 1/L & 0 \\ 0 & 1/L \end{bmatrix} \tag{4.52-e}$$

$$\boldsymbol{B_\varphi} = [0 \quad -\omega_e/L]^T \tag{4.52-f}$$

The machine d/q-axis model in z-domain is finally derived as (4.51) with its parameters listed in (4.52-a)-(4.52 -f). The exponential expression in (4.52-a) is not replaced by its Taylor expansion like that in the discrete adaptive model (4.8-a). This is because $\boldsymbol{A}$ in the actual machine model is constant but $\widehat{\boldsymbol{A}}(k)$ in the discrete adaptive machine model is not.

Because all parameter matrices (i.e., $\boldsymbol{F}, \boldsymbol{G_v}, \boldsymbol{G_\varphi}$) of the machine d/q-axis model (4.51) are constant, it is quite easy to get its small signal equation as follows:

$$\Delta \boldsymbol{I_{dq}}(k+1) = \boldsymbol{F}\Delta \boldsymbol{I_{dq}}(k) + \boldsymbol{G_v}\Delta \boldsymbol{U_{dq}}(k) \tag{4.53}$$

As can be seen from Fig 4.3, the actual rotor position $\theta(k)$ comes from the integration of constant rotor speed. This can be modelled with equation (4.54) and its small signal equation is like (4.55).

$$\theta(k+1) = \theta(k) + \omega_e T_s \tag{4.54}$$

$$\Delta\theta(k+1) = \Delta\theta(k) \tag{4.55}$$

4.4.4 Current Transformation

The “Current transformation” is displayed in Fig 4.7 with a whole diagram (a) and a simplified diagram (b). Similar to the ‘Voltage generation’ in section 4.4.2, the overall diagram, given by Fig 4.7(a), has four frame transformations and one sample time

delay. The dq-axis currents at time instant k (i.e., $\boldsymbol{I_{dq}}(k)$) are transformed to $\alpha\beta$ frame (i.e., $\boldsymbol{I_{\alpha\beta}}(k)$) using the rotor position at time instant k (i.e., $\theta(k)$). Then, it will be transformed to 3-phase currents (i.e., $\boldsymbol{I_{abc}}(k)$) by $\alpha\beta$-to-abc transformation. There is a unit delay after them because the sampled 3-phase current at time instant k will only be used by controller at the next instant k+1.

The two transformations after unit delay (i.e., abc-to-$\alpha\beta$, $\alpha\beta$-to-dq) are executed in the controller to get the sampled currents in the estimated dq frame (i.e., $\tilde{\boldsymbol{I}}_{dq}(k)$) for the current PI controller. The position used in $\alpha\beta$-to-dq transformation is $\hat{\theta}(k-1) - T_s\hat{\omega}_e(k-1)$ instead of $\hat{\theta}(k-1)$ as the unit delay needs to be compensated. The $\hat{\omega}_e(k-1)$ and $\hat{\theta}(k-1)$ instead of $\hat{\omega}_e(k)$ and $\hat{\theta}(k)$ are used at time instant k because the MRAS algorithm is executed after the current transformation.

Similar to 'Voltage generation' in section 4.4.2, the $\alpha\beta$-to-abc and abc-to-$\alpha\beta$ transformations in Fig 4.7(a) can be neglected to have a simplified diagram like Fig 4.7(b) as they don't have any relationship with rotor position and don't affect the analysis result.

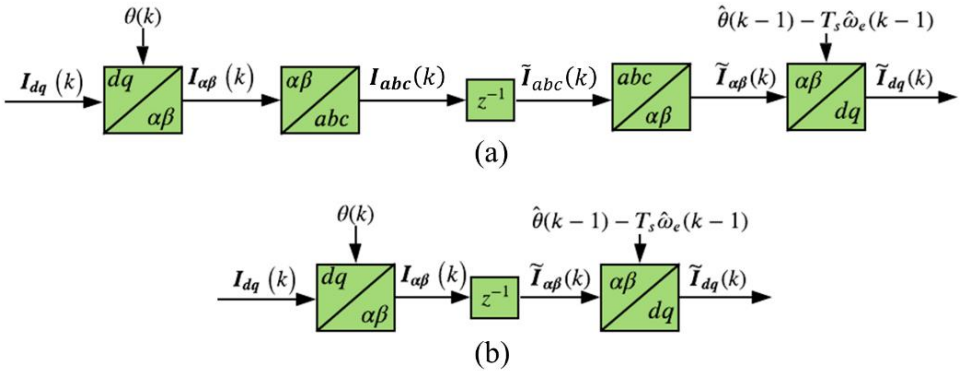


Fig 4.7. Current transformation diagram full (a) and simplified (b) diagram

Just like the equations (4.39)-(4.41) in 'Voltage generation, there are also three equations like (4.56)-(4.58) to describe the "Current transformation". Equation (4.56) describes the real current transformation from dq to $\alpha\beta$-frame; (4.57) describes the

delay of current sampling; (4.58) describes the sampled current transformation from $\alpha\beta$ to dq-frame.

$$\boldsymbol{I}_{\boldsymbol{\alpha\beta}}(k) = \boldsymbol{T}^{-1}\big(\theta\ (k)\big)\boldsymbol{I}_{\boldsymbol{dq}}(k) \tag{4.56}$$

$$\tilde{\boldsymbol{I}}_{\boldsymbol{\alpha\beta}}(k) = \boldsymbol{I}_{\boldsymbol{\alpha\beta}}(k-1) \tag{4.57}$$

$$\tilde{\boldsymbol{I}}_{\boldsymbol{dq}}(k) = \boldsymbol{T}\big(\hat{\theta}(k-1) - T_s\hat{\omega}_e(k-1)\big)\tilde{\boldsymbol{I}}_{\boldsymbol{\alpha\beta}}(k) \tag{4.58}$$

where $\boldsymbol{I}_{\boldsymbol{dq}}(k)$ and $\boldsymbol{I}_{\boldsymbol{\alpha\beta}}(k)$ are the machine currents at time instant k in dq-frame and $\alpha\beta$-frame respectively; $\tilde{\boldsymbol{I}}_{\boldsymbol{dq}}(k)$ and $\tilde{\boldsymbol{I}}_{\boldsymbol{\alpha\beta}}(k)$ are the sampled currents at time instant k in estimated dq-frame and $\alpha\beta$-frame respectively.

Combining (4.56)-(4.58) together, the relationship between machine dq-axis current $\boldsymbol{I}_{\boldsymbol{dq}}(k)$ and sampled current in estimated dq frame $\tilde{\boldsymbol{I}}_{\boldsymbol{dq}}(k)$ can be derived like (4.59) and (4.60). The detail derivation is explained in Appendix B.II.a.

$$\tilde{\boldsymbol{I}}_{\boldsymbol{dq}}(k) = \boldsymbol{T_2}(k)\boldsymbol{I}_{\boldsymbol{dq}}(k-1) \tag{4.59}$$

where

$$\boldsymbol{T_2}(k) = (1-\theta_i^2/2)\boldsymbol{E_2} + (\theta_i - \theta_i^3/6)\boldsymbol{J_2} \tag{4.60}$$

In (4.60), the θ_i has its expression like $\theta_i = \hat{\theta}(k-1) - \theta(k-1) - T_s\hat{\omega}_e(k-1)$.

The small signal equation of (4.59) is shown in (4.61) and its detail derivation is shown in Appendix B.II.b. The expression of $\Delta\theta_i$ is shown in (B.21)

$$\begin{aligned}\Delta\tilde{\boldsymbol{I}}_{\boldsymbol{dq}}(k) = &\big[\big(1-\theta_{\Delta equ}^2/2\big)\boldsymbol{E_2} + \big(\theta_{\Delta equ} - \theta_{\Delta equ}^3/6\big)\boldsymbol{J_2}\big]\Delta\boldsymbol{I}_{\boldsymbol{dq}}(k-1)\\ &+\big[\boldsymbol{J_2}\big(1-0.5\theta_{\Delta equ}^2\big) - \boldsymbol{E_2}\theta_{\Delta equ}\big]\boldsymbol{I}_{\boldsymbol{equ}}\Delta\theta_i\end{aligned} \tag{4.61}$$

Similar to the 'Voltage generation' part in Section 4.4.2, the state vector/variables in (4.61) at time instant k-1 (i.e., $\Delta\boldsymbol{I}_{\boldsymbol{dq}}(k-1)$, $\Delta\hat{\theta}(k-1)$, $\Delta\theta(k-1)$, $\Delta\hat{\omega}_e(k-1)$) should be replaced by new state vector/variables at time instant k (i.e., $\Delta\boldsymbol{I}_{\boldsymbol{dq1}}(k)$, $\Delta\hat{\theta}_1(k)$, $\Delta\theta_1(k)$, $\Delta\hat{\omega}_{e1}(k)$). The $\Delta\hat{\theta}_1(k)$ and $\Delta\hat{\omega}_{e1}(k)$ have been defined in (4.46) and (4.48) respectively, and $\boldsymbol{I}_{\boldsymbol{dq1}}(k)$, $\Delta\theta_1(k)$ are defined in (4.62), (4.63). The number '1'

in the subscripts of the new defined vector/variable represent 1 delay of them compared with their original vector/variable.

$$\Delta \boldsymbol{I_{dq1}}(k+1) = \Delta \boldsymbol{I_{dq}}(k) \tag{4.62}$$

$$\Delta\theta_1(k+1) = \Delta\theta(k) \tag{4.63}$$

Therefore, (4.61) can be rewritten to a new equation like (4.64) which only has state vectors/variables at time instant k. Although (4.64) is not a state evolution equation, it can be integrated into the system state evolution equation by substituting it into other state evolution equations which have the item $\Delta\tilde{\boldsymbol{I}}_{\boldsymbol{dq}}(k)$.

$$\begin{aligned}\Delta\tilde{\boldsymbol{I}}_{\boldsymbol{dq}}(k) = &\left[\left(1-\theta_{\Delta equ}^2/2\right)\boldsymbol{E_2} + \left(\theta_{\Delta equ} - \theta_{\Delta equ}^3/6\right)\boldsymbol{J_2}\right]\Delta\boldsymbol{I_{dq1}}(k)\\ &+\left[\boldsymbol{J_2}\left(1-0.5\theta_{\Delta equ}^2\right) - \boldsymbol{E_2}\theta_{\Delta equ}\right]\boldsymbol{I_{equ}}\cdot\\ &\left[\Delta\hat{\theta}(k-1) - \Delta\theta(k-1) - T_s\Delta\hat{\omega}_e(k-1)\right]\end{aligned} \tag{4.64}$$

4.4.5 Current Closed-Loop State Evolution Expression

Till now, the entire current control loop with sensorless rotor position estimation shown in Fig 4.3 has been modelled in the z-domain and their small-signal models have been derived. In this section, all small signal equations will be synthesized into one state evolution equation. This equation will show the stability of the current closed-loop system.

All small-signal equations are derived in Section 4.3.2 as well as in Section 4.4.1-4.4.4. These equations can be classified into 2 categories, one is the equations of state vectors/variables (Table 4.1), and the other is that of intermediate vectors/variables (Table 4.2). There are 13 state vectors/variables for the current closed-loop system in total, which are listed in Table 4.1. The first 5 state vectors are 2*1 vectors, and the other 8 state variables are scalars. The value of these state variables at time instant $k+1$ will be updated by their 1st-order linear difference equations (i.e., second column of

Table 4.1) based on the system state at time instant k.

Table 4.1. State vectors/variables summary for the system state evolution equation

state vectors/variables	State vectors/variables difference equation
$\Delta \boldsymbol{X_{dq}}(k)$	(4.35)
$\Delta \boldsymbol{U^*_{dq1}}(k)$	(4.45)
$\Delta \boldsymbol{I_{dq}}(k)$	(4.53)
$\Delta \boldsymbol{I_{dq1}}(k)$	(4.62)
$\Delta \hat{\boldsymbol{I}}_{\boldsymbol{dq}}(k)$	(4.11) or (4.21)
$\Delta X_{\omega}(k)$	(4.28)
$\Delta \hat{\omega}_{e1}(k)$	(4.48)
$\Delta \hat{\omega}_{e2}(k)$	(4.49)
$\Delta \hat{\theta}(k)$	(4.31)
$\Delta \hat{\theta}_1(k)$	(4.46)
$\Delta \hat{\theta}_2(k)$	(4.47)
$\Delta \theta(k)$	(4.55)
$\Delta \theta_1(k)$	(4.63)

The vectors/variables listed in Table 4.2 are intermediate vectors/variables, whose results at time instant k depend on the state of other vectors/variables at time instant k. These vectors/variables will not appear in the final system state evolution equation, but their expression listed in Table 4.2 will be used to derive the final system state evolution equation.

Table 4.2. Intermediate vectors/variables summary for the system state evolution equation

Intermediate vectors/variables	Intermediate vectors/variables expression
$\Delta e(k)$	(4.25)
$\Delta \hat{\omega}_e(k)$	(4.29)
$\Delta \boldsymbol{e_{dq}}(k)$	(4.34)
$\Delta \boldsymbol{U^*_{dq}}(k)$	(4.36)
$\Delta \boldsymbol{U_{dq}}(k)$	(4.50)
$\Delta \tilde{\boldsymbol{I}}_{\boldsymbol{dq}}(k)$	(4.64)

To derive the state evolution equation of the entire current close-loop system, all differential equations listed in column 2 of Table 4.1 should be synthesized into one equation as follows:

$$\boldsymbol{X}(k+1) = \boldsymbol{M} \cdot \boldsymbol{X}(k) \tag{4.65}$$

where $\boldsymbol{X}(k)$ is a state vector at time instant k (18 rows, 1 column) including all state vectors/variables in the first column of Table 4.1. $\boldsymbol{M}$ is the 18 rows and 18 columns state matrix, which can describe how this system evolves from time instant k to $k+1$.

The procedure of deriving $\boldsymbol{M}$ is with the assistance of MATLAB as it has so many variables and equations involved, but the basic principle is substituting all equations in Table 4.1 into (4.65), and replacing the intermediate vectors/variables with their expression in the Table 4.2.

The stability of the modelled current closed-loop control system is closely linked with the eigenvalues of matrix $\boldsymbol{M}$, which can be obtained by calculating the equation as follows:

$$|\boldsymbol{M} - \lambda \boldsymbol{E}| = 0 \tag{4.66}$$

where λ represents the eigenvalue of matrix $\boldsymbol{M}$, and $\boldsymbol{E}$ is the 18*18 identity matrix.

As the size of $\boldsymbol{M}$ is 18*18, there will be 18 eigenvalues of $\boldsymbol{M}$. For the discrete math model, if the modulus of all eigenvalues λ are smaller than 1.0, the system is stable at the specific equilibrium operating point. If there is any modulus of λ larger than 1.0, the system will not be stable. The next chapter will use this method to analyse the stability of the system.

4.5 Conclusion

The MRAS sensorless stability analysis in the s-domain can be found in some literature, whilst the existing methodologies cannot deal with our high-speed application scenarios due to the control delays. Therefore, this chapter develops the discrete state evolution model of the MRAS sensorless current closed-loop system. This model is a linearized small signal model which can consider the control delays in the real application. The eigenvalues of the proposed model matrix can be used to evaluate the stability of the MRAS sensorless control system.

Chapter 5. Stability Analysis Procedure and Simulation Validation

The state-evolution and small-signal-based MRAS sensorless current closed-loop model is developed in the last chapter. Using that proposed model, system stability at any operating point can be analysed. However, stability analysis at any single operating point is not enough for system stability evaluation in the full operation range. Therefore, a stability analysis procedure is proposed in this chapter to analyse the overall stability performance of the MRAS sensorless system. In addition, the stability boundaries of MRAS sensorless control under different operating conditions and different control parameters will be calculated and compared with simulation results.

5.1 Stability Analysis Procedure

Although the stability of the current closed-loop system is determined by the eigenvalues of its system state matrix $\boldsymbol{M}$, it is not straightforward since machine and control parameters as well as the equilibrium operating point need to be determined firstly. The machine parameters, given in Table 5.1, are assumed to be constant during the stability analysis and the impacts of these parameters due to temperature or stator saturation change have been neglected. The bandwidth of the current PI controller is designed to be 500Hz.

Table 5.1. Machine parameters and constant control parameters for stability analysis

Symbol	Description	Value
R	Resistance per phase	0.171Ω
L	d- and q-axis inductance per sector	530μH
φ_f	Permanent magnet flux linkage	0.03Vs
k_p	Proportional factor of current PI controller	2
k_i	Integral factor of current PI controller	800

A basic stability analysis step is shown in the flowchart in Fig 5.1. The first step is to determine the control parameters of MRAS sensorless algorithm. Different machine parameters ($k_{pm}, k_{im}, \hat{R}, \hat{L}, \hat{\varphi}_f$) will affect system stabilities as well as estimation accuracy, thus need to be defined in the first step. The second step is to select the equilibrium operating point (i_d^*, i_q^*, n). The next step is to calculate the steady-state values of currents and voltages ($\boldsymbol{I_{equ}}, \boldsymbol{\hat{I}_{equ}}, \boldsymbol{V_{equ}}, \boldsymbol{V_{equ}^*}$). Finally, the state matrix $\boldsymbol{M}$ of the current closed-loop system is obtained and its eigenvalues are calculated to evaluate the system stability.

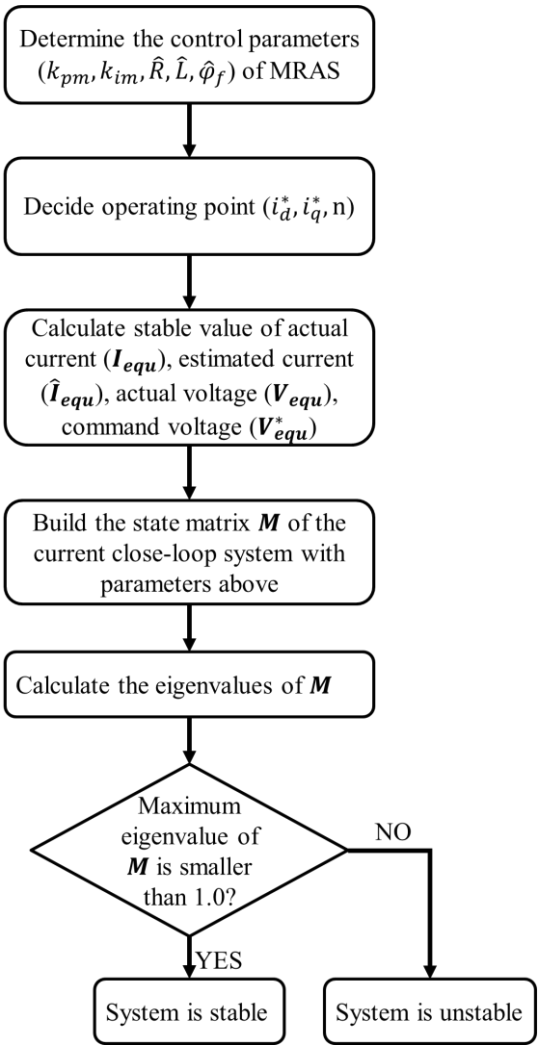


Fig 5.1. The flow chart of stability analysis steps

More complicated analysis of evaluating the system stability will be explained in the following sub-sections.

1) Determine the control parameters of MRAS sensorless algorithm

As shown in Fig 5.1, the first step is to determine the control parameters of the MRAS sensorless algorithm. The selection ranges of these parameters are listed in Table 5.2. The range of k_{pm} and k_{im} are based on some preliminary simulation results, and the estimated machine parameters are selected around the actual machine parameters. It is important to note that k_{pm} and k_{im} will only affect the system stability instead of the estimated position error. It will be proved later that the estimated position error is zero if all estimated machine parameters $(\hat{R}, \hat{L}, \hat{\varphi}_f)$ are the same with the actual machine parameters.

Table 5.2. MRAS sensorless control parameters range for stability analysis

Symbol	Description	Range
k_{pm}	Proportional factor range of MRAS PI controller	1 to 6
k_{im}	Integral factor range of MRAS PI controller	1000 to 15000
$\hat{R}$	Estimated resistance per phase	0.6~1.4*R
$\hat{L}$	Estimated d- and q-axis inductance per sector	0.6~1.4*L
$\hat{\varphi}_f$	Estimated permanent magnet flux linkage	0.6~1.4*φ_f

2) Determine the operating conditions

The operation conditions of this dual three-phase machine are determined by 3 parameters, i.e. $(i_d^*, i_q^*, \mathrm{n})$ as shown in Table 5.3. For our studies, the machine speed range is from 0 to 14.2krpm. The i_d^* is always zero as there is no flux-weakening requirement. The i_q^* is from -30A to 30A, considering both motoring and generating modes.

Table 5.3. Machine operating point range

Symbol	Description	Range
n	Speed	0 to 14.2krpm
i_d^*	d-axis current reference	0A
i_q^*	q-axis current reference	-30A to 30A

3) Calculate the steady-state voltages and currents

If the machine parameters used in MRAS sensorless algorithm are the same as the actual parameters ($\hat{R} = R, \hat{L} = L, \hat{\varphi}_f = \varphi_f$), all current variables in the steady state will be the same (i.e., $\boldsymbol{I_{dq}}(k), \hat{\boldsymbol{I}}_{\boldsymbol{dq}}(k), \tilde{\boldsymbol{I}}_{\boldsymbol{dq}}(k), \boldsymbol{I}^*_{\boldsymbol{dq}}(k)$). This is also true for all voltage variables (i.e., $\boldsymbol{U_{dq}}(k), \boldsymbol{U}^*_{\boldsymbol{dq}}(k)$). However, this is the ideal case and in practice, the estimated position error from MRAS is inevitable. Therefore, the voltage and current transformations in the control algorithm will bring mismatches to the voltage and current variables.

Therefore, the following equations define the steady-state (SS) values of estimated position error, currents, and voltages.

$$\theta_{\Delta equ} = \lim_{k \to \mathrm{SS}} \left(\hat{\theta}(k-1) - \theta(k) \right) \tag{5.1}$$

$$\boldsymbol{I_{equ}} = \lim_{k \to \mathrm{SS}} \left(\boldsymbol{I_{dq}}(k) \right) \tag{5.2}$$

$$\hat{\boldsymbol{I}}_{\boldsymbol{equ}} = \lim_{k \to \mathrm{SS}} \left(\hat{\boldsymbol{I}}_{\boldsymbol{dq}}(k) \right) \tag{5.3}$$

$$\boldsymbol{I}^*_{\boldsymbol{equ}} = \lim_{k \to \mathrm{SS}} \left(\tilde{\boldsymbol{I}}_{\boldsymbol{dq}}(k) \right) = \boldsymbol{I}^*_{\boldsymbol{dq}} \tag{5.4}$$

$$\boldsymbol{V_{equ}} = \lim_{k \to \mathrm{SS}} \left(\boldsymbol{U_{dq}}(k) \right) \tag{5.5}$$

$$\boldsymbol{V}^*_{\boldsymbol{equ}} = \lim_{k \to \mathrm{SS}} \left(\boldsymbol{U}^*_{\boldsymbol{dq}}(k) \right) \tag{5.6}$$

where $\theta_{\Delta equ}$ represents the estimated position error. $\boldsymbol{I_{equ}}$ represents the equilibrium operation point of the machine current in the d/q-axis. $\hat{\boldsymbol{I}}_{\boldsymbol{equ}}$ represents the equilibrium operation point of the estimated current from MRAS adaptive model. $\boldsymbol{I}^*_{\boldsymbol{equ}}$ represents the current reference. $\tilde{\boldsymbol{I}}_{\boldsymbol{dq}}(k)$ is the sampled current using the estimated position $\hat{\theta}$ for abc/dq transformation and will finally be regulated to $\boldsymbol{I}^*_{\boldsymbol{dq}}$. $\boldsymbol{V_{equ}}$ and $\boldsymbol{V}^*_{\boldsymbol{equ}}$ represent the equilibrium operating point of the actual voltage and voltage reference respectively.

In (5.1)-(5.6), there are one unknown scaler ($\theta_{\Delta equ}$) and four unknown 2x1 vectors ($\boldsymbol{I_{equ}}, \boldsymbol{\hat{I}_{equ}}, \boldsymbol{V_{equ}}, \boldsymbol{V^*_{equ}}$). There is also one 2x1 vector ($\boldsymbol{I^*_{equ}}$) already known. Therefore, there are totally 9 unknown variables, and 9 equations are required to calculate a unique solution.

In steady state, the actual machine model and MRAS adaptive model can be expressed as follows:

$$\boldsymbol{A I_{equ}} + \frac{1}{L}\boldsymbol{V_{equ}} + \boldsymbol{G_{\varphi}} = \boldsymbol{I'_{dq}} = \boldsymbol{0} \tag{5.7}$$

$$\boldsymbol{\hat{A}\hat{I}_{equ}} + \frac{1}{\hat{L}}\boldsymbol{V^*_{equ}} + \boldsymbol{\hat{G}_{\varphi}} = \boldsymbol{\hat{I}'_{dq}} = \boldsymbol{0} \tag{5.8}$$

where:

$$\boldsymbol{A} = \begin{bmatrix} -R/L & \omega_e \\ -\omega_e & -R/L \end{bmatrix} \tag{5.9}$$

$$\boldsymbol{G_{\varphi}} = [0 \quad -\omega_e \varphi_f / L]^T \tag{5.10}$$

$$\boldsymbol{\hat{A}} = \begin{bmatrix} -\hat{R}/\hat{L} & \omega_e \\ -\omega_e & -\hat{R}/\hat{L} \end{bmatrix} \tag{5.11}$$

$$\boldsymbol{\hat{G}_{\varphi}} = \left[0 \quad -\omega_e \hat{\varphi}_f / \hat{L}\right]^T \tag{5.12}$$

The relationship between $\boldsymbol{V_{equ}}$ and $\boldsymbol{V^*_{equ}}$ can be expressed as (5.13). A similar relationship between $\boldsymbol{I^*_{equ}}$ and $\boldsymbol{I_{equ}}$ is expressed as (5.14). The Clarke-Park transformation and its inverse transformation can be simplified to linear expression when $\theta_{\Delta equ}$ is close to zero.

$$\boldsymbol{V_{equ}} = \begin{bmatrix} \cos\theta_{\Delta equ} & -\sin\theta_{\Delta equ} \\ \sin\theta_{\Delta equ} & \cos\theta_{\Delta equ} \end{bmatrix} \boldsymbol{V^*_{equ}} \approx \left(\boldsymbol{E_2} - \boldsymbol{J_2}\theta_{\Delta equ}\right)\boldsymbol{V^*_{equ}} \tag{5.13}$$

$$\boldsymbol{I^*_{equ}} = \begin{bmatrix} \cos\theta_{\Delta equ} & \sin\theta_{\Delta equ} \\ -\sin\theta_{\Delta equ} & \cos\theta_{\Delta equ} \end{bmatrix} \boldsymbol{I_{equ}} \approx \left(\boldsymbol{E_2} + \boldsymbol{J_2}\theta_{\Delta equ}\right)\boldsymbol{I_{equ}} \tag{5.14}$$

The MRAS error calculating expression is another one to determine the equilibrium variables. The stable state expression is shown as follows:

$$e = \boldsymbol{I}_{\boldsymbol{equ}}^{*T}\boldsymbol{J_2}\hat{\boldsymbol{I}}_{\boldsymbol{equ}} - \boldsymbol{J_1}\left(\boldsymbol{I}_{\boldsymbol{equ}}^{*} - \hat{\boldsymbol{I}}_{\boldsymbol{equ}}\right)\frac{\widehat{\varphi}_f}{\hat{L}} = 0 \tag{5.15}$$

Based on the analysis above, 9 equations are obtained in (5.7), (5.8), (5.13)-(5.15), which can be used to calculate the 9 unknown variables ($\theta_{\Delta equ}, \boldsymbol{I}_{\boldsymbol{equ}}, \hat{\boldsymbol{I}}_{\boldsymbol{equ}}, \boldsymbol{V}_{\boldsymbol{equ}}, \boldsymbol{V}_{\boldsymbol{equ}}^{*}$). The calculation flowchart is shown in Fig 5.2 below with some equation derivation listed in Appendix B.III.

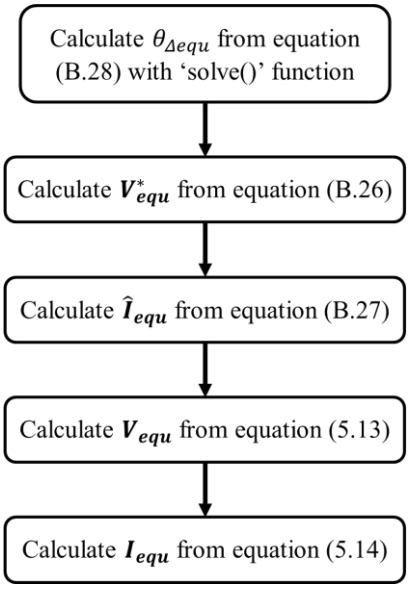


Fig 5.2. Flowchart of equilibrium operating point calculation in MATLAB

4) Calculate eigenvalues of matrix *M*

After the 3 steps above, all parameters and variables in the state matrix $\boldsymbol{M}$ have been determined. The eigenvalues of $\boldsymbol{M}$ thus can be calculated. A MATLAB manuscript based on the steps introduced above is written and attached in Appendix C.

5.2 Simulation Validation

In this section, the proposed eigenvalues-based stability analysis method above will be validated by simulation. Different factors, which will affect the system stability, will be considered such as MRAS PI parameters, different types of MRAS adaptive models, different i_q currents, and different estimated machine parameters. Some insights can be obtained by analysing the system stability at different operating conditions. In this section, the simulation model based on Simulink is built as an important tool for the validation of our proposed small-signal-based analysis.

5.2.1 Simulation Model to Validate The Stability Analysis Method

The simulation model is built in the Simulink and its basic structure is demonstrated in Fig 5.3. It includes d/q-axis current PI controllers, currents and voltages frame transforms, MRAS rotor position and speed estimation, and continuous machine model. Compared with the real application, the outer loop controllers (DC-bus or speed controller) are neglected as they are not considered in this stability analysis. The simulation model built in MATLAB/Simulink is given in Appendix D.

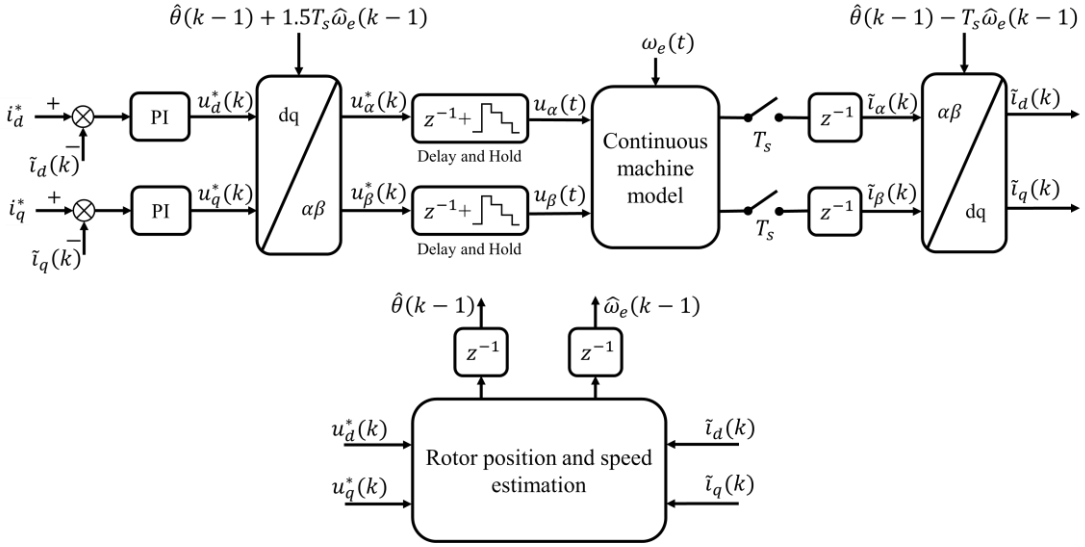


Fig 5.3. Simulation model structure diagram

The power converter is simplified to a unit "delay and hold" block since the voltage reference $u_d^*(k)$ and $u_q^*(k)$ can only be applied to the windings at time instant (k+1). The transformations between $\alpha\beta$ and abc-axis are also neglected as they do not affect the final result. As for the currents, the current sampled at time instant k can only be used at time instant (k+1) due to the long current sampling holding times of the ADC module (about 5us). Therefore, one unit delay is applied to the sampling currents.

The machine used in the simulation is in the continuous-time domain (s-domain) instead of the discrete-time domain (z-domain), which can better represent a real electrical machine. The continuous-time domain machine model adopts the machine parameters listed in Table 5.1. Apart from the machine model, all the others are built by discrete blocks with a sampling frequency 40kHz (same as the PWM frequency).

The following simulation scenarios analyse the system stability under different conditions such as MRAS PI parameters, order of MRAS adaptive model, different iq currents, etc. However, they share the same format: firstly derive the stability result from the small-signal-based state evolution equation and then use the simulation to validate the system stabilities and compared with small-signal-based analysis results.

5.2.2 Stability Analysis of MRAS System with 1st-Order Adaptive Model

The MRAS sensorless algorithm is first proposed in the s-domain. It has been proved in [26] that the MRAS sensorless algorithm is always stable no matter how much the k_{pm} and k_{im} of MRAS PI controller are selected, but this is an ideal situation without consideration of real application constraints such as control delay, voltage saturation, etc. In fact, there must be some limitations of MRAS PI parameters selection due to the relatively large control delay in high speed. In this section, the system stability with 1st-order MRAS adaptive model will be analysed at different MRAS PI parameters (k_{pm}, k_{im}), providing guidance for the parameters selection.

5.2.2.1 Stable Area of MRAS System with 1st-Order Adaptive Model

As the key point of this section is focused on the MRAS PI parameters (k_{pm} and k_{im}), i_d^* and i_q^* are set to 0A where the machine is running at idle mode without any loads. Using the small-signal-based stability analysis method in Section 5.1, a 3D map in Fig 5.4 is obtained to display the stable area (i.e. maximum eigenvalue<1) at different speeds. It can be seen the stable area shrinks when speed increases. This means that without a proper selection of k_{pm} and k_{im}, the system may only stable at low speed and become unstable at a higher speed. As can be seen in Fig 5.4, when the speed is 6krpm, almost all k_{pm} (range from 1 to 6) and k_{im} (range from 0 to 14,000) combinations can make the system stable. These areas have already significantly reduced when the speed increases to 7krpm. When the speed goes beyond 10krpm, the stable areas of k_{pm}, k_{im} combinations become relatively unchanged.

The red line area In Fig 5.4 represents the overlapped stable area at all different speeds. The k_{pm}, k_{im} combinations within this area are suggested for selection as they

can make the system stable at a wider speed range. This figure gives a guideline for control parameter selection to avoid any potentially unstable conditions.

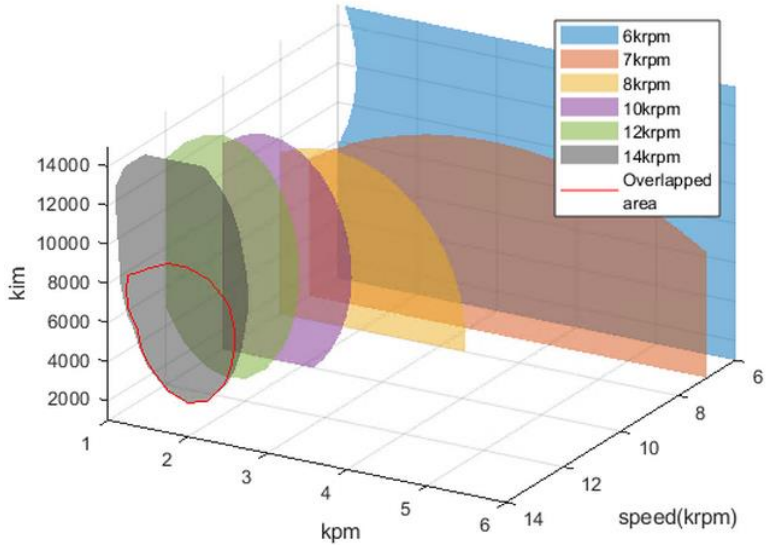


Fig 5.4. The stable area of k_{pm} and k_{im} selection at different speeds for the 1st-order adaptive model

To provide a better guideline of k_{pm} and k_{im} selection, a maximum eigenvalue map in Fig 5.5 is given. The colour represents the maximum eigenvalues at all speed ranges from 6krpm to 14krpm. The steady area is inside the contour line of 1.0 and it is located between $k_{pm} = 1.5 - 2.5$ and $k_{im} = 3000 - 10000$. Therefore, k_{pm} and k_{im} can be selected from this area.

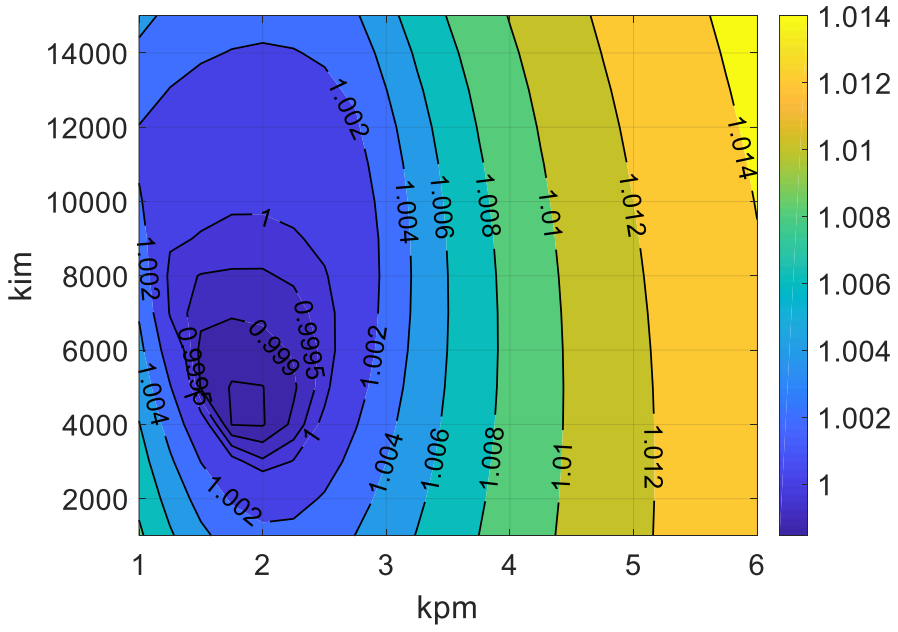


Fig 5.5. The maximum eigenvalues map for the 1st-order adaptive model at all speeds

5.2.2.2 Stability Simulation of MRAS System with 1st-Order Adaptive Model

The stable area shown in Fig 5.4 and Fig 5.5 is calculated from the small-signal-based stability analysis method in section 5.1. This section is going to validate the stability analysis result above by simulation studies.

Fig 5.6 shows the maximum eigenvalue contour lines in different k_{pm} and speed with $k_{im} = 5000$. The red line represents the contour line of 1.0, which is the boundary of the stable operation area. It can be seen that the unstable area is located in the top right corner where is with a higher speed and a bigger k_{pm}. This makes sense because: 1) the control delay deteriorates performance further at higher speed; 2) larger controller gain (k_{pm}) will also cause stability issues. To validate the proposed small-signal model, eight operating points (i.e., a,b,c,d,e,f,g,h) around the red line are selected (detailed parameters listed in Table 5.4) to conduct simulations in the model given in Fig 5.6.

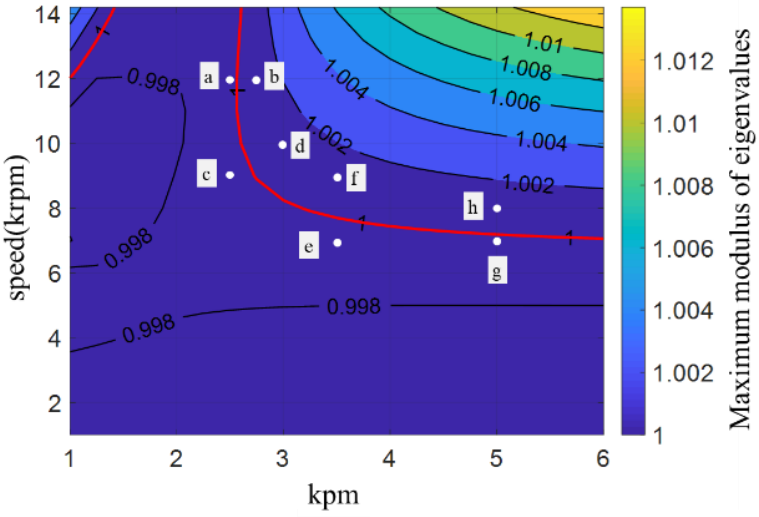


Fig 5.6. The maximum eigenvalue map with k_{im}=5000 for the 1st-order adaptive model

Table 5.4. Selected operating points parameters for 1st-order adaptive model

Operating point	k_{pm}	speed(krpm)	Position in Fig 5.6
a	2.5	12	Stable area
b	2.75	12	Unstable area
c	2.5	9	Stable area
d	3	10	Unstable area
e	3.5	7	Stable area
f	3.5	9	Unstable area
g	5	7	Stable area
h	5	8	Unstable area

The simulation waveforms at those 8 operating points are demonstrated in Fig 5.7. The k_{pm}, as well as the actual and estimated speed, are given in each simulation. It is obvious that the estimated speeds at operating points a,c,e, and g are convergent, but the estimated speeds at operating points b,d,f, and h are divergent. This is exactly what is expected from Fig 5.6. Therefore, the simulation results validate the correctness of the proposed state evolution equation.

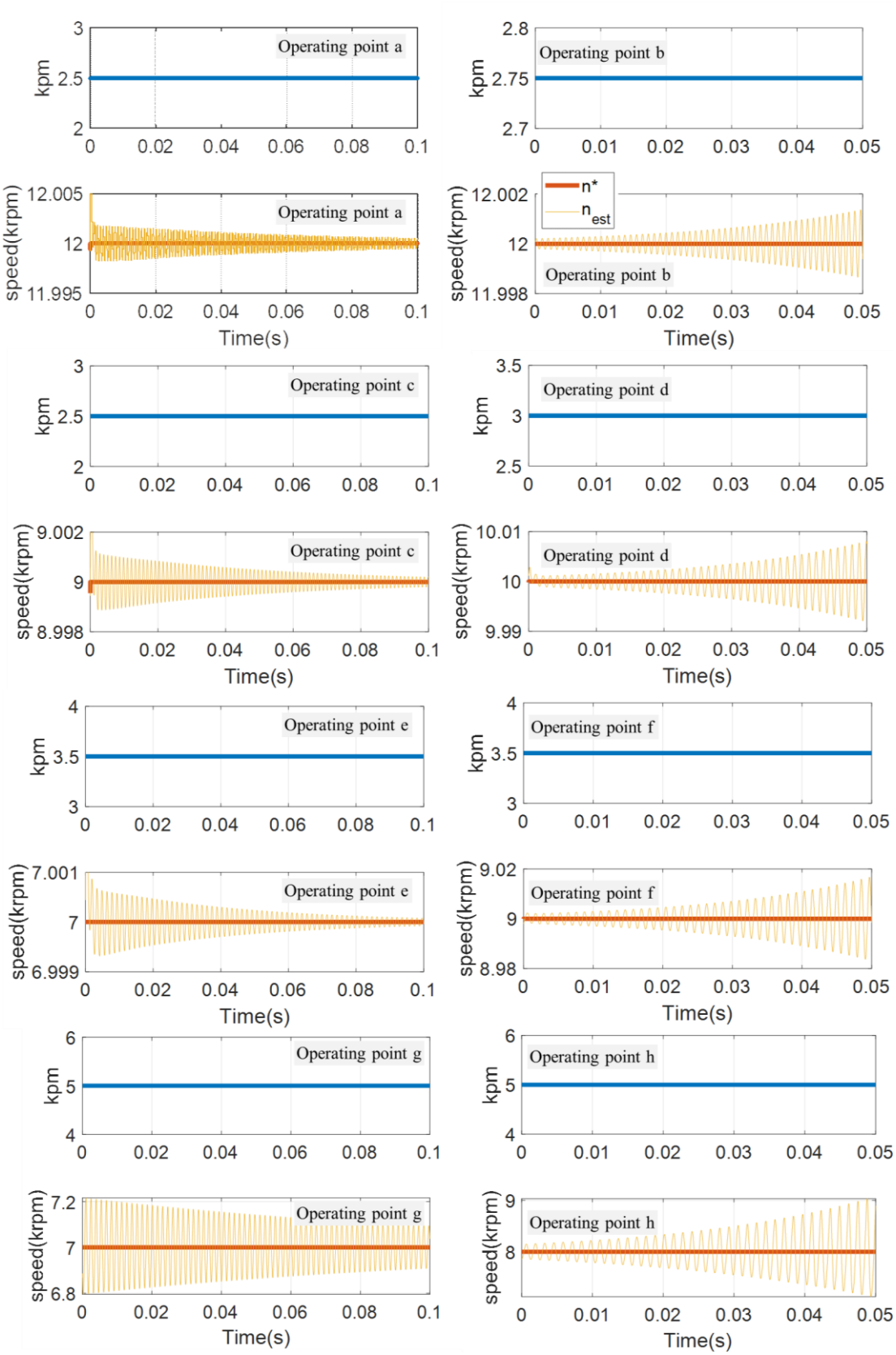


Fig 5.7. Stability simulation results at the 8 operating points in Fig 5.6

5.2.3 Stability Analysis of MRAS System with 2nd-Order Adaptive Model

In section 4.3.2.1, the MRAS adaptive model has two types of small-signal expressions. Depending on the linearization method to the exponential term $\boldsymbol{e}^{\widehat{\boldsymbol{A}}(k)T_s}$, they can be named as 1st-order MRAS adaptive model and 2nd-order MRAS adaptive model respectively.

Although the last section has displayed the stable area of MRAS sensorless control with the 1st-order adaptive model, this stable area will shrink furthermore when considering different i_q and estimated machine parameters ($\hat{R}, \hat{L}, \hat{\varphi}_f$). It is even possible that no stable k_{pm} and k_{im} is available for the 1st-order adaptive model.

Therefore, this section will demonstrate the stable area of MRAS sensorless control with a 2nd-order adaptive model as well as the simulation results.

5.2.3.1 Stable Area of MRAS System with 2nd-Order Adaptive Model

Using the small-signal-based stability analysis method in section 5.1, a 3D map in Fig 5.8 is obtained to display the stable area (maximum eigenvalue<1) at different speeds with the 2nd-order MRAS adaptive model used. As can be seen from it, the stable area shrinks with speed increasing. At the highest speed (14krpm), any k_{pm} higher than 3.5 is unstable no matter how much k_{im} is, but the selection of stable k_{im} at 14krpm is more flexible. So, the system stability is more sensitive to k_{pm} at high speed.

The red line area in Fig 5.8 represents the overlapped stable area at all different speeds. The k_{pm}, k_{im} combinations within this area are suggested for selection as they can make the system stable at a wider speed range. This figure guides control parameters selection and avoiding the possible danger compared with the trial-and-error method in real high-speed tests.

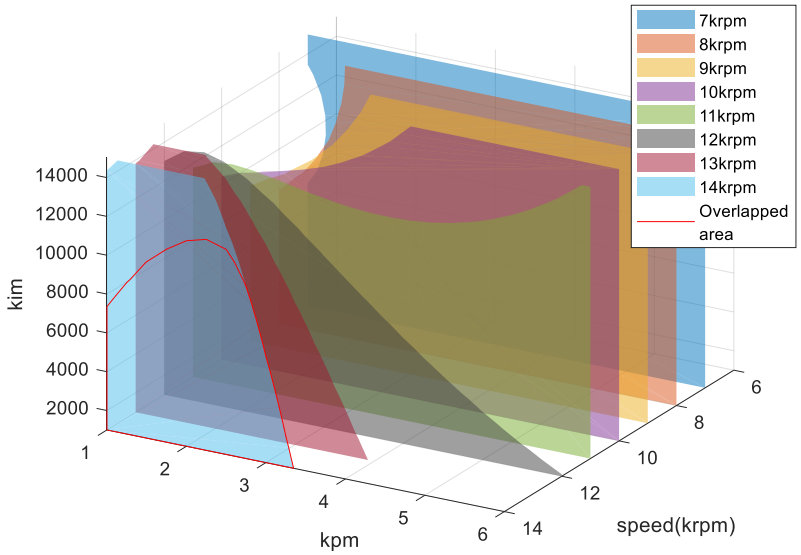


Fig 5.8. The stable area at different speeds for the 2nd-order adaptive model

Similar to the last section 5.2.2, the data to plot Fig 5.8 is processed by calculating the maximum eigenvalue at the same k_{pm} and k_{im} but with all different speed from 7krpm to 14krpm. Then a new maximum eigenvalue map as Fig 5.9 is derived. The contour line of 1.0 is exactly the boundary of the overlapped area in Fig 5.8. The contour lines in Fig 5.9 show the stability trend of the system with the 2nd-order adaptive model, telling engineers which area has a larger stable margin.

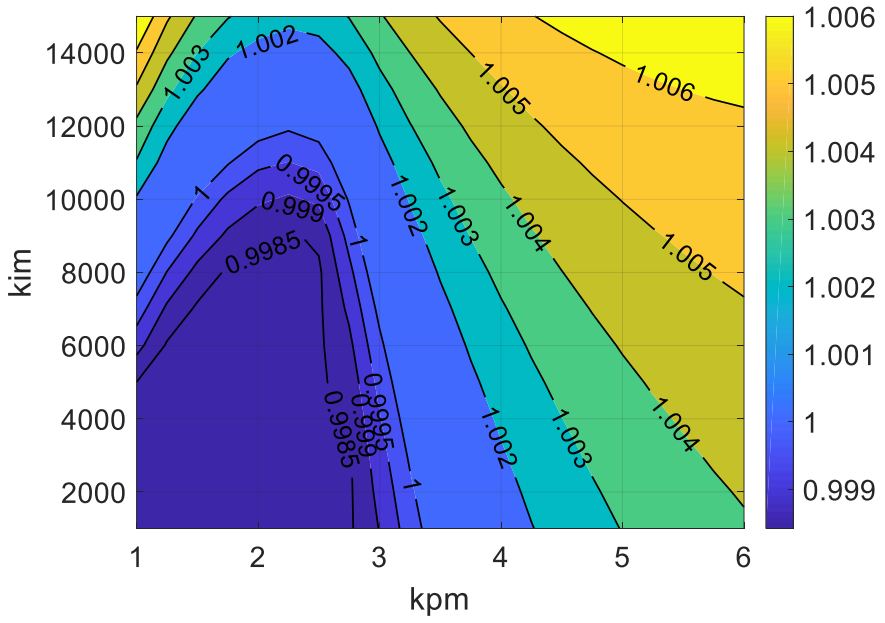


Fig 5.9. The maximum eigenvalues map for the 2st-order adaptive model at all speeds

5.2.3.2 Stability Simulation of MRAS System with 2nd-Order Adaptive Model

This section will validate the stability area with the 2nd-order adaptive model by simulation. To achieve this, a maximum eigenvalue map with different k_{pm} and k_{im} at 14krpm is given by Fig 5.10 first. The red lines represent the stable boundaries, and 8 operating points around the boundary (i.e., a,b,c,d,e,f,g,h) are selected as simulation points to validate the system stability. These 8 points are marked in Fig 5.10, and the k_{pm} and k_{im} of them are listed in Table 5.5.

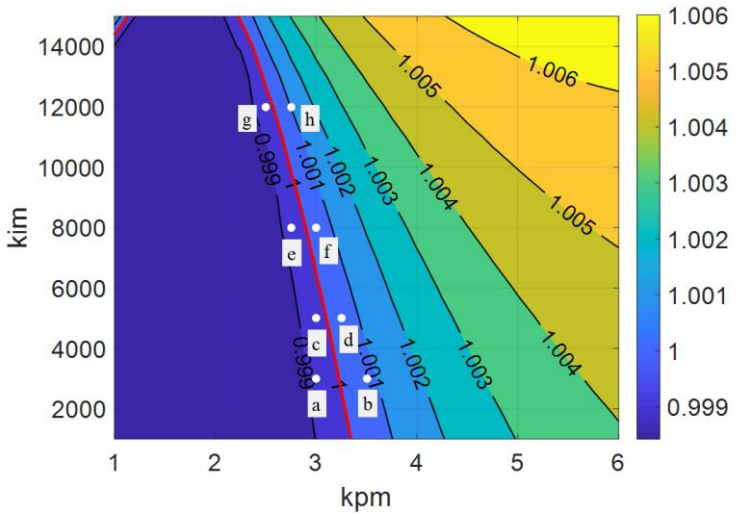


Fig 5.10. The maximum eigenvalue map at 14krpm for the 2nd-order adaptive model

Table 5.5. Selected operating points parameters for 2nd-order adaptive model

Operating point	k_{pm}	k_{im}	Position in Fig 5.10
a	3	3000	Stable area
b	3.5	3000	Unstable area
c	3	5000	Stable area
d	3.25	5000	Unstable area
e	2.75	8000	Stable area
f	3	8000	Unstable area
g	2.5	12000	Stable area
h	2.75	12000	Unstable area

Simulations at the 8 operating points are conducted on the Simulink model discussed in Section 5.2.1 and their results are shown in Fig 5.11. The speed reference (n*), estimated speed (n_{est}), and MRAS error (e) at each operating point are demonstrated. As can be seen from it, the n_{est} and e waveforms are convergent at operating points a,

c, e, g, but divergent at operating points b, d, f, h. These simulation results match well with the operating point locations in Fig 5.10, which proves the correctness of the 2nd-order adaptive model-based current close-loop system.

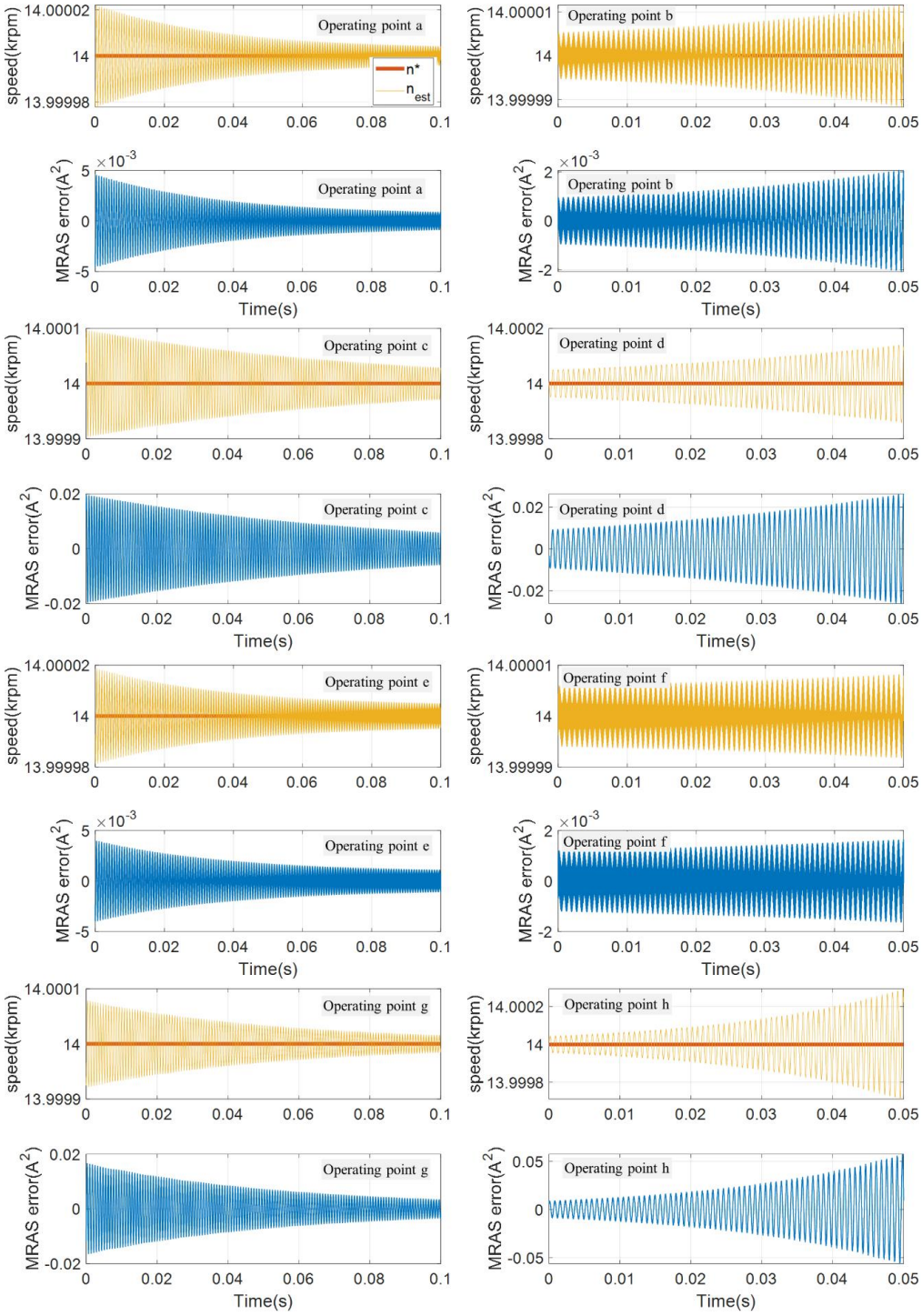


Fig 5.11. Stability simulation results at the 8 operating points in Fig 5.10

5.2.4 Stability Comparison of 1st- and 2nd-Order MRAS Adaptive Model

To compare the performance of 1st and 2nd-order MRAS adaptive models, the stable boundary in Fig 5.5 and Fig 5.9 are plotted together in Fig 5.12 below. The red line represents the stable area boundary of the current closed-loop system with the 1st-order MRAS adaptive model at the whole speed range, and the blue line represents the stable boundary of the same system with the same speed range but with the 2nd-order MRAS adaptive model. It is obvious from it that the 2nd-order adaptive model has a larger stable area of MRAS PI parameters than the 1st-order adaptive model. Although the 2nd-order adaptive model is more complicated and consumes more controller time (about 3us), it is still preferable for our application as the microcontroller we used can handle the increasing computation.

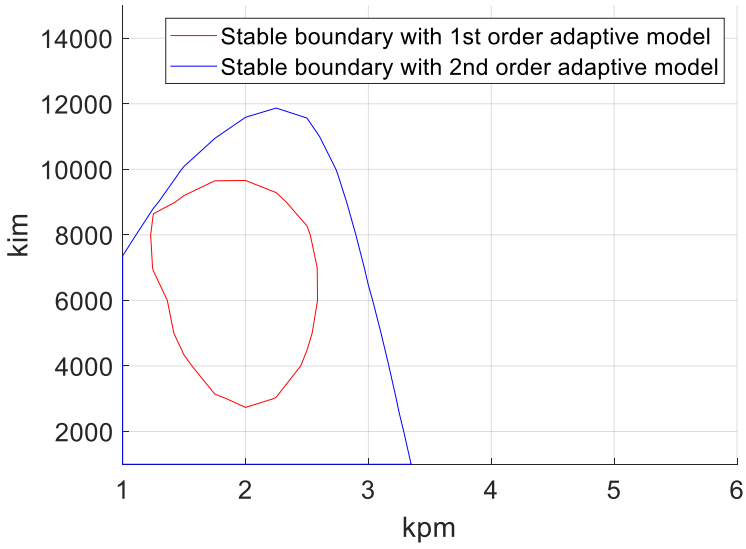


Fig 5.12. Stable area comparison of 1st and 2nd-order adaptive model with speed between 7-14krpm

There are 3 parameters (i.e., k_{pm}, k_{im}, speed) required to be determined in the simulation, but the unstable area in Fig 5.12 does not indicate which speed this system will be unstable for a given set of k_{pm} and k_{im}. Therefore, we fix the $k_{im} = 5000$ and derive the Fig 5.13 which shows the stable areas of the current closed-loop system for

different k_{pm} and speed using 1st and 2nd-order MRAS adaptive model design. For comparison studies, four operating points (i.e., a, b, c, d) are selected as simulation scenarios and all of them are located inside the stable area of the 2nd-order adaptive model but outside the stable area of the 1st-order adaptive model. The parameters of the four operating points are listed in Table 5.6.

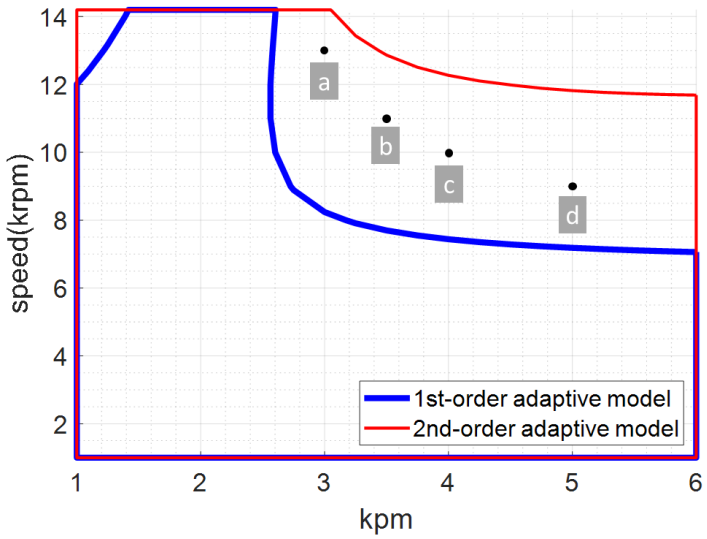


Fig 5.13. Stable area comparison of 1st and 2nd-order adaptive model with k_{im}=5000

Table 5.6. Operating points selections for 1st and 2nd-order adaptive models comparison

Operating point	k_{pm}	k_{im}	Speed (krpm)	Stability for 1st-order adaptive model	Stability for 2nd-order adaptive model
a	3	5000	13	unstable	stable
b	3.5	5000	11	unstable	stable
c	4	5000	10	unstable	stable
d	5	5000	9	unstable	stable

The simulation results at these 4 operating points for the 1st and 2nd-order MRAS adaptive model are demonstrated in Fig 5.14. Figures on the left column show the estimated speed and MRAS error using1st-order MRAS adaptive model. It can be seen that the variables are divergent at all 4 points as the operating point locations outside the 1st-order MRAS adaptive model stable range in Fig 5.13. However, the figures on the right show the convergent estimated speed and MRAS error at all 4 points with the 2nd-order MRAS adaptive model as these four points are within the stable boundary of this method in Fig 5.13. Above all, all the simulation results in Fig 5.14 are consistent

with the stable area shown in Fig 5.13, proving the superiority of the 2nd-order MRAS adaptive model.

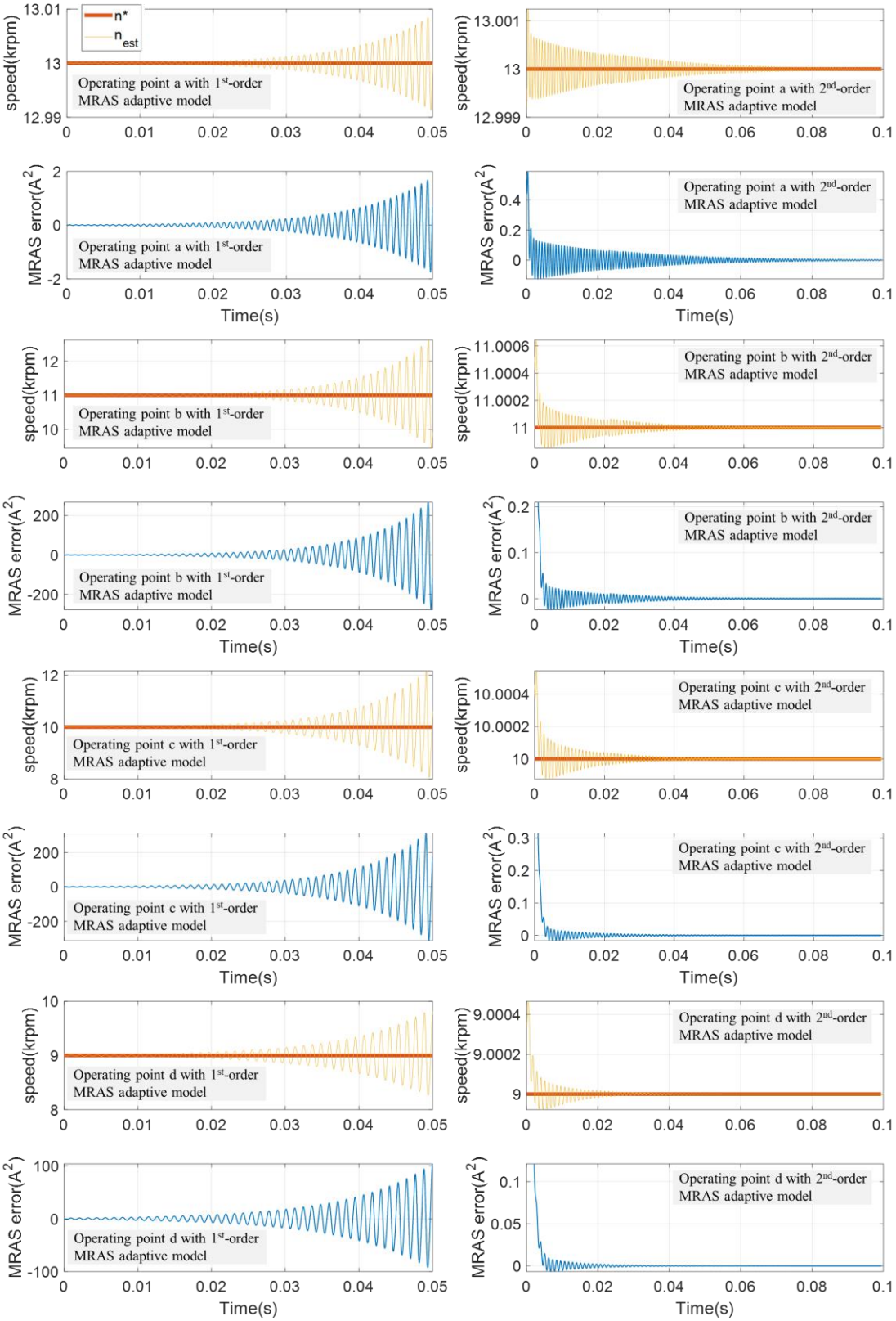


Fig 5.14. Stability simulation results at 4 different operating points (a,b,c,d) in Fig 5.13.

Left column: results from 1st-order MRAS adaptive model; Right column: results from 2nd-order MRAS adaptive model

5.2.5 Stability Comparison with Different Q-Axis Current

All discussions above are under the condition of $i_d = i_q = 0\text{A}$. In this section, the stability performances of the current closed-loop MRAS sensorless system with different i_q currents are analysed. The i_d current is always zero as there is no need for flux weakening for the studied machine.

Based on the analysis in previous sections, the 2nd-order MRAS adaptive model has a larger stable area compared with the 1st-order MRAS adaptive model. As different i_q may cause further shrink of stable area, it is wiser to choose the 2nd-order adaptive model for MRAS sensorless control.

Using the maximum-eigenvalue-based stability analysis method proposed in section 5.1, the stable boundaries at 14krpm with different iq are shown in Fig 5.15. Both positive and negative i_q are considered because machine will work both in motoring and generating modes. It is obvious from Fig 5.15 that the stable area with $i_q = -20\text{A}$ is the largest. With the increasing of current i_q, the stable area will shrink. This indicates i_q will certainly influence the system stability, so the selection of proper MRAS PI parameters should be based on the most severe condition (maximum i_q).

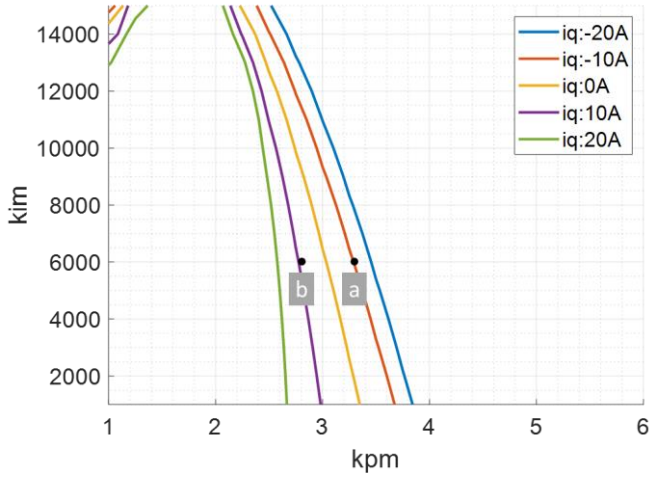


Fig 5.15. Stable boundaries with different iq when speed is 14krpm

To validate the correctness of the conclusion derived above, simulation at the two operating points 'a' and 'b' in Fig 5.15 are conducted with the results shown in Fig 5.16. Table 5.7 list the operating situations and control parameters in the different time slot of Fig 5.16 to provide a clear view. At operating point 'a', simulation with $i_q = -20\text{A}$ (0-0.1s) is stable but unstable with $i_q = 0\text{A}$ (0.15s-0.2s), which is consistent with the point 'a' location in Fig 5.15 (inside blue line but outside yellow line). Similar result is obtained at operating point 'b', where the simulation waveform is stable with $i_q = 0\text{A}$ (0.25s-0.3s) but unstable with $i_q = 20\text{A}$ (0.4s-0.45s), matching with the location of operating point 'b' in Fig 5.15 (inside the yellow line but outside the green line).

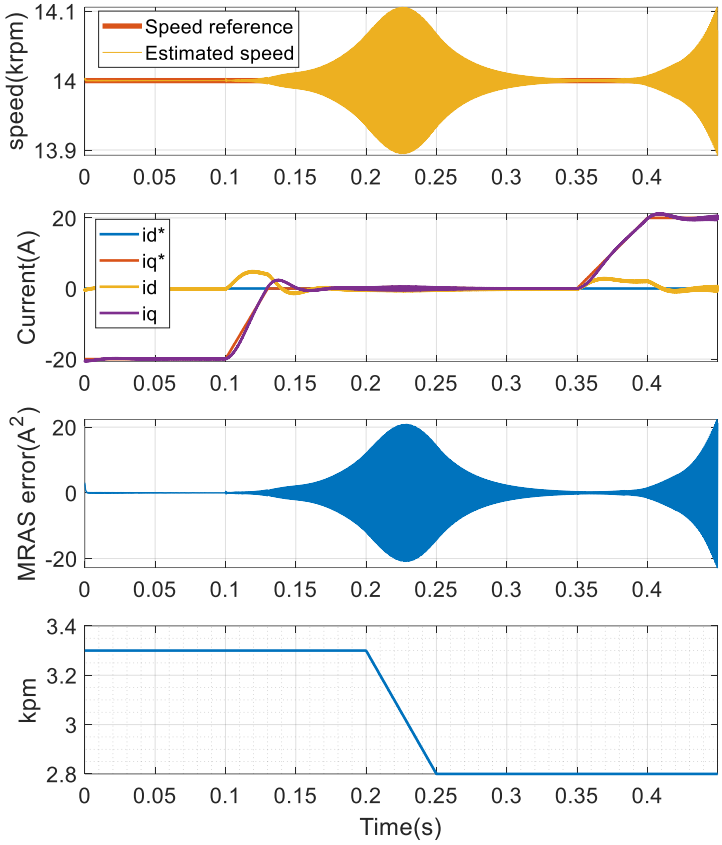


Fig 5.16. Stability simulation results at operating point a and b in Fig 5.15

Table 5.7. Operating situations and control parameters in the different time slots of Fig 5.16

Time(s)	Operating point	k_{pm}	k_{im}	Speed (krpm)	Iq(A)	Stability
0-0.1	a	3.3	6000	14	-20	Stable
0.15-0.2	a	3.3	6000	14	0	Unstable
0.25-0.35	b	2.8	6000	14	0	Stable
0.4-0.45	b	2.8	6000	14	20	Unstable

5.2.6 Machine Parameters Impacts on MRAS Sensorless Control Stabilities

5.2.6.1 MRAS Estimated Position Error Analysis

In the MRAS sensorless algorithm, the machine parameters such as phase resistance, inductance and stator flux linkage will be used to build the adaptive model and control rule. However, these machine parameters vary with temperature, stator steel saturation, etc. The machine parameters for the MRAS algorithm are normally based on the static

measurement results, which may have discrepancies with the actual parameters experiment. These differences may further cause the estimated rotor position error in the MRAS control. As the estimated rotor position is applied to the transformations of voltages and currents, it will cause mismatches between current/voltage references and their actual values. All these effects may further affect the stability of the entire motor drive system.

In this section, the MRAS estimated position error caused by the machine parameters mismatch will be analysed. Once the sensorless control parameters (i.e., $k_{pm}, k_{im}, \hat{R}, \hat{L}, \hat{\varphi}_f$) and operation points ($i_d^*, i_q^*$, n) are determined, the estimated position error ($\theta_{\Delta equ} = \hat{\theta} - \theta$) can be calculated in Appendix B.III. To validate the calculation results, simulations with the same control parameters and operation points are conducted in the Simulink model mentioned in Section 5.2.1. The comparisons of calculation and simulation results of the estimated position error are demonstrated in Fig 5.17-Fig 5.19.

The mismatched parameters include estimated permanent magnet flux linkage($\hat{\varphi}_f$) in Fig 5.17, estimated d-/q-axis inductance($\hat{L}$) in Fig 5.18, and estimated phase resistance($\hat{R}$) in Fig 5.19. It can be seen from Fig 5.17-Fig 5.19 that the position errors from calculation using analytical models well match the position errors from simulation studies.

From Fig 5.17-Fig 5.19, it can be observed that the position error will increase with larger machine parameters mismatch. This indicates the importance of machine parameter estimation accuracy for MRAS sensorless control. We can also conclude from Fig 5.17-Fig 5.19 that larger estimated position errors come with larger current iq magnitudes. The position error is around zero when $i_d = i_q = 0$A, no matter how much of parameter mismatch ratio. Furthermore, we can see in Fig 5.19 that phase resistance

mismatch has little influence on estimated position error compared with the other two factors (permanent magnet flux linkage and d-/q-axis inductance). This is because the analysis is conducted under high-speed (n=14krpm) and the voltage drop on resistance is relatively small.

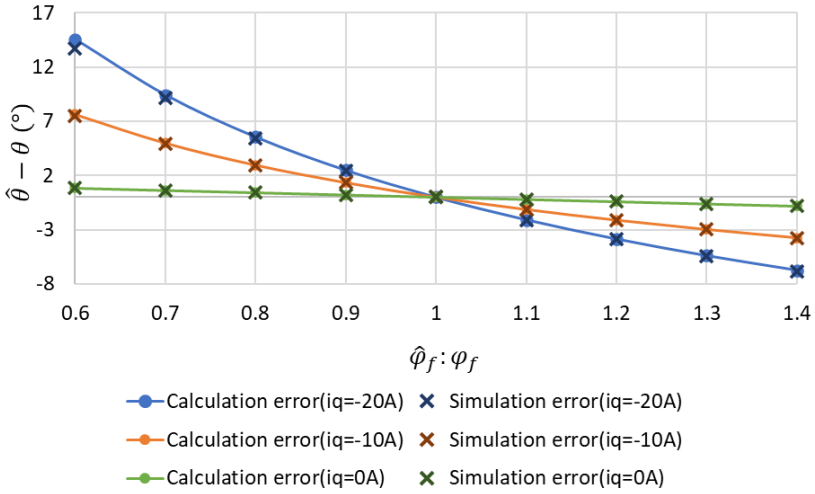


Fig 5.17. Relation between estimated position error and different ratio of estimated to actual permanent magnet flux linkage under n=14krpm, id=0A

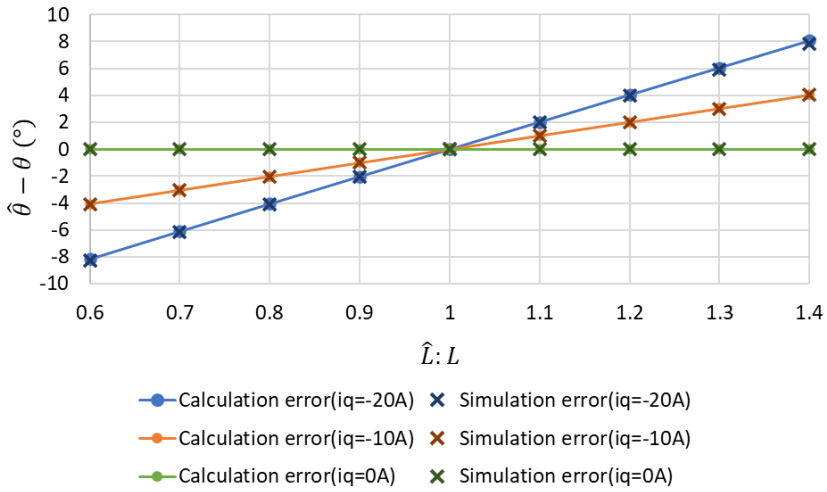


Fig 5.18. Relation between estimated position error and different ratio of estimated to actual d-/q-axis inductance under n=14krpm, id=0A

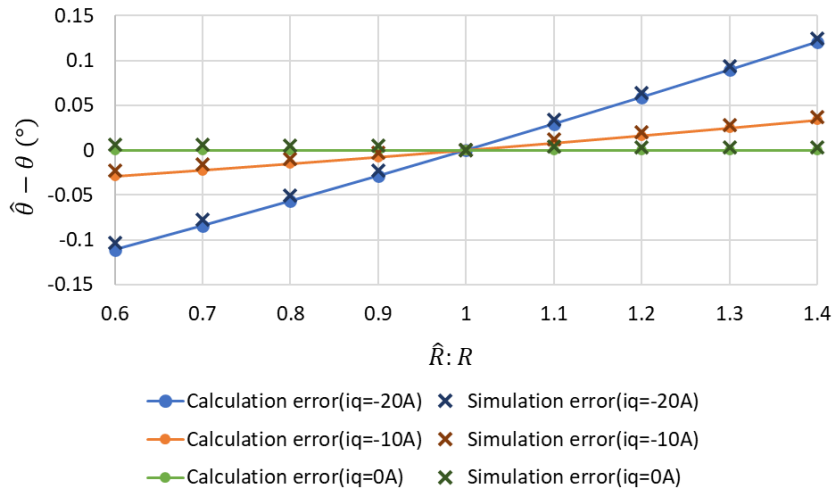


Fig 5.19. Relation between estimated position error and different ratio of estimated to actual phase resistance under n=14krpm, id=0A

5.2.6.2 Stability with Different Estimation Error of Permanent Magnet Flux Linkage

From the previous section, it has been noticed that with machine parameter errors in the reference model, there will be rotor position estimation errors in the MRAS control. As a result, the stable area of the current closed-loop system may also change when MRAS sensorless algorithm is implemented with machine parameter errors in the reference model. In this section, the impact on stability by different estimation errors of permanent magnet flux linkage (indicated by $\hat{\varphi}_f : \varphi_f$) will be discussed.

In Fig 5.20, the stable areas with different $\hat{\varphi}_f : \varphi_f$ ratio at n=14 krpm and $i_d^* = i_q^* = 0A$ are displayed. The orange line and orange area represent the stable boundary and stable area of $\hat{\varphi}_f : \varphi_f = 1.0$, which is a benchmark for comparison. It shows the stable area expands with the increasing of $\hat{\varphi}_f : \varphi_f$ (e.g., 1.2, 1.4), especially on the top area in Fig 5.20 (k_{im}>10000). For the condition of $\hat{\varphi}_f : \varphi_f = 0.6$, there is an unexpected stable area appears on the right of Fig 5.20, but the common stable area is located on the bottom-left of Fig 5.20 where has small k_{pm} and k_{im}.

To validate the stable area in Fig 5.20, simulations are conducted at 4 operating points

(i.e., a, b, c, d). The simulation results are shown and discussed below.

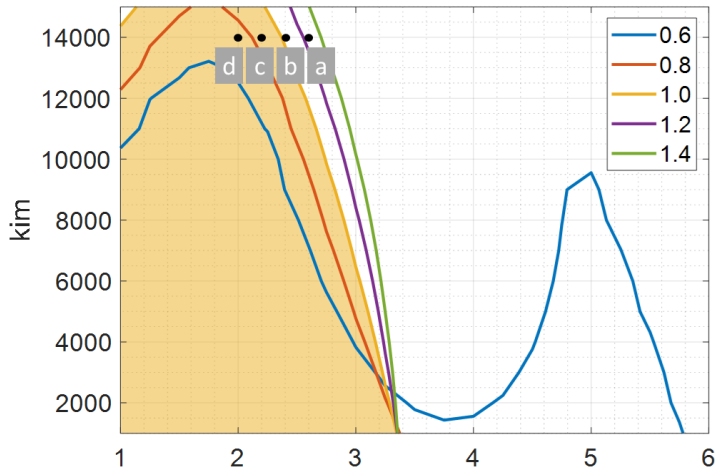


Fig 5.20. Stability area with different $\hat{\varphi}_f : \varphi_f$ ratio at n=14krpm and i_q^*=0A

The simulation result at operating point 'a' is shown in Fig 5.21. During the simulation period, the machine speed is set to 14krpm and i_d^*, i_q^* are set to 0A. The k_{pm} and k_{im} are selected as 2.6 and 14000 matching with the location of operating point 'a'. As can be seen from the simulation waveform, the $\hat{\varphi}_f : \varphi_f$ changes from 1.4 to 1.2 between 0.2s-0.3s. When $\hat{\varphi}_f : \varphi_f = 1.4$, all of the estimated speed, currents and MRAS errors converge to steady states gradually. However, when $\hat{\varphi}_f : \varphi_f = 1.2$, all of them start to oscillate and become divergent. The simulation result matches the location of point 'a' in Fig 5.20, inside the stable boundary of $\hat{\varphi}_f : \varphi_f = 1.4$ but outside the boundary of $\hat{\varphi}_f : \varphi_f = 1.2$.

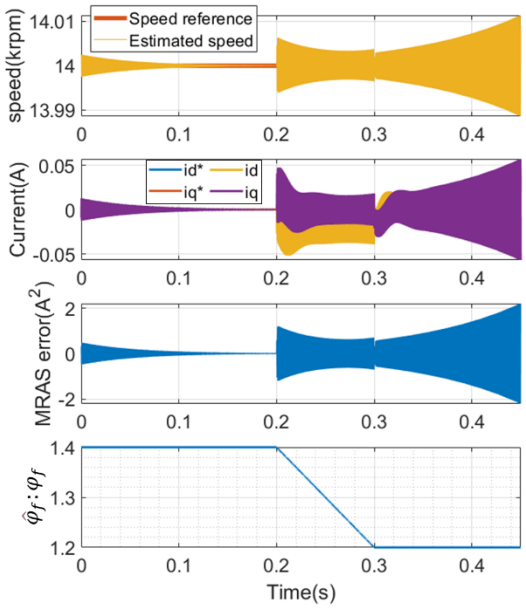


Fig 5.21. Simulation result at operating point 'a' in Fig 5.20 with k_{pm}=2.6, k_{im}=14000

The simulation results at the other 3 operating points (i.e., b, c, d) are demonstrated in Fig 5.22-Fig 5.24 respectively. The speed and d/q-axis current commands are set the same with the simulation scenario at point a. The k_{pm} and k_{im} are selected based on the operating points location in Fig 5.20. The waveform in Fig 5.22 proves the operating point 'b' is stable with $\hat{\varphi}_f : \varphi_f = 1.2$ but unstable with $\hat{\varphi}_f : \varphi_f = 1.0$. The waveform in Fig 5.23 proves the operating point 'c' is stable with $\hat{\varphi}_f : \varphi_f = 1.0$ but unstable with $\hat{\varphi}_f : \varphi_f = 0.8$. The waveform in Fig 5.24 proves the operating point 'd' is stable with $\hat{\varphi}_f : \varphi_f = 0.8$ but unstable with $\hat{\varphi}_f : \varphi_f = 0.6$. All these simulation results match with their operating points location in Fig 5.20. Therefore, Fig 5.21-Fig 5.24 validate the stable boundaries with different $\hat{\varphi}_f : \varphi_f$ ratio in Fig 5.20.

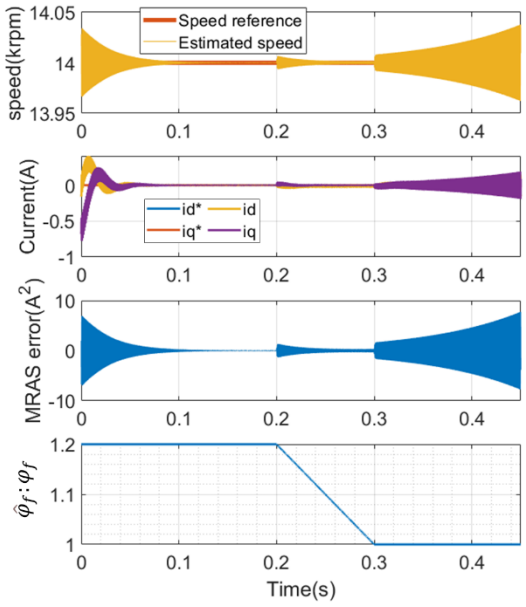


Fig 5.22. Simulation result at operating point 'b' in Fig 5.20 with k_{pm}=2.4, k_{im}=14000

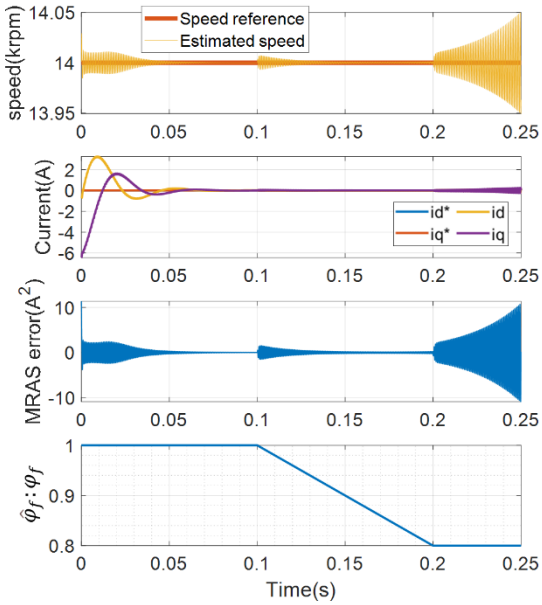


Fig 5.23. Simulation result at operating point 'c' in Fig 5.20 with k_{pm}=2.2, k_{im}=14000

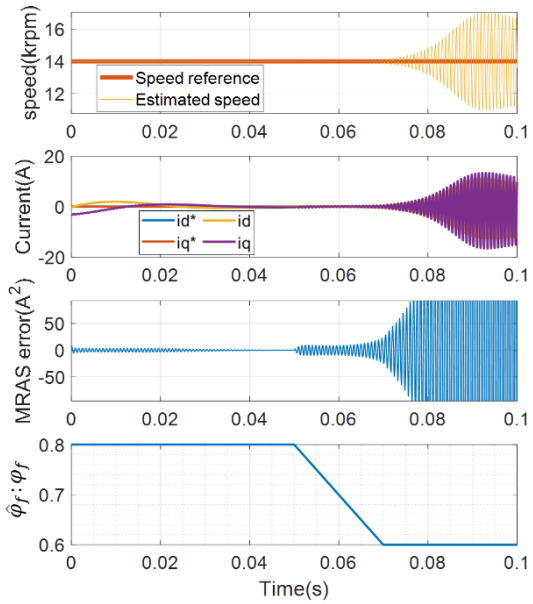


Fig 5.24. Simulation result at operating point 'd' in Fig 5.20 with k_{pm}=2, k_{im}=14000

5.2.6.3 Stability with Different Estimation Error of d/q-Axis Inductances

Apart from the estimation error of permanent magnet flux linkage, the estimation error of d/q-axis inductances will also affect the stable area of the current closed-loop system. In this section, the impact on stability by different estimation errors of d/q-axis inductances (indicated by $\hat{L}: L$) will be discussed.

In Fig 5.25, the stable areas with different $\hat{L}: L$ ratio at n=14krpm, $i_d^* = 0A$, and $i_q^* = -20A$ are displayed, which is based on the method in Section 5.1. The orange line and orange area represent the stable boundary and stable area of $\hat{L}: L = 1.0$, which is a benchmark for comparison. It shows the stable area expands with the increasing of $\hat{L}: L$ (e.g., 1.2, 1.4), especially on the top area in Fig 5.25 with larger k_{im}. Whilst the stable area shrinks with $\hat{L}: L$ going down from 1.0.

To validate the stable area in Fig 5.25, simulations are conducted at 4 operating points (i.e., a, b, c, d). The simulation model has been discussed in Section 5.2.1. The simulation results are shown and discussed below.

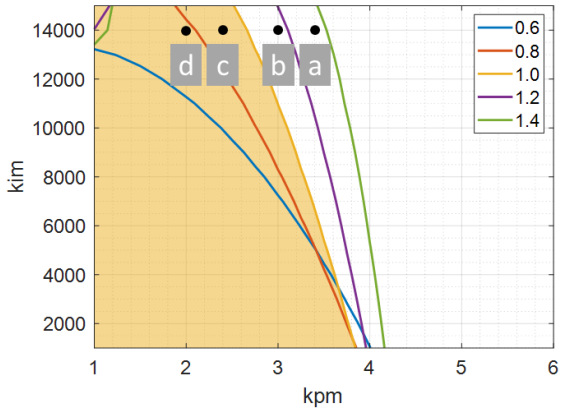


Fig 5.25. Stability area with different $\hat{L}: L$ ratio at n=14krpm and i_q^*=-20A

The simulation result at operating point 'a' is shown in Fig 5.26. During the simulation period, the machine speed is set to 14krpm and i_d^*, i_q^* are set to 0A and -20A separately. The k_{pm} and k_{im} are selected as 3.4 and 14000 matching with the location of operating point 'a'. As can be seen from the simulation waveform, the $\hat{L}: L$ changes from 1.4 to 1.2 between 0.03s-0.05s. When $\hat{L}: L = 1.4$, all of the estimated speed, currents and MRAS errors converge to steady states gradually. However, when $\hat{L}: L = 1.2$, all of them start to oscillate and become divergent. The simulation result matches the location of point 'a' in Fig 5.25, inside the stable boundary of $\hat{L}: L = 1.4$ but outside the boundary of $\hat{L}: L = 1.2$.

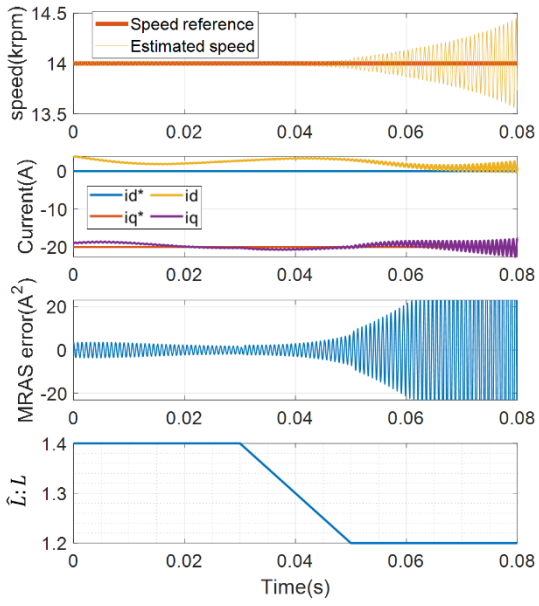


Fig 5.26. Simulation result at operating point 'a' in Fig 5.25 with k_{pm}=3.4, k_{im}=14000

The simulation results at the other 3 operating points (i.e., b, c, d) are demonstrated in Fig 5.27-Fig 5.29 respectively. The speed and d/q-axis current commands are set the same with the simulation scenario at point a. The k_{pm} and k_{im} are selected based on the operating points location in Fig 5.25. The waveform in Fig 5.27 proves the operating point 'b' is stable with $\hat{L}: L = 1.2$ but unstable with $\hat{L}: L = 1.0$. The waveform in Fig 5.28 proves the operating point 'c' is stable with $\hat{L}: L = 1.0$ but unstable with $\hat{L}: L = 0.8$. The waveform in Fig 5.29 proves the operating point 'd' is stable with $\hat{L}: L = 0.8$ but unstable with $\hat{L}: L = 0.6$. All these simulation results match with their operating points location in Fig 5.25. Therefore, Fig 5.26-Fig 5.29 validate the stable boundaries with different $\hat{L}: L$ ratio in Fig 5.25.

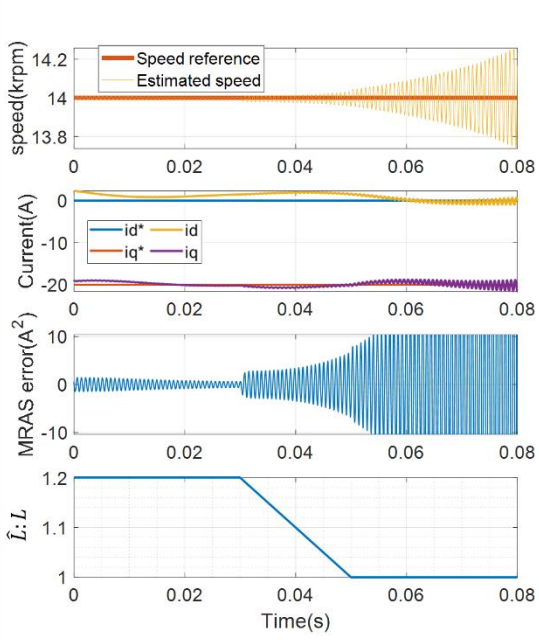


Fig 5.27. Simulation result at operating point 'b' in Fig 5.25 with k_{pm}=3, k_{im}=14000

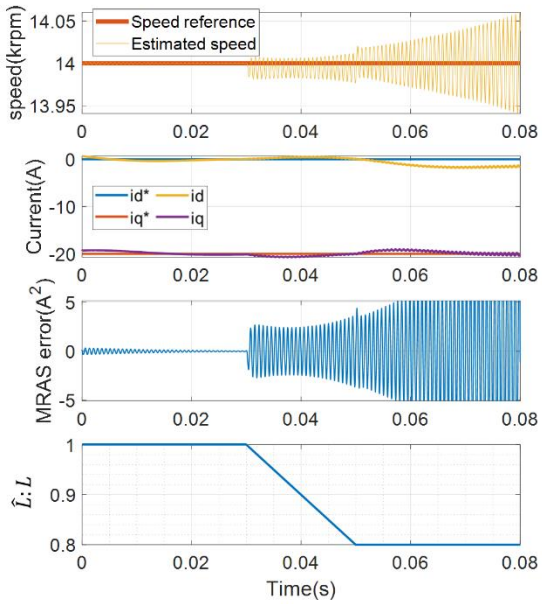


Fig 5.28. Simulation result at operating point 'c' in Fig 5.25 with k_{pm}=2.4, k_{im}=14000

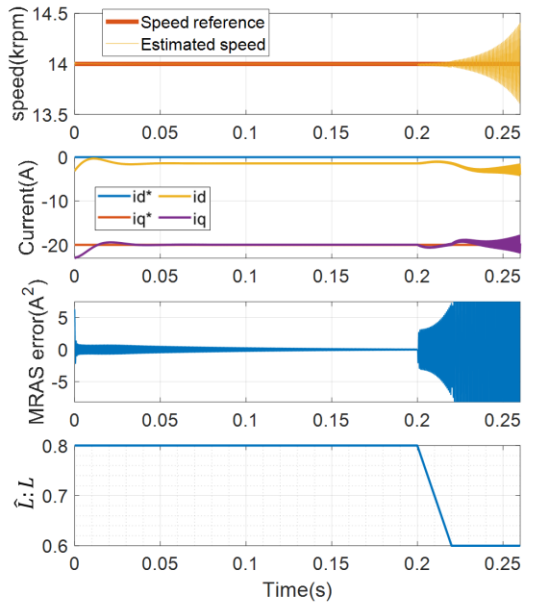


Fig 5.29. Simulation result at operating point 'd' in Fig 5.25 with k_{pm}=2, k_{im}=14000

5.2.6.4 Stability with Different Estimation Error of Phase Resistance

In this section, the impact on the stable area by different estimation errors of phase resistance (indicated by $\hat{R}:R$) will be analysed.

In Fig 5.30, the stable areas with different $\hat{R}:R$ ratio at n=14krpm, $i_d^* = 0A$, and $i_q^* = 20A$ are displayed, which is based on the method in Section 5.1. The orange line and orange area represent the stable boundary and stable area of $\hat{R}:R = 1.0$, which is a

benchmark for comparison. It shows the stable area shrinks with the increasing of $\hat{R}:R$ from 0.6 to 1.4.

To validate the stable area in Fig 5.30, simulations are conducted at 4 operating points (i.e., a, b, c, d). The simulation model has been discussed in Section 5.2.1. The simulation results are shown and discussed below.

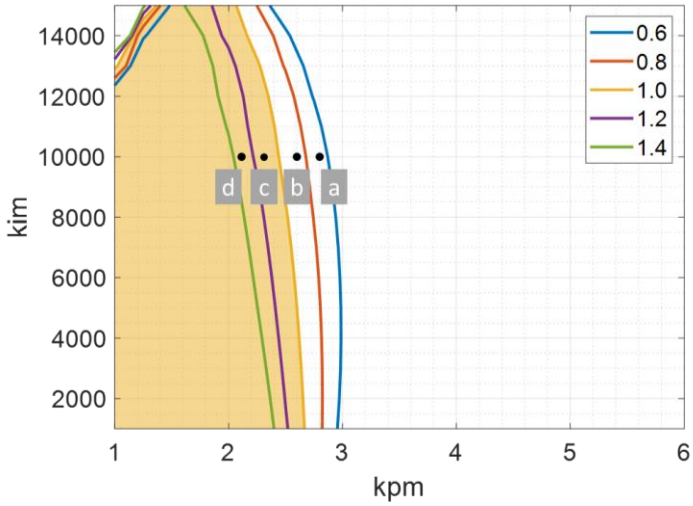


Fig 5.30. Stability area with different $\hat{R}:R$ ratio at n=14krpm and i_q^*=20A

The simulation result at operating point 'a' is shown in Fig 5.31. During the simulation period, the machine speed is set to 14krpm and i_d^*, i_q^* are set to 0A and 20A separately. The k_{pm} and k_{im} are selected as 2.8 and 10000 matching with the location of operating point 'a'. As can be seen from the simulation waveform, the $\hat{R}:R$ changes from 0.6 to 0.8 between 0.1s-0.12s. When $\hat{R}:R = 0.6$, all of the estimated speed, currents and MRAS errors converge to steady states gradually. However, when $\hat{R}:R = 0.8$, all of them start to oscillate and become divergent. The simulation result matches the location of point 'a' in Fig 5.30, inside the stable boundary of $\hat{R}:R = 0.6$ but outside the boundary of $\hat{R}:R = 0.8$.

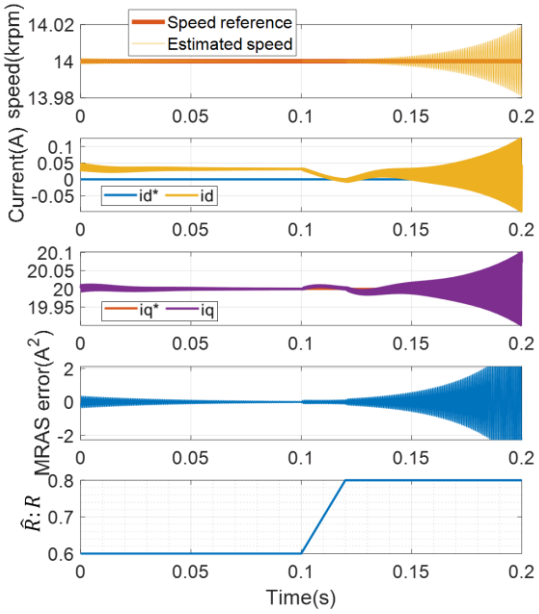


Fig 5.31. Simulation result at operating point 'a' in Fig 5.30 with k_{pm}=2.8, k_{im}=10000

The simulation results at the other 3 operating points (i.e., b, c, d) are demonstrated in Fig 5.32-Fig 5.34 respectively. The speed and d/q-axis current commands are set the same with the simulation scenario at point 'a'. The k_{pm} and k_{im} are selected based on the operating points location in Fig 5.30. The waveform in Fig 5.32 proves the operating point 'b' is stable with $\hat{R}:R = 0.8$ but unstable with $\hat{R}:R = 1.0$. The waveform in Fig 5.33 proves the operating point 'c' is stable with $\hat{R}:R = 1.0$ but unstable with $\hat{R}:R = 1.2$. The waveform in Fig 5.34 proves the operating point 'd' is stable with $\hat{R}:R = 1.2$ but unstable with $\hat{R}:R = 1.4$. All these simulation results match with their operating points location in Fig 5.30. Therefore, Fig 5.31-Fig 5.34 validate the stable boundaries with different $\hat{R}:R$ ratios in Fig 5.30.

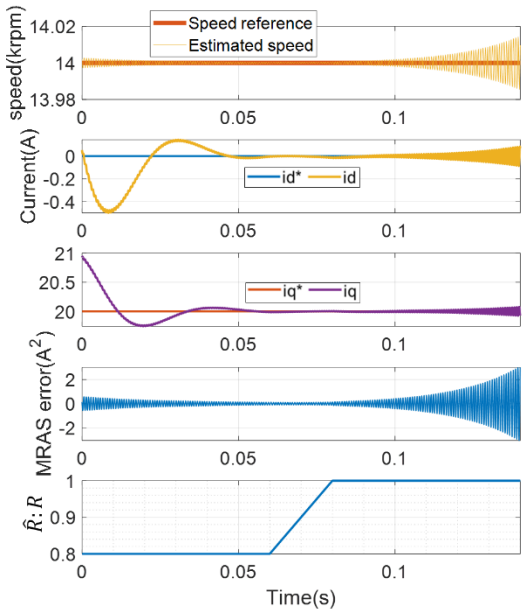


Fig 5.32. Simulation result at operating point 'b' in Fig 5.30 with k_{pm}=2.6, k_{im}=10000

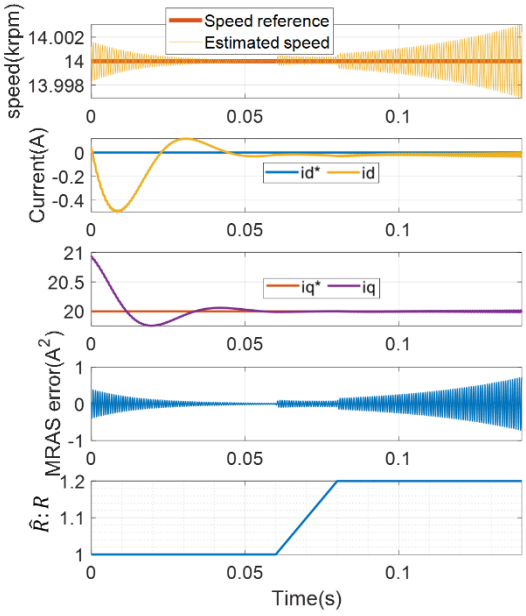


Fig 5.33. Simulation result at operating point 'c' in Fig 5.30 with k_{pm}=2.3, k_{im}=10000

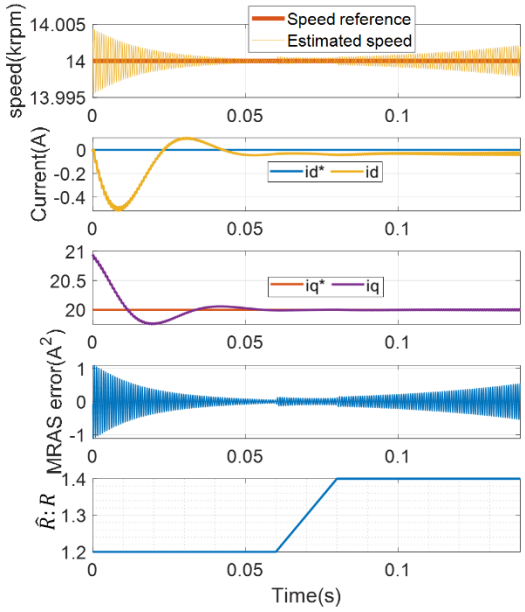


Fig 5.34. Simulation result at operating point 'd' in Fig 5.30 with k_{pm}=2.1, k_{im}=10000

5.2.6.5 Overall Stable Area Considering Machine Parameters Mismatch

5.2.6.5.1 Overall Stable Area Considering Estimation Error of Permanent Magnet Flux Linkage

In Section 5.2.6.2, the stable areas with n=14krpm, $i_d^* = i_q^* = 0$A and $\hat{\varphi}_f : \varphi_f = 0.6 - 1.4$ are demonstrated and validated. However, the stable area will change at different speeds and different current references. The stable area shown in Section 5.2.6.2 is not enough to provide an overall stable area considering the wide speed range and all possible current references. In actual application, the speed and i_q^* can be any value within their allowed range, and $\hat{\varphi}_f : \varphi_f$ is uncertain as well. Therefore, a stable area in all different conditions will be quite useful for the real test. To achieve that, a MATLAB manuscript with the process in Fig 5.35 is built. In Fig 5.35, 3 outer loops are choosing all possible n, i_q^*, and $\hat{\varphi}_f : \varphi_f$ values. Under each combination, the maximum eigenvalues at all (k_{pm}, k_{im}) selections are calculated. This means there are two inner loops for k_{pm} and k_{im} respectively. Then, the latest maximum eigenvalue at

each (k_{pm}, k_{im}) point is compared with the previous maximum value to find the larger one among them. The larger eigenvalue indicates the up-to-date stability at each (k_{pm}, k_{im}) point. Finally, an overall stable area map like Fig 5.36 is derived, considering all possible n, i_q^*, and $\hat{\varphi}_f : \varphi_f$.

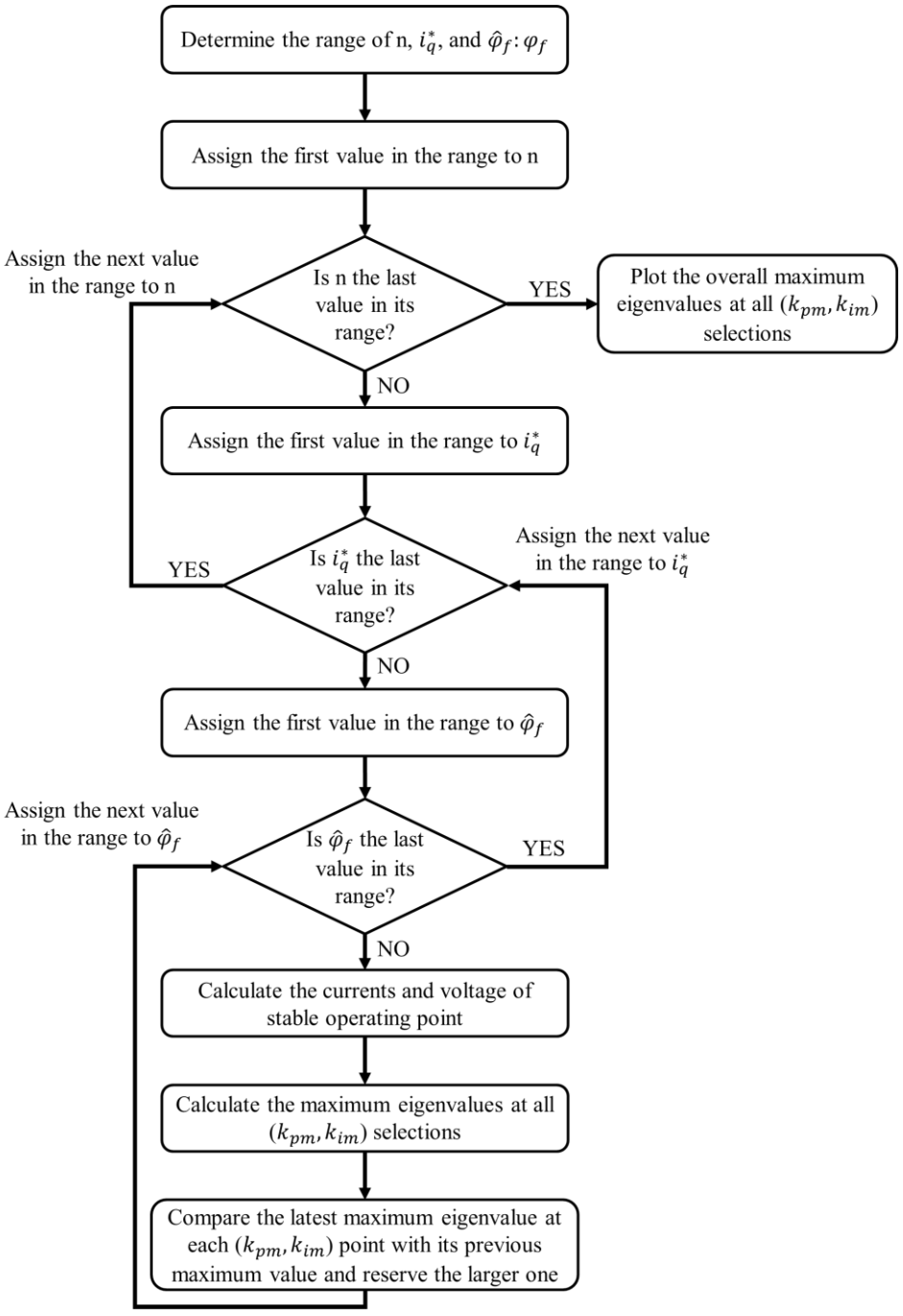


Fig 5.35. The flowchart plotting the overall stable area considering n, i_q^*, and $\hat{\varphi}_f : \varphi_f$ selections

In Fig 5.36 left, the stable area has shrunk a lot compared with the stable area in Fig 5.20 where only the scenario of n=14krpm and $i_q^* = 0$A is considered. The stable area in Fig 5.36 (with contour line=1) has the largest k_{pm} only around 2.0. The stable k_{im} selection has also reduced to about 3500, which is much smaller than the stable k_{im} selection in Fig 5.20. Based on Fig 5.36, the selection of proper k_{pm} and k_{im} can be found considering the estimated error of $\hat{\varphi}_f$, which is more practical as the estimated error is unavoidable in reality.

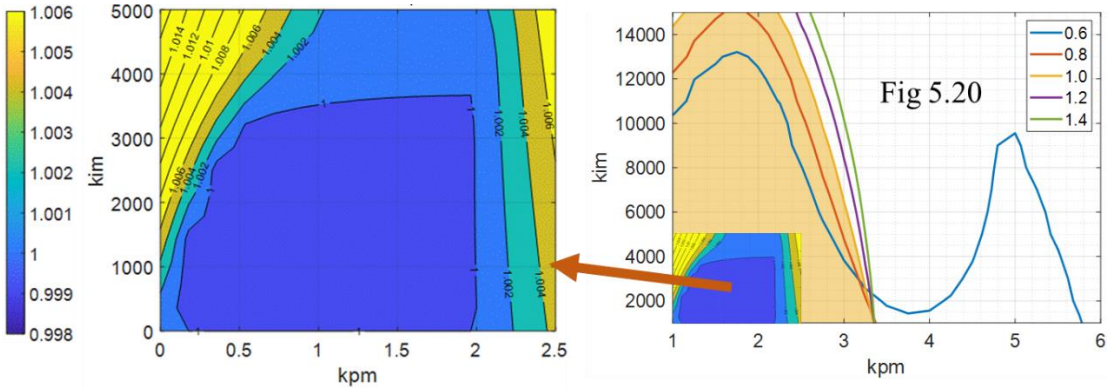


Fig 5.36. Stable area with iq=-30A to 30A, n=0.6-14krpm, and $\hat{\varphi}_f$: φ_f=0.6-1.4

5.2.6.5.2 Overall Stable Area Considering Estimation Error of d/q-Axis Inductances

The overall stable area considering the estimation error of d/q-axis inductances can be obtained using the algorithm shown in Fig 5.37. Comparing the flowchart in Fig 5.37 and the flowchart in the last section (Fig 5.35). The difference is that the flux-linkage-related variables (i.e., $\hat{\varphi}_f$: φ_f, $\hat{\varphi}_f$) are replaced by inductance-related variables (i.e., $\hat{L}$: L, $\hat{L}$). In Fig 5.37, there are 3 outer loops choosing all possible n, i_q^*, and $\hat{L}$: L values. Under each combination, the maximum eigenvalues at all (k_{pm}, k_{im}) selections are calculated. This means there are two inner loops for k_{pm} and k_{im} respectively. Then, the latest maximum eigenvalue at each (k_{pm}, k_{im}) point is compared with the previous maximum value to find the larger one among them. The larger eigenvalue indicates the up-to-date stability at each (k_{pm}, k_{im}) point. Finally, an overall stable area map like Fig

5.38 is derived, considering all possible n, i_q^*, and $\hat{L}$: L.

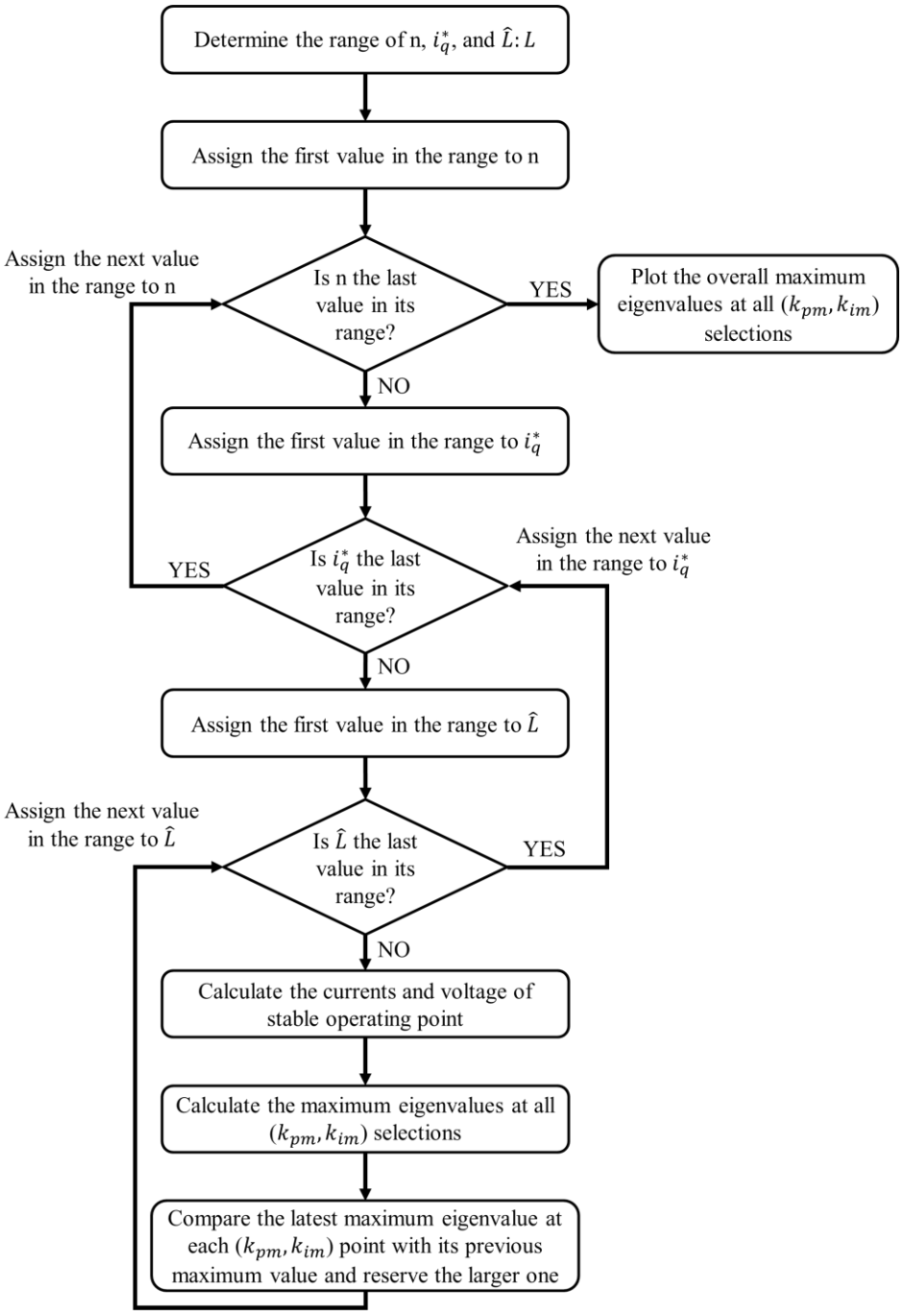


Fig 5.37. The flowchart plotting the overall stable area considering all n, i_q^*, and $\hat{L}$: L selections

In Fig 5.38 left, the stable area has shrunk a lot compared with the stable area in Fig 5.25 only with n=14krpm and $i_q^* = -20$A. The stable area in Fig 5.38 (with contour line=1) has the largest k_{pm} smaller than 2.0. The stable k_{im} selection has also reduced to about 4500, which is much smaller than the stable k_{im} selection in Fig 5.25. Based on Fig 5.38, the selection of proper k_{pm} and k_{im} can be found considering the

estimated error of $\hat{L}$ as well as different iq and speed conditions.

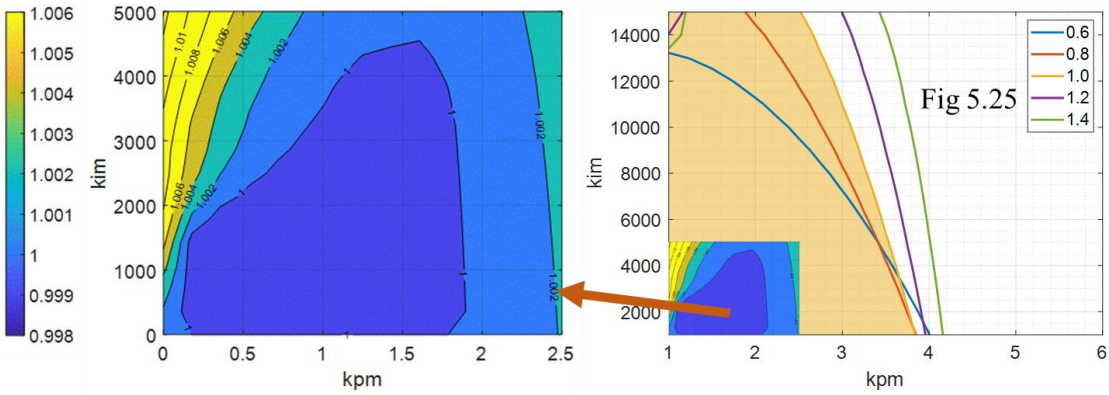


Fig 5.38. Stable area with iq=-30A to 30A, n=0.6-14krpm, and $\hat{L}$: L=0.6-1.4

5.2.6.5.3 Overall Stable Area Considering Estimation Error of Phase Resistance

The overall stable area considering the estimation error of phase resistance can be obtained using the algorithm shown in Fig 5.39. Comparing it with the flowchart in the last section (Fig 5.37). The difference is that the inductance-related variables (i.e., $\hat{L}$: L, $\hat{L}$) are replaced by resistance-related variables (i.e., $\hat{R}$: R, $\hat{R}$). In Fig 5.39, there are 3 outer loops choosing all possible n, i_q^*, and $\hat{R}$: R values. Under each combination, the maximum eigenvalues at all (k_{pm}, k_{im}) selections are calculated. This means there are two inner loops for k_{pm} and k_{im} respectively. Then, the latest maximum eigenvalue at each (k_{pm}, k_{im}) point is compared with the previous maximum value to find the larger one among them. The larger eigenvalue indicates the up-to-date stability at each (k_{pm}, k_{im}) point. Finally, an overall stable area map like Fig 5.40 is derived, considering all possible n, i_q^*, and $\hat{R}$: R.

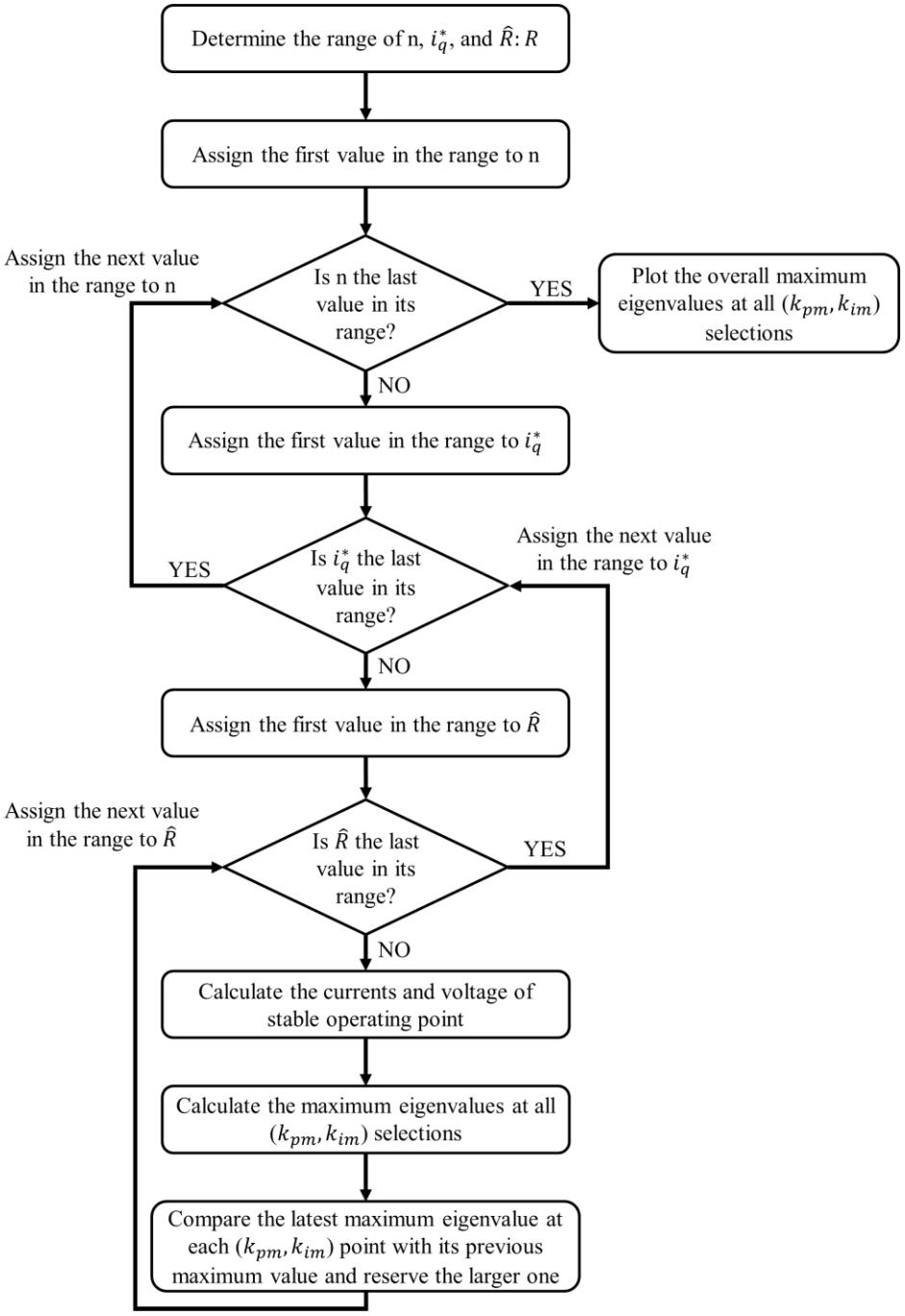


Fig 5.39. The flowchart plotting the overall stable area considering all n, i_q^*, and $\hat{R}$: R selections

In Fig 5.40, the stable area has shrunk a lot compared with the stable area in Fig 5.30 only with n=14krpm and $i_q^* = 20$A. The stable area in Fig 5.40 (with contour line=1) has the largest k_{pm} around 2.0. The stable k_{im} selection has also reduced to about 4000, which is much smaller than the stable k_{im} selection in Fig 5.30. Based on Fig 5.40, the selection of proper k_{pm} and k_{im} can be found considering the estimated error of $\hat{R}$, which is more practical as the estimated error is unavoidable in reality.

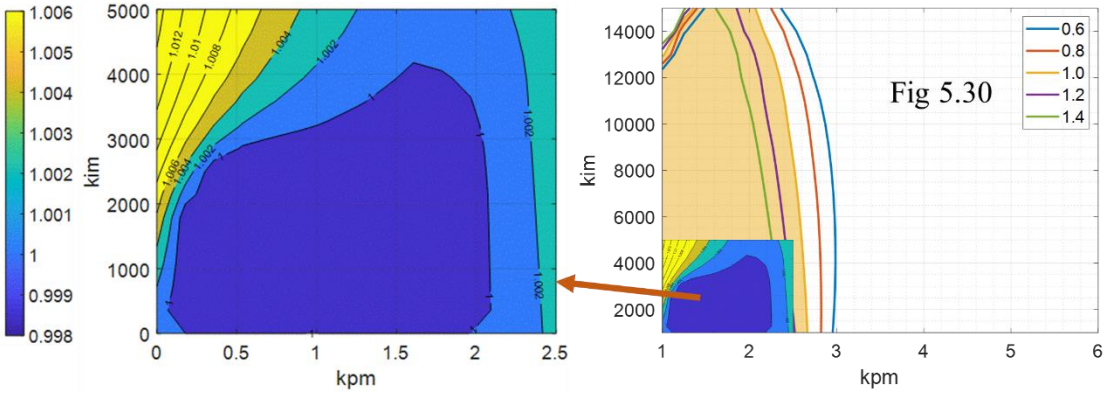


Fig 5.40. Stable area with iq=-30A to 30A, n=0.6-14krpm, and $\hat{R}$: R=0.6-1.4

5.2.7 Simulation Result Summary

The entire section 5.2 uses simulations to validate the proposed eigenvalues-based stability analysis method in section 5.1. All aspects of the MRAS sensorless algorithm are considered in the simulations, such as orders of the adaptive model (1st or 2nd), different load conditions (q-axis current), different speeds, and different estimated machine parameters. All the simulation results match well with the system's maximum eigenvalue at the specific operating point.

With the help of the proposed eigenvalues-based stability analysis method, some important conclusions can be derived. First of all, using the 2nd-order adaptive model enables a larger stable area of MRAS PI factors than the 1st-order adaptive model. Secondly, the stable area at high speed is much smaller than at low speed. Finally, the load condition and estimated machine parameters will affect the stable selection area of MRAS PI factors. Therefore, the overall stable areas considering different load conditions, speeds and machine parameter mismatch (i.e., Fig 5.36, Fig 5.38, Fig 5.40) can guide engineers for MRAS PI factors selection.

5.3 Conclusion

This chapter develops the stability analysis procedure of the MRAS sensorless control system and validates the stability analysis results by simulation.

First of all, in section 5.1, the stability analysis procedure based on the proposed state evolution equation is summarized. This procedure can calculate the maximum eigenvalue of the current closed-loop system at any specific operating point with specific control parameters. A MATLAB manuscript is written to achieve that.

Then, in section 5.2, an MRAS sensorless current closed-loop control system is built in Simulink to simulate the system stability at different operating points. All the simulation results match well with their system maximum eigenvalue calculated from the proposed stability analysis method. The operating conditions with 1st-order and 2nd-order MRAS adaptive models are discussed in Section 5.2.2 and 5.2.3 respectively. Then, in Section 5.2.4, the stable areas for those two types of adaptive models are compared, which proves the superiority of the 2nd-order MRAS adaptive model.

In Section 5.2.5, the influence of different load conditions (iq) on the stable area is investigated. In Section 5.2.6, estimated machine parameters (i.e., $\hat{R}, \hat{L}, \hat{\varphi}_f$) are investigated about their influence over the stable area. Above all, the selections of stable k_{pm} and k_{im} are dependent on many variables such as orders of the adaptive model, q-axis current, estimated machine parameters used in the MRAS algorithm. Whilst the eigenvalue-based stability analysis method proposed in Section 5.1 is always accurate to predict the system stability considering these variables, which provides guidance on control parameters selection.

Chapter 6.

Experimental Prototype

In this chapter, the hardware of the dual three-phase machine drive system will be discussed. The software of this drive system will also be introduced in detail. The cooling system of the power converter and the machine is demonstrated. The power converter composition and layout are explained as well. As for the converter software, this chapter discusses the implementation of control algorithm in two microcontrollers (MCU). The CAN communication protocol between MCUs and host PC is introduced together with the Graphical User Interface (GUI). In addition, this chapter also discusses the integration of the dual three-phase machine and power converter. Finally, the experimental test rig at Nottingham University is presented.

The ACHIEVE prototype was developed by several partners together (PST, NEMA, and Nottingham University). The ACHIEVE machine was designed by Nottingham University and manufactured by NEMA Ltd. The control board of the six-phase converter was designed by PST Ltd, and other boards were designed by me. The control software was developed by me as well.

6.1 Power Electronic Converter Hardware

The hardware of the power converter consists of 4 Print Circuit Boards (PCBs) (i.e., control board, driver board, power board, connector board) as shown in Fig 6.1. These boards are stacked on top of each other to save space for the integration with the engine gearbox. Each PCB hardware will be introduced in detail in the following sections.

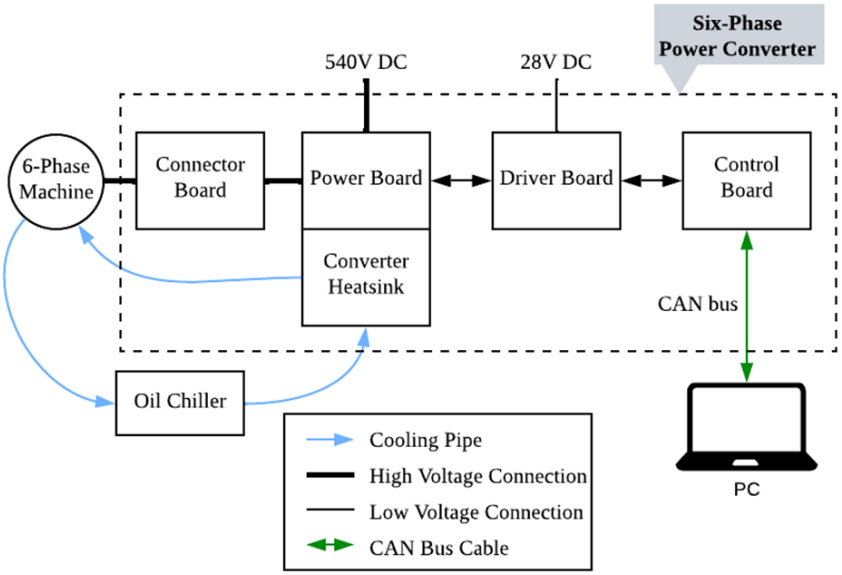


Fig 6.1. Six-phase power converter simple diagram

6.1.1 Control Board

The control board runs the machine control algorithm and communicates with the host PC through the CAN bus. The MCUs applied is TMS320F28375S from Texas Instruments. Due to the high-reliability requirement, there are two MCUs on the control board, and each of them controls one three-phase channel.

The signal diagram of the control board is shown in Fig 6.2. As can be seen, there are two MCUs in the control platform and they can both communicate with the PC through CAN, USB or JTAG. The CAN bus is the only communication method during normal operation and the other two methods are only used during debugging. There are also communication channels between the two MCUs including one high-speed SPI bus, 2 GPIOs (General Purpose Input/Output) and one PWM synchronous signal.

The current signals from phase current sensors ($I_A, I_B, I_C, I_U, I_V, I_W$) are analogous voltages between 0-3.3V to match MCU requirements. There are also two analogous signals (i.e., SiC module temperature T_{sense}, DC bus voltage V_{sense}) feeding into the

MCUs. The stator temperatures are also monitored by 3 RTD (Resistance Temperature Detector) sensors buried in the machine windings. After processing the data and implementing the sensorless control, the PWM signals will be generated and sent out from the MCUs.

A 5V DC power for the control board coming from the DC/DC converter in the driver board is used to supply power to the controller board. Although machine sensorless control will be applied to the actual application, the encoder interface is still necessary during the initial calibration stage and is used for initial debugging.

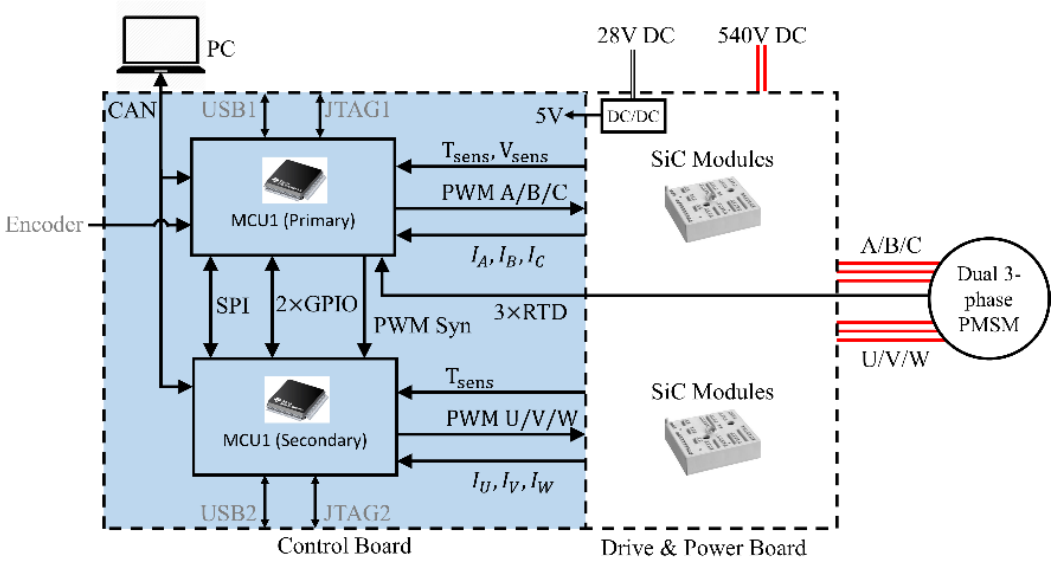


Fig 6.2. Signal diagram of the control board.

The layout views of the control board are shown in Fig 6.3 with some critical components highlighted. The shape is irregular because a propeller shaft needs to pass through the power converter. The big notch on the top allows the six-phase terminals on the power board to connect with the connector board.

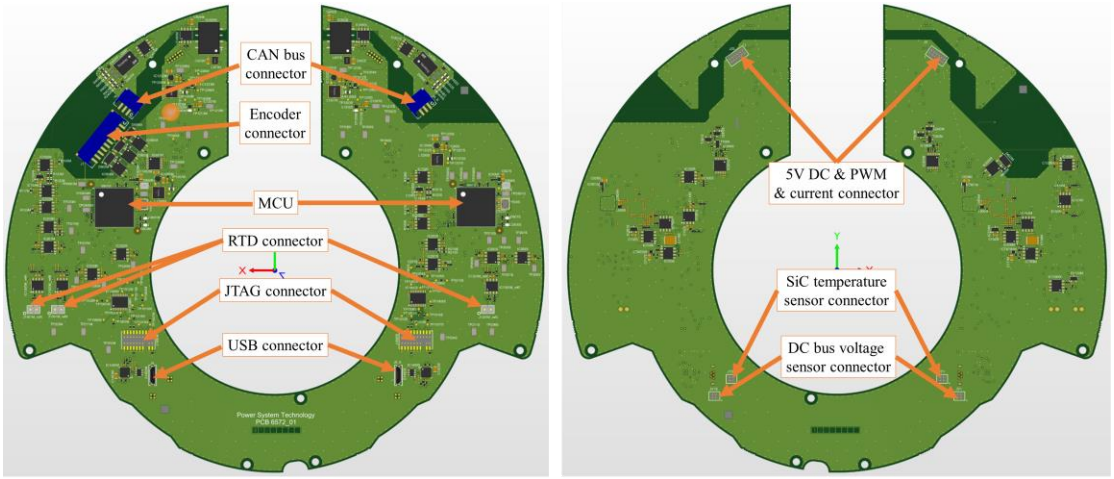


Fig 6.3. Control board layout views

(a) face to the machine; (b) face to the driver board

6.1.2 Driver Board

The driver board has the functions as follows:

1) Split each PWM signal from MCU into two complementary signals for two MOSFETs on one leg.
2) Add dead time to PWM signals.
3) Transform TTL level PWM signals (i.e., 0V, 3.3V) to the gate driver signals of SiC MOSFET (i.e., -3V, 18V).
4) Transform 28V DC power input to 12V and 5V to supply power for components on all boards.
5) Sample DC-bus voltage.
6) Sample SiC MOSFET temperature.

Fig 6.4 is a functional diagram of the driver board. It only shows the generation of gate driver signals for one leg as all the six legs use the same circuit. As can be seen from it, the red lines represent the low voltage circuit which includes driver board DC power conversion, drive signals conversion, and currents/temperature/DC-link voltage

sampling. In contrast, the thick black line represents the 540V DC signal.

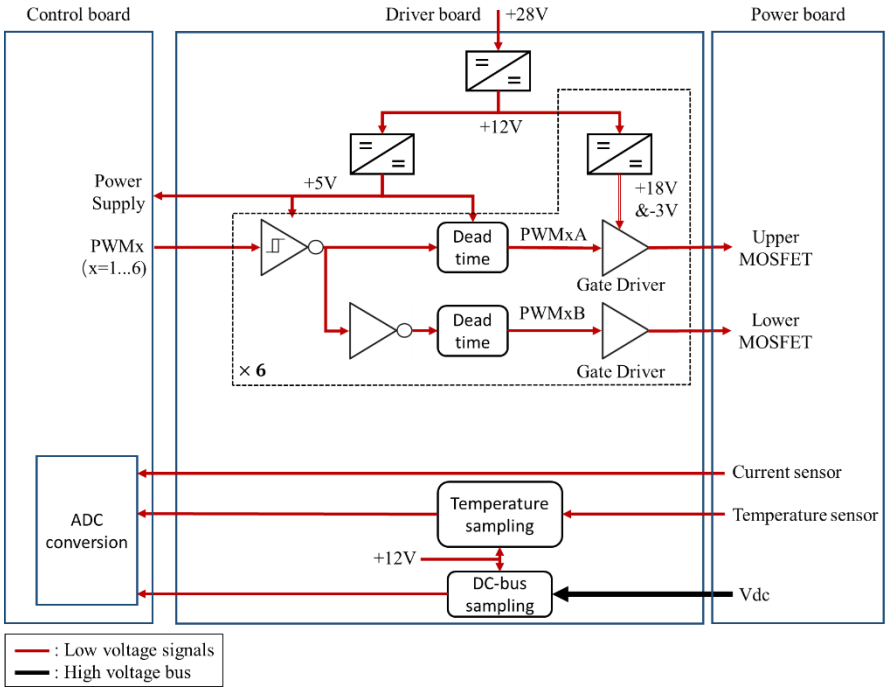


Fig 6.4. Driver board functional diagram

The DC power conversion circuit in the driver board converts the +28V DC input to +12V first. This +12V DC voltage supplies to temperature and DC-bus sampling circuit, which convert power module temperature and DC-link voltage to MCU readable voltage (0-3.3V). In addition, the +12V DC will also be converted to isolated +18V and -3V which are used as SiC MOSFET gate driver voltage. Apart from that, the +5V DC voltage converted from +12V provides power to the control board, logic chips on the driver board, and the current sensor in the power board.

The gate driving signals of SiC MOSFET are amplified by the driver board from 0V/3.3V TTL voltage to -3V/+18V isolated voltage. The TTL signals from the control board will go to a Schmitt-trigger inverter first to prevent the interference of noise. Then, it will be split into two complementary signals and both of their rising edges will be delayed by dead-time circuits. Finally, the signals will be amplified to SiC-MOSFET-compatible driving voltages.

The layout views of the driver board are shown in Fig 6.5. In Fig 6.5(a), the 28V

power input connectors are on the top, and the 540V terminals are on the bottom. The gate driver signals circuit is circled by the red dash line at the middle of the board, and the DC-bus voltage and SiC temperature sampling circuits are circled by the green dash line at the bottom of the board.

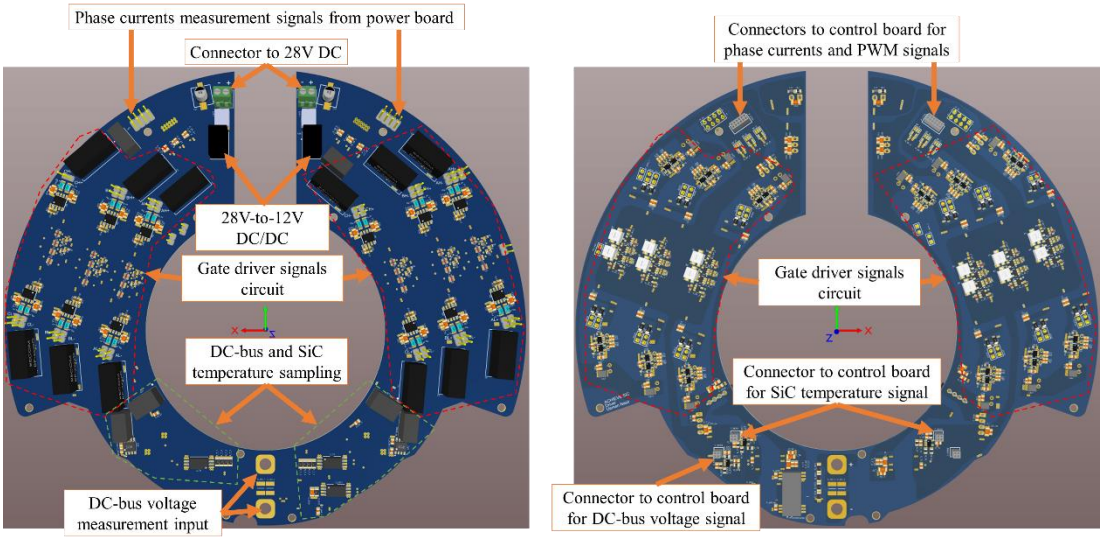


Fig 6.5. Driver board layout views

(a) face to the power board; (b) face to the control board

6.1.3 Power Board

To achieve a high power density of the power converter, the selection of power modules is critical. In Table 6.1, requirements and selected power module maximum ratings are compared. For the power converter, it should be able to sustain a maximum phase current of 30A with 540V DC-bus to achieve 20kW power. Compared with the converter requirement, the selected SiC power module (SKiiP-26ACM12V17) is with maximum drain-source voltage of 1.2kV (thus with more than 600V voltage margin) and 52A maximum current (thus of 22A AC current margin). These margins are considered to protect the power module with voltage and current overshoot in the transient state.

Table 6.1. Power converter requirement and selected power module maximum ratings

Parameter	Requirement	SKiiP-26ACM12V17
Maximum DC voltage	540V	1200V
Maximum AC output current (peak)	30A	52A

The functional diagram of the power board is shown in Fig 6.6. The power module (SKiiP-26ACM12V17) is an integrated 3-phase full bridge coming with an embedded temperature sensor. The power board has two of those modules and they are highlighted in Fig 6.6. The six-phase currents are measured by 6 current sensors. Both temperature and current signals go to the driver board. There are 12 gate driver signals from the driver board and they have +18V or -3V to control the ON and OFF of the 12 MOSFETs.

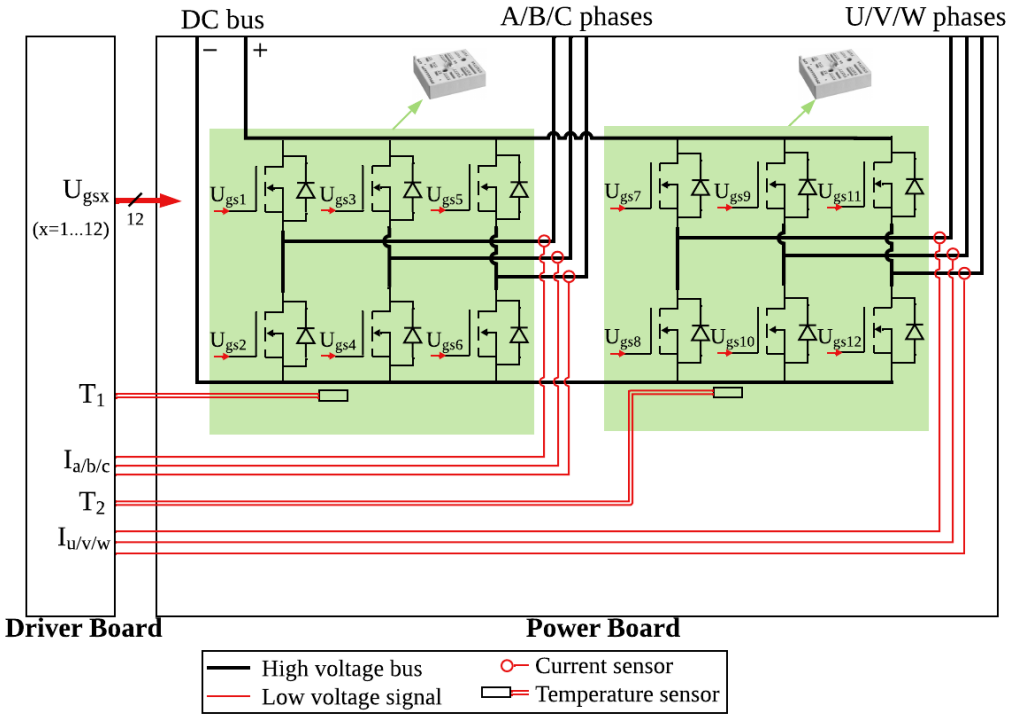


Fig 6.6. Power board functional diagram

The layout views of the power board are shown in Fig 6.7, which shows the positions of connectors, power modules, DC-bus capacitors, and current sensors. There are two power modules in the middle of Fig 6.7(b). These power modules are with two parts on the other side of the board, which are screwed with modules together on the board. The gate driver signal connectors are placed around the module to reduce the stray inductance of signal paths, as well as the module temperature sensor connectors. The

current sensors are on the top of Fig 6.7(b). The DC-bus capacitors are placed on the bottom and both sides of the board. Ceramic capacitors have been chosen due to the consideration of high-temperature environment and space available.

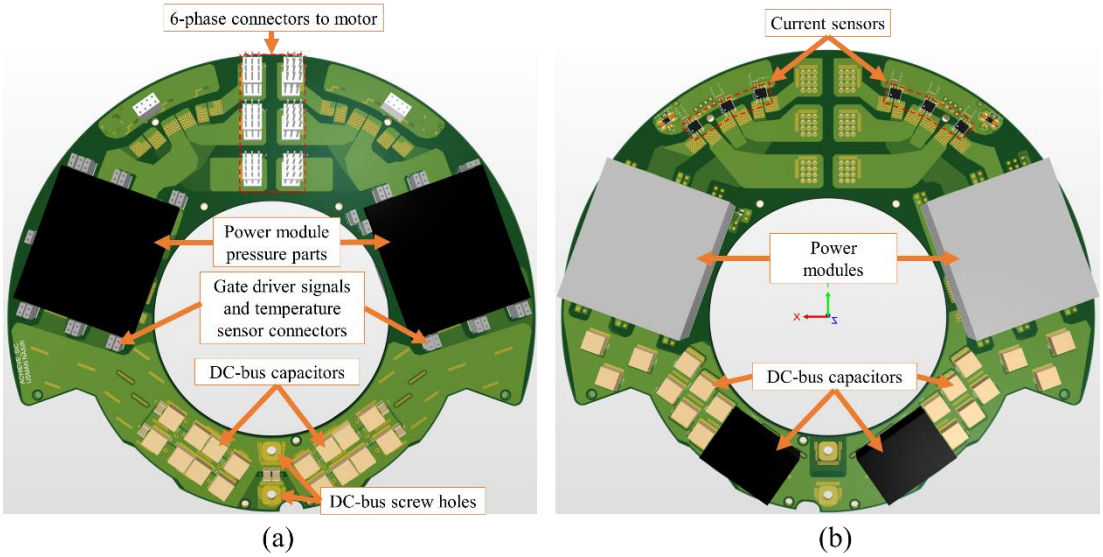


Fig 6.7. Layout views of the power board PCB
(a) face to the driver board, (b) face to the heatsink

6.1.4 Converter Assembly

The control board, driver board, and power board introduced above can form a power converter by stacking them together. However, to integrate this converter with electrical machines and thus to the turboprop engine. The power electronic converter housing would be critical. The housing not only provides support and protection to the PCBs, but also plays the role of heatsink to dissipate the heat from power modules.

The exploded view of this power converter including housing is shown in Fig 6.8. Because the machine will be located on the left side of the converter in Fig 6.8 whilst the power board and heatsink are located on the right, a connector board is necessary to connect the machine terminals to the power board connectors. The two SiC power modules on the power board are attached to the heatsink tightly by screws, and oil coolant flows through the heatsink to take away heat generated by the SiC modules.

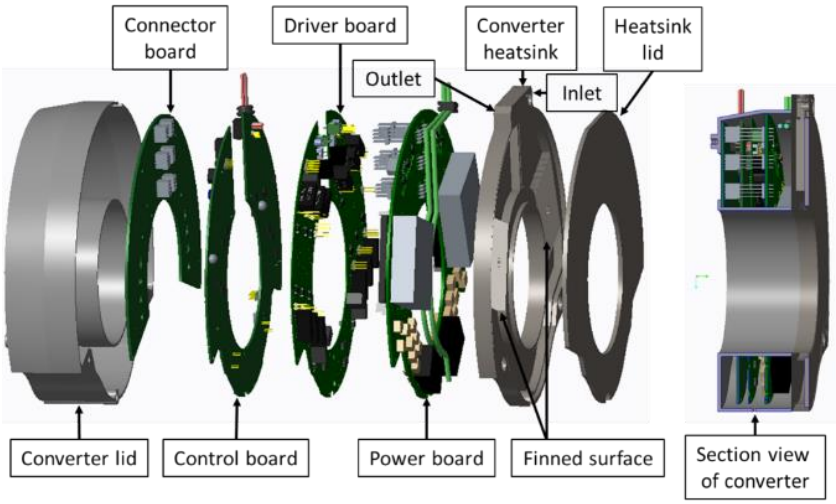


Fig 6.8. Power converter assembly exploded view

Fig 6.9 shows the converter board assembly. The power board is on the top with two SiC power modules and DC-link capacitors on it. Two 10uF CeraLink capacitors and many 0.1uF ceramic capacitors are soldered on the 540V DC-link. The total capacitance of these capacitors is 27uF. Due to the irregular shape of the boards, the 0.1uF small-size capacitors are stacked in the empty area of the power board as much as possible to reduce ripples on 540V DC-link. The other 3 boards (i.e., driver board, control board, connector board) are below the power board and they are connected together as a whole assembly to drive the dual three-phase machine.

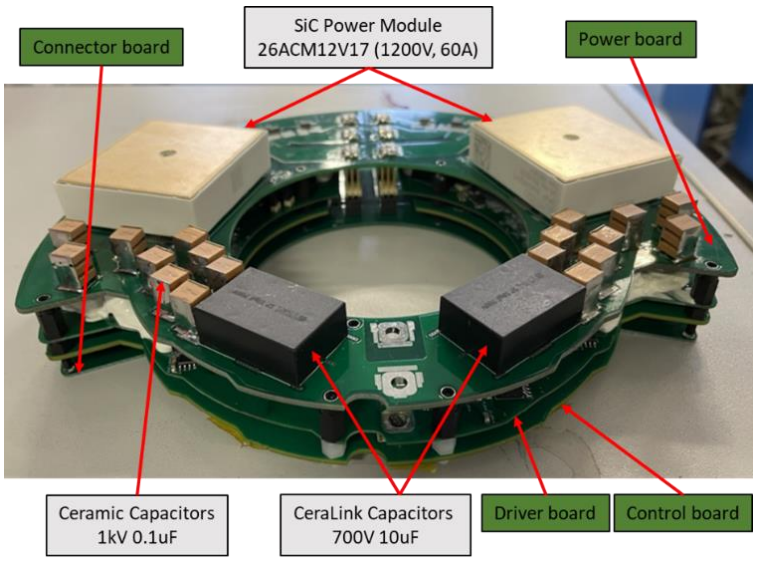


Fig 6.9. Power converter boards assembly

6.1.5 Converter Efficiency Test

In order to test the function and efficiency of the power converter, an experimental setup in Fig 6.10 has been built. The converter boards are assembled into the housing, and the heatsink on the housing is connected to a water chiller. Two DC power supplies provide 28V and 540V power for the converter. A resistor-inductor load bank with 2 independent start-connected 3-phase branches is connected with the 6-phase outputs of the converter.

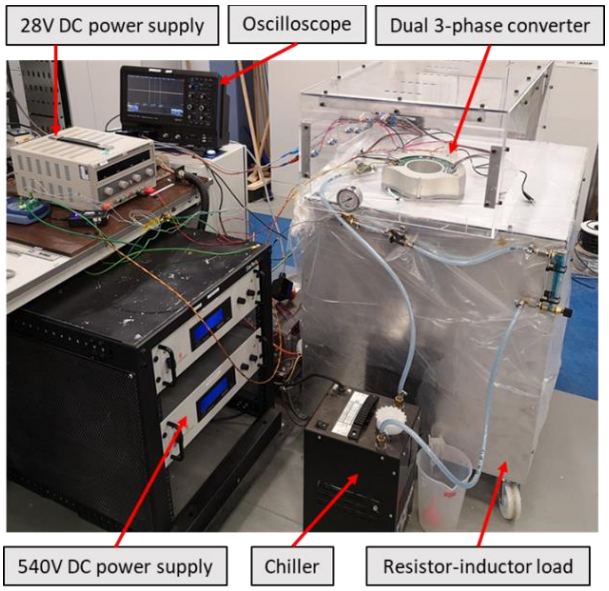


Fig 6.10. Experimental setup of a SiC-based dual 3-phase converter.

With this test set-up introduced above, the power converter is finally tested up to 20kW with the phase currents to 26A. The test results at maximum power are listed in Table 6.2, and the current and voltage waveforms are displayed in Fig 6.11. Based on the actual maximum power achieved by the converter, its power density is calculated up to 11.8kW/L and 9.2kW/kg including the housing.

Table 6.2. Converter test results at maximum power

Parameter	Value
Maximum phase current (peak)	26.0A
Maximum power output	20.08kW
Power density in volume (with housing)	11.8kW/L
Power density in mass (with housing)	9.2kW/kg

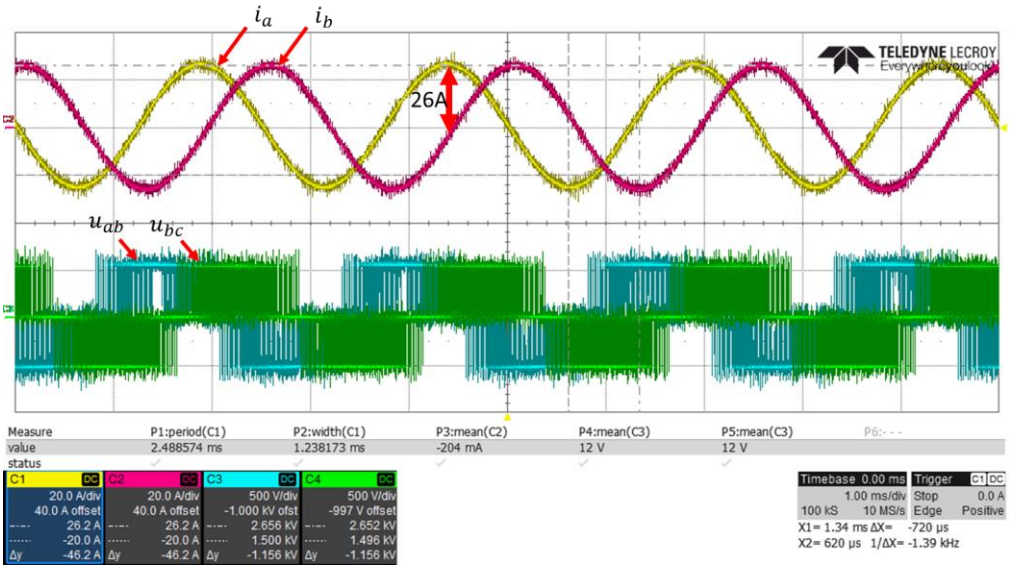


Fig 6.11. Test waveform of phase currents and line-line voltages at maximum power

The efficiency and loss of the converter under different power output conditions are tested and shown in Fig 6.12. The converter efficiency will increase with power increasing and reaches 97.9% when DC power is over 18kW. The power loss of the converter at 18kW is below 400W.

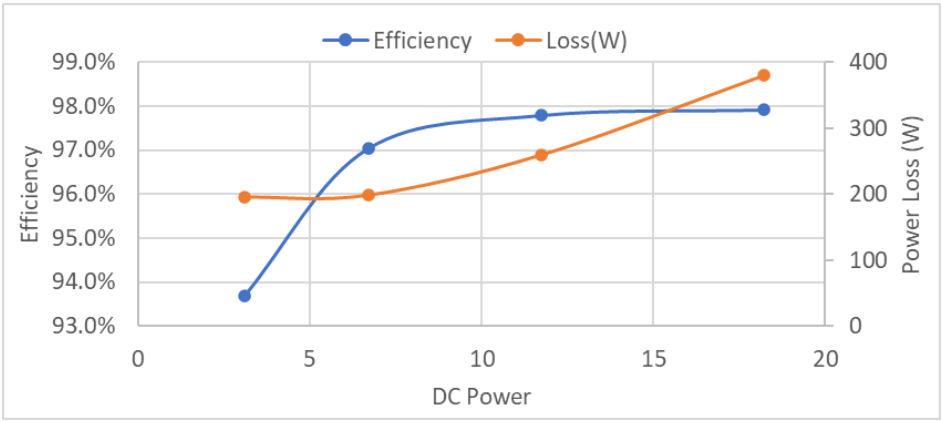


Fig 6.12. Experimental result of efficiency and power loss of the converter

The test results above indicate the converter can output up to 20kW as designed with high power density and high efficiency. All PCBs operate normally despite the strong EMI inside the converter housing due to our EMI mitigation design. The cooling system works well to maintain the components inside the converter at a temperature within their limitations.

6.2 Power Converter Control Software

In this section, the control software in both control board MCUs and host PC will be introduced. Since the MCU has two cores for calculation, the task assignment between the two cores will also be discussed in this section. In addition, as shown in Fig 6.1, the host PC communicates with control board MCUs through the CAN bus. Therefore, the CAN protocol will be discussed as well as the CAN Graphical User Interface (GUI) on the host PC.

6.2.1 MCU Operation Principle

The MCU is TMS320F28375S from the Texas Instruments. It has a 200MHz 32-bit CPU and an independent 32-bit floating-point Control Law Accelerator (CLA) that runs at the same speed (200MHz) [55]. This dual-core structure allows the CLA to focus on the time-critical machine control algorithm and CPU to deal with other non-critical tasks such as receiving and sending CAN messages.

In addition, the TMS320F28375S has 1MB Flash memory, 164KB RAM, and diverse peripherals such as Analog-to-Digital converters (ADC), enhanced Pulse Width Modulator (ePWM), Controller Aera Network (CAN), etc. With the help of these peripherals, the CPU and CLA can focus on the control algorithm with high efficiency.

The flow chart shown in Fig 6.13 demonstrates the MCU operation procedure. Both CPU and CLA will be initialized when MCU is powered on. A periodical CPU interrupt (dashed line in Fig 6.13) at a frequency of 40kHz (selected PWM frequency) will trigger the CLA to run the machine control algorithm. The CLA will update the 6-phase duty cycle to ePWM peripheral directly after the progress is done. After triggering CLA, the CPU will continue doing its jobs such as ADC sampling and CAN messages receive and transmit while CLA will focus on the machine control algorithm. After CAN

messages have been received and transmitted, the CPU will wait for the next trigger command.

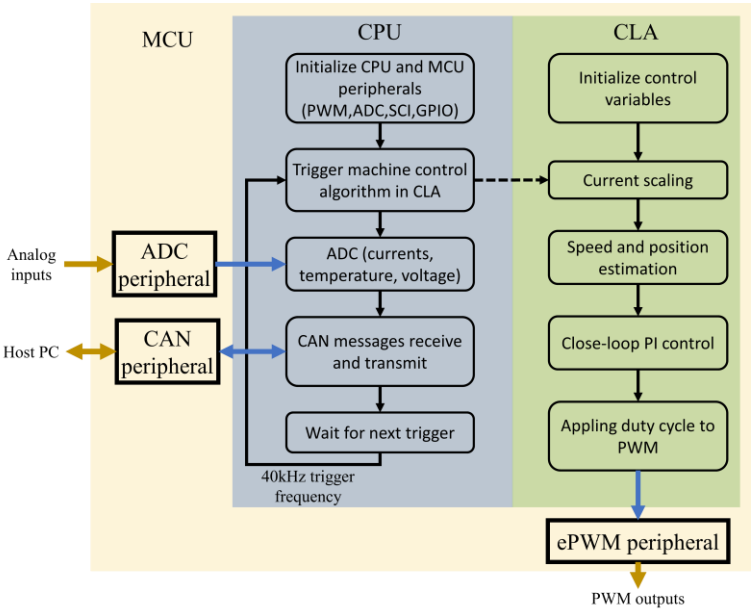


Fig 6.13. MCU operating procedure flow chart

The time sequence arrangements of CPU and CLA, given in Fig 6.14, show the ADC sampling has actually been implemented twice every PWM carrier period after CPU initialization. Except for ADC sampling, the rest time of the CPU is allocated to CAN communication. CPU will be idle after dealing with CAN messages and it will wait for the next ADC trigger. The CLA only runs the machine control algorithm and passes the latest duty cycles to ePWM peripheral module.

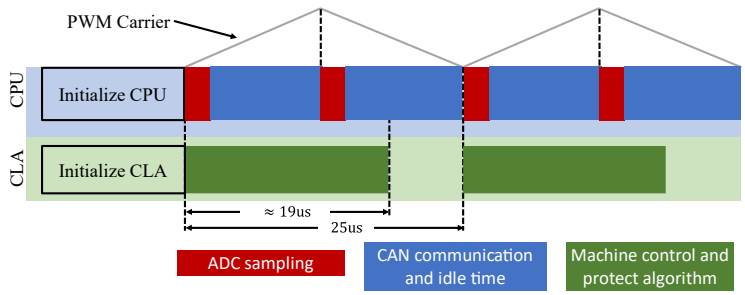


Fig 6.14. CPU and CLA time sequence arrangements

The ePWM peripheral module is responsible for generating PWM pulse signals from the latest duty cycle values received from CLA. The operation principle of ePWM peripheral module waveforms generation is shown in Fig 6.15 considering the A/B/C

three-phase. As can be seen, the duty cycles (i.e., t_A, t_B, t_C) received from CLA have the range between 0 to 1 and they are compared with the PWM carrier signals to generate corresponding PWM waveforms. The "TBPRD" is a period register which can control the frequency of PWM (f_s), and they have the relationship as

$$f_s = \frac{f_{CLK}}{2 \cdot \text{TBPRD}} \tag{6.1}$$

where f_{CLK} represents the frequency of PWM peripheral clock which is configured to 100MHz in this application.

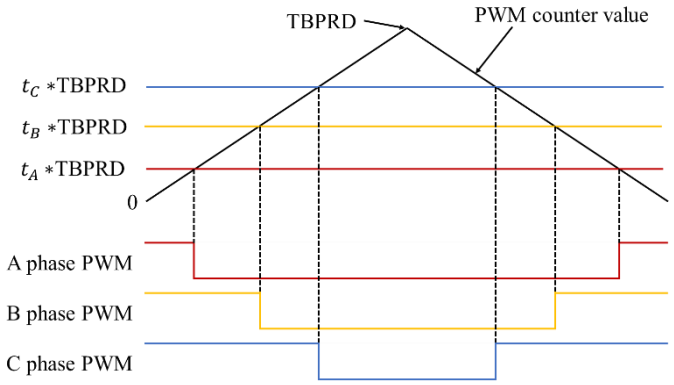


Fig 6.15. ePWM peripheral module operating principle

6.2.2 CAN Communication

The CAN communication is essential for the MCU to communicate with the host PC. The CAN bus also allows microcontrollers and devices to communicate with each other directly [56]. It is a message-based protocol. The CAN bus wiring diagram, given in Fig 6.16, shows all nodes are connected to each other through a two-wire cable. These cables are twisted pairs with 120Ω terminal resistors to absorb the CAN signal energy and prevent signal reflection at the cable ends. The two MCUs are connected to one CAN bus network, and they are distinguished by the CAN message addresses.

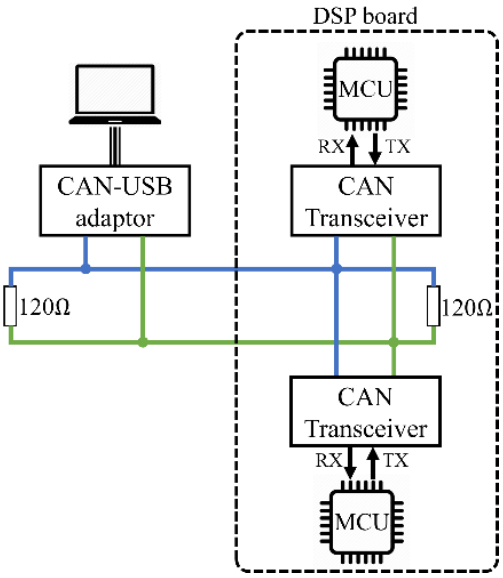


Fig 6.16. CAN bus wiring diagram

The CAN protocol version is ISO11898-1(CAN 2.0B) with a speed of 10kbit/s and 8 bytes of data per message. There are two types of CAN messages (periodical and non-periodical). The periodical messages include the control commands from PC to MCUs and the converter status from MCUs to PC. The non-periodical messages are only used for the new firmware upgrade at the beginning of MCU power-on before the main control algorithm start.

Within this project, the CAN bus cable is the only communication method after converter assembly, therefore, a customized firmware upgrade diagram based on the CAN bus is designed and shown in Fig 6.17.

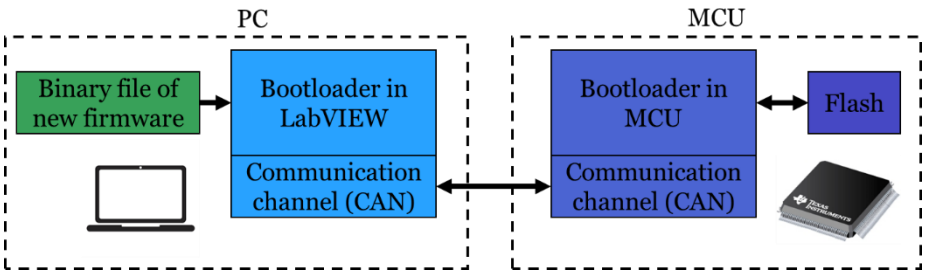


Fig 6.17. MCU firmware upgrade through CAN bus diagram

6.2.3 GUI Design on Host PC

As explained in the last section, CAN communication is used for converter status monitoring, command transmission, and new firmware upgrading. Therefore, a GUI

(Graphical User Interface) is developed using LabView as shown in Fig 6.18. As can be seen, the GUI can display converter states, temperatures, and errors visually and conveniently. It can also send commands to the control board. Apart from those functions, it can also upgrade the new firmware to MCU.

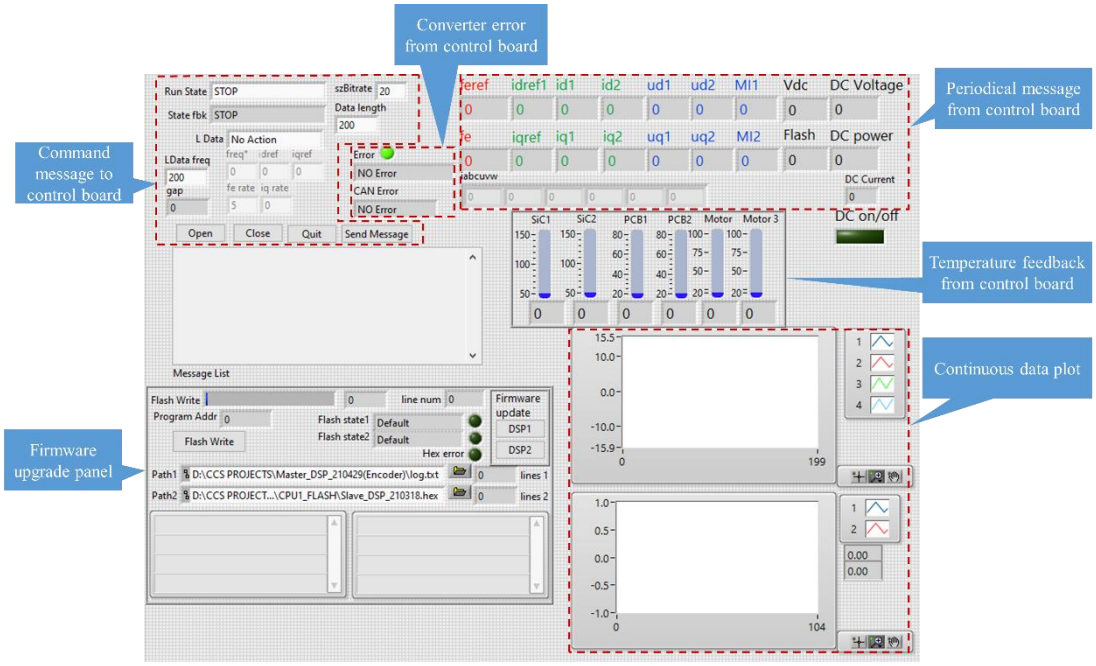


Fig 6.18. GUI layout for CAN communication with control board MCU

6.3 Machine and Power Converter Integration

The integrated assembly of the machine and converter system has its explosion view in Fig 6.19 and the assembly photo in Fig 6.20. The machine and converter housing is closely attached with a hollow shaft going through. There is a bearing seat on the converter side to support the back bearing. As for the cooling, coolant from the chiller will flow to the converter heatsink from the coolant inlet (blue pipe in Fig 6.19) at the top of the converter. Then, the coolant will pass through the heatsink channels, flow out from the heatsink and feed into the machine by the yellow pipe in Fig 6.19. Finally, the coolant flows back to the chiller from the red pipe at the top of the machine in Fig 6.19.

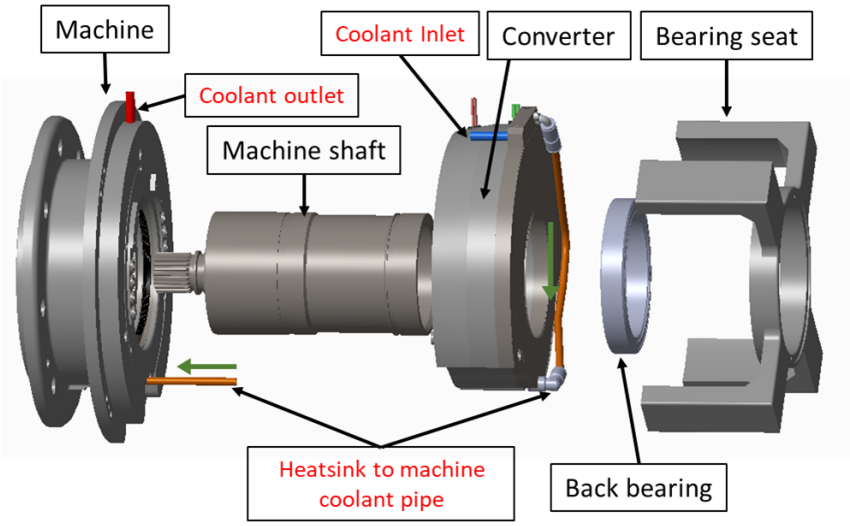


Fig 6.19. Explosion view of the first ACHIEVE prototype

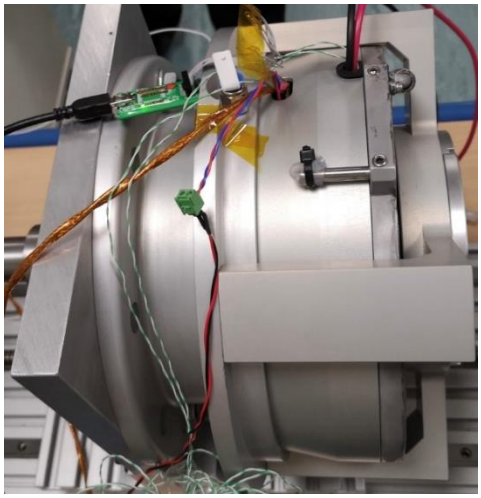


Fig 6.20. Final assembly photo of the first ACHIEVE prototype

6.4 Experimental Test Rig

A test rig has been set up and used to test the developed drive system with sensorless control. The functional diagram is shown in Fig 6.21 and the hardware experimental setup is shown in Fig 6.22. The dual three-phase machine is coupled with an induction motor drive (150kW, 36krpm) based prime mover. During the test, these high-speed machines and drives are located in a dedicated high-speed test room, separated by control panels and humans in the control room as shown in Fig 6.22.

The prime mover can work in two different modes, i.e., speed control mode and

torque control mode. When running at the speed control mode, the prime mover will drive the dual three-phase ACHIEVE machine rotating at a specific speed. When running at the torque control mode, the prime mover will provide a specific load torque to the dual three-phase ACHIEVE machine. The coolant oil temperature is controlled at 50°C.

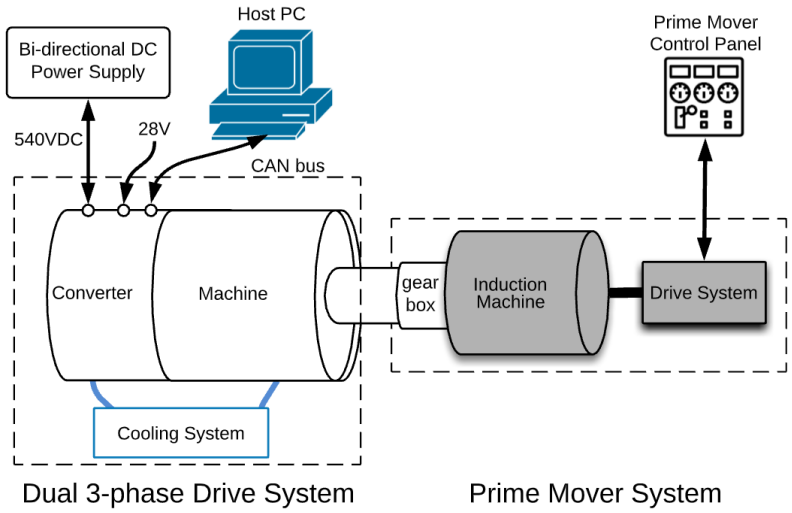


Fig 6.21. Functional test diagram of dual three-phase drive system test rig

As can be seen in Fig 6.22, the power converter is separated with the dual three-phase machine temporarily for convenience of debugging. They were integrated together during the test in the turboprop demonstrator at our project partner site. The control panel for the prime mover and the host PC for ACHIEVE system are placed in the test room as shown in Fig 6.22. Two 30kW bidirectional DC power supplies are connected to the AC/DC converter of the developed ACHIEVE machine drive system. During the test, all measurements of the machine status are recorded by MCUs within the converter and sent to the host PC through CAN bus communication.

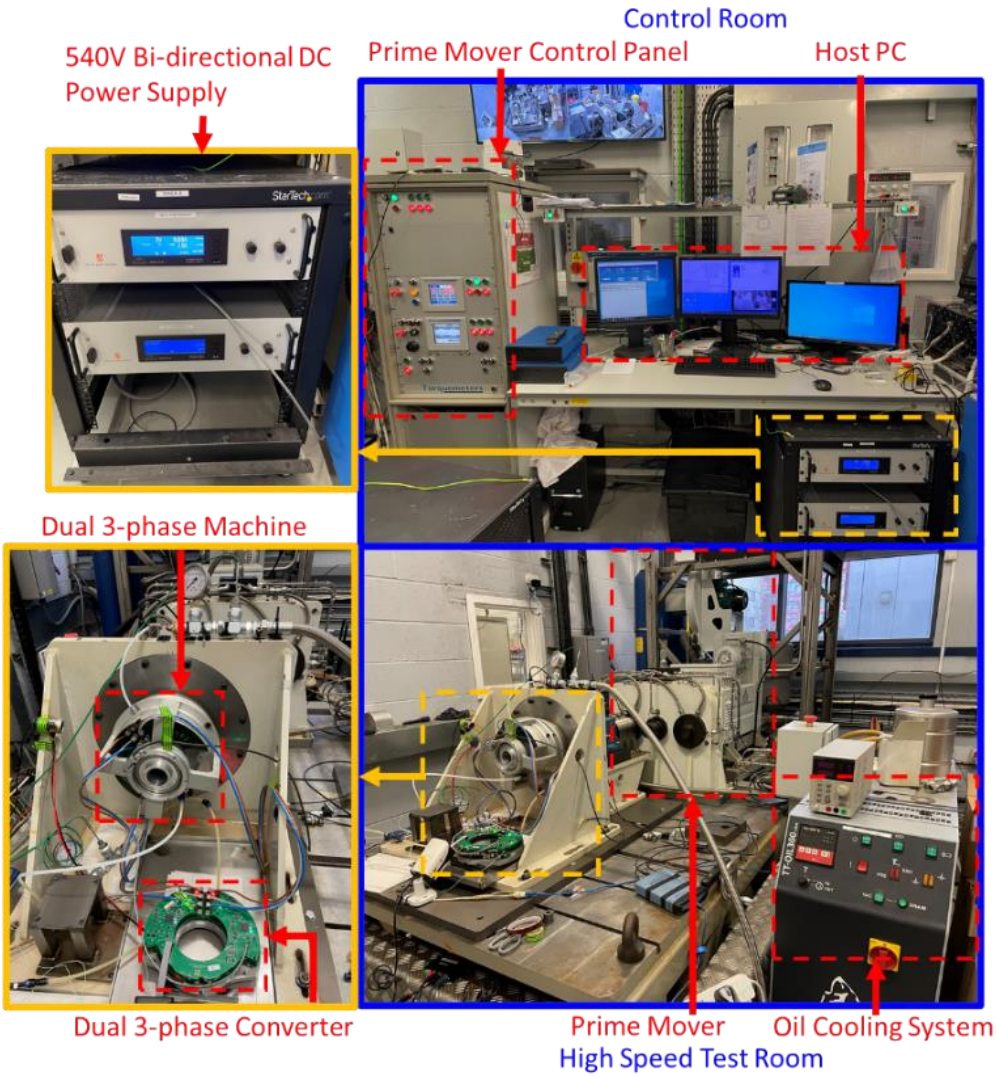


Fig 6.22. Dual three-phase drive system test rig setup

6.5 Conclusion

In this chapter, the experimental prototype of the dual three-phase machine and drive system is introduced in detail. Firstly, in section 6.1, the hardware composition of the power converter is introduced. It includes the control board, driver board, power board, connector board, and housing. Each component is demonstrated and explained. Then the converter assembly is shown, and the converter prototype efficiency is provided.

In section 6.2, the control software in converter MCUs and host PC is introduced. The selected MCU (TMS320F28375S) has two cores for calculation, and the task assignment between the two cores will be discussed in this section. In addition, the CAN protocol will be discussed as well as the CAN GUI on the host PC.

Finally, the dual three-phase machine and converter assembly are demonstrated in section 6.3, and the experimental test rig is introduced in section 6.4. All the content in this chapter wants to give a good understanding to the readers of the experimental prototype to make it convenient to demonstrate the test results in the next chapter.

Chapter 7.

Experimental Validation of Sensorless Motor-Generator Drive System

In this chapter, the experiment results based on the prototype discussed in the last chapter are presented to validate the M-G drive system. First of all, the green-taxiing motoring mode and generation mode test results will be displayed in Section 7.1 and 7.2 respectively. All the tests use sensorless control. Then, in Section 7.3, the 1st and 2nd-order MRAS adaptive models are compared in the experiment, validating the proposed stability analysis method.

7.1 Green-Taxiing Motoring Mode Validation

In the green-taxiing motoring mode, the machine acceleration procedure is shown in Fig 7.1. The machine speed will increase and follow a ramp command. The load will also increase with speed considering the characteristic of a propeller. Due to the lack of a rotor position sensor, the I-F open-loop sensorless control is adopted from 0rpm to 300rpm then the system will switch to MRAS sensorless control when the machine speed is over 300rpm. A switching procedure is adopted to ensure a smooth switching process as explained below.

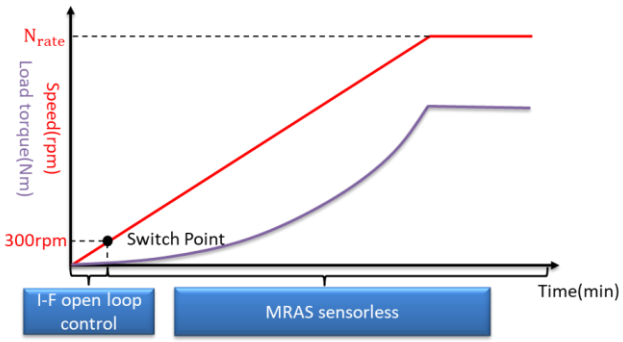


Fig 7.1. Machine acceleration procedure at green-taxiing motoring mode

7.1.1 Control algorithm switching techniques

When the machine starts up from 0 rpm, the system will use I-F open loop sensorless control up to 300 rpm and then switch to the MRAS sensorless control. The change of speed reference (n^*) and q-axis current reference (i_q^*) during the machine start-up process is shown in Fig 7.2. It can be seen that this start-up period can be divided into 4 stages which are explained in the following section.

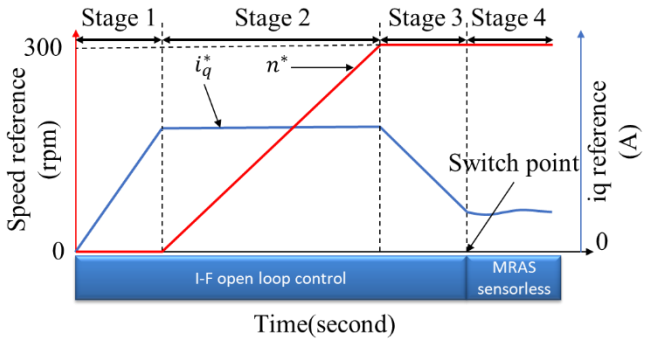


Fig 7.2. Speed and q-axis current reference under I-F open-loop control

In stage 1, the speed reference n^* is set to 0rpm and the current i_q^* will initially build up linearly from 0A. During this stage, the machine rotor will clamp to a position where the rotor flux vector is aligned with the stator flux. Application of a ramp-up type of i_q^* is to smooth the clamping process and thus avoid a mechanical shock to machine bearings.

In stage 2, i_q^* will keep constant with n^* increased linearly. The rotor position reference (θ^*) comes from the integration of n^*. Within this stage, the rotor speed will

follow the reference under open-loop control.

When the reference speed n^* reaches its plateau, the system will enter stage 3 where n^* will keep constant and i_q^* is set to be reduced gradually. While i_q^* is reducing, MRAS sensorless algorithm is running in the background to calculate the estimated rotor position ($\hat{\theta}$). A position error ($\theta^* - \hat{\theta}$) will be used as criteria for switching from I-F open loop control to MRAS sensorless control. The I-F control switching to MRAS control will happen when the position error ($\theta^* - \hat{\theta}$) is close enough to zero (during the experiment, we used 5°).

Within stage 4, the control switching process completes and the $\hat{\theta}$ from MRAS sensorless algorithm will be used in voltage and current ABC/DQ frame transformation. The estimated speed from MRAS sensorless is used for speed control. The current reference i_q^* will thus be from the output of the speed PI controller instead of the outputs from the I-F controller. Till now, the low-speed start-up process is complete, and the MRAS sensorless estimation algorithm will keep running for the entire test process.

7.1.2 Control Diagram of Green-Taxiing Motoring Mode

The entire control algorithm running at green-taxiing motoring mode for the ACHIEVE system is shown in Fig 7.3. The two overlapped yellow areas represent the same algorithms running in the two MCUs. Each MCU controls one three-phase converter. There are two switches (highlighted in red circles) in Fig 7.3 representing the control switches discussed in the previous section. I-F open-loop control is running with switches at position 1 and MRAS sensorless control is at position 2. At I-F open-loop control period, the current reference i_q^* and the speed reference ω_m^* are generated following the trajectory shown in Fig 7.2. The rotor position reference θ^* in this case is from the integration of ω_m^* and feeding into voltage and current ABC/DQ

transformation as assumed rotor position. When the position error ($\theta^* - \hat{\theta}$) is smaller than 5°, the control switch process will be triggered and the control algorithm will be switched from I-F open-loop to MRAS sensorless control, i.e. the switches in Fig 7.3 will change positions from position 1 to position 2. After that, the MRAS sensorless algorithm (blue area in Fig 7.3) estimates rotor position and speed in real-time, which are used by speed and current closed-loop control. Since the machine is normally operated at 12.4krpm-14.2krpm, the speed under 300rpm is only transient and occupies a very limited percentage of its green-taxiing mode operation. The MRAS sensorless control algorithm is the main active control technique during normal operations.

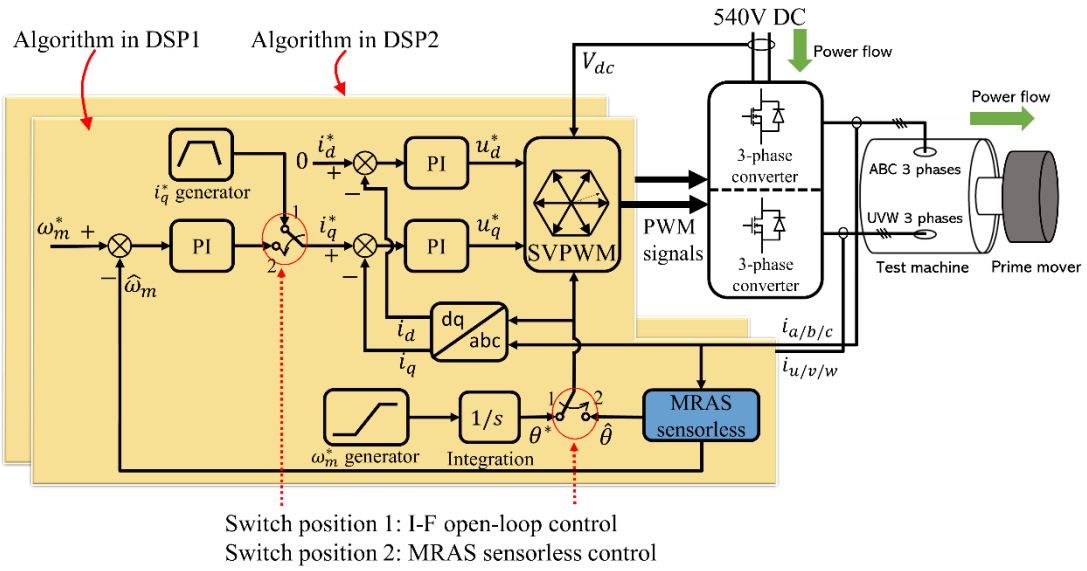


Fig 7.3. Control diagram for green-taxiing motoring mode

7.1.3 Experimental Results

The green-taxiing test will validate the acceleration process from zero speed to the maximum speed (14.2krpm) without a position sensor. To achieve that goal, the prime mover is disconnected with power and driven by the developed ACHIEVE machine.

Fig 7.4 shows the experimental result of I-F open-loop start-up up to 300rpm and the control switching techniques. As can be seen, the speed and current waveforms shown in Fig 7.4(a) and (b) match with the expected waveform in Fig 7.2. The switching point

represents the switching moment from I-F open-loop control to MRAS sensorless control. In Fig 7.4(c), the angle difference ($\theta^* - \hat{\theta}$) between I-F control assumed position and MRAS estimated position converges to zero with i_q reducing. Once this difference is small enough ($< 5°$ in this case), the switching action will be triggered. Then, the machine is under MRAS sensorless control. As can be seen from the Fig 7.4, the actual switching procedure is smooth as expected.

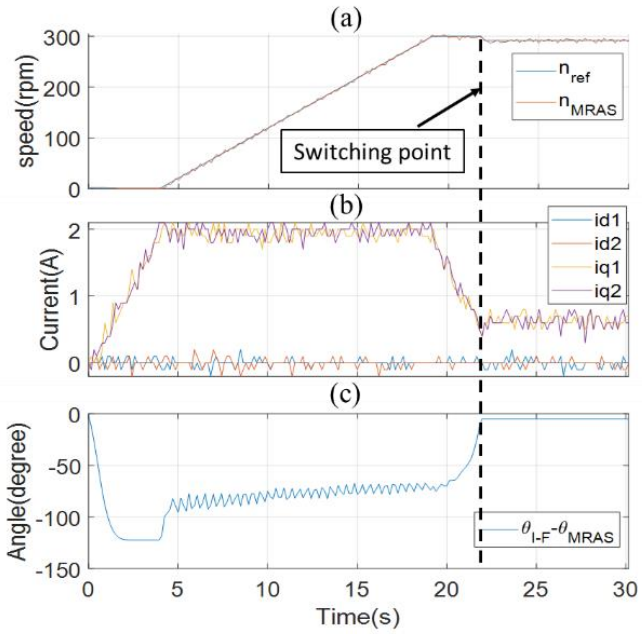


Fig 7.4. Speed and current waveform for I-F open loop start-up from 0 to 300rpm.

Fig 7.5 shows the acceleration under MRAS sensorless control from 300rpm to the maximum speed (14,200rpm). A ramping-up speed reference is given instead of a step command to prevent controller saturation, and the speed accelerates within 60 seconds with a q-axis current below 5A. It can be seen from Fig 7.5(a) that the speed reaches to 14,200rpm smoothly without a large overshot, and the currents are stable during the entire process, which represents a good acceleration performance.

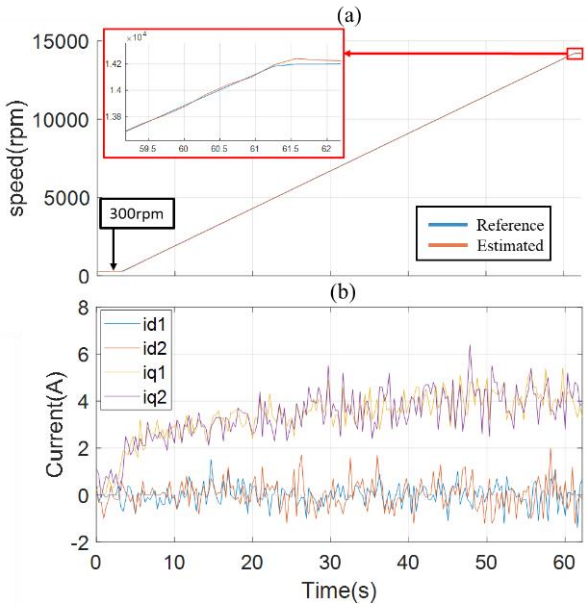


Fig 7.5. Speed and current waveform for MRAS sensorless control acceleration

(a) speed acceleration from 300rpm to 14200rpm. (b) d/q-axis current during acceleration.

The cooling oil temperature is also monitored during the test and listed in Table 7.1. As can be seen, the inlet and outlet coolant temperatures do not change much during the acceleration period. This is due to the fact the prime mover is a freewheel and no load torque has been implemented, thus very small currents are enough for the acceleration.

Table 7.1. Cooling system performance during green taxiing acceleration

Time instant	Inlet temperature	Outlet temperature
When acceleration starts	29℃	33℃
When speed reaches 14.2krpm	29℃	34℃
1 minute after speed reached 14.2krpm	29℃	35℃

7.2 Generation Mode Validation

Within the generation mode, the machine is driven by the turboprop engine with its speed varying between rated speed and maximum speed shown in Fig 7.6. under this condition, the electric machine absorbs mechanical power from the engine shaft and generates electric power to DC-link. The machine should respond rapidly to the power

requirement and keep the DC-link voltage constant with a time-varying shaft speed.

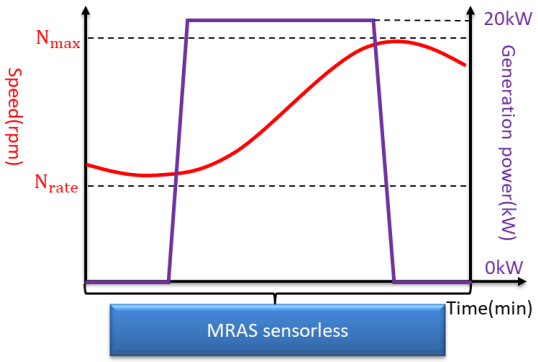


Fig 7.6. Generation mode machine operation diagram

7.2.1 Control Diagram of Generation Mode

In generation mode, the control diagram is shown in Fig 7.7. Compared with green-taxiing mode control, the generation mode control algorithm only has a current inner loop and uses i_q^* as the only input. There is no speed loop as the machine speed will be dominated by the turboprop engine in real applications. The DC-link bus voltage is controlled by the battery connected to the DC bus. Thus, during the generation mode, only the current loops are implemented and the power feeding into the DC bus is controlled by i_q^*.

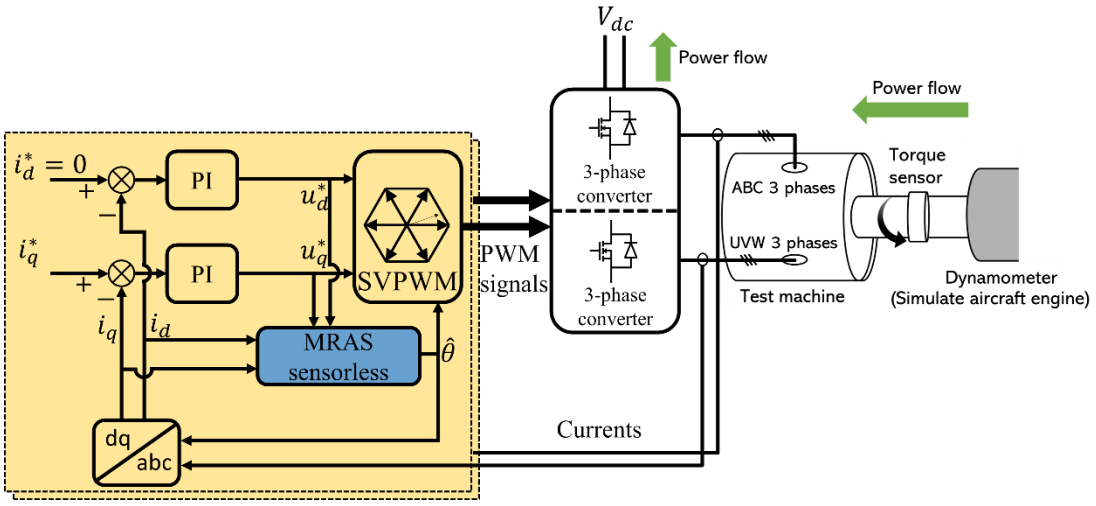


Fig 7.7. Control diagram for generating mode.

7.2.2 Experimental Results

In generating mode, the prime mover is running under speed-controlled mode with

speeds between 12400rpm and 14200rpm. The generating DC-bus power of the dual three-phase machine drive system is controlled by adjusting the q-axis current reference (i_q^*) of the machine. In the following sections, the test results under steady state and dynamic state will be demonstrated.

7.2.2.1 Generation Steady State Test

A serial of steady state tests has been conducted under 12.4krpm and 14.2krpm with different i_q^*, and the result is shown in Table 7.2. The prime mover operates under the speed-controlled mode to maintain the rotor speed constant. For each speed condition, the q-axis current will be set to 4 different reference values (i.e., 0A, -10A, -20A, -30A). The electrical power generated from this ACHIEVE system, i.e., 'Generation power', is measured at the DC-bus. The mechanical power feeding into the generator is derived using the measured average torque (T_{mean}) and the machine speed. The total loss of this ACHIEVE drive system is thus the difference between mechanical power and power received at the DC-bus. It can be calculated by (7.1) as

$$P_{loss} = 1000(T_{mean}\omega_m - P_{DC}) \tag{7.1}$$

where ω_m represents the mechanical rotor speed, and P_{loss} is the total loss of the ACHIEVE drive system including the bearing friction loss, machine copper loss, iron loss and converter loss. The system efficiency (η) of the ACHIEVE system can thus be defined as

$$\eta = \frac{P_{DC}}{P_{DC}+P_{loss}} \tag{7.2}$$

As can be seen from Table 7.2, the system efficiency under all conditions is above 92%, which is a very good performance. The generating DC power also reaches up to 20.94kW at 14.2krpm.

Table 7.2. Test result under generation mode with different q-axis currents

Speed n(krpm)	i_q^*(A)	Generating power P_{DC}(kW)	Mean torque T_{mean}(Nm)	Total loss P_{loss}(W)	System efficiency η
12.4	0	-0.28	0.20	535	
12.4	-10	6.37	5.29	499	92.73%
12.4	-20	12.54	10.35	900	93.31%
12.4	-30	18.33	15.21	1421	92.81%
14.2	0	-0.26	0.18	523	
14.2	-10	7.30	5.32	611	92.28%
14.2	-20	14.50	10.38	935	93.94%
14.2	-30	20.94	15.19	1648	92.70%

Some test waveforms are shown below to demonstrate the machine status under generation mode. Fig 7.8 shows the experimental result under the condition of n =12.4krpm and $i_q^* = -30$A. The waveform data is sampled at 40kHz which is the same as PWM frequency. The estimated speed, given by Fig 7.8(a), can track the actual speed (12.4krpm) despite some noises are observed. In Fig 7.8(b), the average d/q-axis currents are controlled properly and well match their command values. This proves that the current PI control loop works well. The duty cycle in Fig 7.8(c) is a smooth SVPWM waveform with a fundamental frequency component and its third harmonics. All these waveforms prove the machine can work properly at low-end generation speed and full current, i.e., n =12.4krpm and $i_q = -30$A.

The test waveform at another situation, n = 14.2krpm and $i_q^* = -30$A , is demonstrated in Fig 7.9. The estimated speed shown in Fig 7.9(a) is around the actual speed (14.2krpm). The d/q-axis currents (Fig 7.9(b)) and duty cycle (Fig 7.9(c)) also show stable performance as expected.

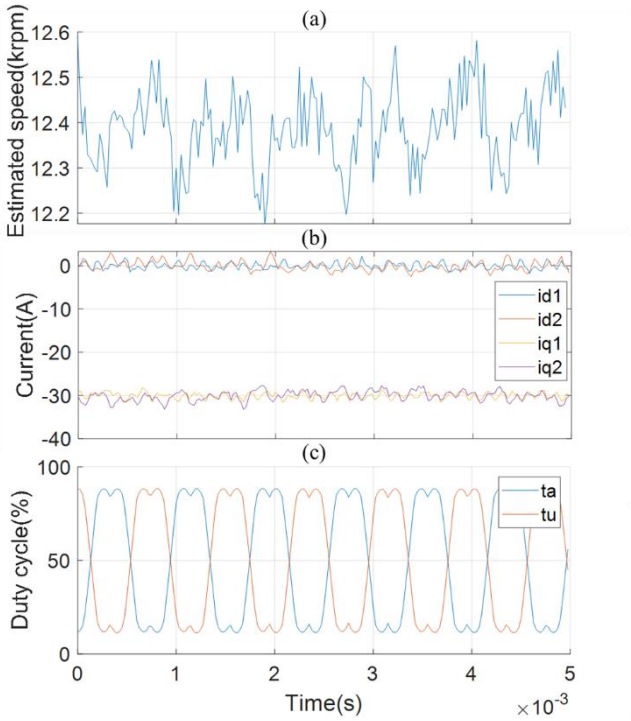


Fig 7.8. Experimental stable state results at n=12.4krpm, iq^*=-30A

(a) estimated speed, (b) d/q-axis currents, (c) duty cycle of A and U phase

When the machine is running under the two situations mentioned above, the stabilized temperatures at different monitoring points are recorded in Table 7.3. As can be seen, the SiC module reaches its maximum up to 106°C, but it is still below the temperature limit of this module (125°C) [57]. The converter board temperature is 42°C, which is far below its limit (85°C). As for the coolant temperature, it has a rise of only 3°C when passing through the power electronic converter. On the contrary, the temperature rises between the inlet and outlet of the machine are quite high with 15°C and 17°C for 12.4krpm and 14.2krpm respectively. The coolant temperature rises in the machine are mainly due to the losses in machine windings. Comparing the coolant temperature rise under the two situations in Table 7.3, it can be seen the heat generated at $n = 14.2$krpm is larger than that at $n = 12.4$krpm, which matches with the total loss listed in Table 7.2.

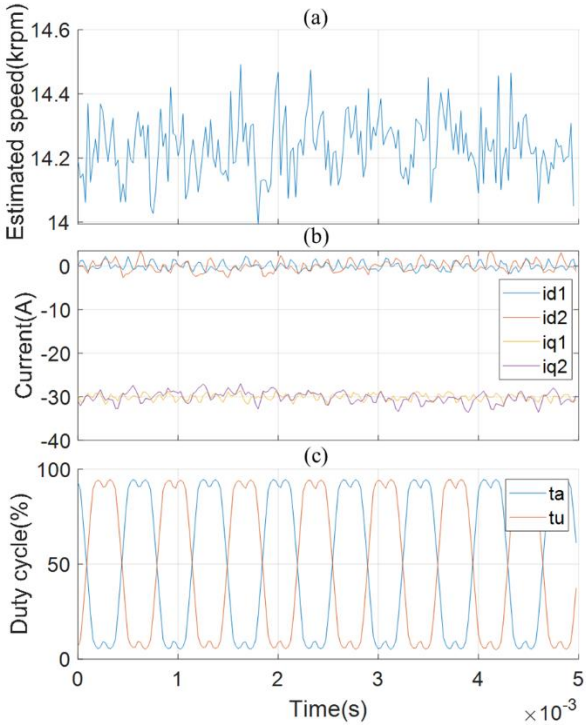


Fig 7.9. Experimental stable state results at speed=14.2rpm, iq*=-30A
(a) estimated speed, (b) d/q-axis currents, (c) duty cycle of A and U phase

Table 7.3. The stabilized temperature under different operating points

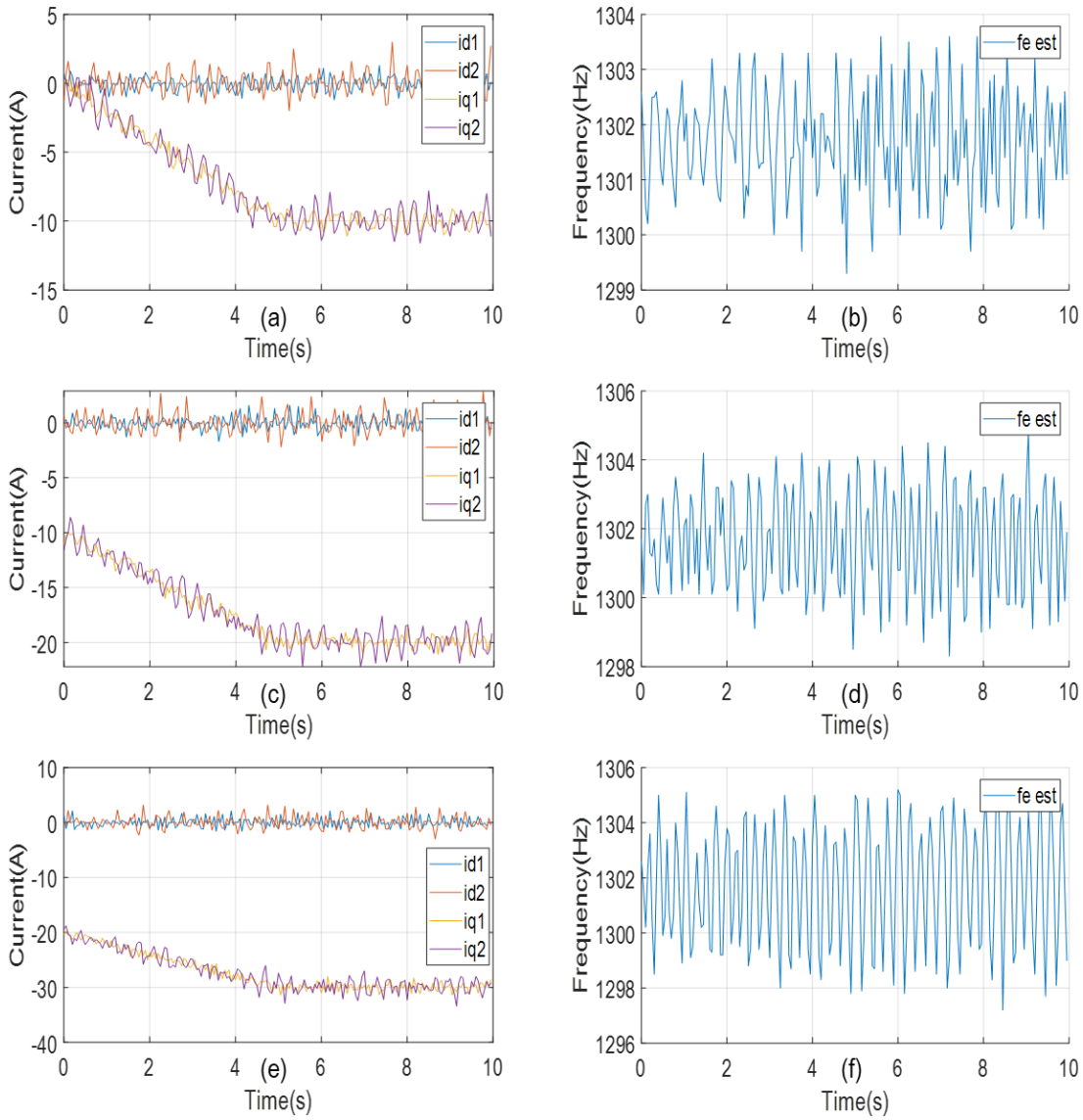
Monitoring point	Stabilized Temperature (°C) at n=12.4krpm, i_q^*=-30A	Stabilized Temperature (°C) at n=14.2krpm, i_q^*=-30A
SiC module 1	78	71
SiC module 2	106	90
Converter board	40	42
Coolant inlet of the power converter	32	30
Coolant outlet of the power converter	35	33
Coolant inlet of machine	35	33
Coolant outlet of machine	50	50

Overall, this section demonstrates the test result of the dual 3-phase machine under generation modes. The test is conducted at different speeds and different powers. The estimated speed, currents, duty cycles, and temperatures are monitored and displayed to demonstrate the performance of the machine. The conclusion is this dual three-phase machine can generate stable DC power as required with all components within its temperature limits.

7.2.2.2 Generation Dynamic State Test

The dynamic generation mode test is conducted under two scenarios. Scenario 1 is holding the speed at 13krpm and changing the q-axis current reference, which will change the generation power correspondingly. Scenario 2 holds the q-axis current at -30A and changes the shaft speed by the prime mover.

In scenario 1, the prime mover drives the ACHIEVE machine up to 13krpm and maintains this speed. At the same time, the ACHIEVE machine operates in the current closed-loop control. The d- and q-axis current references (i_d^*, i_q^*) are set to 0 at the beginning. To validate the dynamic performance, three types of q-axis current changes are conducted at 13krpm, and the test waveforms are given in Fig 7.10. When the i_q^* is set to ramping decrease from 0A to -10A, the d- and q-axis currents and estimated speed are given in Fig 7.10(a) and (b) respectively. As can be seen, the estimated speed keeps around 13krpm during the dynamic period, and the d/q-axis currents follow their references as well. Fig 7.10(c) and (d) demonstrate the currents and estimated speed when i_q^* decreases from -10A to -20A, and Fig 7.10I and (f) are the currents and estimated speed with i_q^* decreasing from -20A to -30A. All the waveforms in Fig 7.10(a)-(f) indicate the sensorless algorithm operates stably despite of i_q^* variation.



(a) Fig 7.10. Experimental dynamic result in scenario 1 with n=13kra) Currents with i_q^* from 0A to -10A; (b) Speed with i_q^* from 0A to -10A; (c) Currents with i_q^* from -10A to -20A; (d) Speed with i_q^* from -10A to -20I(e) Currents with i_q^* from -20A to -30A; (f) Speed with i_q^* from -20A to -30A

In scenario 2, the machine speed is driven up to 12.4krpm by the prime mover at the beginning. The ACHIEVE machine operates in the generation mode with $i_d^* = 0A$, $i_q^* = -30A$. Then, the prime mover increases speed to 14.2krpm with the current reference unchanged. The current and estimated speed waveforms are demonstrated in Fig 7.11. As can be seen from it, when the speed is increasing, the d- and q-axis currents are very stable without any obvious fluctuation. This is what we expect because the control algorithm won't be affected by the speed variation.

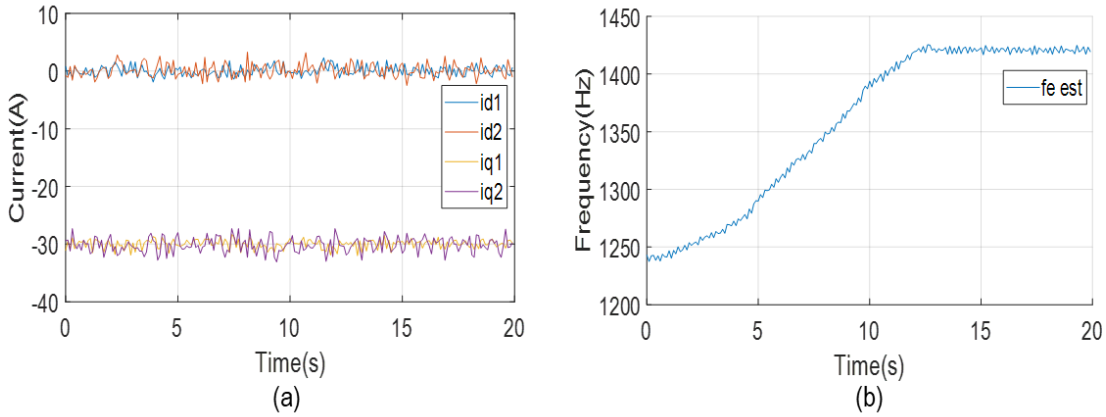


Fig 7.11. Experimental dynamic result in scenario 2 with i_d^*=0A, i_q^*A

(a) (a) Current with speed from 12.4krpm to 14.2krpm; (b) Estimated speed with actual speed changes from 12.4krpm to 14.2krpm

Overall, the test results in scenarios 1 and 2 demonstrate the good dynamic performance of the dual 3-phase machine in generation mode. When the electrical load (i_q) changes, the estimated speed is still effective and stable. When the shaft speed varies, the d- and q-axis currents are still stabilized at their references as well. These test results match our expectations. It can be concluded that the speed variations and generated power won't affect the control algorithm stability.

7.3 Experimental Validation of The Stability Analysis Method

In this section, the test rig will be used to validate the stability analysis method proposed in Chapter 5. The experimental results shown in this section are a supplement to the simulation results in Chapter 5. The experiments are conducted to validate the developed stability analysis method both with the 1st-order MRAS adaptive model and the 2nd-order MRAS adaptive model. The experimental result will also validate the superiority of the 2nd-order adaptive model.

7.3.1 1st-Order MRAS Adaptive Model Validation

The experiment is designed to validate the correctness of the proposed stability analysis method with the 1st-order MRAS adaptive model. The machine will be tested under two operation points shown in Fig 7.12 (i.e., e, f) with their dedicated parameters listed in Table 7.4. The simulation results at those two points are presented in section 5.2.2.

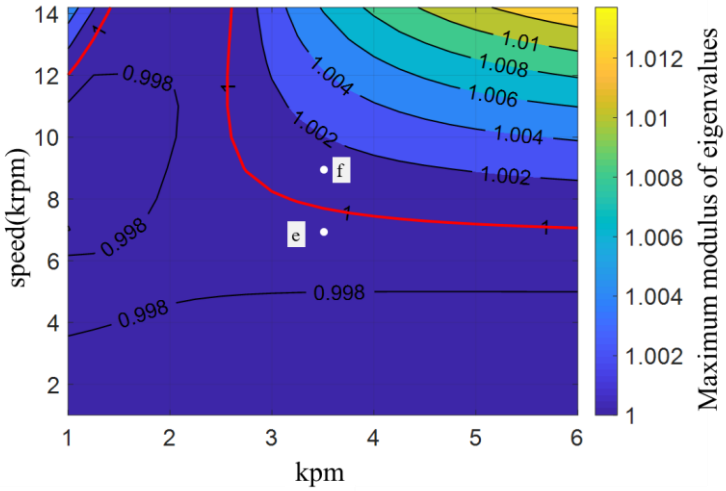


Fig 7.12. The maximum eigenvalue map with k_{im}=5000 for the 1st-order adaptive model

Table 7.4. Selected operating points parameters for 1st-order adaptive model

Operating point	k_{pm}	k_{im}	speed(krpm)	Position in Fig 7.12
e	3.5	5000	7	Stable area
f	3.5	5000	9	Unstable area

In the experiment, the prime mover is under speed-controlled mode and its speed is set to 7krpm and 9krpm as the simulation scenarios at operating points 'e' and 'f'. The machine is under d/q current close loop mode control with current references set to 0A. The factors of the Current PI controller and MRAS PI controller are selected the same as the simulation scenario ($k_{pm} = 3.5, k_{im} = 5000$). All these configurations have only one purpose which is to make sure the experiment condition same as the simulation.

The experimental results of the estimated speed are presented in Fig 7.13. When the

real speed is 7krpm, it can be seen that the estimated speed is around 7krpm as well. The maximum derivation to the real speed is only 7.032krpm. However, when the real speed is 9kprm, the estimated speed fluctuates severely from 8.713krpm to 9.429krpm, indicating the MRAS sensorless control algorithm is not stable anymore. The oscillation frequency is measured as 833Hz.

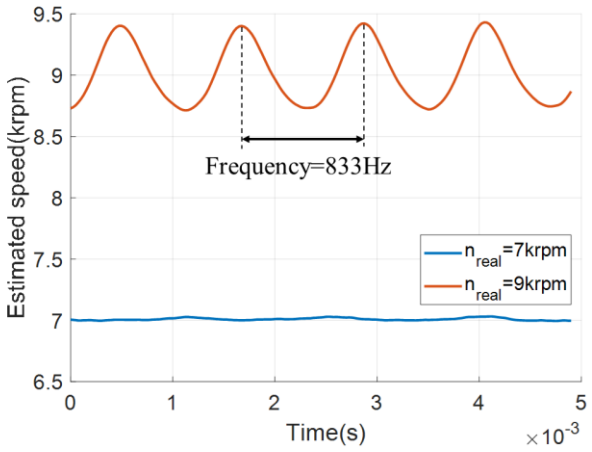


Fig 7.13. Experimental estimated speed comparison with n=7krpm and 9krpm

In Fig 7.14, the d/q-axis currents at those two conditions are demonstrated. The d/q-axis current references are 0A during the test, thus the sampled currents should be also around 0A. When the real speed is 7krpm, the sampled d/q-axis currents for the two 3-phase are given by Fig 7.14 (a), which has an average value of 0A and ripple between -2A to +2A. This ripple has many sources, such as PWM harmonics, current sampling noise, shaft misalignment, etc, but these interferences don't influence the system stability. However, when the real speed is at 9krpm, the current waveform given by Fig 7.14 (b) starts to oscillate and isn't stable anymore. The fluctuating currents can reach up to +15A and down to -13A, which will cause larger torque ripple, higher loss, and even damage to the rotor. Therefore, this situation should be avoided whenever possible.

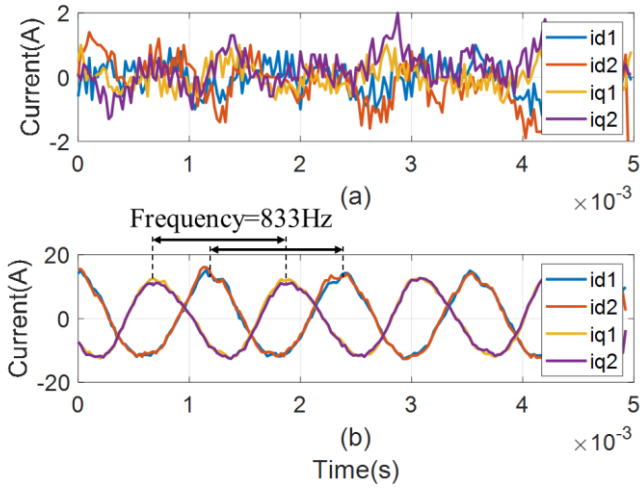


Fig 7.14. Experimental d/q-axis current comparison with n=7krpm (a) and 9krpm (b)

In addition, the oscillation frequencies of the i_d and i_q at 9krpm are also about 833Hz, which are the same as the oscillation frequency of the estimated speed waveform in Fig 7.13. This oscillation frequency is decided by the unstable eigenvalues of its small-signal model. At the operating point with $k_{pm} = 3.5, k_{im} = 5000$ and n=9krpm, there is only one pair of complex eigenvalues with their moduli larger than 1.0, which have been highlighted by red arrows in Fig 7.15 below. Using a MATLAB tool, it can be calculated that the damping factors and natural frequency of this pair of complex eigenvalues are calculated as -0.0081 and 854.7Hz, respectively. Meanwhile, the oscillation frequencies of id/iq and speed are measured as 833Hz, which only has a 2.5% error to the natural frequency of the eigenvalues.

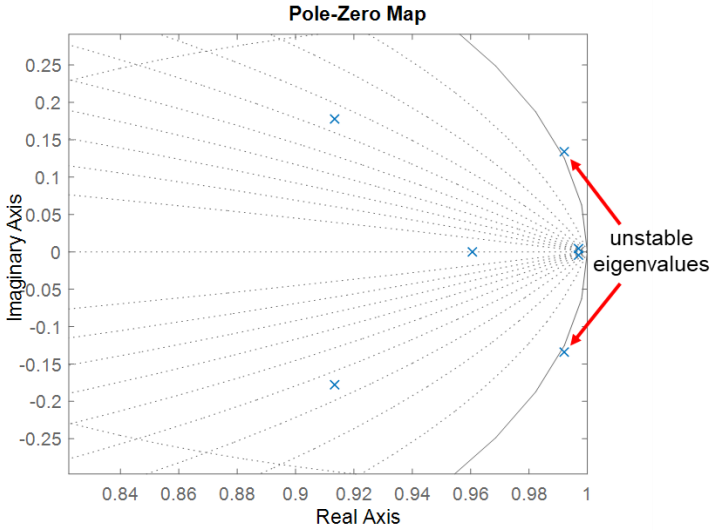


Fig 7.15. The unstable eigenvalues of operating point f in Fig 7.12

Above all, the stability of the experimental result matches the stable boundary in Fig 7.12. In addition, the relationship between the actual oscillation frequency and the natural frequency of the unstable eigenvalues proves the effectiveness of the proposed stability analysis model from another aspect.

7.3.2 2nd-Order MRAS Adaptive Model Validation

To validate the correctness of the 2nd-order MRAS adaptive model, two operating points (m, n in Fig 7.16) are selected during experiments. The maximum eigenvalue contour map in Fig 7.16 shows the stable area of different k_{pm} and speed when $k_{im} = 5000$. The red line represents the stable boundary. The unstable operating point 'm' has $k_{pm} = 4$, $k_{im} = 5000$ and speed=14krpm, and the stable operating point 'n' has $k_{pm} = 3$, $k_{im} = 5000$ and speed=13krpm.

In the experiment, the prime mover is under speed-controlled mode and its speed is set to 14krpm and 13krpm as the operating points 'm' and 'n' indicate. The machine is under d/q current close loop control mode with current references set to 0A. The control algorithm in the microcontroller is generated from the simulation program directly by MATLAB code generator to make sure consistency.

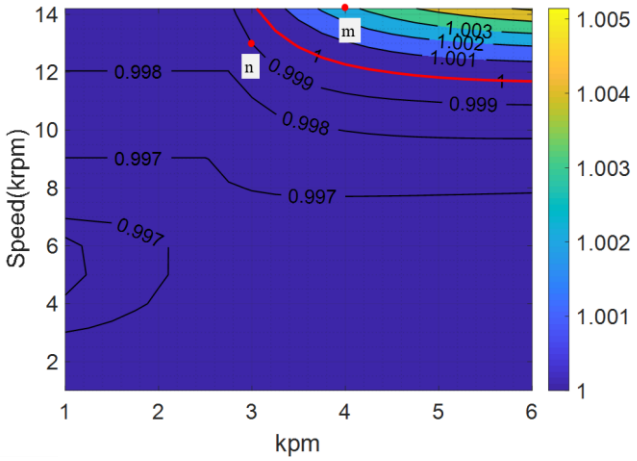


Fig 7.16. The maximum eigenvalue map with k_{im}=5000 for the 2nd-order adaptive model

The experimental results of the estimated speed are presented in Fig 7.17. When testing at operation point 'm', the rotor speed is controlled to 14krpm by the prime mover. The estimated speed has a very large oscillation from 13krpm to 15krpm. The maximum estimated speed is limited to 15krpm by the MRAS sensorless algorithm as the allowed maximum speed is 14krpm. When testing at operating point 'n', the estimated speed is the same as the actual speed (13krpm), indicating the stable and effective operation of the MRAS sensorless algorithm.

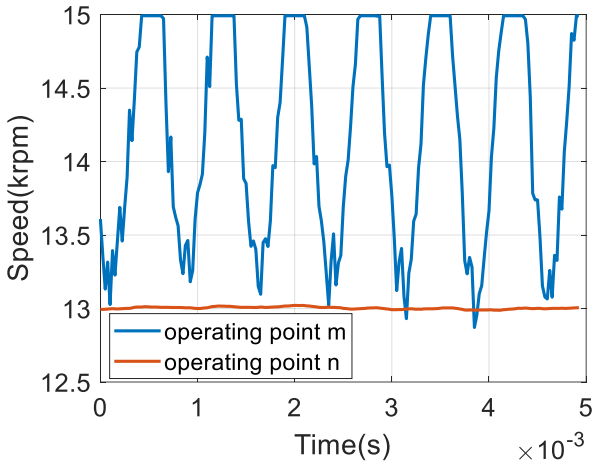


Fig 7.17. Experimental estimated speed comparison at operating points m and n in Fig 7.16

In Fig 7.18, the d/q-axis currents at those two operating points are demonstrated. The d/q-axis current references are 0A during the test, thus the sampled currents should be also around 0A. At the unstable operating point 'm', the sampled d/q-axis currents for

the two 3-phase are given in Fig 7.18(a), which fluctuates between +5A to -5A. However, at the stable operating point 'n', the sampled d/q-axis currents, given by Fig 7.18(b), follow their reference (0A). Above all, the stability of the experimental result matches with the operating points position in Fig 7.16.

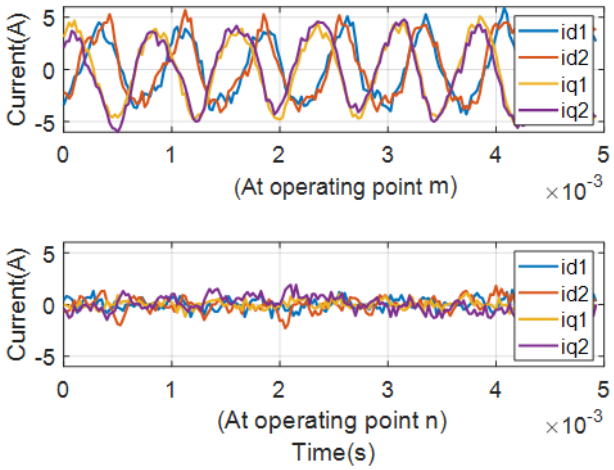


Fig 7.18. Experimental d/q-axis current comparison at operating points m and n in Fig 7.16

7.3.3 Comparison of 1st and 2nd-Order MRAS Adaptive Model

In this section, the experiment will be conducted at the operating point 'a' (i.e., k_{pm}=3, k_{im}=5000, n=5000rpm), shown in Fig 7.19 , using 1st and 2nd-order MRAS adaptive models for comparison studies. As can be seen, operating point 'a' is outside the stable boundary of the 1st-order adaptive model, but inside the stable boundary of the 2nd-order adaptive model. This means that the system will not be stable if 1st-order MRAS is selected but can be stable if 2nd-order MRAS is used. The simulation results at 'a' with the two different orders of adaptive models are presented in section 5.2.4, and the results match the point location. The experiment result in this section will validate the same conclusion.

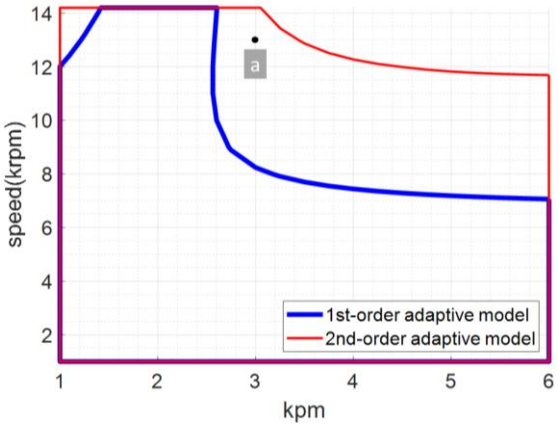


Fig 7.19. Stability boundaries of 1st and 2nd-order adaptive models with k_{im}=5000

The motor speed is controlled by the prime mover at 13krpm. The k_{pm} and k_{im} are set as 3.0 and 5000 respectively. The comparison of estimated speed with different adaptive models is given in Fig 7.20. As can be seen from it, the estimated speed is seriously oscillating with the 1st-order MRAS adaptive model but stable around 13krpm with the 2nd-order MRAS adaptive model. The maximum oscillating current is clamped at 14krpm because a limitation to the estimated speed is added in the MRAS algorithm for protection.

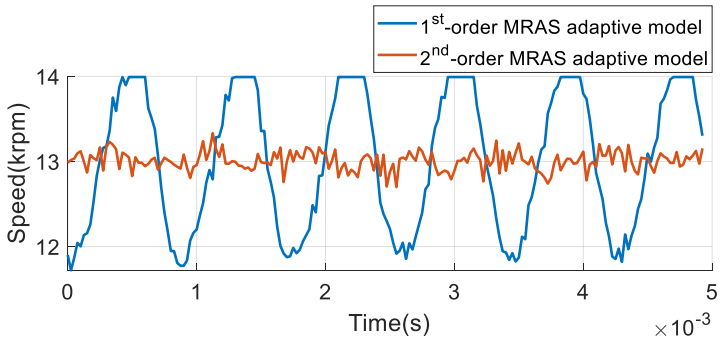


Fig 7.20. Experimental estimated speed comparison for 1st and 2nd-order models at operating point 'a' in Fig 7.19

The sampling currents with the two MRAS adaptive models are demonstrated in Fig 7.21. The currents with 1st order MRAS adaptive model, given by Fig 7.21(a), fluctuate between -5A to +5A, despite the current references are set to 0A. However, the currents with the 2nd-order MRAS adaptive model, shown in Fig 7.21(b), are stable around 0A.

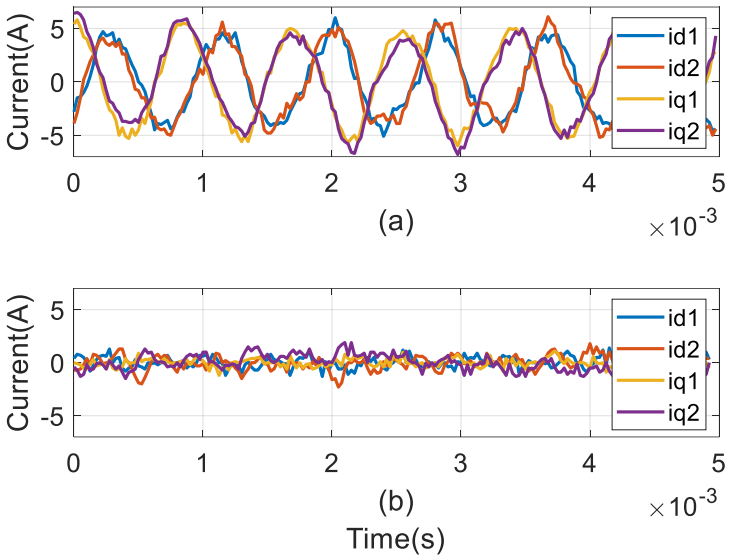


Fig 7.21. Experimental d/q-axis current comparison for 1st and 2nd-order adaptive models at operating point 'a' in Fig 7.19

(a): 1st-order MRAS adaptive model; (b): 2nd-order MRAS adaptive model.

Above all, the experimental result at operating point 'a' shows the stable performance of estimated speed and currents with the 2nd-order MRAS adaptive model as well as the unstable performance with the 1st-order MRAS adaptive model. These results are consistent with the operating point location in Fig 7.19, proving the superiority of the 2nd-order MRAS adaptive model. Therefore, with the guidance of the proposed stability analysis method, we can select proper MRAS PI factors from theoretical analysis first and apply them to real tests with more confidence.

7.4 Conclusion

This chapter shows the experimental results of the dual three-phase M-G drive prototype. Both green-taxiing motoring mode and generation mode are tested under designed speed and power. All monitored machine parameters (i.e., speed, currents, temperatures) indicate the good condition of the M-G drive system. The actual test proves the prototype can accelerate to the designed maximum speed (14.2krpm) and generate enough DC power (20kW) as expected.

In addition, the stability analysis method proposed in Chapter 5 is also validated on this test rig. The experiments of the MRAS sensorless control system with 1st and 2nd-order MRAS adaptive models are presented. The experiments get the same result as the simulation, proving the correctness of the proposed stability analysis method. Furthermore, the experiment result also indicates the superiority of the 2nd-order MRAS adaptive model.

Chapter 8.

Conclusion and Future Work

8.1 Conclusion

This thesis introduces the ACHIEVE electric drive system for the mild-hybridized turboprop. It is an integrated dual 3-phase permanent magnet synchronous machine drive system which works as a generator when the aircraft is in the air, and works as a motor to boost engine start-up when the aircraft is taxiing. It can deliver up to 20kW DC power with speeds from rate speed (12.4krpm) to maximum speed (14.2krpm).

After the machine has been designed by other researchers at Nottingham University, the mathematical models of it were developed by me on both the six-phase frame and the dual d-q frame. The six-phase model is intrinsic and based on the machine parameters (resistance, inductances, magnet flux linkage) from finite element analysis. On the contrary, the dual d-q model is developed on the rotor frame, and is more friendly for control algorithm development as the d- and q-axis are easier to decouple.

The whole speed range sensorless control is proposed for the ACHIEVE machine to meet the project objective. A hybrid sensorless control algorithm was developed for this application. I-F (current-frequency) open-loop control and MRAS (Model Reference Adaptive System) closed-loop control were selected as low and high-speed sensorless methods respectively. Their combination achieved smooth acceleration and stable operation at high speed. The experiment results show the effectiveness of the proposed sensorless methods.

One challenge of MRAS sensorless control for the ACHIEVE application is the stability analysis. There is no clear approach in previous literature about how to analyse the entire MRAS sensorless current closed-loop system in the z-domain with the small signal model. This thesis proposed an eigenvalue-based stability analysis methodology for the ACHIEVE system, which can predict the system stability at any specific operating point. This methodology can guide control parameter selection to ensure steady-state stability. Whilst the transient performance is not part of the research of this thesis.

The ACHIEVE prototype was finally developed by Nottingham University together with other project partners. This thesis includes the author's work on converter and control development, and demonstrates the experimental results of ACHIEVE system at Nottingham University. In addition, the ACHIEVE system was also integrated successfully into the turboprop demonstrator in our project partner facility in France, but the corresponding results were not included in this thesis.

8.2 Future Work

This research project has proposed a mild-hybridized motor-generator drive system for turboprop engines. Several aspects can be investigated further:

- As already mentioned in Chapter 2, the six-phase math model is the most accurate description of the actual machine, whilst the dual d-q models are simplified from it by neglecting the cross-coupling between two 3-phase windings. The simplification makes sense because mutual inductances are relatively small compared with self-inductance. However, it is still a valuable research point to investigate how the cross-coupling of dual 3-phase affects

the control performance.

- Fault monitoring and post-fault control are quite essential topics for this machine. Although this dual three-phase machine was designed to have fault-tolerant capability, my PhD research didn't cover this topic. Many kinds of faults could happen during operation such as winding short circuit, open circuit, demagnetization, etc. The method to distinguish it and the action to deal with it are really useful for aerospace applications.
- The power converter has been tested under the required power rate of the project. Whilst the power can be even higher as the component selections consider some margin. It is worth investigating what the maximum potential is. The reliability of this converter is also a research point.
- Because the two 3-phase channels can work separately, the PWM carriers of the two channels can be configured separately, which leads to the control performance improvement (e.g., torque ripple suppression). Some literature has revealed the possibility of reducing DC-link voltage THD by giving a phase shift to the two-channel carriers. A similar effect can happen on the torque side and need further research.
- The green-taxiing start-up process proposed in this thesis is I-F open-loop sensorless at low speed and MRAS sensorless at high speed. Whilst the I-F open-loop method has inherent drawbacks such as potential start-up failure and initial reverse rotation. Therefore, more advanced low-speed sensorless methods such as high-frequency injection can be applied to this machine to improve the start-up performance.
- As mentioned in Chapter 5, the stable range of MRAS PI parameters can be obtained using the proposed eigenvalue-based stability analysis method.

However, the selection of PI parameters also needs to consider some other impacts such as the transient performance of the controller. Therefore, it's worth investigating more on the PI parameters selection.

- In Chapter 5, the machine parameters used in MRAS sensorless control can affect the estimated position error as well as the stable area. Therefore, the online identification of machine parameters is very important for sensorless control performance. The phase resistance will change with the winding temperature increasing. The machine inductances will also change due to the saturation of lamination. However, the machine parameters that can be monitored are quite limited (e.g., currents, voltages, temperature), so it is a challenging task to identify all the nonlinear machine parameters at the same time.
- The proposed stability analysis method in Chapter 5 only considers the steady state situation, whilst the transient stability of the MRAS sensorless is still uncertain with this method. Therefore, it is worth investigating the dynamic response of the control system with different control parameters.

8.3 List of Publications

The research outcomes include 2 journal papers and 8 conference papers.

The journal papers are:

[1] **Y. Chen**, T. Yang, *et al.,* "Sensorless Control Design of High-Speed Electric Drives in Discrete Time Domain for Mild-Hybrid Turboprop Aircraft Applications," IEEE Transactions on Transportation Electrification, pp. 1–1, 2022.

[2] **Y. Chen**, T. Yang, *et al.*, "Mild hybridisation of turboprop engine with high-power density integrated electric drives," IEEE Transactions on Transportation Electrification, vol. 7782, 2022

The conference papers are:

[1] **Y. Chen** *et al*., "Whole speed range sensorless control for high-speed motor-generator in mild-hybridized turboprop," TSAS2022, 2022.

[2] M. Tang, **Y. Chen**, T. Yang and M. Ilkhani, "Comparison of Three Speed Loop Designs for a High Speed Nine-phase Permanent Magnet Synchronous Machine in More Electric Aircraft," IECON– 48th Annual Conference of the IEEE Industrial Electronics Society, 2022, pp. 1-4.

[3] M. Tang, **Y. Chen** and T. Yang, "Field Weakening Design for a High Speed Nine-phase Permanent Magnet Synchronous Machine in More Electric Aircraft," 2022 IEEE Transportation Electrification Conference & Expo (ITEC), 2022, pp. 1093-1096.

[4] **Y. Chen**, T. Yang, S. Bozhko, U. Nasir, J. R. Rodriguez, and C. F. Garcia, "Model Predictive Control for A Dual Three-Phase Two-Sector Permanent Magnet Synchronous Machine," The 10th International Conference on Power Electronics, Machines and Drives (PEMD 2020), 2021,

[5] **Y. Chen**, S. Bozhko, L. Fan, T. Yang, and M. R. Khowja, "Decoupled Model for Asymmetrical Dual Three Phase Permanent Magnet Synchronous Machine," in 2019 IEEE International Electric Machines & Drives Conference (IEMDC), 2019

[6] L. Fan, T. Yang, **Y. Chen**, and S. Bozhko, "Comparative Study of Sensorless Methods Based on Sliding Mode Observer for Dual Three-Phase Permanent Magnet Synchronous Machine," in The 10th International Conference on Power Electronics, Machines and Drives (PEMD 2020), 2021

[7] Z. Li, **Y. Chen** *et al.*, "Dynamic Modeling of Surface-Mounted Permanent Magnet Motors Considering Saturation," in 2019 IEEE Energy Conversion Congress and Exposition (ECCE), 2019

[8] U. Nasir, S. Chowdhury, A. La Rocca, **Y. Chen** *et al.*, "A SiC based 2-Level Power Converter for Shape-and-Space-Restricted Aerospace Applications," Proc. Int. Conf. Power Electron. Drive Syst., 2019

Appendix A

This appendix will first introduce how to develop the dual three-phase machine model in PLECS. Then, it demonstrates what the simulation models look like in PLECS for the simulations in Chapter 3.

Because the dual three-phase machine is different from the traditional 3-phase machine, there is no ready-built machine model in the simulation platform we used (PLECS). So how to build the dual three-phase machine simulation model will be demonstrated below.

In section 2.2.1, the relationship between the six-phase voltage vector $\boldsymbol{u_s}$ and six-phase current vector $\boldsymbol{i_s}$ is expressed by (2.11). From that expression, it can be seen $\boldsymbol{u_s}$ can be calculated easily with $\boldsymbol{i_s}$ as input. However, because voltage source inverter will be used in our application, $\boldsymbol{u_s}$ instead of $\boldsymbol{i_s}$ should be the input of simulated machine. So, some math derivation is required to build the simulated machine.

Firstly, by moving the current derivative part of (2.11) to the left of the equal sign and the other parts to the right, the new expression can be expressed as follows:

$$\boldsymbol{L_s}\frac{d\boldsymbol{i_s}}{dt} = \boldsymbol{u_s} - R\boldsymbol{i_s} + \omega_e\varphi_f\boldsymbol{\lambda_d} \tag{A.1}$$

Based on (A.1), the current derivative can be calculated depending on the $\boldsymbol{u_s}$, $\boldsymbol{i_s}$, ω_e, and $\boldsymbol{\lambda_d}$. The $\boldsymbol{u_s}$ is not easy to obtain because the neutral point voltage of windings cannot be accessed, but the line-line voltages are easier to get because they are not related to the ground or neutral point. The relationship between phase voltages and line-line voltages is expressed as follows:

$$\boldsymbol{u_{s4}} = \boldsymbol{T_{4\times6}} \cdot \boldsymbol{u_s} \tag{A.2}$$

where $\boldsymbol{u_{s4}} = [u_{ab} \quad u_{bc} \quad u_{uv} \quad u_{vw}]^T$ is a 4*1 vector of line-line voltages; $\boldsymbol{T_{4\times6}}$ is the transforming matrix which has an expression as follows:

$$\boldsymbol{T}_{4\times6}=\begin{bmatrix}1 & -1 & 0 & 0 & 0 & 0\\ 0 & 1 & -1 & 0 & 0 & 0\\ 0 & 0 & 0 & 1 & -1 & 0\\ 0 & 0 & 0 & 0 & 1 & -1\end{bmatrix} \tag{A.3}$$

In addition, (A.1) misses a critical relationship of phase current that the sum of A/B/C phase (also U/V/W phase) currents is zero because of the floating neutral point. Therefore, only 4 currents (i.e., i_a, i_b, i_u, i_v) among those six-phase currents are independent, and they have the relationship as follows:

$$\boldsymbol{i_s}=\boldsymbol{M_{6\times4}}\cdot\boldsymbol{i_{s4}} \tag{A.4}$$

where $\boldsymbol{i_{s4}}=[i_a \quad i_b \quad i_u \quad i_v]^T$ is a 4*1 vector of phase currents; $\boldsymbol{M_{6\times4}}$ is the transforming matrix shown as follows:

$$\boldsymbol{M_{6\times4}}=\begin{bmatrix}1 & 0 & 0 & 0\\ 0 & 1 & 0 & 0\\ -1 & -1 & 0 & 0\\ 0 & 0 & 1 & 0\\ 0 & 0 & 0 & 1\\ 0 & 0 & -1 & -1\end{bmatrix} \tag{A.5}$$

By substituting (A.2) and (A.4) into (A.1), $\boldsymbol{u_s}$ and $\boldsymbol{i_s}$ are replaced by $\boldsymbol{u_{s4}}$ and $\boldsymbol{i_{s4}}$, and the new machine math expression is obtained as follows:

$$\frac{d\boldsymbol{i_{s4}}}{dt}=\text{inv}(\boldsymbol{T_{4\times6}L_sM_{6\times4}})\cdot\left(\boldsymbol{u_{s4}}-R\boldsymbol{T_{4\times6}M_{6\times4}i_{s4}}+\omega_e\varphi_f\boldsymbol{T_{4\times6}\lambda_d}\right) \tag{A.6}$$

where 'inv()' represents the inverse matrix.

Finally, the dual three-phase machine model based on (A.6) can be built with its diagram shown in Fig.A.1 and its actual PLECS model shown in Fig.A.2 below. This model has two controlled current sources for each 3-phase model. The currents are updated from (A.4), and the voltages of the current sources represent the line-line voltages of the machine. The machine speed, assumed to be controlled outside, is another input of this model. By integrating the speed, the rotor position can be calculated, and used in (2.12/14/15) to calculate $\boldsymbol{\lambda_d}$. Then, the current derivatives are calculated by equation (A.6), and the current vector ($\boldsymbol{i_{s4}}$) is updated by an integrator.

Finally, the six-phase currents are calculated by (A.4), and the electromagnetic torque are updated by (2.17).

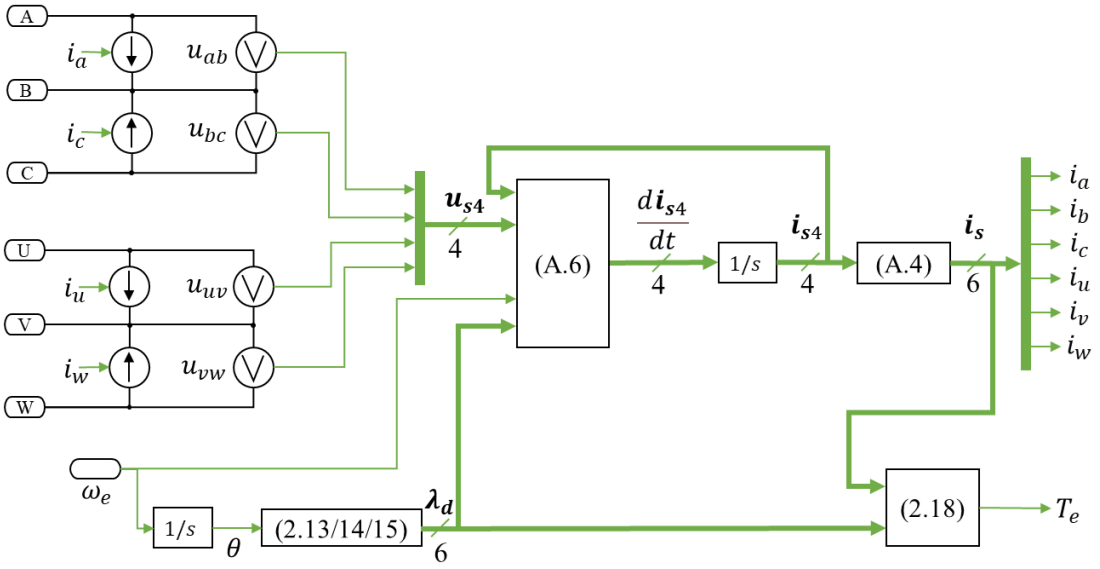


Fig.A.1. Simulation model diagram of this dual three-phase machine

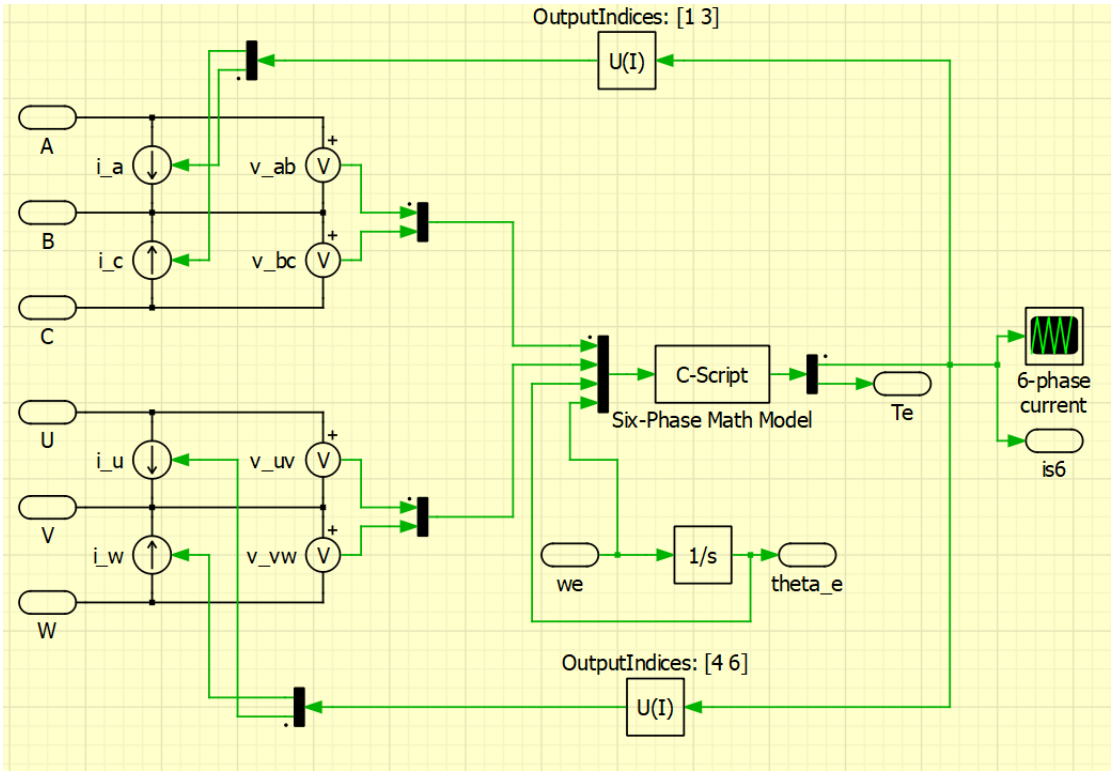


Fig.A.2. Dual three-phase machine simulation model

The rest of the simulation models used in Chapter 3 are demonstrated below:

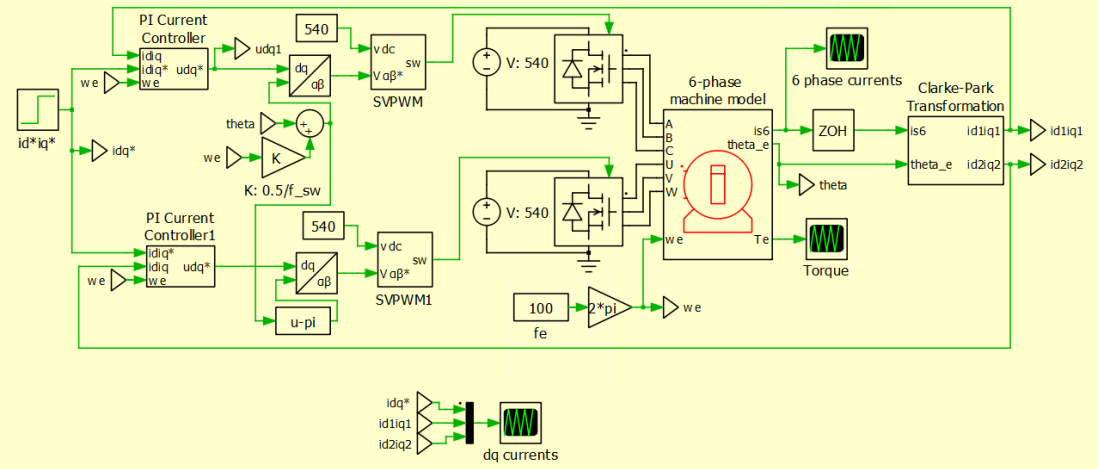


Fig.A.3. Current closed-loop control simulation model consisting of current PI controller (Fig.A.4), current Clarke-Park transformation (Fig.A.5), and dual three-phase machine model (Fig.A.2).

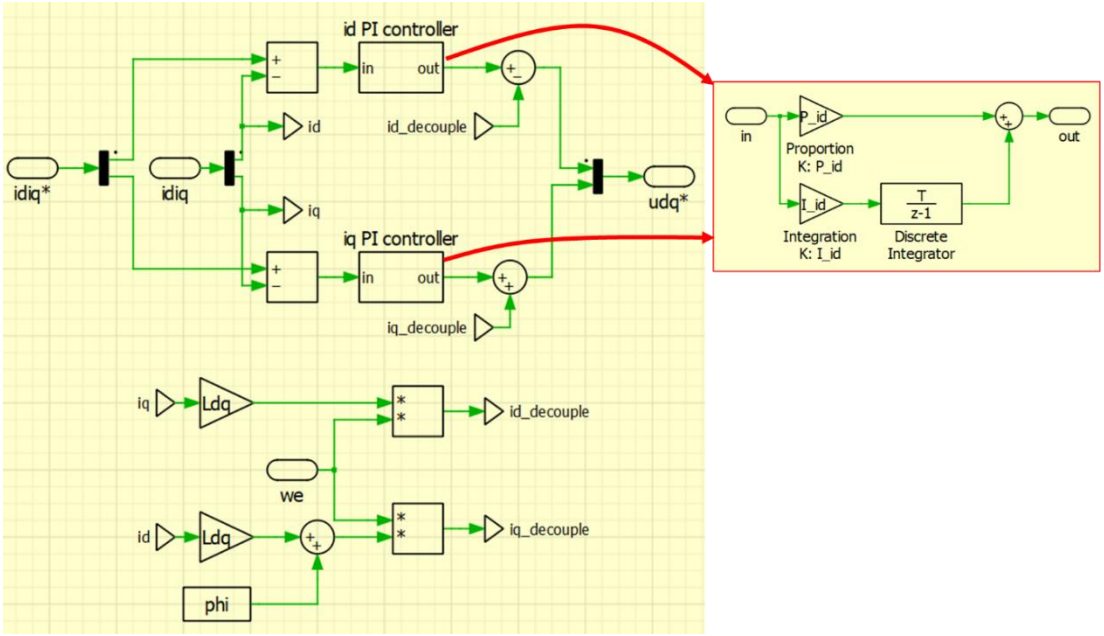


Fig.A.4. Detail of current PI controller

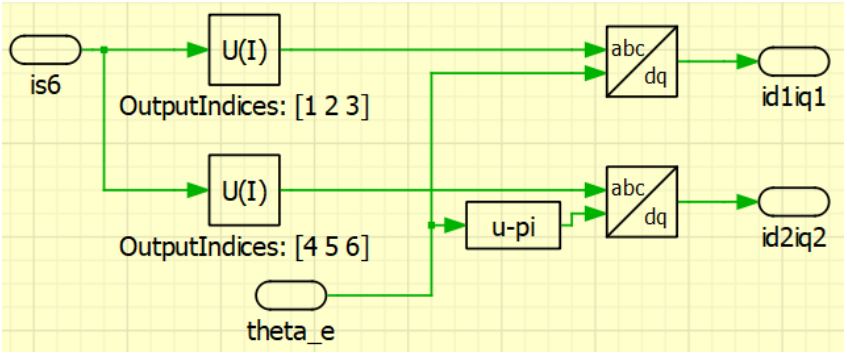


Fig.A.5. Clarke-Park transformation

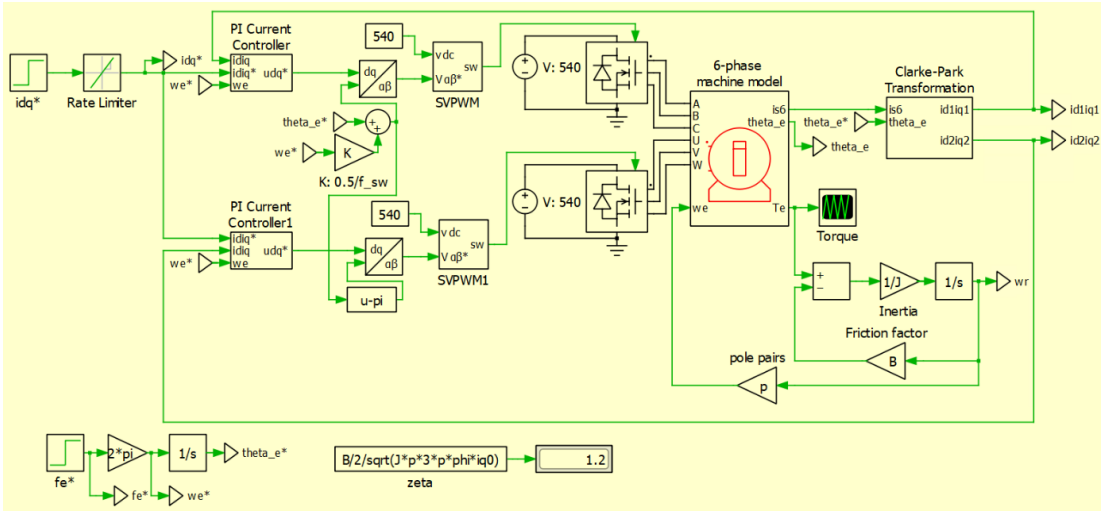


Fig.A.6. I-F open-loop sensorless start-up simulation model

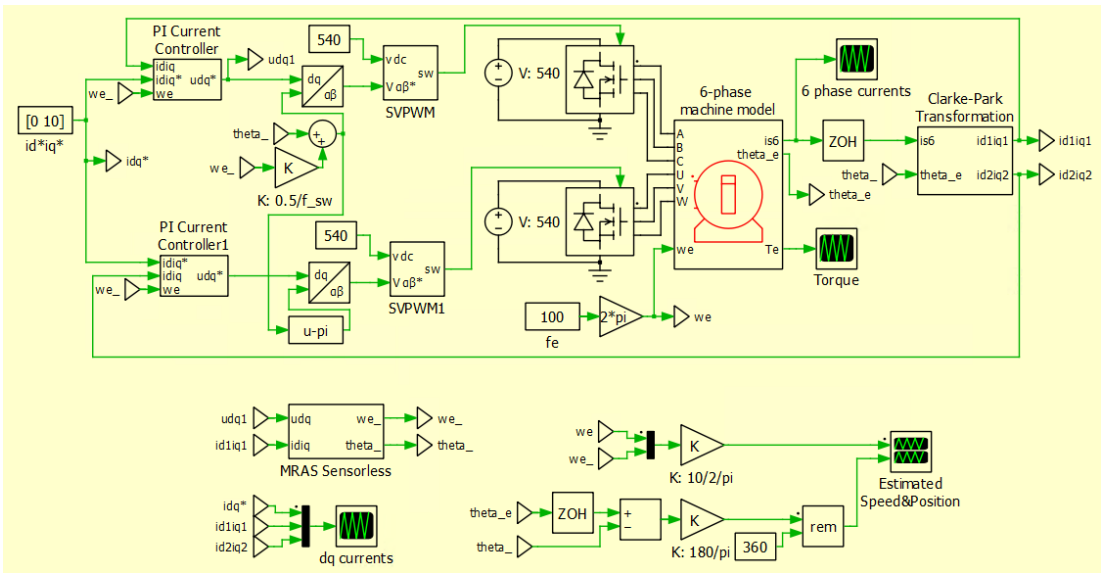


Fig.A.7. MRAS sensorless simulation model

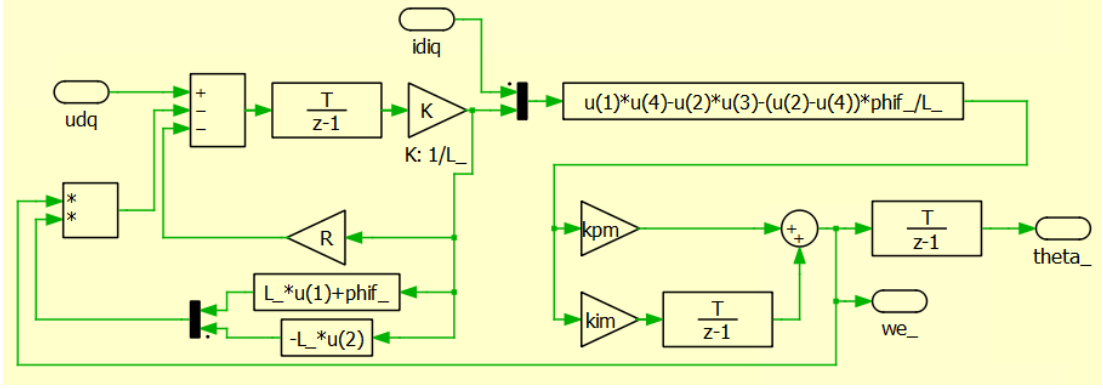


Fig.A.8. 'MRAS sensorless' block in Fig.A.7

Appendix B

This appendix will list the detailed equation derivations in Section 4.4.2 and Section 4.4.4.

I. Voltage Generation (Section 4.4.2) Equation Derivation

a. The Derivation Process of (4.42) And (4.43)

Substituting (4.39) to (4.40), the new expression of $\boldsymbol{U_{\alpha\beta}}(k)$ can be obtained as follows:

$$\boldsymbol{U_{\alpha\beta}}(k) = \boldsymbol{T}^{-1}\left(\hat{\theta}(k-2) + 1.5T_s\hat{\omega}_e(k-2)\right)\boldsymbol{U_{dq}^*}(k-1) \tag{B.1}$$

Then, substituting (B.1) to (4.41), the new expression of $\boldsymbol{U_{dq}}(k)$ can be obtained as follows:

$$\boldsymbol{U_{dq}}(k) = \boldsymbol{T_1}(k)\boldsymbol{U_{dq}^*}(k-1) \tag{B.2}$$

where:

$$\boldsymbol{T_1}(k) = \boldsymbol{T}(\theta\ (k) + 0.5T_s\omega_e)\boldsymbol{T}^{-1}\left(\hat{\theta}(k-2) + 1.5T_s\hat{\omega}_e(k-2)\right) \tag{B.3}$$

Before simplifying the expression of $\boldsymbol{T_1}(k)$ in (B.3), the following derivation of $\boldsymbol{T}(\alpha)\boldsymbol{T^{-1}}(\beta)$ can be obtained by using (4.37) and (4.38).

$$\begin{aligned}\boldsymbol{T}(\alpha)\boldsymbol{T^{-1}}(\beta) &= \begin{bmatrix}\cos\alpha & \sin\alpha\\ -\sin\alpha & \cos\alpha\end{bmatrix}\cdot\begin{bmatrix}\cos\beta & -\sin\beta\\ \sin\beta & \cos\beta\end{bmatrix}\\ &= \begin{bmatrix}\cos(\alpha-\beta) & \sin(\alpha-\beta)\\ -\sin(\alpha-\beta) & \cos(\alpha-\beta)\end{bmatrix}\end{aligned} \tag{B.4}$$

If $\alpha \approx \beta$, $\alpha - \beta$ is close to zero and (B.4) can be linearized as follows:

$$\begin{aligned}\boldsymbol{T}(\alpha)\boldsymbol{T^{-1}}(\beta) &\approx \begin{bmatrix}1-(\alpha-\beta)^2/2 & (\alpha-\beta)-(\alpha-\beta)^3/6\\ -(\alpha-\beta)+(\alpha-\beta)^3/6 & 1-(\alpha-\beta)^2/2\end{bmatrix}\\ &= [1-(\alpha-\beta)^2/2]\boldsymbol{E_2} + [(\alpha-\beta)-(\alpha-\beta)^3/6]\boldsymbol{J_2}\end{aligned} \tag{B.5}$$

where $\boldsymbol{E_2} = \begin{bmatrix}1 & 0\\ 0 & 1\end{bmatrix}, \boldsymbol{J_2} = \begin{bmatrix}0 & 1\\ -1 & 0\end{bmatrix}$.

With the conclusion from (B.5), the expression of $\boldsymbol{T_1}(k)$ in (B.3) can be simplified to (4.43).

b. The Derivation Process of (4.44)

The small signal equation of (4.42) is derived as follows:

$$\Delta \boldsymbol{U_{dq}}(k) = equ\big(\boldsymbol{T_1}(k)\big)\Delta \boldsymbol{U_{dq}^*}(k-1) + \Delta \boldsymbol{T_1}(k) equ\left(\boldsymbol{U_{dq}^*}(k-1)\right) \quad \text{(B.6)}$$

where $equ(*)$ represent the equilibrium operating point value of * when system in stable state, and $\Delta \boldsymbol{U_{dq}^*}(k-1)$, $\Delta \boldsymbol{T_1}(k)$ represent the corresponding small signal variables.

Even considering the estimated machine parameters are not equal to real parameters ($\hat{R} \neq R, \hat{L} \neq L, \hat{\varphi}_f \neq \varphi_f$), the estimated speed will still equate with the actual speed in steady state demonstrated in (B.7), otherwise, the system will not be stable. However, the estimated position will not equate with the actual position due to the machine parameters mismatch. In the stable state, the estimated position error will stabilize to $\theta_{\Delta equ}$ with the expression in (B.8).

$$\lim_{k\to\infty}(\hat{\omega}_e(k-1) - \omega_e) = \lim_{k\to\infty}(\hat{\omega}_e(k-2) - \omega_e) = 0 \quad \text{(B.7)}$$

$$\lim_{k\to\infty}\left(\hat{\theta}(k-1) - \theta(k)\right) = \theta_{\Delta equ} \quad \text{(B.8)}$$

Before calculating the $equ\big(\boldsymbol{T_1}(k)\big)$, the equilibrium value of θ_u needs to be calculated first coming with the procedure in (B.9).

$$\begin{aligned}\lim_{k\to\infty}(\theta_u) &= \lim_{k\to\infty}\left(\theta(k) - \hat{\theta}(k-2) + T_s\big(0.5\omega_e - 1.5\hat{\omega}_e(k-2)\big)\right)\\ &= \lim_{k\to\infty}\left(\theta(k) - \big(\hat{\theta}(k-2) + \hat{\omega}_e(k-2)T_s\big) + 0.5T_s\big(\omega_e - \hat{\omega}_e(k-2)\big)\right)\\ &= \lim_{k\to\infty}\left(\theta(k) - \hat{\theta}(k-1)\right) + \lim_{k\to\infty}\left(0.5T_s\big(\omega_e - \hat{\omega}_e(k-2)\big)\right)\\ &= -\theta_{\Delta equ}\end{aligned} \quad \text{(B.9)}$$

Then, the expression of $equ\big(\boldsymbol{T_1}(k)\big)$ can be obtained in (B.10)

$$\begin{aligned} equ(\boldsymbol{T_1}(k)) &= \lim_{k\to\infty}(\boldsymbol{T_1}(k)) \\ &= \lim_{k\to\infty}\left((1-\theta_u^2/2)\boldsymbol{E_2} + (\theta_u - \theta_u^3/6)\boldsymbol{J_2}\right) \\ &= \left(1-\theta_{\Delta equ}^2/2\right)\boldsymbol{E_2} - \left(\theta_{\Delta equ} - \theta_{\Delta equ}^3/6\right)\boldsymbol{J_2} \end{aligned} \tag{B.10}$$

As for $\Delta\boldsymbol{T_1}(k)$, its final result is calculated in (B.11) by using the expression of $\boldsymbol{T_1}(k)$ in (4.43).

$$\begin{aligned} \Delta\boldsymbol{T_1}(k) &= -\boldsymbol{E_2}\lim_{k\to\infty}(\theta_u)\Delta\theta_u + \boldsymbol{J_2}\left(\Delta\theta_u - 0.5\left[\lim_{k\to\infty}(\theta_u)\right]^2\Delta\theta_u\right) \\ &= \boldsymbol{E_2}\theta_{\Delta equ}\Delta\theta_u + \boldsymbol{J_2}\left(\Delta\theta_u - 0.5\theta_{\Delta equ}^2\Delta\theta_u\right) \\ &= \left[\boldsymbol{J_2}\left(1-0.5\theta_{\Delta equ}^2\right) + \boldsymbol{E_2}\theta_{\Delta equ}\right]\Delta\theta_u \end{aligned} \tag{B.11}$$

where:

$$\Delta\theta_u = \Delta\theta(k) - \Delta\hat{\theta}(k-2) - 1.5T_s\Delta\hat{\omega}_e(k-2) \tag{B.12}$$

Furthermore, we define a new variable $\boldsymbol{V_{equ}^*}$ below as the equilibrium operating point of dq-voltage references to simplify the final expression of (B.6).

$$equ\left(\boldsymbol{U_{dq}^*}(k-1)\right) = \lim_{k\to\infty}\left(\boldsymbol{U_{dq}^*}(k-1)\right) = \boldsymbol{V_{equ}^*} \tag{B.13}$$

Therefore, by substituting (B.10), (B.11), and (B.13) to (B.6), the final small signal equation like (4.44) can be obtained.

II. Current Transformation (Section 4.4.4)

Equation Derivation

a. The Derivation Process of (4.59) And (4.60)

Substituting (4.56) to (4.57), the new expression of $\tilde{\boldsymbol{I}}_{\boldsymbol{\alpha\beta}}(k)$ can be obtained as follows:

$$\tilde{\boldsymbol{I}}_{\boldsymbol{\alpha\beta}}(k) = \boldsymbol{T}^{-1}\left(\theta\ (k-1)\right)\boldsymbol{I_{dq}}(k-1) \tag{B.14}$$

Then, substituting (B.14) to (4.58), the new expression of $\tilde{\boldsymbol{I}}_{\boldsymbol{dq}}(k)$ can be obtained as follows:

$$\tilde{\boldsymbol{I}}_{\boldsymbol{dq}}(k) = \boldsymbol{T_2}(k)\boldsymbol{I}_{\boldsymbol{dq}}(k-1) \tag{B.15}$$

where:

$$\boldsymbol{T_2}(k) = \boldsymbol{T}\big(\hat{\theta}(k-1) - T_s\hat{\omega}_e(k-1)\big)\boldsymbol{T}^{-1}\big(\theta\ (k-1)\big) \tag{B.16}$$

Using the conclusion obtained in (B.5), the expression of $\boldsymbol{T_2}(k)$ can be simplified to (4.59).

b. The Derivation Process of (4.61)

The small signal equation of (4.59) is derived as follows:

$$\Delta\tilde{\boldsymbol{I}}_{\boldsymbol{dq}}(k) = equ(\boldsymbol{T_2}(k))\Delta\boldsymbol{I}_{\boldsymbol{dq}}(k-1) + \Delta\boldsymbol{T_2}(k)equ\left(\boldsymbol{I}_{\boldsymbol{dq}}(k-1)\right) \tag{B.17}$$

where $equ(*)$ represent the equilibrium operating point value of * when system in stable state, and $\Delta\boldsymbol{I}_{\boldsymbol{dq}}(k-1)$, $\Delta\boldsymbol{T}_2(k)$ represent the corresponding small signal variables.

Before Calculating the $equ(\boldsymbol{T_2}(k))$, the equilibrium value of θ_i needs to be calculated first coming with the procedure in (B.22).

$$\begin{aligned}\lim_{k\to\infty}(\theta_i) &= \lim_{k\to\infty}\big(\hat{\theta}(k-1) - \theta(k-1) - T_s\hat{\omega}_e(k-1)\big)\\ &= \lim_{k\to\infty}\big(\hat{\theta}(k-1) - (\theta(k) - T_s\omega_e) - T_s\hat{\omega}_e(k-1)\big)\\ &= \lim_{k\to\infty}\left(\hat{\theta}(k-1) - \theta(k)\right) + \lim_{k\to\infty}\left(T_s\big(\omega_e - \hat{\omega}_e(k-1)\big)\right)\\ &= \theta_{\Delta equ}\end{aligned} \tag{B.18}$$

Then, the expression of $equ(\boldsymbol{T_2}(k))$ can be obtained in (B.19) as follows:

$$\begin{aligned}equ\big(\boldsymbol{T_2}(k)\big) &= \lim_{k\to\infty}\big(\boldsymbol{T}_2(k)\big)\\ &= \lim_{k\to\infty}\left((1-\theta_i^2/2)\boldsymbol{E_2} + (\theta_i - \theta_i^3/6)\boldsymbol{J_2}\right)\\ &= \big(1-\theta_{\Delta equ}^2/2\big)\boldsymbol{E_2} + \big(\theta_{\Delta equ} - \theta_{\Delta equ}^3/6\big)\boldsymbol{J_2}\end{aligned} \tag{B.19}$$

As for $\Delta\boldsymbol{T_2}(k)$, its final result is calculated in (B.20) by using the expression of $\boldsymbol{T_2}(k)$ in (4.60).

$$\begin{aligned}\Delta \boldsymbol{T_2}(k) &= -\boldsymbol{E_2}\lim_{k\to\infty}(\theta_i)\Delta\theta_i + \boldsymbol{J_2}\left(\Delta\theta_i - 0.5\left[\lim_{k\to\infty}(\theta_i)\right]^2\Delta\theta_i\right)\\ &= -\boldsymbol{E_2}\theta_{\Delta equ}\Delta\theta_i + \boldsymbol{J_2}\left(\Delta\theta_i - 0.5\theta_{\Delta equ}^2\Delta\theta_i\right)\\ &= \left[\boldsymbol{J_2}\left(1 - 0.5\theta_{\Delta equ}^2\right) - \boldsymbol{E_2}\theta_{\Delta equ}\right]\Delta\theta_i\end{aligned} \tag{B.20}$$

where

$$\Delta\theta_i = \Delta\hat{\theta}(k-1) - \Delta\theta(k-1) - T_s\Delta\hat{\omega}_e(k-1) \tag{B.21}$$

Furthermore, we define a new variable $\boldsymbol{I_{equ}}$ below as the equilibrium operating point of dq-current to simplify the final expression of (B.17).

$$equ\left(\boldsymbol{I_{dq}}(k-1)\right) = \lim_{k\to\infty}\left(\boldsymbol{I_{dq}}(k-1)\right) = \boldsymbol{I_{equ}} \tag{B.22}$$

Therefore, by substituting (B.19), (B.20), and (B.22) to (B.17), the final small signal equation like (4.61) is obtained.

III. Derivation of $\boldsymbol{\theta_{\Delta equ}}$ in Section 5.1

Replace the $\boldsymbol{V_{equ}}$ in (5.7) by its expression (5.13), a new equation like (B.23) can be obtained.

$$\boldsymbol{A I_{equ}} + \frac{1}{L}\left(\boldsymbol{E_2} - \boldsymbol{J_2}\theta_{\Delta equ}\right)\boldsymbol{V_{equ}^*} + \boldsymbol{G_\varphi} = \boldsymbol{0} \tag{B.23}$$

Multiply $\left(\boldsymbol{E_2} + \boldsymbol{J_2}\theta_{\Delta equ}\right)\boldsymbol{A^{-1}}$ to both sides of (B.23), it can be converted to the following expression:

$$\begin{aligned}\boldsymbol{0} = &\left(\boldsymbol{E_2} + \boldsymbol{J_2}\theta_{\Delta equ}\right)\boldsymbol{I_{equ}}\\ &+\frac{1}{L}\left(\boldsymbol{E_2} + \boldsymbol{J_2}\theta_{\Delta equ}\right)\boldsymbol{A^{-1}}\left(\boldsymbol{E_2} - \boldsymbol{J_2}\theta_{\Delta equ}\right)\boldsymbol{V_{equ}^*}\\ &+\left(\boldsymbol{E_2} + \boldsymbol{J_2}\theta_{\Delta equ}\right)\boldsymbol{A^{-1}}\boldsymbol{G_\varphi}\end{aligned} \tag{B.24}$$

According to equation (5.14), the first item of (B.24) can be replaced by $\boldsymbol{I_{equ}^*}$, so (B.24) can be simplified as follows:

$$\begin{aligned}\boldsymbol{0} = &\boldsymbol{I_{equ}^*}\\ &+\frac{1}{L}\left(\boldsymbol{E_2} + \boldsymbol{J_2}\theta_{\Delta equ}\right)\boldsymbol{A^{-1}}\left(\boldsymbol{E_2} - \boldsymbol{J_2}\theta_{\Delta equ}\right)\boldsymbol{V_{equ}^*}\\ &+\left(\boldsymbol{E_2} + \boldsymbol{J_2}\theta_{\Delta equ}\right)\boldsymbol{A^{-1}}\boldsymbol{G_\varphi}\end{aligned} \tag{B.25}$$

The expression of $\boldsymbol{V}^*_{\boldsymbol{equ}}$ is derived from (B.25) and the derivation is as follows:

$$\begin{aligned}\boldsymbol{V}^*_{\boldsymbol{equ}} &= -L\left[\left(\boldsymbol{E_2}+\boldsymbol{J_2}\theta_{\Delta equ}\right)\boldsymbol{A}^{-1}\left(\boldsymbol{E_2}-\boldsymbol{J_2}\theta_{\Delta equ}\right)\right]^{-1}\left[\boldsymbol{I}^*_{\boldsymbol{equ}}+\left(\boldsymbol{E_2}+\boldsymbol{J_2}\theta_{\Delta equ}\right)\boldsymbol{A}^{-1}\boldsymbol{G_\varphi}\right]\\ &= -L\left[\left(\boldsymbol{E_2}-\boldsymbol{J_2}\theta_{\Delta equ}\right)^{-1}\boldsymbol{A}\left(\boldsymbol{E_2}+\boldsymbol{J_2}\theta_{\Delta equ}\right)^{-1}\right]\left[\boldsymbol{I}^*_{\boldsymbol{equ}}+\left(\boldsymbol{E_2}+\boldsymbol{J_2}\theta_{\Delta equ}\right)\boldsymbol{A}^{-1}\boldsymbol{G_\varphi}\right]\\ &= -L\left[\left(\boldsymbol{E_2}-\boldsymbol{J_2}\theta_{\Delta equ}\right)^{-1}\boldsymbol{A}\left(\boldsymbol{E_2}+\boldsymbol{J_2}\theta_{\Delta equ}\right)^{-1}\boldsymbol{I}^*_{\boldsymbol{equ}}+\left(\boldsymbol{E_2}-\boldsymbol{J_2}\theta_{\Delta equ}\right)^{-1}\boldsymbol{G_\varphi}\right]\\ &= -L\left[\beta^2\left(\boldsymbol{E_2}+\boldsymbol{J_2}\theta_{\Delta equ}\right)\boldsymbol{A}\left(\boldsymbol{E_2}-\boldsymbol{J_2}\theta_{\Delta equ}\right)\boldsymbol{I}^*_{\boldsymbol{equ}}+\beta\left(\boldsymbol{E_2}+\boldsymbol{J_2}\theta_{\Delta equ}\right)\boldsymbol{G_\varphi}\right]\end{aligned} \tag{B.26}$$

where $\beta = 1/(1+\theta^2_{\Delta equ})$.

The expression of $\hat{\boldsymbol{I}}_{\boldsymbol{equ}}$ can be derived from (5.8) as follows:

$$\hat{\boldsymbol{I}}_{\boldsymbol{equ}} = -\hat{\boldsymbol{A}}^{-1}\left(\frac{1}{\hat{L}}\boldsymbol{V}^*_{\boldsymbol{equ}}+\hat{\boldsymbol{G}}_{\boldsymbol{\varphi}}\right) \tag{B.27}$$

By substituting (B.27) into (5.15), a new equation like (B.28) can be derived. The only variable in (B.28) is $\theta_{\Delta equ}$, which is in the expression of $\boldsymbol{V}^*_{\boldsymbol{equ}}$ shown in (B.26). A MATLAB function 'solve()' can be used to calculate $\theta_{\Delta equ}$ from (B.28).

$$\begin{aligned}&\boldsymbol{I}^{*T}_{\boldsymbol{equ}}\boldsymbol{J_2}\hat{\boldsymbol{A}}^{-1}\left(\frac{1}{\hat{L}}\boldsymbol{V}^*_{\boldsymbol{equ}}+\hat{\boldsymbol{G}}_{\boldsymbol{\varphi}}\right)+\boldsymbol{J_1}\left(\boldsymbol{I}^*_{\boldsymbol{equ}}+\hat{\boldsymbol{A}}^{-1}\left(\frac{1}{\hat{L}}\boldsymbol{V}^*_{\boldsymbol{equ}}+\hat{\boldsymbol{G}}_{\boldsymbol{\varphi}}\right)\right)\frac{\hat{\varphi}_f}{\hat{L}}=0\\ \Longrightarrow&\left(\boldsymbol{I}^{*T}_{\boldsymbol{equ}}\boldsymbol{J_2}+\frac{\hat{\varphi}_f}{\hat{L}}\boldsymbol{J_1}\right)\hat{\boldsymbol{A}}^{-1}\left(\frac{1}{\hat{L}}\boldsymbol{V}^*_{\boldsymbol{equ}}+\hat{\boldsymbol{G}}_{\boldsymbol{\varphi}}\right)+\boldsymbol{J_1}\boldsymbol{I}^*_{\boldsymbol{equ}}=0\end{aligned} \tag{B.28}$$

Appendix C

This appendix lists the MATLAB manuscripts for MRAS sensorless stability analysis discussed in Section 5.1.

File name: plot_sum.m

Explanation: This MATLAB manuscript is the top-level code to calculate the maximum eigenvalue of the MRAS sensorless current closed-loop system.

```
%{
This m file calculates the eigenvalue of different kpm,kim, and fe under specific
R/L/phif_ratio, Idqr. It will call two functions:
V_I_equ_calculation() returns equilibrium V&I;
pole_plot3_parameter_mismatch() returns max eigenvalue.
%}
clear; clc;
in.R=0.171;
in.L=530E-6;
in.phif=0.03;
in.R_ratio=1;
in.L_ratio=1;
in.phif_ratio=1;
in.Ts=1/40e3;
in.kp=2;
in.ki=800;
in.Idqr=[0;0];
in.order = 1;
in.decouple = 0;
fe_arry=900;
kpm_arry = 3.5;
kim_arry = 5000;
%% start of for loop
for z=1:size(kpm_arry,2)
for j=1:size(kim_arry,2)
for i=1:size(fe_arry,2)
   in.kpm=kpm_arry(z);
   in.kim=kim_arry(j);
   in.fe=fe_arry(i);

   %% call equ V and I calculation function
   if z==1 && j==1
      y_equ(i)=V_I_equ_calculation(in);
   end
   %% get equ value
   in.Idqest = y_equ(i).Idqest; %estimated I
   in.Idq    = y_equ(i).Idq; %true I
   in.Udqr = y_equ(i).Udqr; %reference V
   in.Udq   = y_equ(i).Udq;   %true V
```

```
    in.theta_err2 = y_equ(i).theta_err2; %table theta error

    %% call eigenvalue calculation function
    y(z,j,i)=pole_plot3_parameter_mismatch(in);

    disp(['Order:' num2str(in.order) '; Decouple:' num2str(in.decouple) ...
            '; R_r:' num2str(in.R_ratio) ...
            '; L_r:' num2str(in.L_ratio) ...
            '; phif_r:' num2str(in.phif_ratio) ...
            '; kpm:' num2str(in.kpm) ...
            '; kim:' num2str(in.kim) ...
            '; fe:' num2str(in.fe)...
            '; idq:' num2str(in.Idqr')...
            '; Max eig is:' num2str(y(z,j,i).maxvector)])
end
disp(' ');
end
end
```

File name: V_I_equ_calculation.m

Explanation: This manuscript has a function called 'V_I_equ_calculation()'. This function calculates the equilibrium operating point of machine based on the inputs (machine and control parameters).

```
function y=V_I_equ_calculation(in)
    %% parameters setup
    R  = in.R;
    R_ = R*in.R_ratio;
    y.R_ratio = in.R_ratio;

    L   = in.L;
    L_ = L*in.L_ratio;
    y.L_ratio = in.L_ratio;

    phif  = in.phif;
    phif_ = phif*in.phif_ratio;
    y.phif_ratio=in.phif_ratio;

    fe=in.fe;
    y.fe=in.fe;

    we=2*pi*fe;
    E2=eye(2);
    J2=[0 1;-1 0];
    J1=[0 1];
    Idqr=in.Idqr;
    y.Idqr=Idqr;
    %% calculate dtheta
    syms dtheta
    Ji=Idqr'*J2+J1*phif_/L_;
    A  =[-R/L we;    -we -R/L];
    A_=[-R_/L_ we; -we -R_/L_];
```

```
    Gphi  =[0;-we*phif/L];
    Gphi_=[0;-we*phif_/L_];
    beta=1/(1+dtheta^2);
    M=(E2+J2*dtheta)*A*(E2-J2*dtheta)*beta^2;
    Udq=-L*(M*Idqr+beta*(E2+J2*dtheta)*Gphi);
    Idq_=-A_\(Udq/L_+Gphi_);
    e=Idqr'*J2*Idq_-J1*(Idqr-Idq_)*phif_/L_;
    result = solve(e==0,dtheta);
    result2=vpa(result)/3.1415926*180;
    [aa, index]=min(abs(result2));
    y.theta_err  =double(result2(index));
    y.theta_err2= y.theta_err/180*pi;
    %% calculate Udq/Udq*/Idq/Idqest
    y.Idq    = (E2+J2*y.theta_err/180*pi)\Idqr;
    y.Udq  = -L*(A*y.Idq+Gphi);
    y.Udqr =(E2-J2*y.theta_err/180*pi)\y.Udq;
    y.Idqest=-A_\(y.Udqr/L_+Gphi_);
end
```

File name: pole_plot3_parameter_mismatch.m

Explanation: This file has a function called 'pole_plot3_parameter_mismatch()'. This function calculate all the eigenvalues of the MRAS sensorless current closed-loop system and return the maximum eigenvalue. This eigenvalue represents the stability of the current closed-loop system.

```
%% calculate pole location at z plane
% this function linearize sin&cos to 2 items
function [y] = pole_plot3_parameter_mismatch(in)
y=in;
%% define constant var
E2=eye(2);
J2=[0 1;-1 0];
J1=[0 1];
Ts=in.Ts;%40e3;
%% define PI parameters
kp=in.kp;
ki=in.ki;
kpm=in.kpm;
kim=in.kim;
Pi=ki*Ts;
Ii=kp+ki*Ts;
Pw=kim*Ts;
Iw=kpm+kim*Ts;
%% define motor parameter
R=in.R;
R_=R*in.R_ratio;
L=in.L;
L_=L*in.L_ratio;
phif=in.phif;
phif_=phif*in.phif_ratio;
Phif_=[0;phif_];
fe=in.fe;
```

```
we=2*pi*fe;

%% use equvilibrium V and I
Iequ_r = in.Idqr; %reference I
Iequ_e = in.Idqest; %estimated I
Iequ_t  = in.Idq; %true I
Vequ_r = in.Udqr; %reference V
Vequ_t = in.Udq;   %true V
theta_err_equ = in.theta_err2; %table theta error
%% Current PI controller intermediate variables
Ii2 = E2*Ii+we*L_*J2;
J5 = Phif_-L_*J2*Iequ_r;
%% motor state equation
A=[-R/L, we;
  -we, -R/L];
F=expm(A*Ts);
Gv=((F-E2)/A)/L;
%% MRAS current estimation
if in.order == 1 %MRAS use 1st order estimation
   A_=(1-Ts*R_/L_)*E2+we*Ts*J2;
   B_=Ts*(J2*Iequ_e-Phif_/L_);
   D_=Ts/L_;
elseif in.order==2 %MRAS use 2nd order estimation
   b0=1-R_*Ts/L_+(R_*Ts/L_)^2/2;
   b1=-Ts^2/2*E2;
   b2=(Ts-R_*Ts^2/L_)*J2;
   b3=Ts^2/(2*L_)*J2;
   b4=(Ts/L_-R_*Ts^2/(2*L_^2))*E2;
   b5=-b3*J1'*phif_;
   b6=-b4*J1'*phif_;
   A_=b1*we^2+b2*we+E2*b0;
   B_=2*b1*we*Iequ_e+b2*Iequ_e+b3*Vequ_r+2*b5*we+b6;
   D_=b3*we+b4;
else
   error('No MRAS order selected');
end
%% MRAS error calculation
C1_=Iequ_r'*J2+phif_/L_*J1;
C2_=Iequ_e'*J2+phif_/L_*J1;

%% Calculate matrix M with new matrix method
i1=[1 2]; i2=[3 4]; i3=[5 6]; i4=[7 8]; i5=[9 10]; i6=11; i7=12; i8=13; i9=14;
i10=15; i11=16; i12=17; i13=18;
M = zeros(18,18);
M(i1,i1)    = E2;
M(i3,i3)    = F;
M(i4,i3)    = E2;
M(i5,i5)    = A_;
M(i6,i6)    = 1;
M(i8,i7)    = 1;
```

```
M(i9,i9)     = 1;
M(i10,i9)   = 1;
M(i11,i10) = 1;
M(i12,i12) = 0;%1;
M(i13,i12) = 1;
% calculate intermediate varible: dIdq_tilde(k)
dIdq_t = zeros(2,18);
dIdq_t(:,i4)  = (1-0.5*theta_err_equ^2)*E2+(theta_err_equ-theta_err_equ^3/6)*J2;
dthetai = [zeros(1,11), -Ts,0,0,1,0,0,-1];
dIdq_t = dIdq_t+(J2*(1-0.5*theta_err_equ^2)-E2*theta_err_equ)*Iequ_t*dthetai;
% calculate intermediate variable: dedq(k)
dedq = -dIdq_t;
% calculate intermediate variable: de(k)
de = zeros(1,18);
de(1,i5)  = C1_;
de = de-C2_*dIdq_t;
% calculate intermediate variable: dUdq1*(k)
if in.decouple == 1 %consider current decouple
   dUdq1 = Ii2*dedq;
   dUdq1(:,i1) = dUdq1(:,i1)+Pi*E2;
   dUdq1(:,i7) = dUdq1(:,i7)+J5;
else
   dUdq1 = Ii*dedq;
   dUdq1(:,i1) = dUdq1(:,i1)+Pi*E2;
end
% calculate intermediate variable: dUdq(k)
dUdq=zeros(2,18);
dUdq(:,i2)  = (1-0.5*theta_err_equ^2)*E2-(theta_err_equ-theta_err_equ^3/6)*J2;
dthetau= [zeros(1,12), -1.5*Ts,0,0,-1,1,0];
dUdq=dUdq+(J2*(1-0.5*theta_err_equ^2)+E2*theta_err_equ)*Vequ_r*dthetau;
% calculate intermediate variable: dwe(k)
dwe = Iw*de;
dwe(1,i6) = dwe(1,i6)+Pw;
% calculate final mateix m
M = M+[dedq; dUdq1; Gv*dUdq; zeros(2,18); B_*dwe+D_*dUdq1; de; dwe;
zeros(1,18); Ts*dwe; zeros(4,18)];

%% Calculate eigenvalue of system matrix M and plot
[y.vectors, y.eig_matrix]=eig(M);
y.eig_arry=diag(y.eig_matrix);
y.maxvector=max(abs(y.eig_arry));
```

Appendix D

The Fig.D.1 below shows the simulation model used in the Section 5.2.

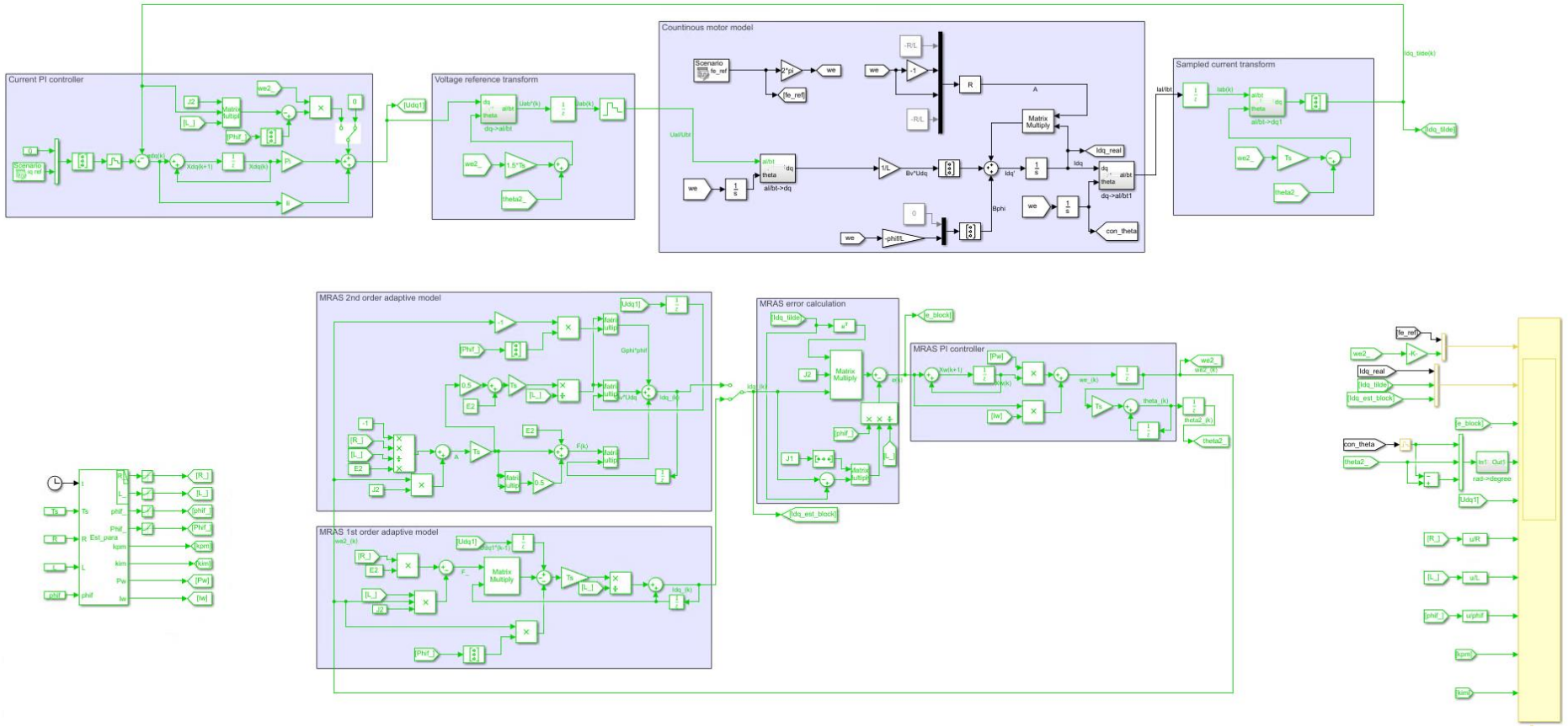


Fig.D.1. MRAS sensorless current closed-loop system simulation model in Simulink

References

[1] "The Climate Crisis – A Race We Can Win | United Nations." https://www.un.org/en/un75/climate-crisis-race-we-can-win (accessed May 07, 2022).

[2] "What Is Climate Change? | United Nations." https://www.un.org/en/climatechange/what-is-climate-change (accessed May 07, 2022).

[3] "Take Action for the Sustainable Development Goals - United Nations Sustainable Development." https://www.un.org/sustainabledevelopment/sustainable-development-goals/ (accessed May 07, 2022).

[4] "COP 26 declaration: International Aviation Climate Ambition Coalition - GOV.UK." https://www.gov.uk/government/publications/cop-26-declaration-international-aviation-climate-ambition-coalition/cop-26-declaration-international-aviation-climate-ambition-coalition (accessed May 07, 2022).

[5] "COP26: securing net zero aviation | Vision | University of Nottingham." https://www.nottingham.ac.uk/vision/securing-net-zero-aviation (accessed May 07, 2022).

[6] V. Madonna, P. Giangrande, and M. Galea, "Electrical Power Generation in Aircraft: Review, Challenges, and Opportunities," *IEEE Trans. Transp. Electrif.*, vol. 4, no. 3, pp. 646–659, 2018, doi: 10.1109/TTE.2018.2834142.

[7] X. Roboam, B. Sareni, and A. Andrade, "More electricity in the air: Toward optimized electrical networks embedded in more-electrical aircraft," *IEEE Ind. Electron. Mag.*, vol. 6, no. 4, pp. 6–17, 2012, doi: 10.1109/MIE.2012.2221355.

[8] J. A. Rosero, J. A. Ortega, E. Aldabas, and L. Romeral, "Moving towards a more electric aircraft," *IEEE Aerosp. Electron. Syst. Mag.*, vol. 22, no. 3, pp. 3–9, 2007, doi: 10.1109/MAES.2007.340500.

[9] L. Fan, "Sensorless Control of Motoring / Generating System for Future More-Electric Turboprop Aircraft," 2021.

[10] A. Barzkar and M. Ghassemi, “Electric power systems in more and all electric aircraft: A review,” *IEEE Access*, vol. 8, pp. 169314–169332, 2020, doi: 10.1109/ACCESS.2020.3024168.

[11] “Small Air Transport TA | Clean Aviation.” https://www.clean-aviation.eu/clean-sky-2/programme-overview-and-structure/clean-sky-2-structure/small-air-transport-ta (accessed May 08, 2022).

[12] “Beechcraft 1900 - Wikipedia.” https://en.wikipedia.org/wiki/Beechcraft_1900 (accessed May 08, 2022).

[13] “Turboprop - Wikipedia.” https://en.wikipedia.org/wiki/Turboprop (accessed May 08, 2022).

[14] “Tech TP demonstrator forges ahead | Clean Aviation.” https://www.clean-aviation.eu/tech-tp-demonstrator-forges-ahead (accessed May 09, 2022).

[15] “Clean Sky VirtualFair.” https://cleansky.virtualfair.be/hangar (accessed May 09, 2022).

[16] G. K. Singh, “Multi-phase induction machine drive research—a survey,” *Electr. Power Syst. Res.*, vol. 61, no. 2, pp. 139–147, 2002, doi: https://doi.org/10.1016/S0378-7796(02)00007-X.

[17] M. R. Khowja, G. Vakil, C. Gerada, T. Yang, S. Bozhko, and P. Wheeler, “Trade-off Study of a High Power Density Starter-Generator for Turboprop Aircraft System,” *IECON 2019 - 45th Annu. Conf. IEEE Ind. Electron. Soc.*, vol. 1, pp. 1435–1440, 2019, doi: 10.1109/iecon.2019.8926961.

[18] N. Bianchi and M. Dai Pre, “Use of the star of slots in designing fractional-slot single-layer synchronous motors,” *IEE Proc. - Electr. Power Appl.*, vol. 153, no. 3, p. 459, 2006, doi: 10.1049/ip-epa:20050284.

[19] “Simcenter MAGNET | Siemens Digital Industries Software.” https://www.plm.automation.siemens.com/global/en/products/simcenter/magnet.html (accessed Jul. 27, 2021).

[20] S. N. Vukosavic, *Electrical Machines*. Springer New York, 2013. doi: 10.1007/978-1-4614-0400-2.

[21] G. Wang, M. Valla, and J. Solsona, “Position sensorless permanent magnet synchronous

machine drives - A review," *IEEE Trans. Ind. Electron.*, vol. 67, no. 7, pp. 5830–5842, 2020, doi: 10.1109/TIE.2019.2955409.

[22] S. Il Kim, J. H. Im, E. Y. Song, and R. Y. Kim, "A New Rotor Position Estimation Method of IPMSM Using All-Pass Filter on High-Frequency Rotating Voltage Signal Injection," *IEEE Trans. Ind. Electron.*, vol. 63, no. 10, pp. 6499–6509, Oct. 2016, doi: 10.1109/TIE.2016.2592464.

[23] G. Scarcella, G. Scelba, and A. Testa, "High performance sensorless controls based on HF excitation: A viable solution for future AC motor drives?," *Proc. - 2015 IEEE Work. Electr. Mach. Des. Control Diagnosis, WEMDCD 2015*, pp. 178–187, Aug. 2015, doi: 10.1109/WEMDCD.2015.7194527.

[24] S. Medjmadj, D. Diallo, M. Mostefai, C. Delpha, and A. Arias, "PMSM drive position estimation: Contribution to the high-frequency injection voltage selection issue," *IEEE Trans. Energy Convers.*, vol. 30, no. 1, pp. 349–358, 2015, doi: 10.1109/TEC.2014.2354075.

[25] L. Chen, G. Götting, S. Dietrich, and I. Hahn, "Self-sensing control of permanent-magnet synchronous machines with multiple saliencies using pulse-voltage-injection," *IEEE Ind. Appl. Soc. - 51st Annu. Meet. IAS 2015, Conf. Rec.*, Dec. 2015, doi: 10.1109/IAS.2015.7356811.

[26] Y. Liang and Y. Li, "Sensorless control of PM synchronous motors based on MRAS method and initial position estimation," *ICEMS 2003 - Proc. 6th Int. Conf. Electr. Mach. Syst.*, vol. 1, pp. 96–99, 2003.

[27] Y. Shi, K. Sun, L. Huang, and Y. Li, "Online identification of permanent magnet flux based on extended Kalman filter for IPMSM drive with position sensorless control," *IEEE Trans. Ind. Electron.*, vol. 59, no. 11, pp. 4169–4178, 2012, doi: 10.1109/TIE.2011.2168792.

[28] A. Andersson and T. Thiringer, "Motion sensorless IPMSM control using linear moving horizon estimation with luenberger observer state feedback," *IEEE Trans. Transp. Electrif.*, vol. 4, no. 2, pp. 464–473, Jun. 2018, doi: 10.1109/TTE.2018.2790709.

[29] W. Qiao, X. Yang, and X. Gong, "Wind speed and rotor position sensorless control for direct-drive PMG wind turbines," *IEEE Trans. Ind. Appl.*, vol. 48, no. 1, pp. 3–11, 2012, doi: 10.1109/TIA.2011.2175877.

[30] Y. Zhao, C. Wei, Z. Zhang, and W. Qiao, “A Review on Position/Speed Sensorless Control for Permanent-Magnet Synchronous Machine-Based Wind Energy Conversion Systems,” *IEEE J. Emerg. Sel. Top. Power Electron.*, vol. 1, no. 4, pp. 203–216, Dec. 2013, doi: 10.1109/JESTPE.2013.2280572.

[31] A. M. Alshawish, R. Ahmadi, and A. Nejadpak, “An optimization based method for design of the adaptive mechanism parameters in a model adaptive reference system estimator in a sensorless motor drive system,” in *2015 IEEE Power and Energy Conference at Illinois (PECI)*, IEEE, Feb. 2015, pp. 1–5. doi: 10.1109/PECI.2015.7064924.

[32] M. Rashed, P. F. A. MacConnell, A. F. Stronach, and P. Acarnley, “Sensorless indirect-rotor-field-orientation speed control of a permanent-magnet synchronous motor with stator-resistance estimation,” *IEEE Trans. Ind. Electron.*, vol. 54, no. 3, pp. 1664–1675, 2007, doi: 10.1109/TIE.2007.895136.

[33] K. K. Prabhakaran and A. Karthikeyan, “Electromagnetic torque-based model reference adaptive system speed estimator for sensorless surface mount permanent magnet synchronous motor drive,” *IEEE Trans. Ind. Electron.*, vol. 67, no. 7, pp. 5936–5947, 2020, doi: 10.1109/TIE.2020.2965499.

[34] Y. Zhang, Z. Yin, X. Sun, and Y. Zhong, “On-line identification methods of parameters for permanent magnet synchronous motors based on cascade MRAS,” *9th Int. Conf. Power Electron. - ECCE Asia "Green World with Power Electron. ICPE 2015-ECCE Asia*, pp. 345–350, 2015, doi: 10.1109/ICPE.2015.7167808.

[35] Young Sam Kim, Sang Kyoon Kim, and Young Ahn Kwon, “MRAS based sensorless control of permanent magnet synchronous motor,” in *SICE 2003 Annual Conference (IEEE Cat. No.03TH8734)*, Aug. 2003, pp. 1632-1637 Vol.2. doi: 10.1080/07313569408955561.

[36] B. Wuri Harini, A. Subiantoro, and F. Yusivar, “Stability of the Rotor Flux Oriented Speed Sensorless Permanent Magnet Synchronous Motor Control,” in *IEEE International Symposium on Industrial Electronics*, IEEE, Jun. 2018, pp. 283–289. doi: 10.1109/ISIE.2018.8433862.

[37] T. Orlowska-Kowalska and M. Dybkowski, “Stator-current-based MRAS estimator for a wide range speed-sensorless induction-motor drive,” *IEEE Trans. Ind. Electron.*, vol. 57, no. 4, pp.

1296–1308, 2010, doi: 10.1109/TIE.2009.2031134.

[38] P. Syam, R. Kumar, S. Das, and A. K. Chattopadhyay, “Review on model reference adaptive system for sensorless vector control of induction motor drives,” *IET Electr. Power Appl.*, vol. 9, no. 7, pp. 496–511, Aug. 2015, doi: 10.1049/iet-epa.2014.0220.

[39] S. Yang, P. Cao, and X. Zhang, “Stability analysis of q-axis rotor flux based model reference adaptive system updating rotor time constant in induction motor drives,” *Trans. Electr. Mach. Syst.*, vol. 1, no. 2, pp. 109–116, 2017, doi: 10.23919/TEMS.2017.7961292.

[40] Y. He, W. Hu, Y. Wang, J. Wu, and Z. Wang, “Speed and Position Sensorless Control for Dual-Three-Phase PMSM Drives,” in *2009 Twenty-Fourth Annual IEEE Applied Power Electronics Conference and Exposition*, IEEE, Feb. 2009, pp. 945–950. doi: 10.1109/APEC.2009.4802776.

[41] X. Qi, Fang and Deng, Zhiquan and Qiu, Zhijian and Wang, “Sensorless technology of permanent magnet synchronous motors based on MRAS,” *Diangong Jishu Xuebao/Transactions China Electrotech. Soc.*, vol. 22, pp. 53--58, 2007, doi: 10.19595/j.cnki.1000-6753.tces.2007.04.009.

[42] M. Ohara and T. Noguchi, “Sensorless control of surface permanent-magnet motor based on model reference adaptive system,” *Proc. Int. Conf. Power Electron. Drive Syst.*, no. December, pp. 608–614, 2011, doi: 10.1109/PEDS.2011.6147313.

[43] Z. Wang, K. Lu, and F. Blaabjerg, “A Simple Startup Strategy Based on Current Regulation for Back-EMF-Based Sensorless Control of PMSM,” *IEEE Trans. Power Electron.*, vol. 27, no. 8, pp. 3817–3825, Aug. 2012, doi: 10.1109/TPEL.2012.2186464.

[44] A. Ştirban, I. Boldea, G. D. Andreescu, D. Iles, and F. Blaabjerg, “Motion sensorless control of BLDC PM motor with offline FEM info assisted state observer,” in *Proceedings of the International Conference on Optimisation of Electrical and Electronic Equipment, OPTIM*, 2010, pp. 321–328. doi: 10.1109/OPTIM.2010.5510439.

[45] M. Fatu, R. Teodorescu, I. Boldea, G. D. Andreescu, and F. Blaabjerg, “I-F starting method with smooth transition to EMF based motion-sensorless vector control of PM synchronous motor/generator,” in *PESC Record - IEEE Annual Power Electronics Specialists Conference*,

2008, pp. 1481–1487. doi: 10.1109/PESC.2008.4592146.

[46] G. Ellis, “Control System Design Guide,” *Control Syst. Des. Guid.*, 2012, doi: 10.1016/C2010-0-65994-3.

[47] Young Sam Kim, Sang Kyoon Kim, and Young Ahn Kwon, “MRAS based sensorless control of permanent magnet synchronous motor,” in *SICE 2003 Annual Conference (IEEE Cat. No.03TH8734)*, Aug. 2003, pp. 1632-1637 Vol.2.

[48] C. Li, G. Wang, G. Zhang, N. Zhao, and Di. Xu, “Review of parameter identification and sensorless control methods for synchronous reluctance machines,” *Chinese J. Electr. Eng.*, vol. 6, no. 2, pp. 7–18, 2020, doi: 10.23919/CJEE.2020.000007.

[49] X. Xiao, Y. Li, M. Zhang, and Y. Liang, “A sensorless control based on MRAS method in interior permanent-magnet machine drive,” *Proc. Int. Conf. Power Electron. Drive Syst.*, vol. 1, pp. 734–738, 2005, doi: 10.1109/peds.2005.1619782.

[50] F. Briz, M. W. Degner, A. Diez, and R. D. Lorenz, “Generalization of linear control tools for complex vectors,” *IFAC Proc. Vol.*, vol. 35, no. 1, pp. 241–246, 2002, doi: 10.3182/20020721-6-ES-1901.00121.

[51] F. Briz, M. W. Degner, and R. D. Lorenz, “Analysis and design of current regulators using complex vectors,” *IEEE Trans. Ind. Appl.*, vol. 36, no. 3, pp. 817–825, 2000, doi: 10.1109/28.845057.

[52] J. Holtz, J. Quan, J. Pontt, J. Rodríguez, P. Newman, and H. Miranda, “Design of fast and robust current regulators for high-power drives based on complex state variables,” *IEEE Trans. Ind. Appl.*, vol. 40, no. 5, pp. 1388–1397, 2004, doi: 10.1109/TIA.2004.834049.

[53] L. Sepulchre, M. Fadel, and M. Pietrzak-David, “Improvement of the digital control of a high speed PMSM for vehicle application,” *2016 11th Int. Conf. Ecol. Veh. Renew. Energies, EVER 2016*, 2016, doi: 10.1109/EVER.2016.7476346.

[54] Bon-Ho Bae and Seung-Ki Sul, “A compensation method for time delay of full digital synchronous frame current regulator of PWM AC drives,” in *Conference Record of the 2001 IEEE Industry Applications Conference. 36th IAS Annual Meeting (Cat. No.01CH37248)*,

IEEE, 2001, pp. 1708–1714. doi: 10.1109/IAS.2001.955763.

[55] “TMS320F28375S-Q1 data sheet, product information and support | TI.com.” https://www.ti.com/product/TMS320F28375S-Q1 (accessed Feb. 17, 2023).

[56] “CAN bus - Wikipedia.” https://en.wikipedia.org/wiki/CAN_bus (accessed Aug. 19, 2021).

[57] “MiniSKiiP.” http://semikron.by/en/MiniSKiiP/ (accessed Mar. 04, 2021).